



NRL/MR/6793--93-7387

AD-A272 020



An 85 GHz Quasioptical Gyroklystron Experiment

RICHARD P. FISCHER
ARNE W. FLIFLET
WALLACE M. MANHEIMER

*Beam Physics Branch
Plasma Physics Division*

October 29, 1993

DTIC
ELECTE
NOV 08 1993
S B D

93-27217



Approved for public release; distribution unlimited.

93 11 5 003

REPORT DOCUMENTATION PAGE			Form Approved OMB No. 0704-0188	
Public reporting burden for this collection of information is estimated to average 1 hour per response, including the time for reviewing instructions, searching existing data sources, gathering and maintaining the data needed, and completing and reviewing the collection of information. Send comments regarding this burden estimate or any other aspect of this collection of information, including suggestions for reducing this burden, to Washington Headquarters Services, Directorate for Information Operations and Reports, 1215 Jefferson Davis Highway, Suite 1204, Arlington, VA 22202-4302, and to the Office of Management and Budget, Paperwork Reduction Project (0704-0188), Washington, DC 20503.				
1. AGENCY USE ONLY (Leave Blank)	2. REPORT DATE October 29, 1993	3. REPORT TYPE AND DATES COVERED Interim		
4. TITLE AND SUBTITLE An 85 GHZ Quasioptical Gyroklystron Experiment		5. FUNDING NUMBERS J0 -67-3046-04		
6. AUTHOR(S) Richard P. Fischer, Arne W. Fliflet, and Wallace M. Manheimer				
7. PERFORMING ORGANIZATION NAME(S) AND ADDRESS(ES) Naval Research Laboratory Washington, DC 20375-5320		8. PERFORMING ORGANIZATION REPORT NUMBER NRL/MR/6793-93-7387		
9. SPONSORING/MONITORING AGENCY NAME(S) AND ADDRESS(ES) Office of Naval Research Department of Energy Arlington, VA 22217-5660 Washington, DC 20545		10. SPONSORING/MONITORING AGENCY REPORT NUMBER		
11. SUPPLEMENTARY NOTES				
12a. DISTRIBUTION/AVAILABILITY STATEMENT Approved for public release; distribution unlimited.			12b. DISTRIBUTION CODE	
13. ABSTRACT (Maximum 200 words) The design and test of a new type of millimeter-wave tube called a quasioptical gyroklystron is reported. The device comprises a pair of quasioptical resonators separated by a drift region, which is powered by an annular electron beam with typical parameters 75 kV beam voltage, 6 A current, and an electron pitch angle of 1.9. The gyroklystron is operated as a free-running oscillator, a mode-primed oscillator, an amplifier, and a phase-locked oscillator. The output resonator is tilted by 2° relative to the plane perpendicular to the electron beam axis, which is predicted to increase the efficiency and operating region of stable, single-mode operation. Experimental measurements indicate that the output is single-moded over nearly all the gyroklystron operating parameter space. A new regime of operation has been studied called alpha priming, where the electron beam parameters are ramped to obtain higher power and efficiency. Peak electronic efficiencies of 22% are measured in a single mode with peak output powers up to 150 kW at 85.5 GHz in 13 microsecond pulses. A depressed collector is added to the experiment to increase the overall efficiency of the tube to greater than 30%. Capacitive probes in the drift tube are used to measure the average pitch angle of the beam electrons, and the results are compared to electron trajectory simulations. Experimental measurements of the output radiation are compared to time-dependent, multimode computer simulations, which demonstrate the advantages of mode priming by prebunching the electron beam and alpha priming. The experimental efficiencies are the highest obtained using a quasioptical gyrotron, and the present experiment also represents the state-of-art in high power phase-locked sources at frequencies near 100 GHz.				
14. SUBJECT TERMS Gyroklystron Quasioptical gyrotrons Gyrotrons Phase Locking Quasioptical gyroklystron			15. NUMBER OF PAGES 197	
			16. PRICE CODE	
17. SECURITY CLASSIFICATION OF REPORT UNCLASSIFIED	18. SECURITY CLASSIFICATION OF THIS PAGE UNCLASSIFIED	19. SECURITY CLASSIFICATION OF ABSTRACT UNCLASSIFIED	20. LIMITATION OF ABSTRACT UL	

Table of Contents

<u>Section</u>	<u>Page</u>
List of Tables	iv
List of Figures	v
Chapter I. Introduction	1
Chapter II. Linear Theory Calculations	14
A. Bunching in a Nonuniform Magnetic Field	14
B. Effect of Velocity Spread and Nonuniform Magnetic Field in Drift Region ..	22
Chapter III. Quasioptical Resonators	31
A. Properties of Quasioptical Resonators	31
B. Cold Tests of Prebunching Resonators	40
Chapter IV. Experimental Apparatus and Diagnostics	53
A. Description of the Experiment	53
B. Millimeter-Wave Diagnostics	72
Chapter V. Experimental Results	78
A. Beam Alpha Measurements	78
B. Mode Priming By Prebunching the Beam	88
C. Alpha Priming	101
D. Mirror Alignment and Second Harmonic Radiation	116
E. Depressed Collector Studies	122
F. Amplifier Operation	128
G. Phase Locking	138
Chapter VI. Multimode Simulations and Discussion	148
A. Generalized Gyrotron Theory	148
B. Alpha Priming Simulations	154
C. Mode Priming Simulations	164
D. Discussion	175
Chapter VII. Conclusion	179
Acknowledgements	182
References	183

List of Tables

<u>Number</u>		<u>Page</u>
1	Summary of prebunching resonator parameters	52
2	Original electron gun design specifications.	55
3	Summary of typical output resonator parameters	68
4	Electron gun parameters for simulations	80
5	Measured and calculated output frequencies with good alignment. . . .	117
6	Measured and calculated output frequencies with misalignment.	119
7	Measured and calculated second harmonic frequencies with misalignment.	120
8	Measured and calculated prebuncher frequencies.	121
9	Experimental parameters for peak efficiency using alpha priming. . . .	153
10	Parameters for multimode simulations.	155

Accession For	
NTIS GRA&I	<input checked="" type="checkbox"/>
DTIC TAB	<input type="checkbox"/>
Unannounced	<input type="checkbox"/>
Justification	
By _____	
Distribution/	
Availability Codes	
Dist	Avail and/or Special
A-1	

DTIC QUALITY INSPECTED 8

List of Figures

<u>Number</u>	<u>Page</u>
1 Cross-section of a quasioptical resonator with annular electron beam.	3
2 Schematic of a two-resonator quasioptical gyroklystron	7
3 Schematic of a mode-locked gyroklystron showing feedback.	8
4 The magnetic field produced on-axis by the cross-bore magnet.	18
5 The change in perpendicular momentum versus frequency detuning.	19
6 Same as Figure 5 for $\alpha = 1.0$	21
7 Velocity spread coefficient versus frequency detuning.	26
8 Same as Figure 7 for $\kappa_0 = 0.8$	28
9 Bunching parameter q versus electron pitch angle α	30
10 Schematic diagram of a quasioptical resonator with input coupling.	32
11 Calculated Q versus mirror separation for the output resonator.	35
12 Output resonator Q versus separation with large coupling holes.	36
13 Output resonator losses versus separation with large coupling holes.	37
14 Calculated Q versus coupling hole radius for the prebuncher.	39
15 Fractional slot loss versus coupling hole radius for the prebuncher.	39
16 Schematic diagram of the cold test set-up.	42
17 Reflection measurements from a prebunching resonator.	44
18 Measured reflection from the prebunching resonator Macor rings.	46
19 Cold test schematic for the final prebunching resonator.	47
20 Measured transmitted signal versus input coupling hole diameter.	48
21 Measured reflection coefficient versus input coupling hole diameter.	49
22 Measured radial scans of the prebunching resonator.	51
23 Photograph of the prebunching resonator and mirror holder.	52
24 Schematic diagram of the quasioptical gyroklystron experiment.	53
25 Schematic diagram of the modulator used in the experiment.	56
26 Beam expansion without a collector trim coil.	58
27 Beam expansion with a collector trim coil.	59
28 Oscilloscope traces of the cathode voltage and collector current.	61

<u>Number</u>		<u>Page</u>
29	Photograph of the drift tube assembly.	62
30	Photograph of the drift tube without the prebunching resonator.	64
31	Normalized $\beta_{ }$ versus pitch angle α	67
32	Resonator Q versus mirror misalignment.	71
33	Simplified schematic of the millimeter-wave diagnostics.	73
34	Cold test set-up used to measure calorimeter absorption.	74
35	Schematic diagram of the heterodyne system.	75
36	Cold test apparatus for the phase detector.	76
37	Diagnostic set-up for phase-locked operation.	77
38	Geometry for the electron trajectory simulations.	79
39	Beam alpha as a function of mod anode voltage divider.	79
40	Calculated beam quality as a function of mod anode voltage divider.	81
41	$\beta_{ }$ as a function of mod anode voltage at 13 A.	82
42	Measured and calculated α as a function of mod anode voltage at 13 A.	84
43	Calculated α as a function of interaction efficiency.	85
44	Measured and calculated α as a function of cathode voltage.	86
45	Intercepted current as a function of cathode voltage.	87
46	Efficiency of the free-running oscillator versus beam voltage.	88
47	Output pulse shape of the free-running oscillator.	90
48	Calculated starting currents of several longitudinal modes.	91
49	Efficiency versus voltage for EIO mode priming operation.	92
50	Detector pulse showing mode competition between two modes.	93
51	Efficiency versus frequency detuning with EIO mode priming.	95
52	Efficiency versus cathode voltage for EIO mode priming at 4.5 A.	96
53	Efficiency versus frequency detuning for EIO mode priming at 4.5 A.	97
54	Alpha versus cathode voltage for three voltage divider settings.	97
55	EIO position for mode priming during rise of the voltage pulse.	100
56	Beam parameters (a) without and (b) with alpha priming.	103
57	Efficiency versus voltage for alpha priming at 10 A.	104

<u>Number</u>	<u>Page</u>
58	Efficiency versus frequency detuning for alpha priming at 10 A. 105
59	Oscilloscope traces: (a) alpha priming and (b) no priming. 106
60	Efficiency versus current for the three operating regimes. 109
61	Several calculated magnetic field tapers used in the experiment. 112
62	Measured efficiency versus magnetic field taper in the output resonator. 113
63	Optimized cathode voltage versus current for mode and alpha priming. . 114
64	Measured efficiency versus collector voltage depression. 123
65	Uncollected current during depressed collector operation. 124
66	Set-up used to measure the EIO phase chirp through the input resonator. 129
67	Phase detector signals showing the phase chirp of the EIO. 130
68	Beat frequency between the EIO and free-running gyrotron. 131
69	Input and output signals during amplifier operation. 132
70	Measured amplifier gain as a function of beam voltage. 133
71	Amplifier operation at the onset of oscillations in the output resonator. 135
72	Balanced mixer signals for the amplifier as the phase shifter is varied. . 137
73	Gyroklystron operation without (a) and with (b) prebunching. 139
74	Gyroklystron operation as the EIO is tuned past the locking edge. . . . 141
75	Balanced mixer traces during phase-locked operation. 142
76	EIO drive power versus phase-locking bandwidth. 144
77	Phase locking at the beginning of the EIO drive pulse. 145
78	Stability region for a pencil beam with $\mu = 10$ 149
79	Stability region for an annular beam with $\mu = 10$ 150
80	Stability region for an annular beam in a tilted resonator. 151
81	Stability region for a pencil beam with $\mu = 17$ 152
82	Evolution of modes for $V = 74.8$ kV and $\delta = 3.3$ 157
83	Efficiency versus detuning δ for $V = 74.8$ kV. 158
84	Same as Figure 83 for 0.4 mm beam displacement. 159
85	Alpha priming and no priming simulations and measurements. 160
86	Alpha priming measurements and simulations versus δ 161

<u>Number</u>	<u>Page</u>
87	Alpha priming measurements and simulations versus voltage for $\alpha = 1.6$. 162
88	Alpha priming measurements and simulations versus δ for $\alpha = 1.6$ 163
89	Simulation with no priming for $V = 70.4$ kV and $\alpha = 1.6$ 165
90	Mode priming simulation for $V = 70.4$ kV and $\alpha = 1.6$ 166
91	Simulations and measured efficiency versus voltage for mode priming. . 167
92	Efficiency versus δ for gyrokystron mode priming. 168
93	Efficiency versus cathode voltage for different bunching parameters. . . 169
94	Efficiency versus time for gyrokystron mode priming at 75 kV. 170
95	Efficiency versus beam voltage for gyrokystron mode priming at 2.5 A. 171
96	ψ as a function of time for $V = 69.5$ kV. 174

AN 85 GHz QUASIOPTICAL GYROKLYSTRON EXPERIMENT

Chapter I

Introduction

For over twenty-five years, gyrotrons have been under development as efficient, high-power sources of coherent electromagnetic radiation[1,2]. As evidence of the rapid progress in recent years, several companies now commercially market gyrotrons with high average power. However, more research is required to fulfill stringent device requirements for future systems. Possible applications of these devices include heating and current profile control in magnetic fusion plasmas, drivers for particle accelerators, high resolution millimeter-wave radar, active atmospheric sensing, and electromagnetic wigglers for free electron lasers. The common element that makes the gyrotron attractive for these varied uses is its ability to provide higher power at higher frequencies than conventional microwave tubes.

The possibility of using millimeter waves for electron cyclotron resonance heating (ECRH) of fusion plasmas has provided a great impetus for source development. Future fusion experiments will require tubes which will operate stably in a single mode and deliver 1 MW or more per unit. Current research programs are concentrating on generating high-power radiation at frequencies of approximately 140 GHz, with future goals of 1 MW at 280 and 560 GHz. These power requirements are several orders of magnitude higher than present sources can provide. There are also a number of applications where phase stability and coherence are important, such as drivers for linear accelerators and high-frequency radar. Gyrotrons with both of these attributes, high power and phase control, would certainly generate a good deal of interest.

The gyrotron converts the transverse energy of the electron beam to radiation fields via the cyclotron maser instability[3,4], where electrons bunch in phase space due to the relativistic mass effect. A conventional gyrotron tube is comprised of a magnetron injection gun, a beam tunnel, a cylindrical cavity, a beam collector, and a vacuum window. In a gyro device, electrons with a large transverse energy spiral along an applied axial magnetic field. When such a beam passes through a cavity where a harmonic of the cyclotron frequency is close to the resonant frequency of the cavity, there can be an efficient exchange of energy between the beam and the wave fields.

Since the frequency of the radiation depends upon the strength of the magnetic field and not an intricate slow wave structure, large cavities may be utilized which have moderate energy density and provide high output powers. Gyrotrons usually operate in a high-order cavity mode and care must be taken to ensure that the device operates in the desired mode.

There are many device configurations which exploit the cyclotron maser instability, including gyrotron oscillators, gyroklystrons, and gyro travelling wave tubes. The most advanced tube in the gyro family is the single-cavity gyromonotron oscillator. Recent experimental results include operation at 140 GHz at power levels of 1.3 MW in 3 μ sec pulses with 40% efficiency[5]. The highest average power attainable to date in devices with comparable frequency is approximately 100 kW continuous-wave (cw)[6], with a near-term development goal of 400 kW. One active area of research is maximizing the efficiency of these high frequency gyrotrons at high beam currents[7]. Possible reasons for low efficiency at high current include a deterioration of the beam's transverse energy, electrostatic instabilities in the electron beam, mode competition effects in the cavity, space charge effects, nonoptimum bunching of the electron beam, and the inability to access the high efficiency region of the parameter space. A novel cavity has been used to increase the bunching of the beam at the entrance of the output cavity and reduce sideband mode competition[8]. This technique has improved both the peak power and efficiency of the gyrotron at a beam current of 40 A.

As the frequency and power of gyrotrons are increased, the dimensions of the cavity must increase to keep ohmic losses at a tolerable level. However, the mode separation in the resonator scales inversely with the volume, i.e. $\Delta\omega/\omega \sim (\lambda/L)^3$. At millimeter wavelengths, the mode density is so high that stable, single-mode emission may be impossible. In 1981, Sprangle *et al.* proposed a variation of the conventional gyrotron called the quasioptical gyrotron (QOG)[9]. This device has the potential for generating high average power at millimeter and submillimeter wavelengths with improved mode stability good efficiency.

The resonator in the quasioptical gyrotron is formed by a pair of spherical mirrors separated by many radiation wavelengths, as shown in Figure 1. The finite size of

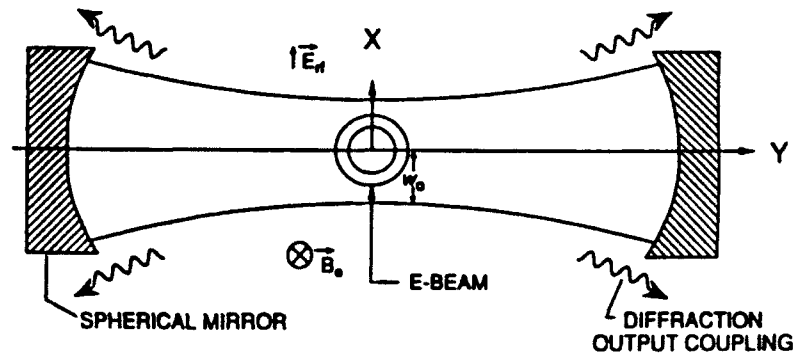


Figure 1: Cross-section of a quasioptical resonator with annular electron beam.

the mirrors causes large diffraction losses for high-order transverse cavity modes. The quality factors for these modes are typically five times less than that of the fundamental TEM_{00l} mode. Thus, only a single transverse mode will oscillate in the gyrotron. The mode density is effectively reduced to that of a one-dimensional resonator where $\Delta\omega/\omega \sim (\lambda/L)$. The resonator mode is approximately Gaussian in shape with a field maximum at the center of the mirror. Since the resonator mirrors are well removed from the interaction region, the ohmic heating density at the mirrors can be made small. The large mirror separation is advantageous because it provides a large interaction region, allowing for high input beam power with low power densities.

In the QOG, the direction of electron beam propagation is perpendicular to the axis of the resonator so that the collection of the radiation is separate from that of the electron beam. This geometry is advantageous for high power devices and allows for a simplified depressed collector. For a symmetric quasioptical resonator, the diffraction losses around the mirrors increase as the mirror separation is increased. However, the radiation waist near the center of the cavity is insensitive to changes in mirror separation. This allows for a method of varying the output coupling while holding the beam-wave interaction length constant. This is a feature unique to the QOG that is advantageous experimentally, since the output coupling is directly related to the electric field strength in the cavity. If the electric field strength becomes too large in the cavity, the separation between the mirrors can be increased to reoptimize the efficiency and

further increase the power.

The first QOG experiment was carried out by Hargreaves *et al.* in 1984 at the Naval Research Laboratory (NRL)[10]. This experiment was performed using an electron beam voltage of 60 kV and a maximum current of 17 A. The mirror separation was 4 cm, which corresponds to a longitudinal mode separation $\Delta f = c/2d = 3.75$ GHz. Since the interaction bandwidth was of the order of the mode density, single-mode operation was expected and observed in the experiment. The highest measured efficiency was 11% and the maximum output power was 80 kW. It was estimated that the electronic efficiency was significantly larger due to large ohmic losses in the resonator and nonoptimum output coupling.

More recent experiments at NRL have utilized a larger resonator and a high power electron gun[11,12]. Typical mirror separations are 25 cm, with the ability to vary the separation from 20 to 28 cm from outside the superconducting magnet dewar. This mirror holder allows for optimization of mirror alignment and translation of the entire resonator with fixed mirror separation to study coupling of the beam to the standing fields in the quasioptical resonator. The new gun, which is identical to the electron gun used in the MIT megawatt gyrotron oscillator program, provides up to 50 A of current at voltages up to 100 kV. To date, the maximum power from this QOG device is 600 kW with a peak efficiency of 13%. Recent results on a QOG have also been obtained at Lausanne[13], and a review of quasioptical gyrotron development is given in [14].

A theoretical model has been developed to calculate the efficiency of the QOG in both single-mode and multimode operation. Under single-mode conditions with a pencil beam placed on a field maximum in the output resonator, it can be shown that the nonlinear analysis is identical to that of the conventional gyrotron except for several normalization constants. Thus, the extensive theory previously developed for the gyrotron may be used[15]. When the effect of the annular electron beam is considered, an averaging process must be performed. Because of the standing fields in the resonator, electrons at different positions experience different electric fields. Some particles pass through field maxima while some pass through nulls. Thus, the efficiency of the QOG will be less than that of a conventional gyrotron due to the beam geometry.

An ideal geometry would use a sheet-beam electron gun where beamlets are placed on field maxima. An alternative is to tilt the resonator axis by a few degrees with respect to the plane perpendicular to the direction of beam propagation[16]. In this geometry, each electron passes through the standing fields of the odd and even longitudinal modes in the resonator. This yields better mode suppression and better single-mode efficiency at the expense of requiring larger electric fields in the resonator. Recent experimental results have shown that the tilted resonator increases the single-mode efficiency (9%) but has little effect on the maximum efficiency (12%) and the parameter space available for stable single-mode operation[17].

The theoretical problem becomes more complicated when more than one longitudinal mode is present in the resonator. For large mirror separations, many longitudinal modes experience gain and the output would be expected to be multimoded. However, it has been shown that it is possible for one mode to nonlinearly suppress other modes[16,18]. Hence, there are regimes where the mode density is high but the output is single-moded. This behavior has been confirmed experimentally under high-power operation, although the output of the QOG is usually multimoded. In a conventional gyrotron, the detuning between the operating frequency and the relativistic cyclotron frequency is selected by adjusting the magnetic field or the beam voltage. In the QOG, however, the detuning is determined by the nonlinear dynamics of the multimode evolution. Hence, it is difficult to predict if the output will be single-moded, and even more difficult to operate the gyrotron at optimum detuning.

Most gyrotron applications require a single-mode output, so that suppressing unwanted longitudinal modes is of interest in the QOG. Even if multimode operation is permitted, it is not clear whether the optimum efficiency of single-mode operation can be obtained. Multimode theoretical efficiencies are comparable to optimum single-mode efficiencies in the QOG[19,20,21], although both of these predictions overestimate experimental results to date. Peak experimental efficiencies are on the order of 14% while multimode simulations predict over 25%.

One technique which can be used to select the optimum longitudinal mode in the output resonator is to use an external source to set up the rf field at the desired fre-

quency. This may be accomplished by direct injection of radiation into the output resonator[22,23] or by prebunching the electron beam in an upstream resonator[23]. Direct injection requires a high power circulator or isolator so that the external source is not locked by the gyrotron. The input coupling system would also have to sustain the high electric fields and large average power flow from the output resonator. These requirements are difficult to satisfy at millimeter wavelengths, so prebunching the electron beam is considered here.

A two-resonator quasioptical gyroklystron, shown in Figure 2, comprises a pair of open resonators separated by a field-free drift region. An extended interaction oscillator (EIO) is used to excite the first resonator. Electron cyclotron absorption provides electrons in the prebunching resonator with a "kick" in perpendicular momentum, depending upon their entrance gyrophase, so that the particles gyrate at different frequencies in the drift region. If the strength of the electric field in the first resonator and the length of the drift region are chosen properly, the electrons will arrive at the output resonator strongly bunched in gyrophase angle and will efficiently give up their energy to the wave fields. Additional cavities and drift regions can be added to increase the phase bunching of the electrons at the entrance of the output cavity.

In much of this work, we consider the case where the beam current is above the threshold current of the output resonator in the absence of a prebunching signal. Thus, this regime of operation is fundamentally different than the gyroklystron amplifier. The strength of the prebunching signal and the frequency difference between the two sources has a profound effect on the operation of the gyroklystron. If the prebunching signal is sufficiently large and the frequency difference small, the gyroklystron will operate as a locked oscillator where the equilibrium has a specified phase[24]. Here the steady state operation of the output resonator depends upon the amplitude, frequency, and phase of the prebunching signal. It is in this regime that the electrons are strongly prebunched and the peak gyroklystron transverse efficiency is higher than that of the single cavity gyrotron[25]. The drive signal is present throughout the duration of the oscillation and has a strong effect on the steady state of the oscillator. A perturbation theory for phase locking by prebunching the electron beam is presented in [26], while the slow-time-scale

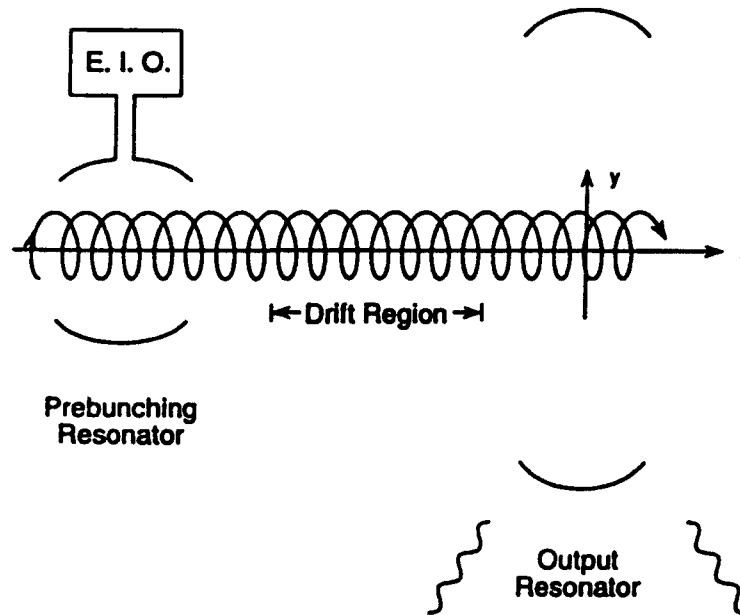


Figure 2: Schematic of a two-resonator quasioptical gyrokystron

equations of motion are solved for both direct injection and prebunching in [27] for a cavity gyrotron.

A second region of operation is the mode-primed gyrokystron, where the external source is used only during the build-up of fields in the output resonator[23]. The pre-bunched electron beam selects a particular longitudinal mode in the output resonator, which is given an initial advantage over neighboring modes. If this mode is stable with respect to decay into sidebands, it will grow and nonlinearly suppress satellite modes. The prebunching signal is used to mode prime the oscillator, and does not affect the frequency of the final state. The main advantage to mode priming is that the beam pre-modulation need only be large compared to the noise present at the start of oscillation in the output resonator. This reduces the power requirement for the millimeter-wave source, which is often a limitation at high frequencies.

Another configuration is the mode-locked gyrokystron, shown in Figure 3, where a portion of the output is fed back into the input resonator[28]. The mirror separation of the prebunching resonator is chosen so that only one mode in the output spectrum is resonant in the prebuncher. Thus, the input resonator acts like a filter and the feedback

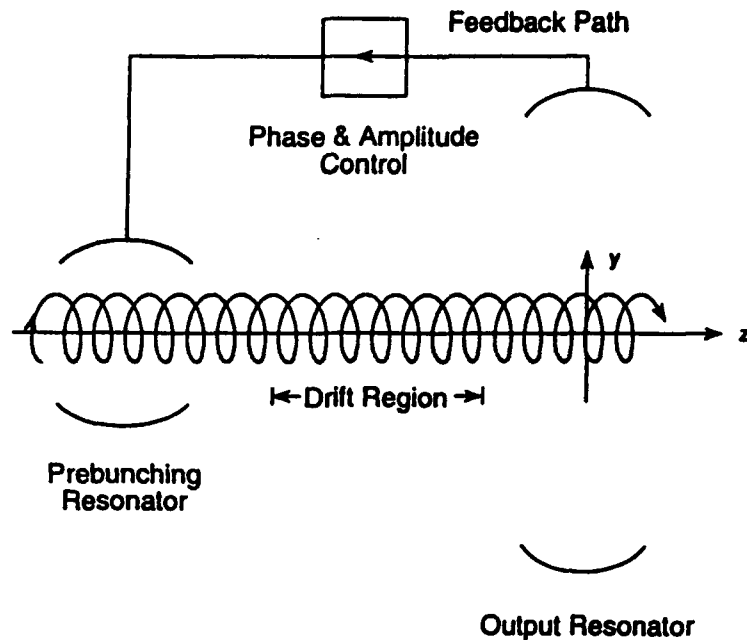


Figure 3: Schematic of a mode-locked gyrokystron showing feedback.

of the desired longitudinal mode is accomplished without an external source. In the mode-locked case, the frequency of the oscillator is fixed and there is a relative phase between the two resonators, although the equilibrium doesn't have a selected phase.

An alternative technique which does not require an external source is the gyrokystron oscillator[29]. This device is operated at a beam current slightly above the threshold current for the prebunching resonator. The electric field in the first resonator will modulate the electron beam and excite that particular frequency in the output resonator. If the current is increased further, the strong rf fields in the input resonator will introduce a large energy spread to the electrons and spoil the efficient oscillation in the output resonator. Thus, this type of device will only operate over a limited range of parameters.

There has been much more experimental and theoretical work on gyrotron oscillators than gyrokystrons. Recent experimental results have been outstanding at a number of research facilities. In an early study, Varian Associates designed and tested a 28 GHz two-cavity gyrokystron at the fundamental cyclotron frequency in 1977[30]. The tube operated with a maximum gain of 40 dB and an output power of 50 kW. This

was far below the design goal of 200 kW. There was a good deal of difficulty getting the tube to operate in the desired TE_{01} mode due to spurious oscillations in the input cavity and beam tunnel. Both the TE_{11} and TE_{21} modes could propagate in the drift tube. After the tube was loaded with lossy material, stable operation was possible, albeit at low efficiency. The low efficiency was attributed to space charge effects, velocity spread, or gyro-TWT amplification of parasitic modes in the drift region. The same year Varian constructed a second-harmonic gyroklystron which was to operate at 10.4 GHz[31]. This tube was plagued by spurious oscillation at the fundamental frequency. It was concluded that more work was required to effectively load the fundamental in the presence of the second harmonic. In 1978 the Soviets reported on a pre-1967 gyroklystron which achieved an efficiency of 70%[32]. However, virtually no details of the experiment were given so it is difficult to derive much benefit from this work.

One of the more successful gyroklystrons tested to date has been the Naval Research Laboratory's 4.5 GHz three-cavity tube[33]. This gyroklystron achieved a maximum output power of 52 kW, 33% efficiency, and a small signal gain of 22 dB. The experiment was designed so that only the fundamental TE_{101} mode could oscillate in the rectangular cavities and the drift regions between the cavities were cut-off to propagating modes. Hence, this tube did not experience problems with unwanted oscillations in the input cavities or drift spaces that plagued earlier gyroklystrons. The estimated ratio of perpendicular to parallel velocity ratio in this experiment is 1, so that the experimental perpendicular efficiency is 60%. This experiment definitively demonstrated that high efficiency is possible in a gyroklystron configuration. This tube was also operated in the locked-oscillator regime where a low power input signal controls a high power oscillation. Since the output is locked in frequency and phase, this type of device is attractive for applications where phase control is important. Another useful effect observed was that of mode priming. Here, the system was operated where several longitudinal modes could oscillate simultaneously. However, by injecting a small signal into the input cavity, the electron beam is premodulated before it enters the output cavity. The premodulation manifests itself by preferentially exciting one of the modes in the output cavity. The technique of mode priming should prove useful in highly

overmoded devices where mode competition is an issue and it is difficult to operate in the desired mode.

The University of Maryland has undertaken an ambitious program to develop a high peak-power gyrokystron for advanced accelerator applications[34,35]. The ultimate goal of the program is to provide 100 MW in a 0.8 μsec pulse at 17.4 GHz. An intermediate milestone is the development of a 30 MW gyrokystron amplifier with a pulse length of approximately 1 μsec . This design is approximately three orders of magnitude greater in peak power than the best gyrokystron to date. A good deal of effort has gone into suppressing stray oscillations in the drift regions and the cavities, where a theoretical model has been developed to calculate the quality factor for the various modes that can oscillate in the tube. It has been shown that a large number of modes have starting currents below the intended operating current of the gyrokystron. The solution to this problem is to resistively load the drift sections and beam tunnel with lossy ceramic, which has increased the stability of the tube and allowed for the propagation of larger beam currents. Recent results include pulsed amplifier operation at 9.97 GHz up to 29 MW in 1.2 μsec pulses with 26 dB gain and 31% efficiency[36,37, 38]. Also, operation has been achieved with the output cavity operating at the second harmonic so that the output frequency is 19.94 GHz with 25 MW output power and 25% efficiency[39].

Results on millimeter-wave gyrokystron experiments in the former Soviet Union have recently become available[40]. At a frequency of 35 GHz, a two-cavity gyrokystron operating in the TE_{02} mode has produced 1 MW output power in 100 μsec pulses with 20 dB gain, 25% efficiency, and a duty factor of 10^{-2} . A 94 GHz gyrokystron amplifier has achieved 65 kW peak power with 25% efficiency and 30–35 dB gain using four cavities in the TE_{01} mode. These encouraging experimental results demonstrate that high power and efficiency are possible using gyrokystrons, which are attractive where phase and frequency control are important issues.

Most gyrokystron experiments to date have operated with relatively large electric fields in the input resonator and short drift spaces to minimize the deleterious effects of velocity spread. Because of experimental constraints, the quasioptical gyrokystron is

designed with a long drift region and modest electric fields in the prebunching resonator. This approach is made possible because the electron beam is nearly perpendicular to the axis of the resonator so that $k_z \cong 0$. Thus, the quasioptical gyrokystron is relatively insensitive to a spread in pitch angle.

There are a number of other technical advantages in using an open resonator in the design of a gyrokystron. Since high order transverse modes are not excited, spurious oscillations in the input and output resonators are eliminated. This was one of the most severe problems encountered in early gyrokystrons. In the QOG, the path of the output radiation is perpendicular to the direction of propagation of the electron beam. Thus, there is a high degree of isolation between the input and output resonators, which is required for klystron operation. The drift region between cavities has often been troublesome for gyrokystrons. However, the drift tube design used in the QOG is the same as that in the MIT and Varian megawatt gyrotron oscillator designs. It has been proven effective in suppressing oscillations in the oscillator configuration and should present no difficulties in the two-cavity device.

This report describes the design and test of an 85 GHz quasioptical gyrokystron and is organized as follows. Chapter II contains the linear theory used to design much of the gyrokystron experiment. Here it is shown that a relatively long drift region may be used if care is taken when specifying the magnetic field values in the two resonators. Under these conditions, the phase bunching of the electrons is preserved in the presence of velocity spread and a large bunching parameter may be obtained. The design of the quasioptical resonators used in the experiment is presented in Chapter III. This work on the prebunching resonator represents the first application of coupling to a quasioptical resonator with large diffraction losses. The cold test measurements of the low- Q input resonator are compared to a diffraction-theory model, and good agreement is obtained. Chapter IV describes the experimental apparatus and diagnostics. Millimeter-wave diagnostics are used to measure the average power from the experiment, the frequency, the pulse shape, and the frequency and phase difference between the input and output sources.

The experimental results are presented in Chapter V. First, capacitive probes in

the drift tube are used to measure the average pitch angle of the beam electrons. These measurements are compared with calculations, and are in reasonable agreement with the electron trajectory simulations. Experimental observations of mode priming are then documented. This is the first demonstration of mode priming in a highly overmoded oscillator at frequencies near 100 GHz. The output of the gyrokystron is single-moded although the mode density is high, which represents the first operation of a QOG in a single mode at peak power and efficiency. Mode priming by prebunching the electron beam allows operation at higher frequency detuning and efficiency than a free-running oscillator. A new technique called alpha priming is also described. Here, the beam alpha ($\alpha = v_{\perp}/v_{\parallel}$) is ramped to excite a high frequency mode during the rise of the voltage pulse. This results in even higher detunings and efficiencies, with a peak measured electronic efficiency of 22% in a single longitudinal mode. Studies of mirror alignment and second harmonic radiation are described, which may prove to be quite important in obtaining high power operation of a QOG. The addition of a simple, single-stage depressed collector is presented, which increases the overall efficiency of the gyrokystron to greater than 30% with a collector efficiency of 50%. In the next section, the gyrokystron is operated in the amplifier regime by lowering the average α of the electron beam so that the output resonator is below the oscillation threshold. Measurements of amplifier gain, bandwidth, chirp of the drive source, and phase measurements are described, along with a brief discussion of the gain predictions from linear theory. Typical operating parameters in the amplifier regime are 18 dB gain, 10% efficiency, and 30 kW output power. The last section of this chapter is devoted to phase-locking measurements performed on the gyrokystron by prebunching the electron beam in an upstream resonator. The gyrokystron is locked over the entire linewidth of the output resonator with a peak power of 70 kW and 16% efficiency. Comparisons are made with nonlinear phase-locking theory.

Chapter VI contains a brief discussion of the experimental measurements in the context of normalized gyrotron parameters, so that comparisons with theory are more easily understood. Time dependent, multimode simulations are then presented for the cases of mode priming and alpha priming. Both of these phenomena are observed in

the simulations, and demonstrate the advantage of increasing the frequency detuning so that the gyrokystron operates in the hard excitation regime. A general discussion of the experimental observations and theoretical calculations is also presented in this chapter. Conclusions and suggestions for future research are discussed in Chapter VII.

Chapter II

Linear Theory Calculations

The linear and nonlinear theory of quasioptical gyroklystrons has been presented by a number of researchers[19,20]. The most common configuration considered is a low- Q prebunching resonator, a drift region, and a high- Q output resonator. Linear theory is used to calculate the phase bunching of the electrons in the prebunching resonator and drift region since the assumed electric fields are small or zero. The bunched electrons can then be injected into the output resonator, where the equations of motion are self-consistently integrated for a population of particles with predetermined entrance phases. This is in contrast to the single-cavity gyrotron, where the phase bunching and energy extraction occur in the same cavity.

In the present experiment, the magnetic field is nonuniform for much of the region preceding the output resonator. The first section of this chapter calculates the phase bunching of the electrons in the tapered field produced by the superconducting magnet. It is shown that a field gradient reduces the bunching parameter somewhat but poses no serious limitations to the experiment. Section B examines the effect of velocity spread on the linear efficiency of the gyroklystron. The nonuniform magnetic field can be used to minimize the deleterious effect of thermal spread by detuning the cyclotron frequencies in the two resonators. This calculation determines the position of the prebunching resonator so that the bunching is preserved in the presence of pitch angle spread in the drift region. This section also includes the calculation of the starting current of the prebunching resonator and the bunching parameter for typical experimental conditions.

A. Bunching in a Nonuniform Magnetic Field

The equations which describe the spacial evolution of the slow phase and the momentum of the particles can be written[19,20]

$$\frac{d\theta}{dz} = \frac{m}{p_z}(\Omega - \gamma\omega) + \frac{em\gamma}{2p_{\perp}p_z}E(z)\sin ky_g \sin \theta \quad (1)$$

$$\frac{dp_{\perp}}{dz} = \frac{-em\gamma}{2p_z}E(z)\sin ky_g \cos \theta + \frac{1}{2} \frac{p_{\perp}}{B} \frac{dB}{dz} \quad (2)$$

$$\frac{dp_z}{dz} = -\frac{p_z^2}{2p_z} \frac{1}{B} \frac{dB}{dz}. \quad (3)$$

These equations, known as the slow time scale equations of motion, are derived under the assumption that the wave fields evolve on a time scale much longer than the cyclotron period. The beam-wave interaction is taken to occur at the fundamental cyclotron frequency under the weakly relativistic limit ($\gamma - 1 \ll 1$). The slowly varying gyrophase angle is defined $\theta = \psi - \omega t$, where ψ is the particle phase, k is the free space wavenumber, $y_g = y + (p_z/m\Omega) \cos \psi$, and the electric field is polarized in the x-direction for the geometry in Figure 1. The slow phase of an unperturbed particle is

$$\theta = \theta_0 + \frac{m}{p_z}(\Omega - \gamma\omega)z, \quad (4)$$

where $z = 0$ is the position of the prebunching resonator and θ_0 is the random phase of the particle at the entrance of the resonator. In general, the relativistic mass factor (γ), the nonrelativistic cyclotron frequency (Ω), and the parallel momentum of the particle (p_z) are also functions of position. If the particle is in resonance with the wave ($\Omega = \gamma\omega$), then the slow phase is independent of p_z to first order. Under this condition, electrons would tend to bunch in the longitudinal direction but remain in gyrophase synchronism as they traverse the drift region.

The mirrors which make up the resonator are chosen to support only the fundamental transverse mode (TEM₀₀). Higher order transverse modes have much larger diffraction losses and typically have quality factors three to five times less than the fundamental mode. However, any second harmonic radiation present in the resonator will be associated with a much larger quality factor than the fundamental. Second harmonic radiation is neglected in the present analysis. The assumed radiation profile is Gaussian:

$$E(z) = E_{01} \exp \left[-\frac{z^2}{w_{01}^2} \right]. \quad (5)$$

Here, w_{01} is the radiation waist at the center of a symmetric resonator and the subscript denotes the first resonator. The radiation waist at the center of the resonator is given by[41]

$$w_{01} = \sqrt{\frac{\lambda}{\pi}} \left(\frac{d}{2} \right)^{\frac{1}{4}} (R_c - d/2)^{\frac{1}{4}}. \quad (6)$$

In this equation, d is the mirror separation and R_c is the radius of curvature of the mirrors. The separation between mirrors is determined by the allowed Ohmic heating density while the mirror radius and curvature are chosen for an appropriate diffractive output coupling coefficient.

Consider the case of a uniform magnetic field in the prebunching resonator. The change in perpendicular momentum for an electron which traverses the input resonator with a low amplitude electric field can be calculated by integrating Eq. (2) using the unperturbed gyrophase.

$$\Delta p_{\perp} = \frac{-em\gamma_0}{2p_{z0}} \int_{-\infty}^{\infty} E(z) \sin ky_g \cos[\theta_0 + \frac{m}{p_{z0}}(\Omega - \gamma_0\omega)z] dz. \quad (7)$$

Here it has been assumed that $p_z = p_{z0}$ is a constant of the motion and the relativistic mass factor γ is constant through the first resonator. If the magnetic field is uniform through the prebunching resonator, $\Omega = \Omega_0$ and the integral can be performed analytically yielding

$$\Delta p_{\perp} = -\frac{\sqrt{\pi}em\gamma_0 w_{01}}{2p_{z0}} E_{01} \sin ky_g \cos \theta_0 \exp\left[\frac{-(\Omega_0 - \gamma_0\omega)^2 w_{01}^2 m^2}{4p_{z0}^2}\right]. \quad (8)$$

The change in perpendicular momentum is a function of the entrance phase of the particle, so that some electrons gain energy while some lose energy. Note that the change in perpendicular momentum is due to the electric field in the prebuncher and occurs over a distance of approximately $2w_{01}$.

In the field-free drift region,

$$\frac{d\theta}{dz} = \frac{m}{p_{z0}}(\Omega_0 - \gamma\omega) \simeq \frac{m}{p_{z0}}(\Omega_0 - \gamma_0\omega - \frac{p_{\perp}\Delta p_{\perp}}{\gamma_0 m^2 c^2} \omega). \quad (9)$$

Here, the relativistic mass factor has been modified to include the "kick" from the prebunching resonator.

$$\gamma \simeq \gamma_0(1 + \frac{p_{\perp}\Delta p_{\perp}}{m^2 c^2 \gamma_0^2}) \quad (10)$$

The particles gyrate at slightly different frequencies in the drift space due to the relativistic mass effect. The slow phase of the particle at the entrance of the second resonator is $\theta = \theta_0 + \Delta\theta$ where

$$\Delta\theta = \frac{m}{p_{z0}}(\Omega_0 - \gamma_0\omega)(L + z) + q \cos \theta_0 \sin ky_g \quad (11)$$

and

$$q = \frac{\sqrt{\pi}\omega p_{\perp} e E_{01} w_{01} L}{2p_{z0}^2 c^2} \exp\left[-\frac{(\Omega_0 - \gamma_0\omega)^2 w_{01}^2 m^2}{4p_{z0}^2}\right]. \quad (12)$$

The variable z has been redefined so that $z = 0$ is now at the center of the power resonator and L is the separation between the two resonators. The shape of the electron beam is contained in the $\sin ky_g$ factor, so that pencil beams, annular beams, and sheet beams can be considered. The quantity q is known as the bunching parameter in the gyroklystron literature[19], and serves as a measure of the phase bunching of the electrons at the entrance of the output resonator. As will be shown later, the linear efficiency is optimized for $q = 1.8$, although somewhat higher values are required in the nonlinear regime.

If the magnetic field is not uniform in the prebunching resonator, the expression for Δp_{\perp} must be modified. The nonrelativistic cyclotron frequency is now a function of position

$$\Omega(z) = \Omega_0 + \delta\Omega(z), \quad (13)$$

where $\delta\Omega(z)$ is a small quantity compared to Ω_0 which contains the nonuniformity of the magnetic field. The change in perpendicular momentum is now

$$\Delta p_{\perp} = \Delta p_{\perp\theta} + \frac{1}{2} \int \frac{p_{\perp}}{B} dB \quad (14)$$

where

$$\Delta p_{\perp\theta} = \frac{-em\gamma_0}{2} \int \frac{E(z)}{p_z(z)} \sin ky_g \cos \theta dz \quad (15)$$

and

$$\theta = \int \frac{m}{p_z(z)} (\Omega_0 + \delta\Omega(z) - \gamma_0\omega) dz. \quad (16)$$

It is assumed that the relativistic mass factor is constant with respect to position. This should be a good approximation for the purpose of calculating the momentum change in the first resonator since the electric field is small and the change in particle energy is small ($\Delta\gamma/\gamma_0 \ll 0.01$). To first order, the second term on the right side of Eq. (14) is independent of the entrance phase of the particle and does not contribute to the gyrophase bunching in the drift region. Thus, $\Delta p_{\perp\theta}$ is the quantity of interest to determine the effect of the nonuniform magnetic field on the gyrophase bunching.

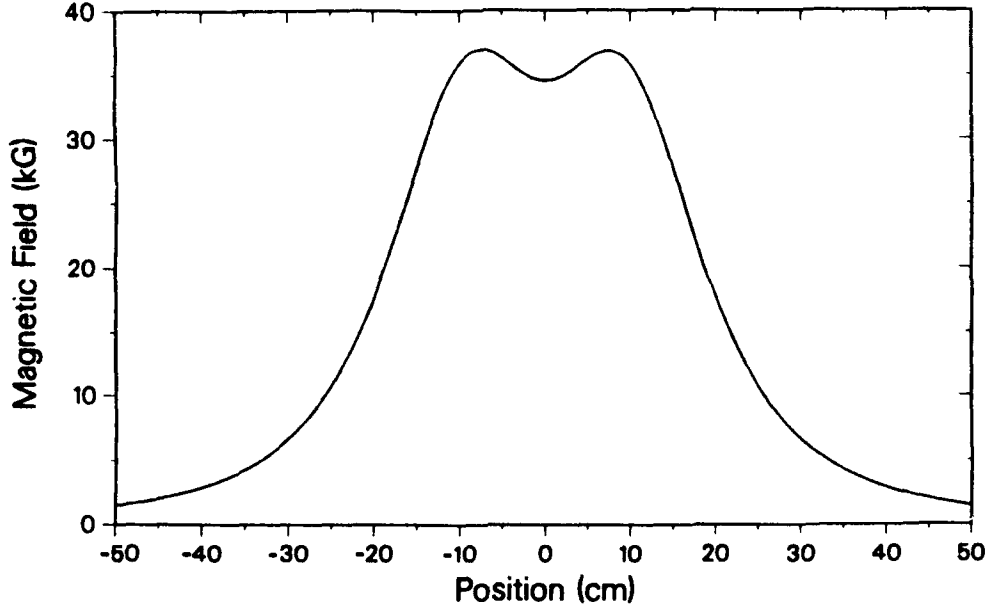


Figure 4: The magnetic field produced on-axis by the cross-bore magnet.

The superconducting magnet used in the quasioptical gyrokystron experiment has a magnetic field with a positive taper for much of the region preceding the power resonator. A plot of the magnetic field versus position is shown in Figure 4. The slope of the magnetic field near the first peak is approximately 0.9 kG/cm at the position $z = -10$ cm. The magnetic field may be written $B = B_0 + \delta B(z)$, where $\delta B(z) = 0.9z$. Here z is given in centimeters, the magnetic field is in units of kG, and $z = 0$ is referenced to the center of the prebunching resonator. This expression may be substituted into Eq. (15) to calculate $\Delta p_{\perp\theta}$. The parallel momentum of the particle is also a function of axial position due to the variation of the magnetic field. Since p_{\perp}^2/B is an adiabatic invariant, the change in parallel velocity caused by the nonuniform field is

$$\delta v_z(z) = \frac{-v_{\perp 0}^2}{2v_{z0}} \frac{\delta B(z)}{B_0}. \quad (17)$$

The parallel momentum can now be expressed

$$p_z(z) = p_{z0} \left[1 - \frac{\alpha^2}{2} \frac{\delta B(z)}{B_0} \right]. \quad (18)$$

The preceding expressions for $E(z)$, $p_z(z)$, and $\delta\Omega(z)$ can now be substituted into

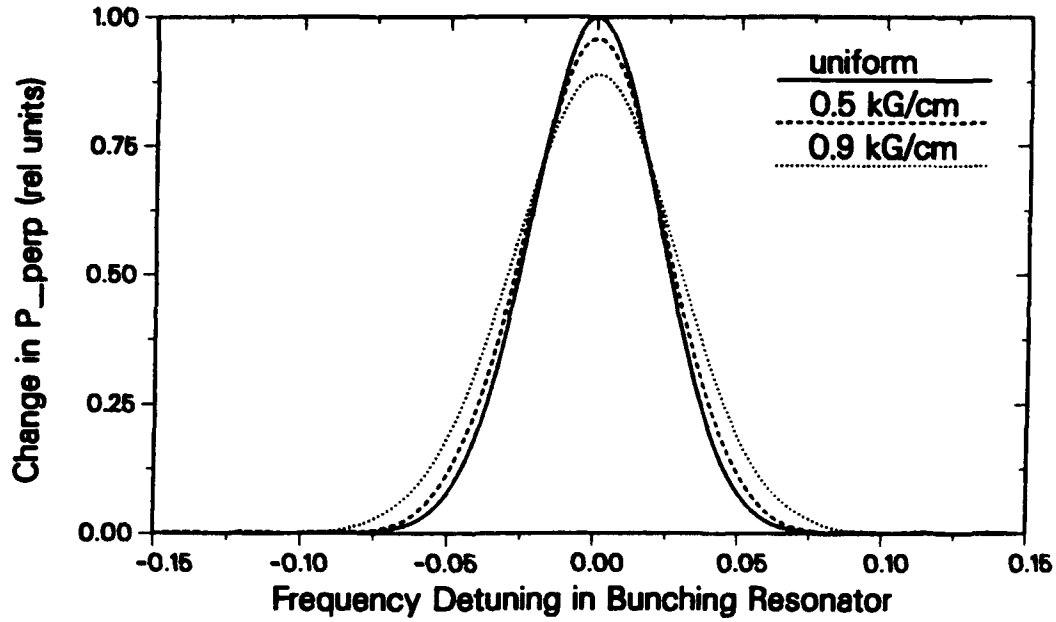


Figure 5: The change in perpendicular momentum versus frequency detuning in the prebunching resonator for $\alpha = 1.56$. The solid, dashed, and dotted curves correspond to magnetic field gradients of 0.0, 0.5, and 0.9 kG/cm, respectively.

Eq. (15). Although it is impossible to perform this integration analytically, it is straightforward to implement numerically.

Typical results of the integration of Eq. (15) are shown in Figure 5. The solid curve corresponds to the change in perpendicular momentum for a particle which traverses the prebunching resonator with a uniform magnetic field. The broken curves correspond to magnetic field gradients in the prebunching resonator of 0.5 and 0.9 kG/cm. There is a shift in gyrophase angle between the uniform and nonuniform cases which has been suppressed, since the entrance phase into the prebuncher (θ_0) is arbitrary. The variation in gyrophase shift is smooth in the detuning range between $\pm 5\%$. All of the plots are normalized to the change in perpendicular momentum in the uniform field for zero detuning.

The calculation is performed for a frequency of 85 GHz, a beam voltage of 70 kV, and $\alpha = 1.5$, where $\alpha = v_{\perp}/v_{\parallel}$. The mirror separation is 8 cm and the radius of curvature is 20 cm, which correspond to the values of the mirrors used in the prebunching

resonator. The first resonator must be driven at a frequency close to the relativistic cyclotron frequency for the prebunching to be effective. As the magnetic field gradient is increased, the effectiveness of the bunching decreases. The degradation in bunching is approximately 11% for a magnetic field taper of 0.9 kG/cm for the parameters listed above at zero detuning. For this resonator, the radiation waist is 0.94 cm so that the magnetic field changes by approximately $\pm 5\%$ over 4 waist radii. The effect of the nonuniform field can be made smaller by decreasing the radiation waist in the prebunching resonator. The reduction in the bunching parameter occurs for both positive and negative field tapers, where the dominant contribution is the variation of detuning $\Delta\omega = \omega - \Omega(z)/\gamma$ as the particles move away from resonance at the $z = 0$ position.

Figure 6 shows the results of the calculation of $\Delta p_{\perp\theta}$ for $\alpha = 1.0$. Although the shape of the curves is similar, the smaller transverse energy results in a smaller change in perpendicular momentum. Since $\Delta p_{\perp\theta}$ scales as $1/p_z$, the ratio between the two curves is approximately 1.27 for a beam voltage of 70 kV. The bandwidth associated with the prebunching is somewhat larger for lower α . This information is important because it is usually difficult to get an accurate estimate of the electron pitch angle in the experiment. A spread in α in the first resonator will introduce a spread in the bunching parameter, therefore the nonlinear efficiency should be calculated for the resultant distribution in q .

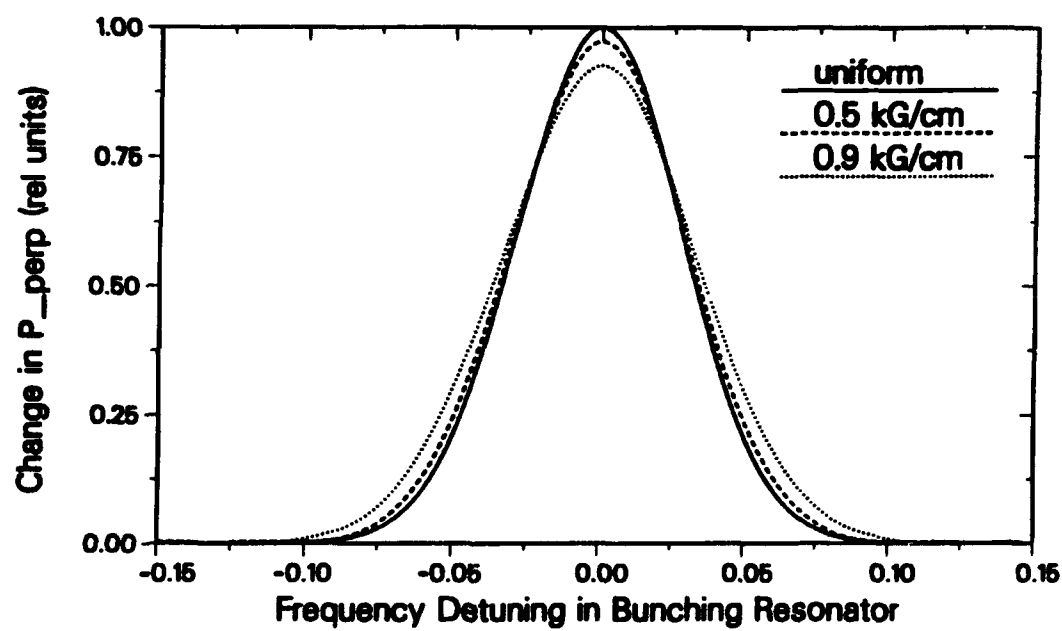


Figure 6: Same as Figure 5 for $\alpha = 1.0$.

B. Effect of Velocity Spread and Nonuniform Magnetic Field in Drift Region

A large value of bunching parameter is desired so that the gyrokystron will operate at peak efficiency. This can be accomplished by increasing the strength of the prebunching field and/or increasing the separation between the resonators. Increasing the separation between resonators makes this region susceptible to velocity spread effects. It has been shown that the linear efficiency of the quasioptical gyrokystron can be made independent of velocity spread to first order by choosing an appropriate frequency detuning $\Delta\omega = \omega - \Omega_0/\gamma$ [19]. This result was derived under the condition $\langle\Delta B\rangle = 0$, where the average magnetic field variation is defined

$$\langle\Delta B\rangle \equiv \frac{1}{L} \int_0^L \delta B(z) dz. \quad (19)$$

In the present experiment, the average variation of the field is nonzero so that the previous calculations for the optimum frequency detuning are not valid. This section calculates the effects of velocity spread in the drift region using the experimental magnetic field profile.

One quantity of interest is the small signal efficiency when a uniform magnetic field is considered. The energy that the particle gives up to the radiation field in the second resonator can be written

$$\Delta W = e \int v_x E_x dt = e \int (p_x/p_z) E_x dz. \quad (20)$$

The expressions for the electric field and the perpendicular momentum are those from linear theory:

$$p_x = p_\perp \cos \psi = p_\perp \cos(\omega t + \theta) \quad (21)$$

$$E_x = E_{02} \sin ky_g \exp\left[-\frac{z^2}{w_{02}^2}\right] \cos(\omega t + \phi_0). \quad (22)$$

Here, ϕ_0 is the phase difference between the rf fields in the two resonators and the subscript 2 denotes the second resonator. Integrating Eq. (20) and averaging over the gyroperiod yields

$$\Delta W(y_g, \theta_0) = \frac{e w_{02} \sqrt{\pi} E_{02} p_\perp}{2 p_{z0}} \exp\left[-\frac{(\Omega_0 - \gamma_0 \omega)^2 w_{02}^2 m^2}{4 p_{z0}^2}\right] \sin ky_g$$

$$\times \cos \left[\frac{m(\Omega_0 - \gamma_0 \omega)}{p_{z0}} L - \phi_0 + \theta_0 + q \sin k y_g \cos \theta_0 \right]. \quad (23)$$

This expression for ΔW may be integrated over a uniform distribution in entrance phase θ_0 and an arbitrary distribution in the y -direction $f(y_g)$.

$$\langle \Delta W \rangle = \frac{e w_{02} \sqrt{\pi} E_{02} p_{\perp 0}}{2 p_{z0}} \exp \left[-\frac{(\Omega_0 - \gamma_0 \omega)^2 w_{02}^2 m^2}{4 p_{z0}^2} \right] \sin \left[\phi_0 - \frac{m(\Omega_0 - \gamma_0 \omega)}{p_{z0}} L \right] F(q) \quad (24)$$

where

$$F(q) = \int J_1(q \sin \xi) \sin \xi f_y(\xi) d\xi. \quad (25)$$

The function $F(q)$ depends upon the shape of the beam, where ξ is the variable of integration in the y -direction. For example, a pencil beam gives $F(q) = J_1(q)$, so that the linear efficiency maximizes for $q = 1.84$. It can be seen that the linear efficiency of the gyrokystron is maximum for zero detuning

$$\frac{\Delta \omega}{\omega} = \left(1 - \frac{\Omega_0}{\omega \gamma_0} \right) = 0. \quad (26)$$

This is in contrast to the single-cavity gyrotron, where the output frequency is always greater than the relativistic cyclotron frequency. However, both the gyrotron and gyrokystron reach optimum efficiency in the nonlinear regime for similar positive detuning values[25].

The change in slow phase in the drift region is

$$\Delta \theta = - \int_0^L \left(\omega - \frac{\Omega}{\gamma} \right) \frac{dz}{v_z}. \quad (27)$$

If the magnetic field is uniform through the drift region and the electrons are monoenergetic, the change in slow phase can be written

$$\Delta \theta = - \left(\omega - \frac{\Omega}{\gamma_0} \right) \frac{L}{v_z}. \quad (28)$$

It can be seen that a spread in parallel velocity will cause a distribution in gyrophases for electrons at the second resonator when the detuning between the cyclotron frequency and the bunching frequency is not zero. When this spread in gyrophase is approximately $\frac{\pi}{2}$, the bunching will completely deteriorate in the drift region and the device will operate as a single-cavity QOG.

It is of interest to calculate the effect of velocity spread in a uniform magnetic field for future comparison. Consider a frequency detuning $\frac{\Delta\omega}{\omega} = 3\%$, which results in good nonlinear efficiency for many gyrotrons. A $\pm 10\%$ spread in the parallel velocity of the electrons should be easily attainable using magnetron injection guns. The maximum length of the drift tube is determined by setting the variation in gyrophase to $\frac{\pi}{2}$. The drift length is written

$$L = \frac{\pi}{2} \frac{v_{z0}}{\Delta v_z \Delta \omega}. \quad (29)$$

For a beam voltage of 70 kV and a pitch angle of 1.5, the maximum length of the drift region is calculated as 22λ . The length of the drift region can be increased by lowering the average α of the beam.

When the magnetic field in the drift region is not uniform, the cyclotron frequency and parallel momentum can again be written $\Omega(z) = \Omega_0 + \delta\Omega(z)$ and $p_z(z) = p_{z0} - \delta p_z(z)$. It is assumed that $\gamma = \gamma_0$ in the drift region for the present discussion, since only velocity spread of the beam electrons is considered here. The change in slow phase in the drift region is now

$$\Delta\theta = - \int_0^L \frac{dz}{v_{z0}} \left(\omega - \frac{\Omega_0}{\gamma_0} \right) + \int_0^L \frac{\delta\Omega(z)}{\gamma_0} \frac{dz}{v_{z0}} + \int_0^L \left(\omega - \frac{\Omega_0}{\gamma_0} \right) \frac{\delta v_z(z)}{v_{z0}^2} dz. \quad (30)$$

Here the second order term proportional to $\delta v_z(z)\delta\Omega(z)$ has been dropped. The first term of Eq. (30) is a constant with respect to z inside the integral. The other two terms depend upon the nonuniform field. Substituting the previous expression for the average magnetic field variation results in

$$\Delta\theta = - \frac{L}{v_{z0}} \left(\omega - \frac{\Omega_0}{\gamma_0} \right) + \frac{eL}{m\gamma_0 v_{z0}} \langle \delta B \rangle + \frac{v_{\perp 0}^2}{2v_{z0}^2} \frac{L}{v_{z0}} \left(\omega - \frac{\Omega_0}{\gamma_0} \right) \langle \delta B \rangle. \quad (31)$$

The technique used in this section is to expand $\Delta\theta$ in terms of the trajectory pitch angle κ , where κ is defined[19]

$$v_{z0} \equiv v_0 \cos \kappa \quad (32)$$

$$v_{\perp 0} \equiv v_0 \sin \kappa. \quad (33)$$

Now, the change in slow phase can be expressed

$$\Delta\theta = \frac{L}{v_0 \cos \kappa} \left(\frac{\Omega_0}{\gamma_0} - \omega \right) + \frac{eL}{m\gamma_0 v_0 \cos \kappa} \langle \delta B \rangle - \frac{L \langle \delta B \rangle}{2v_0 \cos \kappa} \left(\frac{\Omega_0}{\gamma_0} - \omega \right) \tan^2 \kappa. \quad (34)$$

The change in gyrophase angle can be expanded in terms of $\delta\kappa$ so that

$$\Delta\theta = A_1\delta\kappa + \frac{1}{2}A_2(\delta\kappa)^2 + \Delta\theta_0 \quad (35)$$

where $\Delta\theta_0$ is the change in slow phase for $\kappa = \kappa_0$. The expansion coefficients are

$$A_1 = \frac{L}{v_0}(\omega - \frac{\Omega_0}{\gamma_0}) \sec \kappa_0 \tan \kappa_0 - \frac{eL}{m\gamma_0 v_0} \langle \delta B \rangle \sec \kappa_0 \tan \kappa_0 \\ + \frac{L}{2v_0} \frac{\langle \delta B \rangle}{B_0} (\omega - \frac{\Omega_0}{\gamma_0}) [2 + 3 \tan^2 \kappa_0] \sec \kappa_0 \tan \kappa_0 \quad (36)$$

$$A_2 = \frac{L}{v_0}(\omega - \frac{\Omega_0}{\gamma_0}) \sec \kappa_0 [1 + 2 \tan^2 \kappa_0] - \frac{eL}{m\gamma_0 v_0} \langle \delta B \rangle \sec \kappa_0 [1 + 2 \tan^2 \kappa_0] \\ + \frac{L}{2v_0} \frac{\langle \delta B \rangle}{B_0} (\omega - \frac{\Omega_0}{\gamma_0}) \sec \kappa_0 [2 + 13 \tan^2 \kappa_0 + 12 \tan^4 \kappa_0]. \quad (37)$$

The linear efficiency of the gyrokystron is a convenient measure of the effect of velocity spread that can be treated analytically. Thermal spread of electron velocities will principally effect the the sine factor of Eq. (24) because its argument is integrated over the entire drift region. The exponential factor is due to the force bunching in the output resonator where the integration is performed over $2w_{02}$. Thus, the linearized efficiency with velocity spread can be calculated by averaging over the sine factor if the drift region is much longer than the radiation waist ($L \gg w_{01}, w_{02}$). Assume a Gaussian distribution in pitch angle $\kappa = \kappa_0 + \delta\kappa$

$$f(\delta\kappa) = \frac{1}{\sqrt{2\pi}a} \exp[-\frac{\delta\kappa^2}{2a^2}]. \quad (38)$$

The expression for $\langle \Delta W \rangle$ may now be averaged over the distribution in κ .

$$\langle \Delta W \rangle = \frac{1}{2} e w_{02} \sqrt{\pi} E_{02} \tan \alpha_0 \exp[-(\omega - \frac{\Omega_0}{\gamma_0})^2 w_{02}^2 / 4 v_{z0}^2] F(q) \sin(\phi_0 - \bar{\theta}) \\ \times (1 + a^4 A_2^2)^{-1/4} \exp[-\frac{1}{2} A_1^2 a^2 / (1 + a^4 A_2^2)]. \quad (39)$$

In the preceding equation,

$$\bar{\theta} = \Delta\theta(\kappa_0) + \frac{1}{2} \tan^{-1} A_2 a^2 - \frac{1}{2} A_1^2 A_2 a^4 / (1 + a^4 A_2^2). \quad (40)$$

The small signal efficiency of the gyrokystron without thermal spread is obtained by setting $a = 0$ in the preceding equations. When thermal spread is considered,

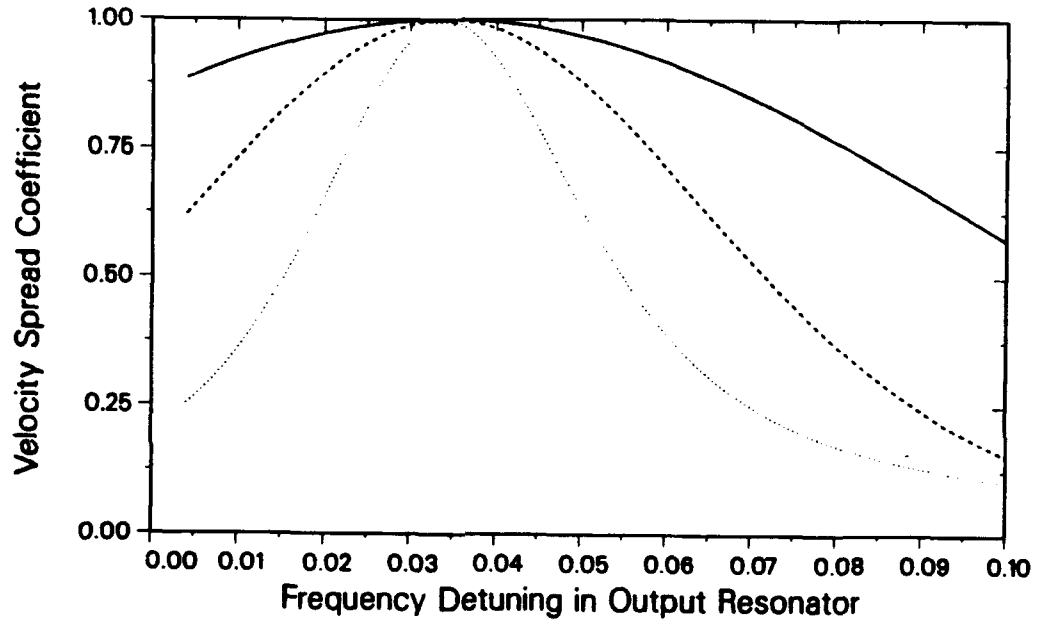


Figure 7: Velocity spread coefficient, defined in Eq. (41), versus frequency detuning between the two resonators. The pitch angle distribution is Gaussian with mean $\kappa_0 = 1.0$ and standard deviation $a = 0.025, 0.05$, and 0.1 for the solid, dashed, and dotted curves, respectively.

the coefficients A_1 and A_2 modify the expression for efficiency in Eq. (39). These coefficients depend upon the separation between resonators L , the mean value of α , and the magnetic field nonuniformity $\langle \delta B \rangle$. Define the velocity spread coefficient

$$C(a) = (1 + a^4 A_2^2)^{-1/4} \exp \left[-\frac{1}{2} A_1^2 a^2 / (1 + a^4 A_2^2) \right]. \quad (41)$$

This coefficient describes the degradation of the linear efficiency due to velocity spread and varies between 0 and 1, where $C(a) = 0$ results in $\eta = 0$. The result of the calculation is shown in Figure 7 for an average nonuniformity of the magnetic field of 4.1%, which is the value for the QOG magnet for $L \sim 10$ cm. The mean value of pitch angle is $\kappa_0 = 1.0$ ($\alpha = 1.56$), while the three curves correspond to pitch angle spreads $a = 0.025, 0.05$, and 0.1 . The corresponding values of $\Delta\alpha$ are approximately $\pm 5\%$, 10% , and 20% . The velocity spread coefficient maximizes at a frequency detuning between the two resonators of approximately 3.6%, which is where the linear efficiency is maximum. It is assumed that the prebunching resonator is driven near the cyclotron frequency so that the beam is bunched effectively.

Figure 8 shows the results of the calculation of the thermal spread coefficient for $\kappa_0 = 0.8$, which corresponds to $\alpha = 1.0$. The full width at half maximum of the velocity spread for the three curves is $a = 0.025, 0.05$, and 0.10 , yielding similar values for $\Delta\alpha$. The maximum of the curves is shifted slightly to the right and now occurs at $\Delta\omega/\omega = 3.7\%$. The point where the effect of spread is minimized depends only weakly upon the average value of α , so that fixing the frequency detuning does not constrain the allowed values of v_\perp/v_\parallel . The main dependence of the optimum frequency detuning is on the average nonuniformity of the magnetic field. The magnetic field shape can be varied somewhat in the experiment, which allows for a technique to tune the optimum frequency difference between the input and output resonators. Another feature of Figure 8 is that the bandwidth of the interaction increases with decreasing α_0 for large velocity spreads. Thus, it may be desirable to operate in this regime to lower the effect of thermal spread.

The size of the bunching parameter is of considerable importance to the operation of the gyrokystron. The condition for starting oscillation in the first resonator with

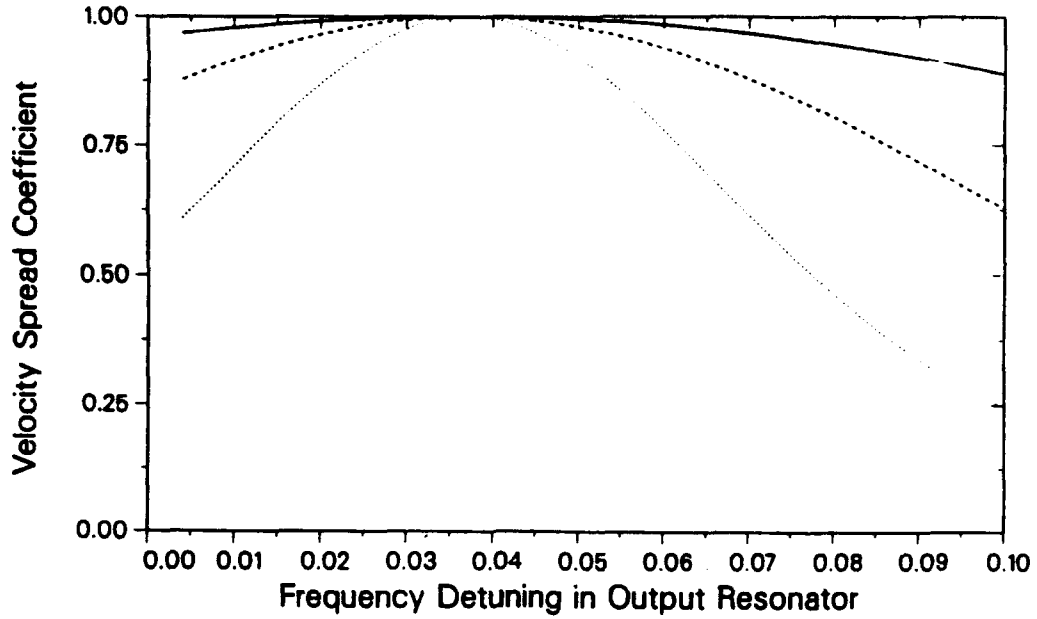


Figure 8: Same as Figure 7 for $\kappa_0 = 0.8$.

an annular electron beam with optimum frequency detuning can be expressed[4,21]

$$P_b Q \geq \frac{2c^5 \epsilon_0 m^2}{e^2} \exp\left[\frac{1}{2}\right] \left(\frac{d}{w_{01}}\right) \gamma_0 (\gamma_0 - 1) \frac{\beta_{z0}^3}{\beta_{\perp 0}^2} \frac{2}{1 \pm J_0(kr_b)}. \quad (42)$$

In the above equation P_b is the input beam power in Watts, d is the mirror separation, r_b is the beam radius, and β is the ratio of the particle velocity to the speed of light. Considering the geometry of the annular beam is important because some electrons pass through nulls of the standing fields in the resonator, which decreases the efficiency of the interaction. If the guiding center radius r_b is somewhat greater than the wavelength, then $J_0(kr_b) \sim 0$ and Eq. (42) can be written

$$P_b Q \geq 4.6 \times 10^9 \left(\frac{d}{r_{01}}\right) \gamma_0 (\gamma_0 - 1) \frac{\beta_{z0}^3}{\beta_{\perp 0}^2}. \quad (43)$$

As an example, consider a prebunching resonator with a mirror separation of 8 cm and mirror radius of curvature 20 cm. For a frequency of 85 GHz, the radiation waist is 0.94 cm. An electron beam voltage of 70 kV corresponds to a relativistic mass factor $\gamma_0 = 1.137$, and assuming $\alpha = 1.5$ yields $\beta_{\perp 0} = 0.40$ and $\beta_{z0} = 0.266$. If the quality factor (Q) of the resonator is 2000, then the threshold current of the prebunching

resonator is 4.8 A. The Q of the input resonator is determined by the diameter of the mirrors and the size of the coupling hole.

The electric field in the bunching resonator determines the magnitude of the bunching parameter. A fundamental relation between the energy stored in the resonator and power dissipated by losses is

$$Q = \omega W_{em} / P_l, \quad (44)$$

where W_{em} is the stored electromagnetic energy and P_l is the average power lost. For a Fabry-Perot resonator, the stored energy can be written[43]

$$W_{em} = \frac{\pi}{8} \epsilon_0 w_{01}^2 d E_0^2. \quad (45)$$

Here, ϵ_0 is the permeability of free space and all quantities are in MKS units. For the resonator described above and an input power of 375 Watts, the electric field at the center of the resonator is $E_{01} = 1.67 \times 10^5$ V/m. The total power available from the EIO is 1500 Watts, so the value 375 Watts should be a conservative estimate of the power coupled into the TEM₀₀ mode.

If the drive frequency is sufficiently close to the relativistic cyclotron frequency in the first resonator, then the exponential term in Eq. (12) is approximately one. The bunching parameter can now be written

$$q \sim \sqrt{\pi \omega p_{\perp}} e E_{01} w_{01} L / 2 p_{z0}^2 c^2. \quad (46)$$

The separation L between the two resonators is 10 cm for a detuning of 3.6%, yielding a bunching parameter $q = 2.4$. Tran *et al.* have shown that the optimum bunching parameter for peak efficiency with a pencil beam placed on a field maximum is approximately 3.[25] The optimum value of q for an annular beam is somewhat greater due to variation of electric field across the beam. Thus, the maximum bunching in this example is somewhat less than optimum.

It can be seen from Eq. (12) that the bunching parameter scales as p_{\perp} / p_z^2 , so that reducing $v_{\perp} / v_{\parallel}$ to 1.0 reduces the bunching parameter by approximately 50% for a beam voltage of 70 kV. This operating regime (low α) is of interest because velocity spread effects will be smaller and the gyrokystron can operate at higher current before the prebunching resonator oscillates. A plot of the bunching parameter is given in

Figure 9 as a function of beam alpha. Note that rather large values of q are obtained for $\alpha \sim 2$. In this regime, it may be possible to overbunch the gyrokystron so that the bunching parameter is too large and the interaction efficiency decreases.

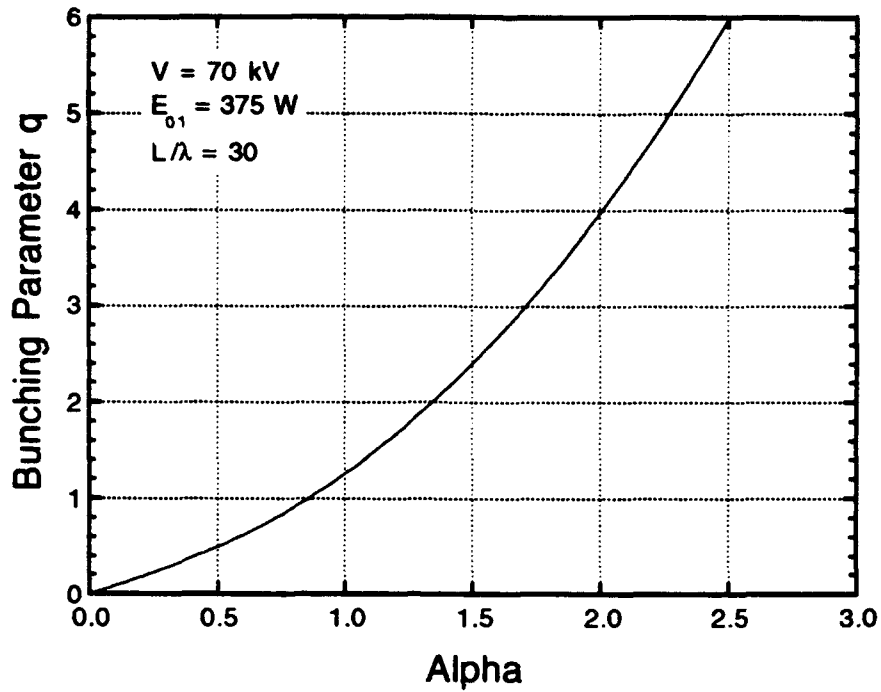


Figure 9: Bunching parameter q versus electron pitch angle α .

Chapter III

Quasioptical Resonators

A. Properties of Quasioptical Resonators

The quasioptical gyrotron derives its name from the use of a quasioptical resonator in the interaction region of the gyrotron. Fabry-Perot resonators have been used extensively throughout the electromagnetic spectrum including the optical, infrared, millimeter, and microwave regions. The most common reason for using an open resonator is to minimize losses and obtain a large quality factor (Q). In the millimeter-wave band, applications of quasioptical resonators include the measurement of dielectric properties of solids, liquids, and gasses, scattering studies, magnetic resonance in materials, frequency measurement, and as a system component (ie-filter, mixer, diplexer). A review of work using open resonators at millimeter-wave and microwave frequencies is given in [42].

A schematic diagram of an open resonator is shown in Figure 10, which consists of a pair of mirrors separated by many radiation wavelengths. The resonator mirrors are usually curved, which tends to focus the radiation into a beam and reduces diffraction losses around the mirrors. This type of resonator is much easier to align than one with planar mirrors. The modes of the resonator may be calculated analytically if diffraction around the mirrors is neglected but the focusing effect of the curved mirrors is considered. The modes can be written as products with Laguerre polynomials in cylindrical coordinates where the lowest order transverse mode, denoted the TEM_{00} mode, is Gaussian. The wavefront of the mode is planar at the beam waist and is equal to the radius of curvature of the mirror at the mirror surface. The resonator mirrors used in the present experiment are symmetric except for the input and output coupling holes.

There are two very different open resonators used in the quasioptical gyrotron experiment. The first resonator is used to prebunch the electrons while the second is used for extracting rf energy from the beam. The output resonator has a high quality factor (Q) to allow for the large electric fields necessary for the efficient transfer of energy between the electrons and the rf fields. The mirror separation is variable so

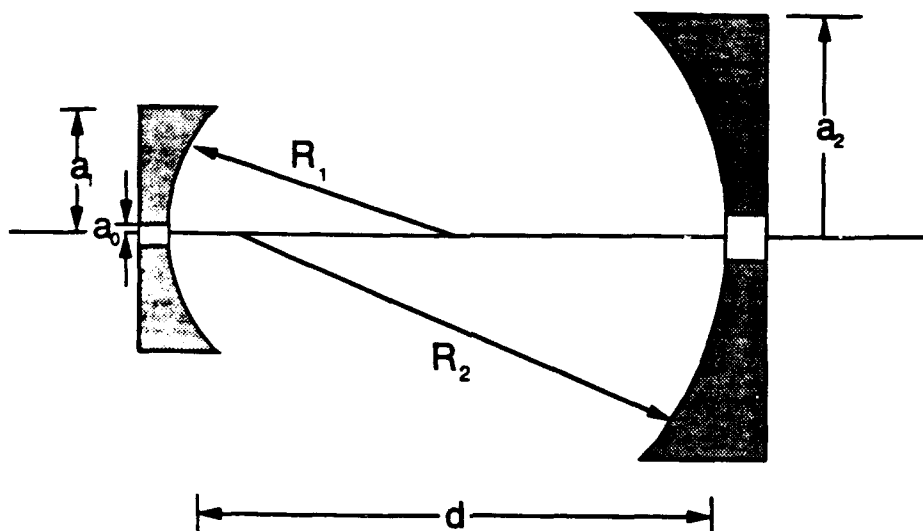


Figure 10: Schematic diagram of a quasioptical resonator with input coupling.

that the frequency is continuously tunable. This feature is important for a number of reasons. First, the radii of curvature of the mirrors can be chosen so that the Q varies rapidly over a given range of mirror separations. The radiation waist of the resonator mode is insensitive to changes in separation, thereby allowing one to vary the electric field strength while the interaction length remains essentially constant. If the fields in the resonator become too large, the mirror separation can be increased to reduce the fields and reoptimize the efficiency. A second attribute of the variable separation is that it allows for a method to match the resonant frequencies of the two resonators during the hot test of the tube. This is desirable in many instances including phase-locked, mode-primed, and amplifier operation where the electrons should be bunched near the frequency of the output resonator. Variable separation also allows for beam coupling studies by translating the entire resonator across the electron beam. Finally, the experiment is performed in a cold-bore superconducting magnet which may affect the alignment when cooled to cryogenic temperatures. Variable position mirrors allow for optimized alignment during the hot test of the gyrotron.

The function of the input resonator is to prebunch the electron beam before it

reaches the main resonator. This requires a low- Q resonator which does not oscillate in the presence of the beam. Strong oscillations will tend to introduce a large energy spread among the electrons and spoil the interaction in the output resonator. The prebuncher mirrors can be fixed to simplify construction since the output mirror separation is adjustable. The resonator must provide a means of efficient coupling to the external source while preserving the TEM_{00} mode. The low Q is obtained by reducing the size of the mirrors, which increases the diffraction losses around the mirror edges. A comparable amount of power may be lost from the coupling aperture(s).

The quality factor (Q) of a quasioptical resonator can be written

$$Q = \frac{4\pi d}{\lambda f_L} \quad (47)$$

where d is the separation between the resonator mirrors and f_L is the fractional round-trip loss. The three loss mechanisms which are important in this work are ohmic, diffraction, and coupling losses. The total Q of the resonator can be expressed

$$\frac{1}{Q} = \frac{1}{Q_\Omega} + \frac{1}{Q_{d,c}} \quad (48)$$

where Q_Ω is the ohmic Q and $Q_{d,c}$ is the Q associated with the diffraction and coupling losses. The ohmic Q is calculated according to [43,44]

$$Q_\Omega = \frac{d}{2}(f\pi\mu_0\sigma)^{\frac{1}{2}}. \quad (49)$$

Here μ_0 is the permeability of free space and σ is the conductivity of the mirrors. Gold-plated mirrors are used in the output resonator with a conductivity of 4.5×10^7 Siemens/m. The ohmic Q increases linearly with mirror separation and can be neglected for large values of output coupling.

The diffraction/coupling Q is calculated separately from Q_Ω using a computer code to evaluate the losses[45]. The program solves the integral equations of the open resonator as a matrix eigenvalue problem, yielding the eigenfunctions. Inputs to the code include the wavelength of the radiation, the mirror radii, the curvature of the mirrors, the separation between mirrors, the dimensions of coupling holes, and a parameter which specifies the mesh size. Outputs from the code include the diffraction losses, the coupling losses, and the electric field distribution along the surface of each mirror for

the TEM_{00} and TEM_{10} modes. The subscripts refer to the radial and angular mode numbers, respectively, and higher-order transverse modes may be analyzed. The solution from the code converges rapidly for output couplings above 1%. The code has been compared to results from a number of published works on open resonators. Three resonator geometries have been considered: symmetric mirrors without coupling holes, symmetric mirrors with coupling holes, and asymmetric resonators with one coupling hole. Good agreement is obtained between the code and the published results for all three geometries.

The quality factor of the output resonator used in the gyrokystron experiment is plotted in Figure 11 as a function of mirror separation. The total Q and the diffractive Q at a frequency of 85 GHz are given by the solid and dashed curves, respectively. The mirrors are gold plated with a mirror diameter of 5.6 cm and a radius of curvature of 38.7 cm. There is a bevel around each of the mirrors which reduces the effective diameter to 5.5 cm. The separation between mirrors can be varied between 20-28 cm in the experiment by adjusting micrometers from outside the magnet dewar. The total Q varies from 47,000 to 24,000 over the range of interest in the experiment, with corresponding values of round-trip diffractive output coupling increasing from 1.3 to 4.4%. Ohmic losses are relatively small and decrease from 13.8 to 4.5% of the diffractive losses as the separation is increased. Changing the mirror separation from 20 to 24 cm provides an excellent way to reduce the electric field in the output resonator during hot tests. The flat portion of the curves indicate that the losses are increasing approximately linearly with mirror separation. This type of behavior is expected from ray optics considerations, where the diffraction can be thought of as propagating from a point source at the center of the resonator.

An extensive series of cold tests of high- Q quasioptical gyrotron output resonators is presented in [47]. Radiation is coupled into the resonator using a small centered hole in one of the mirrors, while the diffracted radiation is detected using a standard-gain horn positioned behind one of the mirrors. Thus, the total Q can be measured as a function of mirror separation. Good agreement is obtained between the measured data and theoretical values calculated from scalar diffraction theory using the computer

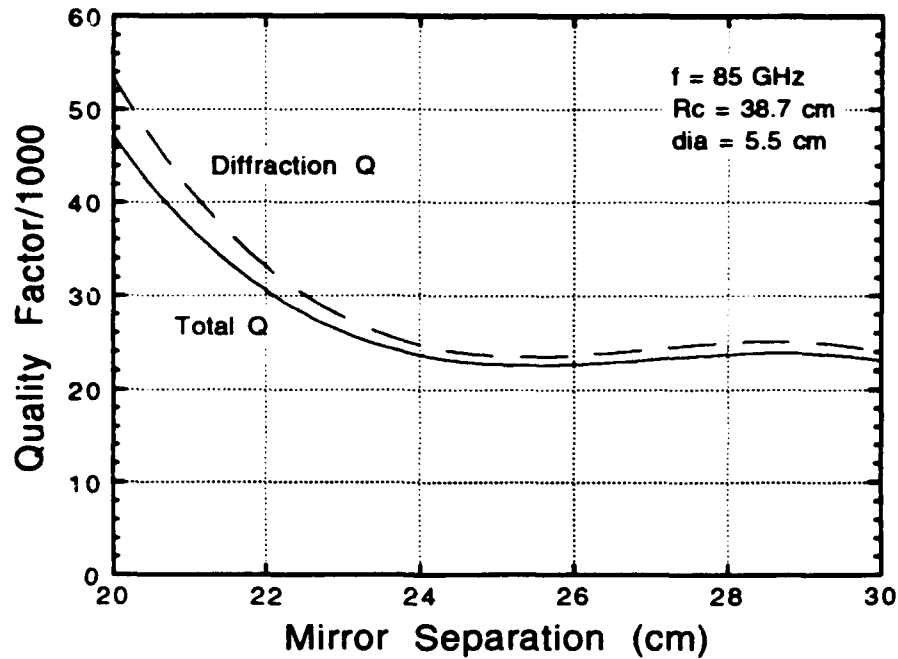


Figure 11: Calculated Q versus mirror separation for the output resonator.

code. This work showed that the code is a valid tool to design output resonators at millimeter wavelengths using small coupling holes and relatively small output coupling values.

The size of the coupling hole can have a large effect on the resonator losses and mode pattern. A small hole at the center of the mirror primarily excites the TEM_{00} mode, which has an electric field peak on axis. The next higher radial mode, the TEM_{10} , has a null at this position and is weakly coupled. The coupling hole is considered small if the hole losses are a small fraction of the total resonator losses. As the hole diameter increases, more power is lost through the aperture. Ultimately, a large hole will distort the TEM_{00} mode so that it no longer has a peak on axis. There is a minimum at the hole and the maximum is shifted towards the mirror edge, so that the new pattern resembles the TEM_{10} mode. The TEM_{10} mode, on the other hand, is minimally affected by the presence of the coupling hole. One would expect that the total Q for these modes could become comparable in this regime where the coupling hole is large and the fundamental mode is distorted.

An example of the degrading effect of a large coupling hole on the TEM_{00} mode

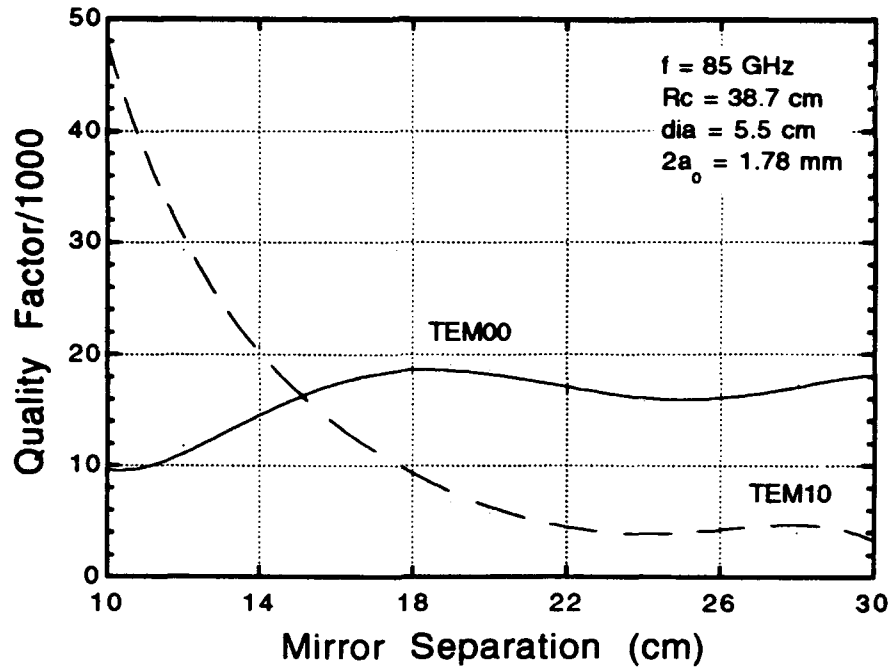


Figure 12: Output resonator Q versus separation with large coupling holes.

can be seen in Figure 12. The quality factors of the TEM_{00} and TEM_{10} modes are denoted by the solid and dashed curves, respectively. The dimensions of the mirrors are the same as in Figure 11, except there is a 1.78 mm-diameter centered hole in each mirror. For separations shorter than 15 cm, the fundamental transverse mode actually has a lower Q due to coupling losses and field deformation. For large mirror separations the power lost through the coupling hole is small for both modes and the fundamental mode is again dominant. The ratio of coupling losses to total losses for each mode is plotted in Figure 13 as a function of mirror separation. The TEM_{10} mode is largely unaffected by the presence of the hole since it has a field minimum on axis. The maximum power lost through the aperture for this mode is 1.2% of the total resonator losses. For smaller mirror separations, the Q of the fundamental mode is largely determined by the aperture, where the maximum power coupled through the hole for the fundamental mode is approximately 50%. This is a standard result for quasi-optical resonators, which precludes the use of a centered coupling hole for efficient output coupling. The fields of the TEM_{00} mode get pushed away from the aperture so that the maximum hole loss cannot exceed $\sim 50\%$ of the total losses.

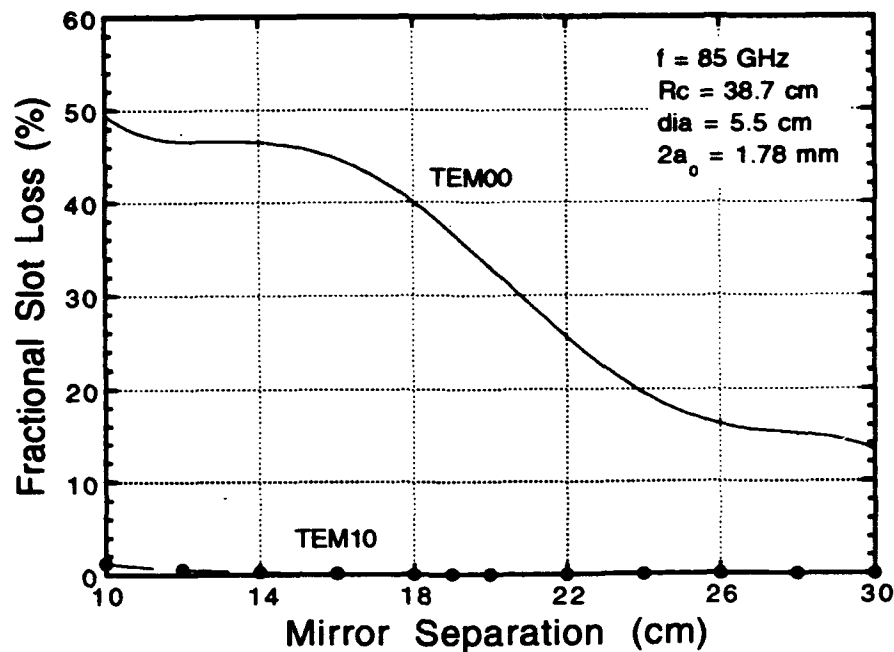


Figure 13: Output resonator losses versus separation with large coupling holes.

The prebunching resonator for the gyrokystron experiment requires a low- Q quasi-optical resonator, which is accomplished by reducing the size of the mirrors. A centered hole in one mirror provides input coupling, while a second aperture in the other mirror can be used to monitor the input resonator. One would expect that a given coupling hole will have a smaller effect on a low- Q resonator than a high- Q resonator, and this is indeed the case. Such a geometry is considered in Figure 14, where the mirror diameters are 3.1 cm, the radii of curvature are 20 cm, and the mirror separation is 7 cm. The solid and dashed curves correspond to the quality factors of the TEM_{00} and TEM_{10} modes, respectively. The higher-order transverse mode is essentially unaffected by the presence of the centered coupling holes. The Q of the fundamental mode drops from 6600 to 2100 as the radius of the coupling holes increases to 1 mm. However, the mode pattern of this mode is largely unaffected by the increased coupling, in contrast to the previous case with the larger mirrors.

The calculated fractional slot loss for both modes is shown in Figure 15 as a function of coupling hole radius. The slot loss for the TEM_{00} mode is still increasing approximately linearly for an aperture radius of 1 mm, which indicates that the mode pattern

has not been disturbed significantly. The discrete points correspond to the slot loss for the next higher transverse mode. Although these values are less than 1%, the Q of the fundamental mode is still larger. This is an important consideration when designing the prebuncher since the fundamental transverse mode should have the lowest starting current.

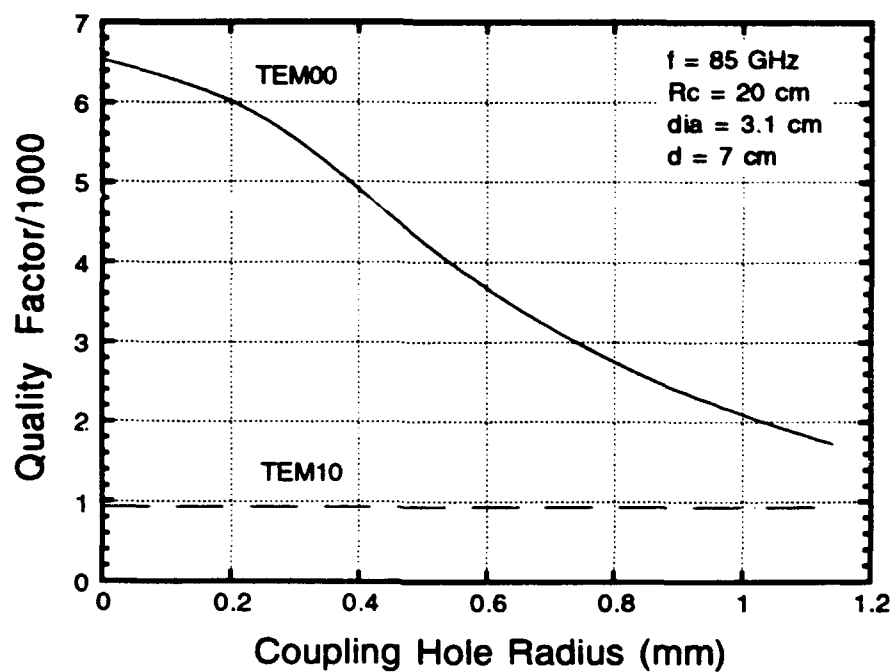


Figure 14: Calculated Q versus coupling hole radius for the prebuncher.

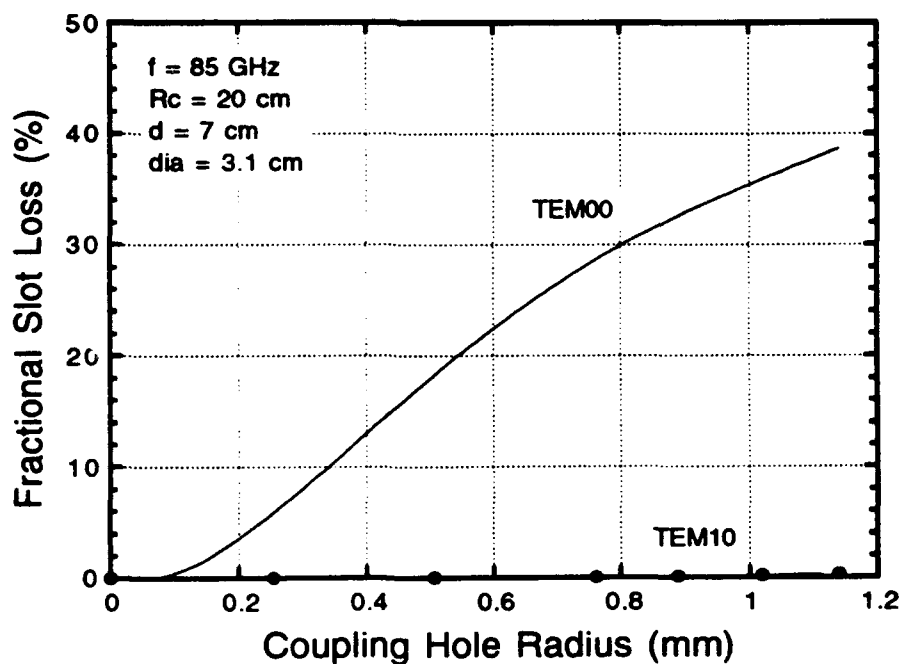


Figure 15: Fractional slot loss versus coupling hole radius for the prebuncher.

B. Cold Tests of Prebunching Resonators

In order to understand the behavior of a quasioptical resonator during cold tests, first consider the case of a closed resonant cavity. Coupling to such a cavity is often accomplished by drilling a pair of holes in the cavity and driving one hole with a section of rectangular waveguide operating in the TE_{10} mode[48,49]. The aperture will couple the transverse magnetic field in the waveguide to the corresponding magnetic field in the resonator, since the tangential electric field at the wall is zero. The two loss mechanisms in this type of cavity are ohmic losses and coupling losses. Cold tests are performed by monitoring the reflected and transmitted signals from the cavity, where the initial cavity has two small holes. The most common strategy is to keep the output hole size fixed while increasing the input hole diameter. For a small input hole, the reflected signal is approximately 100% near the resonant frequency of the cavity and a small transmitted signal is observed. The Q of the cavity is obtained by measuring the full-width at half maximum (FWHM) of the transmitted resonance and applying the relation $Q = f/\Delta f$, where f is the resonant frequency of the cavity and Δf is the FWHM. For a small input hole, the coupling losses are small and the measured Q is close to the unloaded Q (Q_0). As the diameter of the input hole is increased, the reflected signal near resonance decreases while the transmitted signal on-resonance increases as more power is coupled into the cavity. Off-resonance, 100% of the power is reflected and no power is transmitted. The loaded Q of the cavity can be expressed $Q_L = Q_0/(1 + \beta)$, where $\beta = Q_0/Q_e$. The value β is known as the coupling factor of the cavity and Q_e is the external Q due to coupling losses. The reflection from the cavity drops to zero at the point $\beta = 1$, which is known as critical coupling. The region $\beta > 1$ is referred to as overcoupled while $\beta < 1$ is undercoupled. The power reflection coefficient from the cavity can be written

$$R = \frac{(1 - \beta)^2}{(1 + \beta)^2}. \quad (50)$$

As the cavity becomes overcoupled, the power reflection coefficient approaches 1. The usual goal in the cold test is to optimize power transfer to the cavity and measure the loaded Q . This is accomplished by increasing the input hole diameter until $R = 0$ so

that critical coupling is achieved.

Cold tests of quasioptical resonators (low- Q prebunching resonators in particular) are more difficult to interpret than closed cavities because there are more loss mechanisms. The Q of the unloaded resonator is dominated by diffraction of the TEM_{00} mode around the mirrors. This implies that the power reflected from the resonator off-resonance is not necessarily 100%, which contrasts with the closed cavity result. There is also the possibility that radiation at the resonant frequency which is transmitted past the input aperture is nonresonantly scattered out of the resonator. This power can be thought of as consisting of higher-order modes which are necessary to match boundary conditions at the input coupling hole. The prebunching resonator in the gyrokystron experiment represents the first time that a low- Q open resonator has been tested at millimeter wavelengths.

Preliminary cold tests of prebunching resonators were performed using a 94 GHz IMPATT oscillator to test the basic properties of low- Q open resonators with large coupling holes. The IMPATT can be swept in frequency by applying a 5 Volt ramp to the frequency modulation port. The output power is approximately 20 mW and the maximum frequency modulation is ~ 100 MHz. This source has the advantage that the frequency is very stable on a sweep-to-sweep basis with a frequency jitter less than 1 MHz, which allows for the precise measurement of the Q of the prebunching resonator. A 10 mW backward wave oscillator (BWO) is used for measurements at 85 GHz, although the sweep-to-sweep variation precludes accurate Q measurements. A schematic diagram of the cold test set-up is shown in Figure 16, where the waveguide elements are standard WR-10 components in rectangular waveguide. The interferometer comprises a pair of 15.2 cm-diameter mirrors with a hole for input coupling and another to monitor the transmitted signal. The interferometer has a Q of approximately 70 000 and is mounted using a precision micrometer, which allows one to measure the frequency very accurately and to calibrate the sweep of the IMPATT. Initial measurements used the swept IMPATT to drive the prebuncher while the reflection was monitored using a directional coupler, detector, and an oscilloscope. The signal reflected from the prebuncher is compared to a 100% reflection from a perfect short circuit placed at the

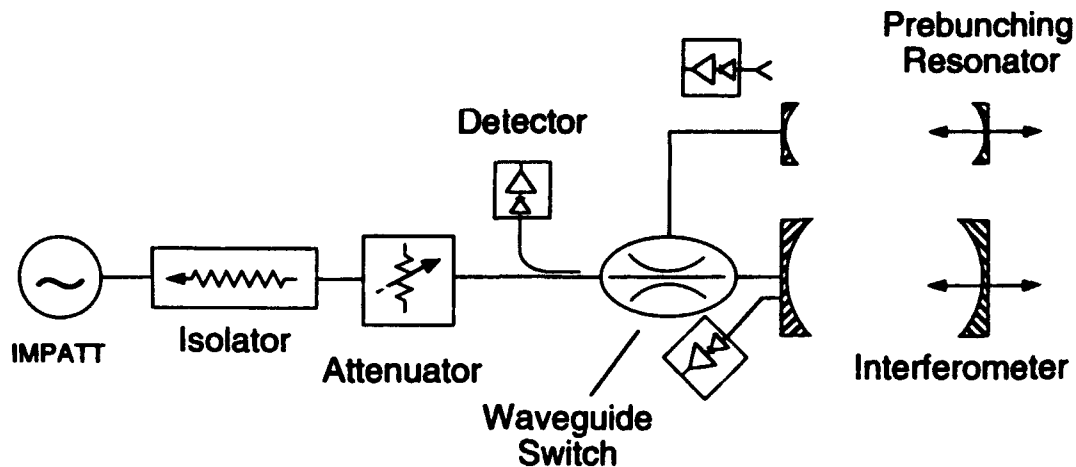


Figure 16: Schematic diagram of the cold test set-up.

input mirror or off another port of the waveguide switch. The Q of the prebuncher is determined by measuring the FWHM of the transmitted resonance, where a portion of the diffracted signal is collected using a standard-gain horn beyond the mirror edge.

One of the first prebunching resonators tested consisted of a pair of mirrors 3.1 cm in diameter with a radius of curvature of 20 cm. The mirrors are mounted on a pair of optical mirror mounts and translated on a rail to vary the separation. The mirror alignment, which must be accurate to better than several degrees, is optimized using a HeNe laser. The input mirror is machined out of aluminum with a small centered coupling hole and a counter bore from the back surface of the mirror to accept a waveguide flange. Some representative oscilloscope traces of reflection signals from the prebuncher are shown in Figure 17 for a mirror separation of 4.5 cm. The top trace in each oscillograph is the 100% reference reflection from a short circuit while the lower signal is the reflected signal from the prebuncher. For a coupling hole diameter of 0.91 mm, there is no discernible dip in the reflection due to the resonator. The characteristic dip appears for a coupling hole diameter of 1.32 mm, which is similar in appearance to that expected in a closed cavity measurement. As the input hole size is increased

further, a large asymmetry appears due to the interference effects caused by the phase shift in the resonator. The reflection off-resonance is much less than the 100% value observed for smaller hole sizes. Finally, a large hole (1.85 mm) causes approximately 100% reflection on-resonance, which is analogous to the overcoupled case in the closed cavity. However, the reflection is nearly zero as the frequency of the source moves away from resonance, which is probably due to radiation scattered nonresonantly around the mirrors.

One of the main conclusions from the data in Figure 17 is that a large fraction of the incident power can be coupled to the TEM_{00} mode. From the last oscillograph, essentially 100% of the power is reflected on-resonance even though the coupling is large. The cross-sectional dimensions of WR-10 waveguide are 2.54×1.27 mm, so that nearly all of the power would be radiated past the 1.8 mm diameter coupling hole in the absence of the far resonator mirror. It is therefore reasonable to expect that a large portion of the incident power is coupled to the mode of interest for smaller coupling holes. A direct measurement of the strength of the fields in the prebunching resonator is performed during the next series of cold tests. A large volume of data was obtained for the Q of the prebunching resonator as a function of mirror separation and input coupling hole diameter. As is the case for the output resonator, the measured values of Q are in agreement with those calculated from scalar diffraction theory.

The frequency of operation of the quasioptical gyrokystron experiment is determined by the availability of a suitable source, in this case a high power 85 GHz EIO. A 75-110 GHz BWO is used for the cold test of the final prebunching resonator. The BWO frequency is varied by sweeping the beam voltage (typically 2 kV), so that the BWO is not nearly as stable as the solid state IMPATT. Consequently, the reflection and transmission measurements are performed using the BWO while the final loaded Q is obtained using the EIO.

A new pair of mirrors, 3.1 cm in diameter with radius of curvature of 20 cm, are used for the experiment. Each mirror is machined with a small centered coupling hole and a counter-bore from the back to accept a WR-10 waveguide flange. The mirrors are cold tested using the rigid mount that is used in the hot test experiment. In the

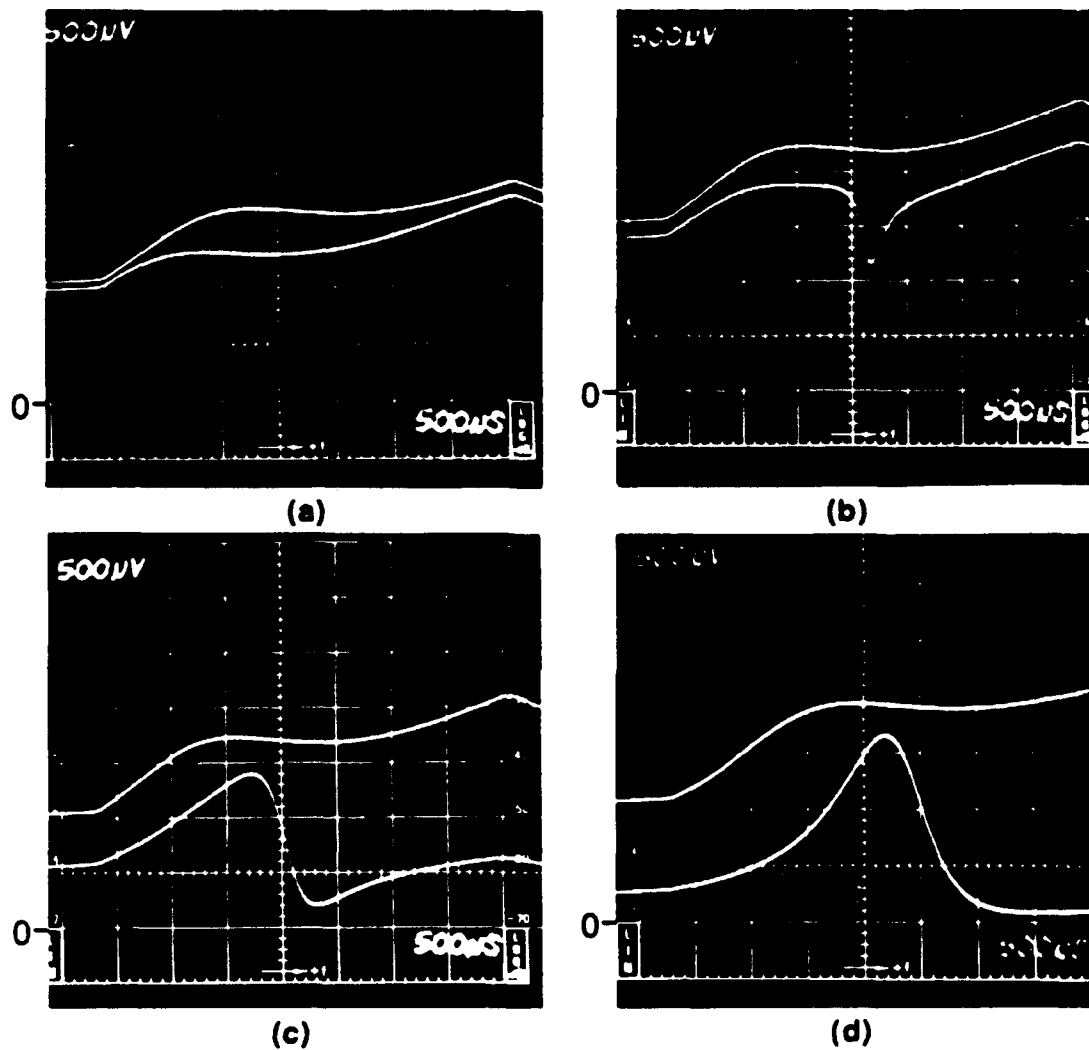


Figure 17: Reflection measurements from a prebunching resonator. The oscillographs in (a)–(d) correspond to coupling hole diameters of 0.91, 1.32, 1.60, and 1.85 mm, respectively.

cold test, one hole is used to drive the resonator while the other monitors the strength of the fields in the prebuncher. The separation between the mirrors is fixed at 7 cm so that the prebuncher assembly fits inside the 14.6 cm diameter of the main crossbore in the superconducting magnet.

The prebuncher mirrors are surrounded by lossy ceramic rings which serve two purposes. First, the rings absorb the radiation which is diffracted around the prebuncher mirrors in the experiment. If this radiation were allowed to propagate past the mirrors, it would be free to interfere with gyrokystron operation by reflecting off surfaces inside the magnet dewar. Secondly, the lossy rings isolate the prebunching mirrors from the supporting structure of the mirror holders. This ensures that the Q of the prebuncher is due solely to the mirrors and not the mirror holder. Additional lossy material is required at several places in the drift tube assembly to load spurious gyrotron oscillations where the magnetic field is strong. The ceramic Macor was chosen for all of these regions because of its short lead time, ready availability, easy machining, and low cost. The thickness of the ceramic is chosen to be an odd number of quarter wavelengths in the dielectric to resonantly absorb at the design frequency. The published values for the real and imaginary parts of the dielectric constant for Macor at 85 GHz are $\epsilon = 5.685 - j0.082$ [50]. However, variations often occur during the production of the ceramic, so in-house measurements were performed to determine the dielectric properties.

The standard technique which is used to measure the dielectric properties of a material is to compare the reflection from the sample under test to the 100% reference reflection from a perfect short circuit. The BWO is swept from 75-100 GHz and transitioned from the TE_{10} mode in rectangular waveguide to the TE_{11} mode in circular guide with an inside waveguide diameter of 1.27 cm. This waveguide is far from cut-off in W-band, so that the incident radiation is nearly a plane wave. A slab of lossy material is inserted between the end of the circular guide and a copper plate. The reflection from the lossy ceramic is compared to the plate alone, with the results displayed on a scalar network analyzer. The resonant frequency of the absorption maximum is related to the magnitude of the dielectric constant, while the depth of the absorption is related

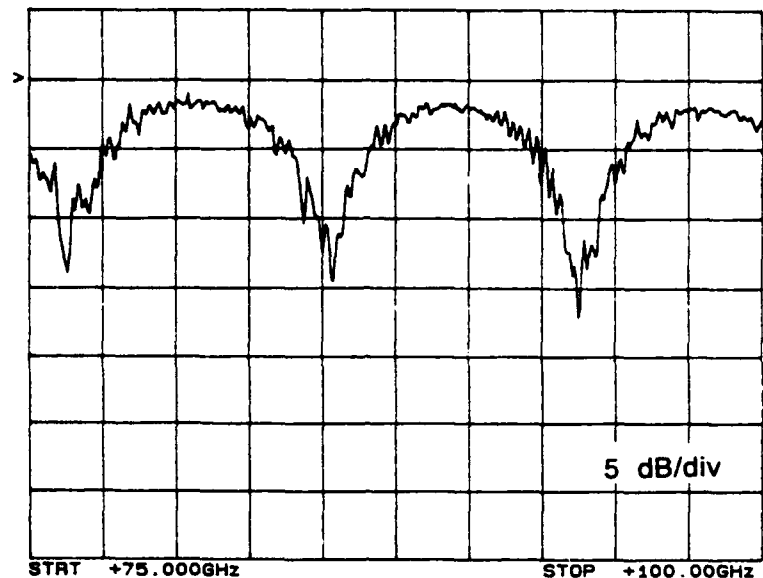


Figure 18: Measured reflection from the prebunching resonator Macor rings. The frequency is swept from 75–100 GHz and the vertical scale is 5 dB/div.

to the loss tangent of the material. Using this information from the initial cold test, the final pieces are machined to resonantly absorb at 85 GHz. The cold test of the rings used in the quasioptical gyrokystron experiment is shown in Figure 18. The thickness of the rings is 0.277 inch, with a measured loss of more than 10 dB near 85 GHz. The reflection from the Macor as a function of frequency is in excellent agreement with simple transmission line theory using the permittivity values measured in the cold test. The separation between the prebuncher mirrors can be varied slightly using shims so that the frequency of operation exactly matches the maximum absorption of the rings.

The cold test set-up used to measure the reflection and transmission from the prebunching resonator used in the experiment is shown in Figure 19. The BWO is operated in “ Δf ” mode where the source is swept over a narrow range about the center frequency of the resonator. The reflected signal is measured via a directional coupler and a detector, while the transmitted signal is detected through the coupling hole in the far mirror. The frequency is measured using the interferometer in Figure 16 or

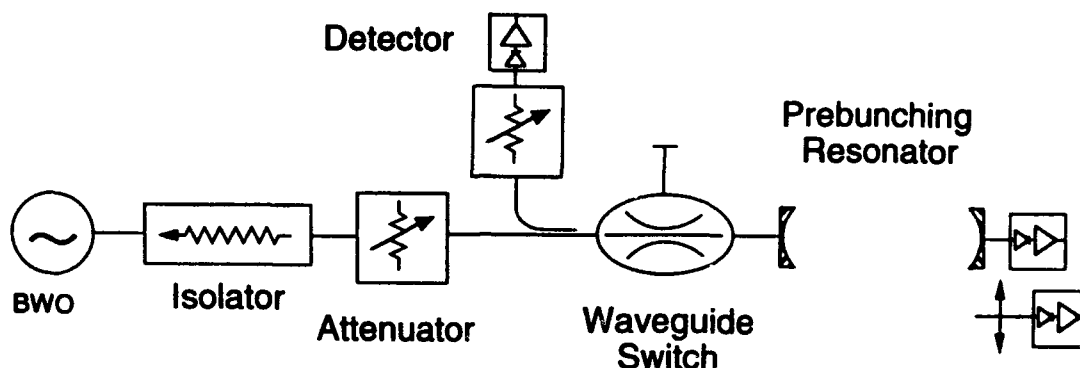


Figure 19: Cold test schematic for the final prebunching resonator.

simply a standard WR-10 frequency meter off an unused port on the waveguide switch. The reference short circuit used in the reflection measurements is obtained by placing a small piece of copper tape over the input coupling hole in the resonator mirror or over the aperture of an appropriate length of waveguide. The latter is preferred since it makes a better rf contact and does not allow for any spacial gaps between the waveguide and the short circuit. Various attenuators are used throughout the circuit to reduce the effects of standing waves. Also shown in Figure 19 is a radiation pick-up and a detector. A section of WR-10 is used to map-out the pattern of the diffracted radiation by moving the pick-up radially away from the mirror's edge in small increments.

The prebunching resonator mirrors are initially identical with a 0.8 mm diameter coupling hole and a coupling wall thickness of 0.3 mm. The reflection and transmission from the resonator are measured, the input coupling hole diameter is increased in small increments, and the procedure repeated. The signal transmitted to the far coupling hole is plotted in Figure 20 as a function of input coupling hole diameter. The size of the output coupling hole remains fixed for this data. For input holes below 1 mm in diameter, essentially all of the power is reflected and only a small transmitted reso-

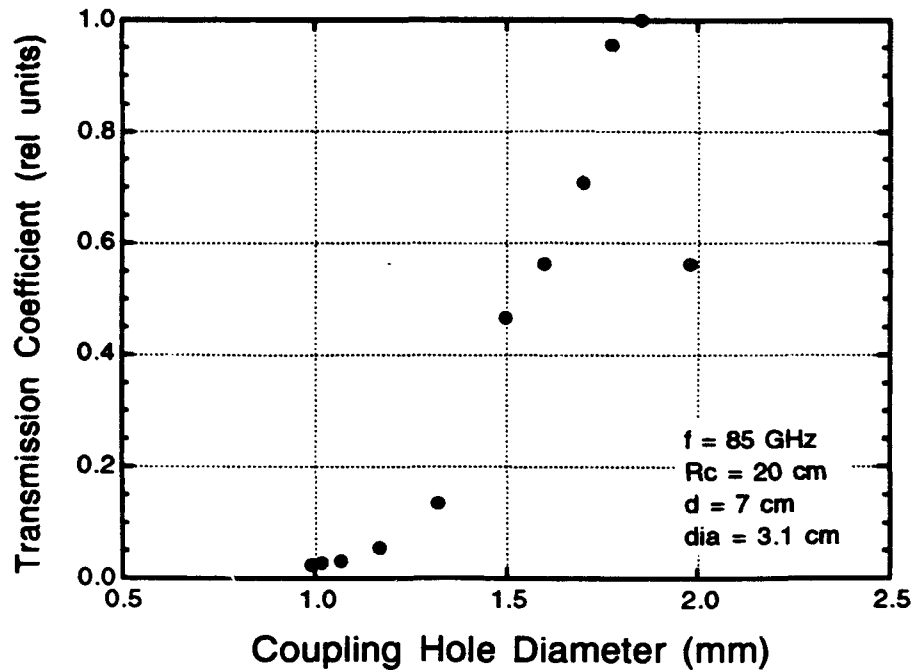


Figure 20: Measured transmitted signal versus input coupling hole diameter.

nance is observed. As the input aperture is increased, the transmitted signal increases monotonically by 20 dB. The transmitted resonance is symmetric in shape as the frequency is swept, and there is very little background radiation detected off-resonance. This indicates that the signal from the far coupling hole is due to the TEM_{00} mode in the resonator with little contribution from nonresonant radiation. Maximum input coupling is obtained for a hole size of 1.8 mm, which is the size of the input hole in the prebunching resonator used in the experiment. A third mirror, identical except for the size of the coupling hole, is used to obtain the last data point at a diameter of 2 mm. At this point the resonator is overcoupled and the power coupled into the prebuncher decreases markedly.

A plot of the power reflection coefficient versus input coupling hole diameter for the prebuncher used in the experiment is given in Figure 21. For input holes less than 1 mm in diameter, the reflection from the resonator is essentially 100%. The reflection from the resonator decreases as the size of the coupling hole increases, due to both resonant mode coupling and nonresonant scattering. The waveform of the reflection takes on an asymmetric shape for hole sizes greater than approximately 60 mils. The

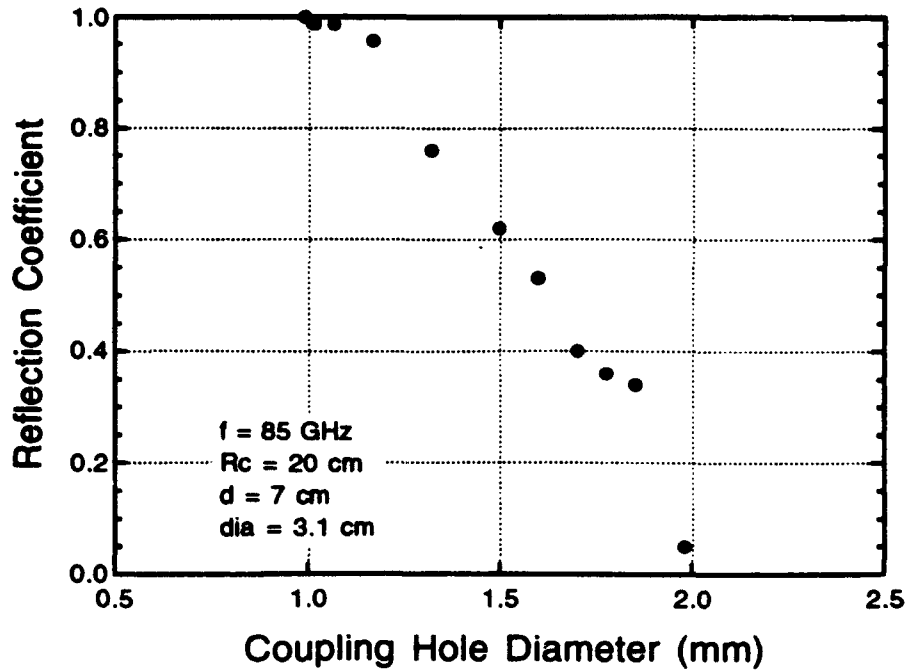


Figure 21: Measured reflection coefficient versus input coupling hole diameter.

minimum reflected signal occurs for a frequency somewhat greater than the resonant frequency of the prebuncher, in contrast to the closed cavity result. All of the data shown in Figure 21 is obtained at the resonant frequency. The point of maximum transmission corresponds to a reflection of approximately 35%, which is the optimum coupling for this resonator. Further increasing the coupling hole size decreases the reflection but also decreases the power coupled into the mode of interest. This result is quite different from the closed cavity case, and indicates that power is transmitted past the input aperture but is not coupled to the TEM_{00} mode.

If 35% of the incident power is reflected, then the maximum power coupled into the fundamental transverse mode is 65%. The technique used to determine the amount of radiation coupled into the desired mode is to measure the absolute power transmitted to the far coupling hole. The previously described measurement on the prebuncher transmission was a relative measurement where the transmitted signals were normalized to the maximum transmission. The output coupling hole was small so that it is a small perturbation on the losses of the resonator. Consider a symmetric prebunching resonator with a coupling hole diameter of 1.88 mm, a mirror diameter of 3.175 cm,

a 0.5 mm bevel on each mirror, and a mirror separation of 7 cm. The value for Q calculated by the diffraction code is 2030, while the calculated fractional slot loss is 29% of the total resonator losses. If the reflection coefficient is assumed to be 0.35, then the maximum signal transmitted to the far hole will be 9.4% (-10.3 dB). The dimensions of this resonator are very similar to those considered in Figure 14.

The EIO is used to measure the FWHM of this resonator during cold test, yielding a measured value of $Q = 2000$. Again, this is in excellent agreement with the quality factor calculated from scalar diffraction theory. The BWO is used in the measurement of the power transmitted to the far coupling hole for this resonator, which is 9.3 dB down from the incident signal. This corresponds to a measured fractional slot loss of approximately 12%, which is close to the calculated value of 9.4%. This measurement clearly indicates that a large fraction of the transmitted power is coupled into the mode of interest in the prebunching resonator. The fact that the transmission is slightly larger than the calculated value may be related to the sensitivity of the calculated values on the resonator dimensions.

Another effort was made to differentiate between diffraction of the TEM_{00} mode and nonresonant scattered radiation. The radiation diffracted beyond the mirror is mapped-out using a section of WR-10 waveguide (without the flange) and a detector. The mirrors are mounted in optical mounts so that the separation can be varied. The BWO is swept about the resonant frequency of the prebunching resonator and the pattern is obtained by scanning the waveguide radially away from the mirror edge. The mirror separation is then varied by a small amount so that the resonant frequency is shifted. The pattern is scanned again for this nonresonant case. The diffraction patterns are shown in Figure 22 as a function of distance from the mirror. The diffracted signal for the TEM_{00} mode shows a large peak near the mirror edge, which is to be expected. The nonresonant radiation has very little structure and shows none of the variation associated with the fundamental transverse mode. The radial scans confirm that most of the incident power is coupled to the mode of interest and is not scattered from the resonator.

A photograph of the prebunching resonator used in the gyrokystron experiment is

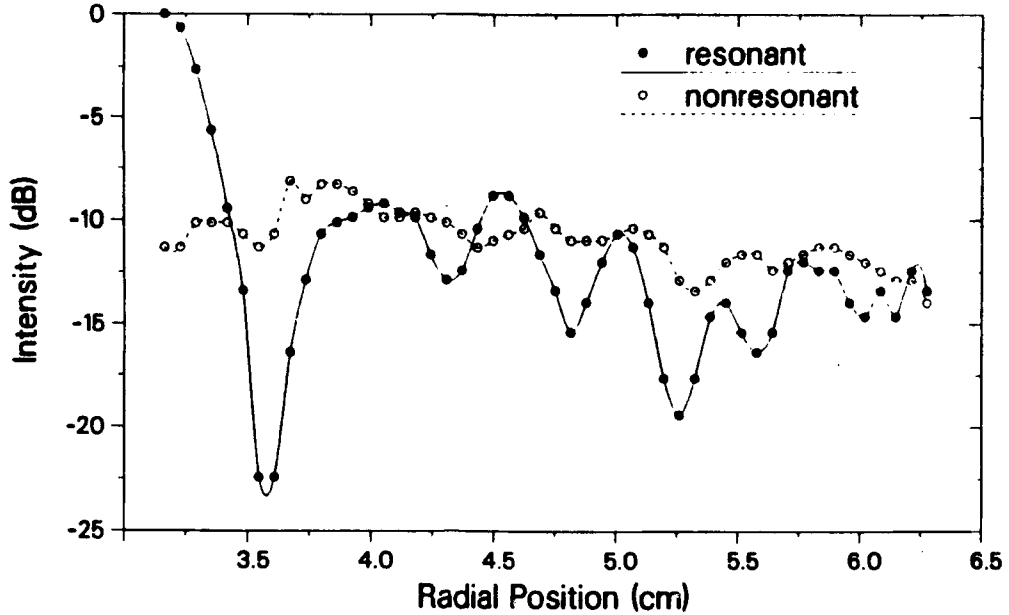


Figure 22: Measured radial scans of the prebunching resonator.

shown in Figure 23. Ohmic losses in this resonator are a small fraction of the total losses, so that a material with a relatively low conductivity, such as aluminum, can be used for the mirrors. There is a circular hole in each of the mirrors for coupling, while the separation between the mirrors is fixed at 7 cm. The mirror holder is fabricated so that the mirrors are parallel to within 0.5° . This specification is verified on the cold test bench by passing the HeNe laser beam through the coupling holes and checking the alignment. The ceramic surrounding the mirrors is designed to absorb the 85 GHz radiation which is coupled out of the resonator via diffraction. The counter-bore in the back of each mirror accepts the flange from standard WR-10 waveguide. In the experiment, the electron beam propagates from the bottom to the top in the photograph. Thus, the polarization of the electric field from the input TE_{10} mode is horizontal to couple to the perpendicular motion of the electrons. The parameters of the prebunching resonator are summarized in Table 1.

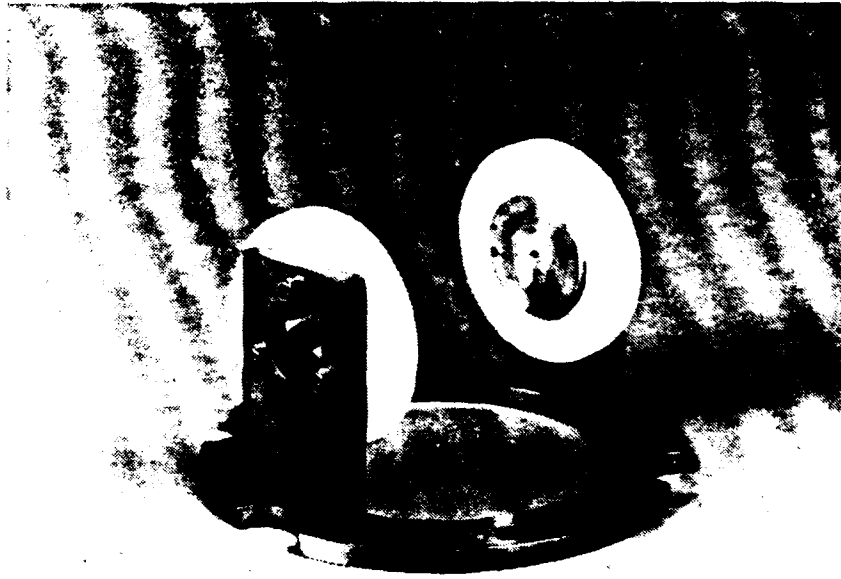


Figure 23: Photograph of the prebunching resonator and mirror holder.

Mirror Separation	7 cm
Mirror Diameter	3.175 cm
Radius of Curvature	20.3 cm
Radiation Waist	0.92 cm
Coupling Hole Diameter	1.83 mm
Total Q	2000
Ohmic Q	122000
Output Coupling	12.5%
Diffraction Loss	8.3%
Coupling Loss	4.1%

Table 1: Summary of prebunching resonator parameters

Chapter IV

Experimental Apparatus and Diagnostics

A. Description of the Experiment

The schematic diagram of the quasioptical gyrokystron experiment is shown in Figure 24. The superconducting magnet is capable of producing fields up to 50 kG on-axis in the main bore (vertical direction in the figure). The field is produced by an arrangement of seven coils, positioned directly above and below the crossbore, with a separation between the two main coils of slightly greater than a Helmholtz pair. Consequently, there is a 7% dip in the magnetic field at the center of the crossbore, as shown in Figure 4. The coils are driven by two separate power supplies so that the magnetic field profile can be varied to provide a positive or negative taper through the interaction region in the output resonator.

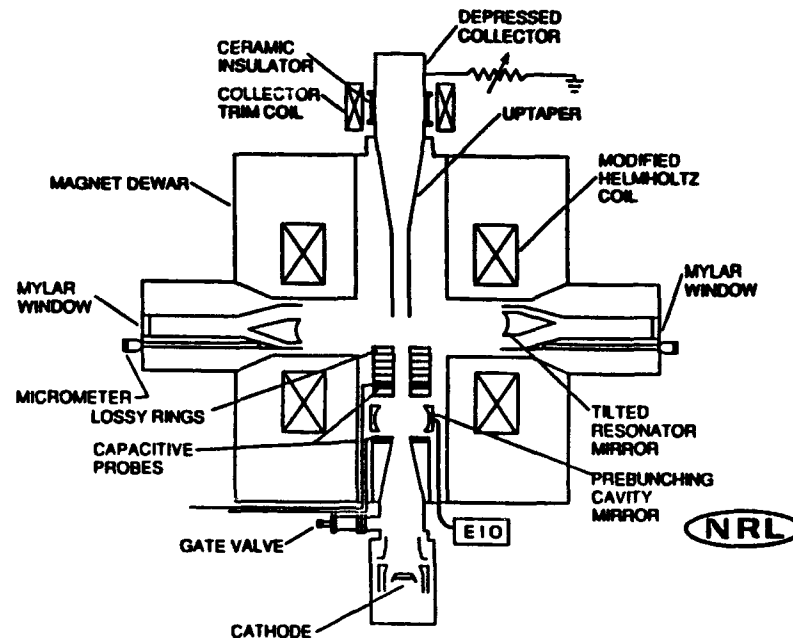


Figure 24: Schematic diagram of the quasioptical gyrokystron experiment.

In the cold bore superconducting magnet, the tube shares the same vacuum as the magnet dewar. The superconducting coils are immersed in a liquid Helium reservoir at 4°K, and there is also a liquid Nitrogen jacket at 77°K to thermally insulate the Helium dewar. These dewars act as a cryopump so that a base pressure of 1×10^{-8}

Torr is obtained. A 30 L/sec ion pump is located atop the magnet off a vacuum port which serves mainly as a pressure diagnostic during hot tests. The pressure inside the tube during operation is typically 3×10^{-8} Torr at a repetition rate of a few pulses per second. The magnet is filled with liquid Helium before running the gyrokystron each day due to the rather large rate of evaporation in the present experiment. Care must be taken to ensure that the magnet dewar does not run out of liquid Helium or Nitrogen, otherwise both the pressure and temperature will rapidly increase.

The magnetron injection gun (MIG), mounted to a flange at the base of the dewar, produces an annular electron beam in the fringing fields of the main coils. Table 2 lists the nominal operating specifications of the gun, which is the same as that used in the Varian and MIT gyrotron programs. The electron gun was originally designed for use in a 140 GHz conventional cavity gyrotron operating in the $TE_{15,2}$ mode[7]. The exact operating conditions for the gun in the quasioptical gyrokystron experiment are somewhat different, and will be described in detail in the next chapter. The magnetic field required for 85 GHz operation is approximately 33.4 kG, and the magnetic compression ratio of the magnet used in the experiment is slightly lower than the original design value. These differences require a smaller mod anode voltage, although the performance of the electron gun is still very good. The maximum voltage of the gun has been pushed to 110 kV, with a maximum current of 60 A. The values for α , $\Delta v_{\perp}/v_{\perp}$, and cavity beam thickness are calculated values obtained using an electron gun simulation program[51]. The beam is formed using a thermionic emitter strip which is heated to $\sim 1000^{\circ}\text{C}$ by applying approximately 110 W of AC power to the heater coil. The gun is mounted using a gate valve so that the gun vacuum is preserved when the experiment is brought up to atmospheric pressure and temperature.

A schematic diagram of the modulator used to power the electron gun is shown in Figure 25. The dc power supply charges a 12 stage pulse forming network (PFN), located at the top right of the figure, which is discharged via a thyatron. The resulting pulse is directed to a 1:12 step-up transformer to reach voltages up to 100 kV. The intermediate anode, also referred to as the mod anode, is charged using a resistive divider circuit which can be adjusted between 0.5-99.5% of the cathode voltage in 1%

Beam Voltage	80 kV
Beam Current	35 A
Mod Anode Voltage	25.2 kV
Cavity Magnetic Field	55.5 kG
Magnetic Compression	30
$\alpha = v_{\perp}/v_{\parallel}$	1.93
$\Delta v_{\perp}/v_{\perp}$	3.9%
Cavity Beam Radius	5.3 mm
Cavity Beam Thickness	0.59 mm
Cathode Current Density	5.0 A/cm ²
Cathode Radius	2.9 cm
Cathode Angle	23°
Anode Angle	3°

Table 2: Original electron gun design specifications.

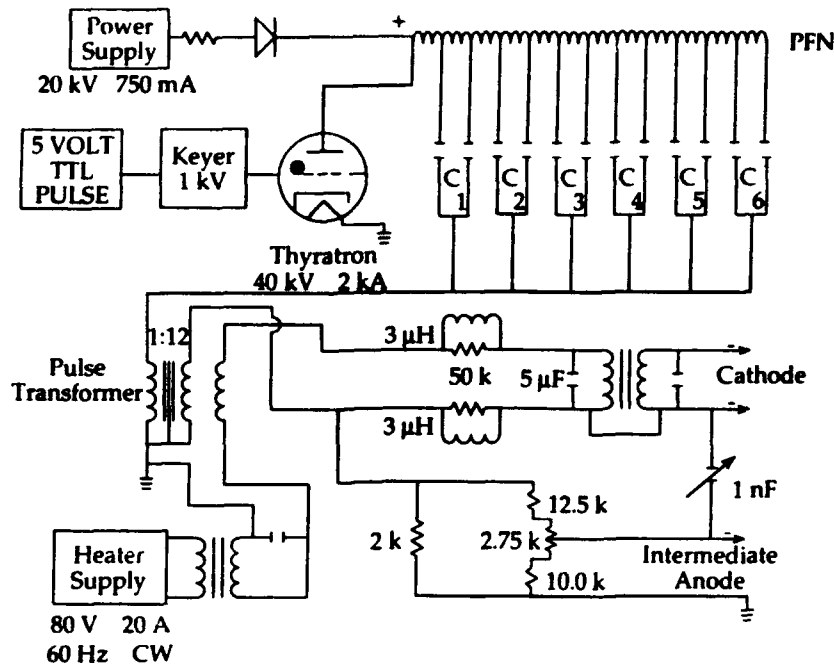


Figure 25: Schematic diagram of the modulator used in the experiment.

steps. An oil-filled load box is placed between the modulator and the electron gun so that changes to the circuit can be made quickly and easily. All resistors used in the load box are the flat, woven type which are cooled by the oil and do not vary in resistance as the voltage is increased. Most of the current from the modulator passes through the shunt resistors, shown at the bottom of the figure, so that the modulator is terminated with a matched load impedance. This is required since the electron gun impedance changes radically during the pulse. The pitch ratio of the electrons ($\alpha = v_{\perp}/v_{\parallel}$) is varied by adjusting the mod anode voltage. The capacitance between the cathode and mod anode is varied to change the evolution of α as a function of time during the rise of the voltage pulse. As will be seen in the next chapter, the evolution of α and γ in time has important effects on the operation of the gyroklystron.

The electron beam is collected at the top of the experiment and outside of the magnet dewar. The collector is electrically isolated from the dewar using a ceramic break so that depressed collector studies may be performed. Different values of resistance are placed between the collector and ground so that the beam is collected at a negative potential during the duration of the 13 μ sec pulse. The resistors are the woven type

described earlier and are immersed in oil in the load box. The collector is water cooled so that high average power can be obtained, and is also bakeable to reduce outgassing.

The section immediately proceeding the collector is referred to as the uptaper, and is shown in Figure 24. The uptaper guides the electron beam from the high magnetic field region near the main resonator to the low field region at the collector. There are numerous holes drilled in this piece to load low frequency gyrotron oscillations and allow for more efficient vacuum pumping. Because of geometrical constraints, a portion of the electron beam is often collected on the uptaper, which is undesirable during depressed collector operation.

To understand the trajectories of the beam electrons in this region, consider Busch's Law which is derived from the conservation of angular momentum.

$$B_c r_c^2 = B(r_g^2 - r_l^2) \quad (51)$$

Here the subscript c refers to the cathode and r_g and r_l are the guiding center radius and Larmor radius, respectfully. High frequency gyrotrons operate with large magnetic compression ratios and high magnetic fields so that $r_l \ll r_g$. The previous equation may now be written $r_g \cong r_c \sqrt{B_c/B}$. The electron beam thickness for the magnetron electron gun used in the experiment is on the order of $3r_l$, so that the outermost electrons reach a maximum radius of $r_{max} = r_g + \frac{3}{2}r_l$. The Larmor radius is defined $r_l = v_\perp \gamma / \Omega$, where Ω is the nonrelativistic cyclotron frequency and v_\perp is the perpendicular velocity of the beam electrons. Conservation of magnetic moment implies that p_\perp^2/B is a constant of the motion. The above relations may be used to calculate the maximum diameter of the electron beam in an adiabatically varying magnetic field.

A trim coil is placed at the position where the uptaper ends to compress the beam into the collector. First consider the case where the trim coil current is zero, as seen in Figure 26. The beam diameter is smallest at the position $z = 0$, which is at the center of the crossbore. The magnet currents are 48.5 and 48.2 A for the upper and lower coils, respectfully, yielding a magnetic field of 33.42 kG at the output resonator. The axial magnetic field is calculated using the standard formulae for solenoids, given by Montgomery in [52]. Given the position, current, dimensions, and number of turns of the solenoids, the magnetic field is calculated by summing the contributions of the

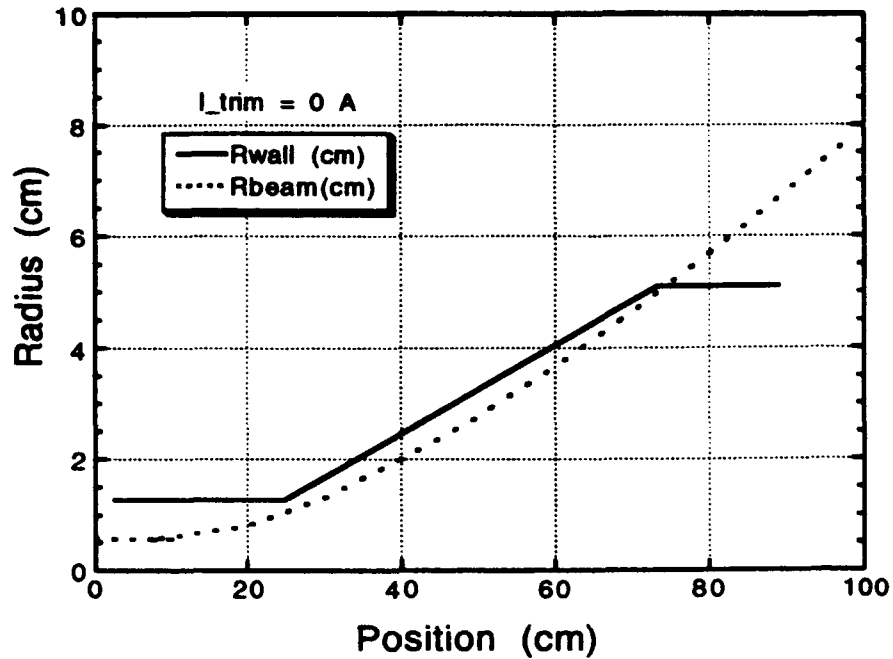


Figure 26: Beam expansion without a collector trim coil.

different coils. The beam is collected on the uptaper near the position $z = 73$ cm, although it nearly intersects at $z = 25$ cm.

For a trim coil current of 300 A the trajectories of the electrons are much different. The trim coil is positioned between 92-102 cm, and it can be seen in Figure 27 that none of the beam intersects the uptaper. The trim coil provides 2.08 kG in the center of the solenoid, which is much greater than the fringing field of the main coils. In the experiment, the trim coil is driven by two separate power supplies capable of 600 A total current. However, the maximum current is limited to about 300 A due to the large amount of heat dissipated in the coil during dc operation. The trim coil is water cooled and the supplies are connected to flow switch interlocks to prevent melting the coil in the event that the flow is interrupted. For the calculation shown in Figure 27, the electron beam voltage is 70 kV and $\alpha = 1.5$ in the output resonator. Lower values of α result in smaller Larmor radii and smaller electron beam diameters. Varying the trim coil current and the average α of the beam provides a diagnostic to directly measure the beam thickness, which yields information on the average α and the spread in pitch angle.

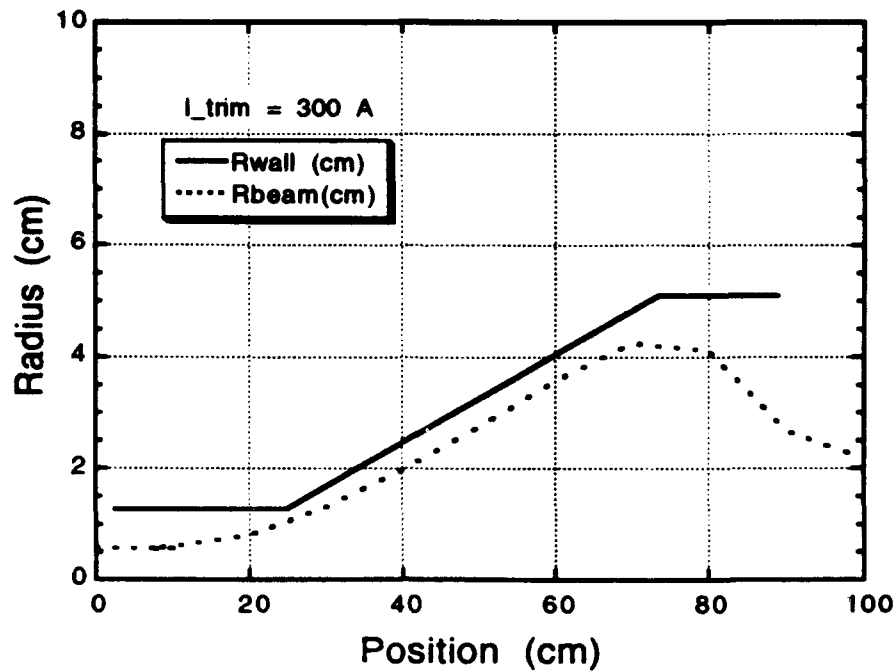


Figure 27: Beam expansion with a collector trim coil.

There are a number of current monitors located throughout the gyrokystron to determine where the electron beam is collected. These include the cathode, collector, mod anode, uptaper, drift tube, collector tip, and dewar. The current monitors are manufactured with tolerances of $+1\% / -0\%$, and are calibrated in-house using several techniques which confirm the original specifications. This information is particularly important when calculating the rf efficiency of the interaction. Under optimum operating conditions, essentially 100% of the current reaches the collector. However, a good deal of data is collected where the trim coil current is less than 300 A, so that some of the current is collected on the uptaper. During the assembly of the tube, the uptaper was partially shorted to the dewar so that they are no longer electrically isolated. Although a quantitative comparison of these currents is not possible, they can be used to determine when current is collected on either the uptaper or dewar. Summing the contributions from the collector, uptaper, and dewar monitors yields the current measured at the cathode. No current is observed on the mod anode, drift tube, or collector tip during normal operation.

The cathode and mod anode voltages are measured using capacitive voltage mon-

itors located in the load box. Careful calibration of these monitors is required for accurate measurements of efficiency and frequency detuning, as well as voltage measurements for electron trajectory simulations. A commercial high voltage probe is used to calibrate the monitors in situ up to 40 kV. The electrical connections to the electron gun are unchanged during the calibration, since changes in the capacitance of the circuit affect the voltage induced on the monitors. The ratio of mod anode-to-cathode voltage is then measured up to cathode voltages over 80 kV. The ratio of the two is constant as a function of voltage with a measured variation of less than 0.4%, which approaches the error in the measurement. This result confirms that the voltage monitors are linear and the resistive divider circuit is constant as a function of voltage.

Typical oscilloscope traces of the cathode voltage and the collector current are shown in Figure 28. The voltage pulse has a 12 μsec flat top and a 5 μsec risetime. The 12 stage PFN induces $\pm 1.3\%$ voltage ripple with 6 periods during the flat top of the pulse. Reducing the ripple to below 1% has no effect on the output radiation from the gyrotron in the present experiment. The risetime of the voltage pulse is limited by the inductance of the 1:12 step-up transformer, where the PFN rise is approximately 1 μsec . The collector current initially rises very quickly due to temperature-limited operation. The current reaches the final flat-top value more slowly, since it is space charge limited under these conditions. This effect is also observed in that increasing the cathode voltage increases the current emitted from the electron gun.

A photograph of the drift tube assembly is shown in Figure 29, where the electron gun mounts to the bottom flange. The annular electron beam is generated outside the magnet dewar and then passes through the beam tunnel, which comprises a section of green-fired stainless steel with slots to load low frequency gyrotron oscillations. The beam tunnel is electrically isolated from the gun flange using ceramic insulators. The beam passes through the drift tube, which is composed of alternating copper and ceramic rings which are designed with varying thicknesses to load high frequency gyrotron oscillations in the high magnetic field region. The copper rings are tapered on the inside edge to reduce the probability of oscillations due to gyrotron interactions with the conducting wall. The drift tube is interrupted for 5 cm to allow for the prebunching

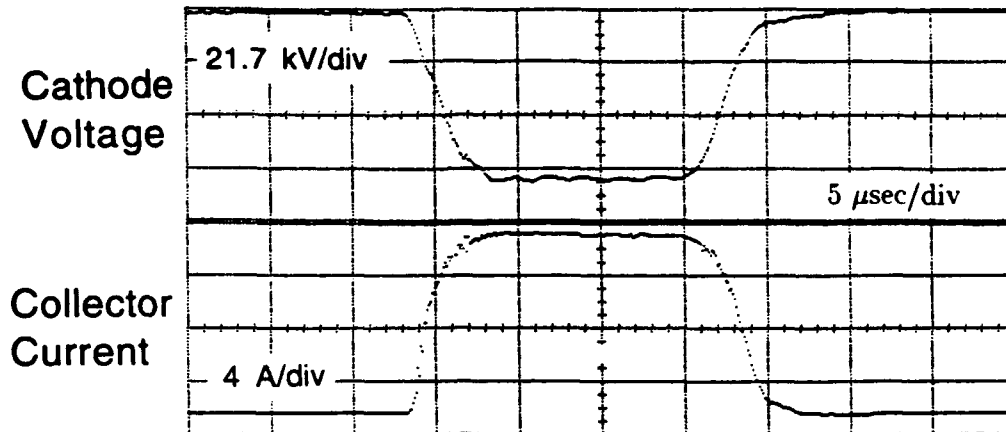


Figure 28: Oscilloscope traces of the cathode voltage and collector current.

resonator, whose axis is perpendicular to the direction of beam propagation. There is a 1.15 cm radius crossbore cut through the drift tube to accommodate the prebuncher radiation waist of 0.92 cm. A ceramic sleeve is located inside the drift tube in this region with a thickness to resonantly absorb rf radiation at 85 GHz.

The input and output signals from the prebunching resonator are transmitted through standard WR-10 rectangular waveguide to vacuum windows mounted on the bottom flange near the gun. The windows are fabricated using a thin piece of Mylar which is epoxied to a stainless steel high vacuum flange. The thickness of the Mylar is less than $\lambda/20$ in the dielectric, which results in a very wide transmission bandwidth. Although not suitable for high average power, the windows have a reflection loss of less than 1 dB, are low cost, and require only a short lead time.

The operating frequency of the quasioptical gyrokystron experiment is determined by the availability of a suitable source, in this case an 85 GHz extended interaction oscillator (EIO). The EIO produces 1.8 kW peak power in pulses up to 2 μ sec with a maximum duty factor of 0.5%. Both the pulse width and the pulse repetition rate are continuously variable from the control panel, although the experiment is usually

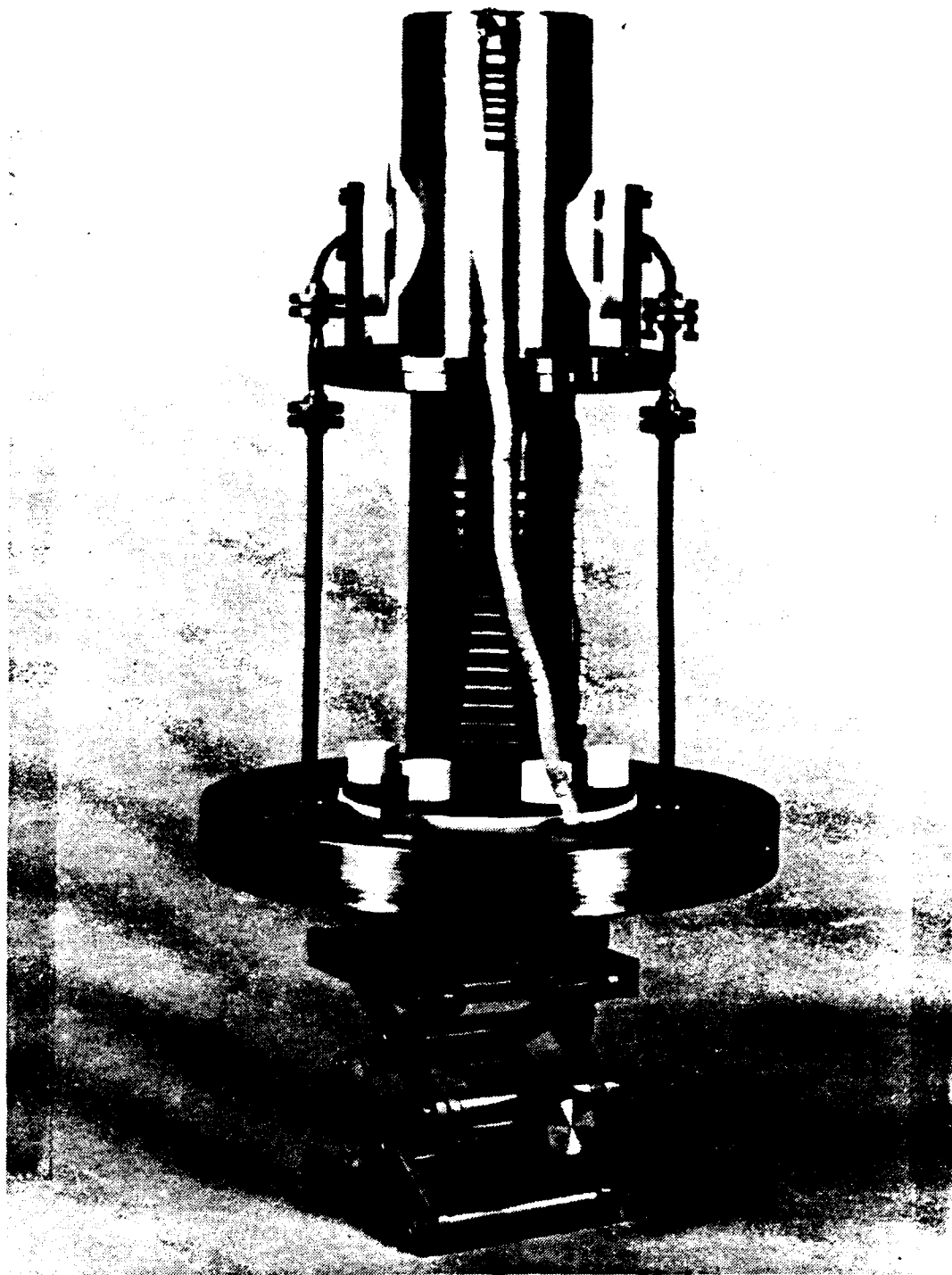


Figure 29: Photograph of the drift tube assembly.

operated at only a few pulses per second. The EIO is mechanically tunable between 84–86 GHz via a micrometer drive and frequency controller. Varying the beam voltage of the EIO allows fine tuning of the frequency of up to ± 300 MHz. Precise control of the frequency is accomplished quickly and is very important during phase-locking investigations. For pulse lengths shorter than $0.5 \mu\text{sec}$, the frequency spectrum of the EIO is temporally limited ($\Delta f \Delta T \sim 1$). However, longer pulses are affected by a voltage droop in the grid circuit of the EIO so that large frequency chirps are observed. For example, a $2 \mu\text{sec}$ pulse has >10 MHz downward droop during the pulse. This subject will be discussed more fully in the next chapter in the amplifier section. The power supply and modulator of the EIO are mounted on a freon cooling plate so that the operating temperature remains below 30°C .

Another photograph of the drift tube is shown in Figure 30 where the prebunching resonator is removed, giving a clearer view of the interior. There are a pair of vertical slots that run the length of the drift tube to allow for the posts of two capacitive probes[53]. The probes have the same inside dimensions as the copper rings and are used to measure the average α of the beam electrons. The outside diameter of the probes is somewhat smaller than the drift tube radius so that the probes do not touch the drift tube wall. The copper discs are held in place with a small lip on the ceramic rings directly above and below each probe. The posts and wire leads are electrically isolated from the dewar and drift tube using ceramic pieces which can be seen in Figure 29. A voltage is induced on the probes when the beam is present which is proportional to the longitudinal charge density. The average pitch ratio of the electrons can then be calculated if the beam energy and current are known.

An idealized geometry of the capacitive probes is given by considering two long concentric cylinders which are electrically isolated from each other. With an electron beam at the center of the cylinders, Gauss' Law is used to calculate the electric field E_r between the electrodes.

$$\int E_r r d\phi dz = -\frac{1}{\epsilon} \int \rho r dr d\phi dz \quad (52)$$

In this equation, ρ is the volume charge density of the beam and ϵ is the dielectric constant of the medium. The electric field is obtained by integrating the previous

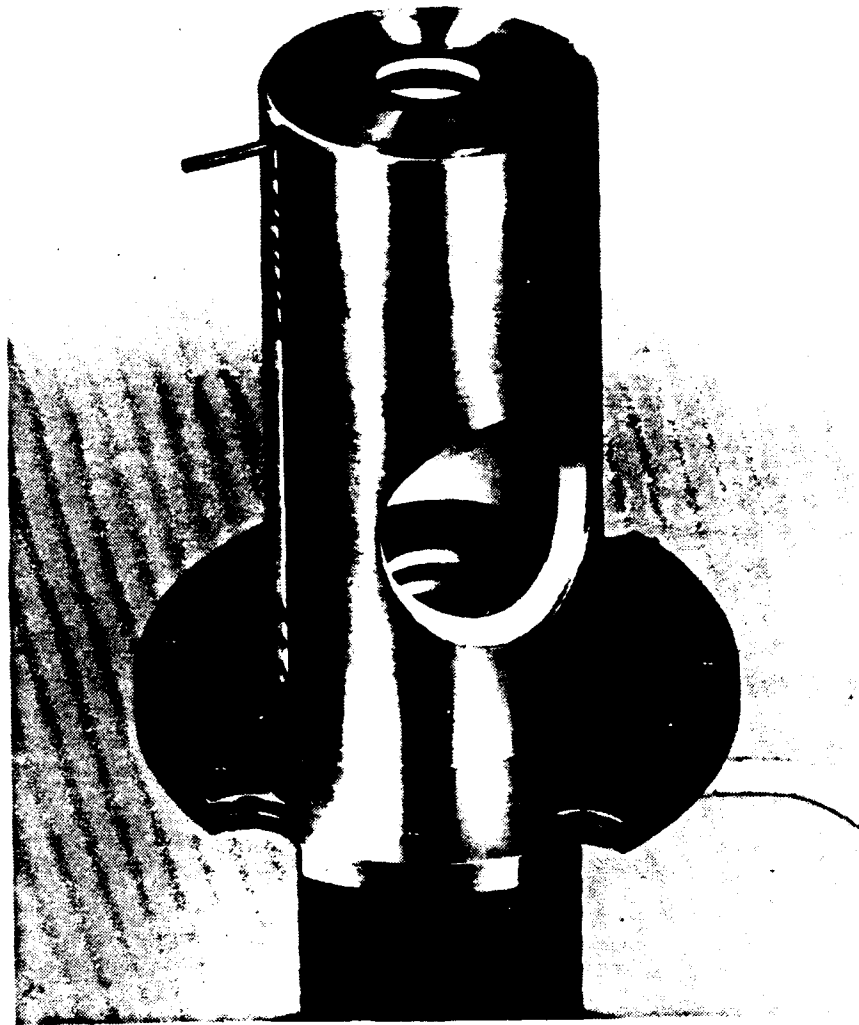


Figure 30: Photograph of the drift tube without the prebunching resonator.

equation.

$$E_r = -\frac{\xi}{\epsilon} \frac{1}{2\pi r} \quad (53)$$

Here $\xi = \int \rho r dr d\phi$ is the charge per unit length at the center of the cylinders. The voltage induced on the inner cylinder is obtained by integrating the electric field from the inner surface to the outer surface.

$$V_p = \frac{\xi}{2\pi\epsilon} \ln(r_o/r_i) \quad (54)$$

The parameters r_o and r_i are the radii of the outer and inner cylinders, respectively. The capacitance per unit length of the probe for this geometry is written $C_p = 2\pi\epsilon/\ln(r_o/r_i)$. The longitudinal charge density can be expressed $\xi = I_b / \langle v_{||} \rangle$, where I_b is the beam current and $\langle v_{||} \rangle$ is the average longitudinal velocity of the electrons.

The probes used in the experiment are thin discs so that the expression for the capacitance given above for the idealized geometry is not valid. The capacitance of the probe is determined experimentally by reducing the pitch ratio of the beam so that $\alpha \sim 0$. If there is no perpendicular component of the velocity, then $\beta_{||0} = \sqrt{1 - \gamma^{-2}}$, where β is the ratio of the particle velocity to the speed of light. The experimentally-derived probe capacitance is then calculated using the expression $C_p = I_b / V_p v_{||0}$. Low values of pitch angle are obtained in the experiment by lowering the mod anode voltage via the resistive divider circuit. However, it is unrealistic to expect a beam with $\alpha = 0$ and no spread in pitch angle. Electron trajectory simulations indicate that the minimum alpha is approximately 0.3 for the beam formed in the gyrokystron experiment. Hence, the probe capacitance is calculated using the appropriate longitudinal velocity for this minimum value of α .

A refinement to this calculation for α is the inclusion of space charge depression in the drift tube. The voltage depression for a thin annular beam propagating in a conducting cylinder is given by[54]

$$\Delta V = \frac{I_b}{2\pi\epsilon v_{||}} \ln(r_w/r_b), \quad (55)$$

where r_w and r_b are the wall and beam radii, respectfully. In the quasioptical gyrokystron experiment, the ratio $r_b/r_w = 0.61$. For a beam voltage of 70 kV, a beam

current of 10 A, and $\alpha = 1.5$, there is a 1.4 kV voltage depression in the drift tube. Although this is a rather small effect in the present experiment where the current is less than 15 A, the space charge depression factor is included in the data analysis for completeness. Space charge depression is important when the gyrotron is operated at high power where the beam current is greater than 50 A.

The main idea behind the capacitive probe is the measurement of the average $\beta_{||}$ of the electrons when the beam current and energy are known. This limits the use of the capacitive probes to electron beams where the average pitch ratio is on the order of 1 or 2. Consider the case where the beam electrons have no perpendicular component of velocity: $\beta_{\perp} = 0$. The parallel component of the electron velocity is written $\beta_{||0} = \sqrt{1 - \gamma^{-2}}$ for some arbitrary γ . For the case of finite α , the parallel velocity is expressed $\beta_{||} = \beta_{||0} / \sqrt{\alpha^2 + 1}$. The normalized longitudinal velocity is plotted in Figure 31 as a function of the electron pitch angle. For values of α between 0 and 0.3, the longitudinal velocity of the electrons varies by only 4%, which is very difficult to measure in an experiment. On the other hand, a pitch ratio of 1.0 results in a normalized longitudinal velocity ratio of 0.71, which is easily discernible in the laboratory. Accordingly, a $\pm 5\%$ margin of error in the measurement of $\beta_{||0}$ for an average $\alpha = 0.3$ results in values of α ranging between 0 and 0.5. For a mean pitch ratio on the order of 1.7, the same margin of error in the longitudinal velocity causes a variation in α of only $\pm 5\%$.

The capacitive probes are placed in the drift tube immediately before and after the prebunching resonator, which corresponds to directly before and after the first peak in the magnetic field. The probes provide several important functions beside measuring the average pitch ratio of the beam. It has been speculated that the magnetic field minima at the center of the crossbore causes electrons to become trapped in this region. Electrons which lose a significant amount of perpendicular energy to the rf fields could be mirrored before reaching the second magnetic field maxima. The capacitive probes measure longitudinal charge density, therefore comparing probe signals before and after the first maxima indicates whether electrons are reflecting. Another benefit of the probes occurs during depressed collector operation. If the collector depression

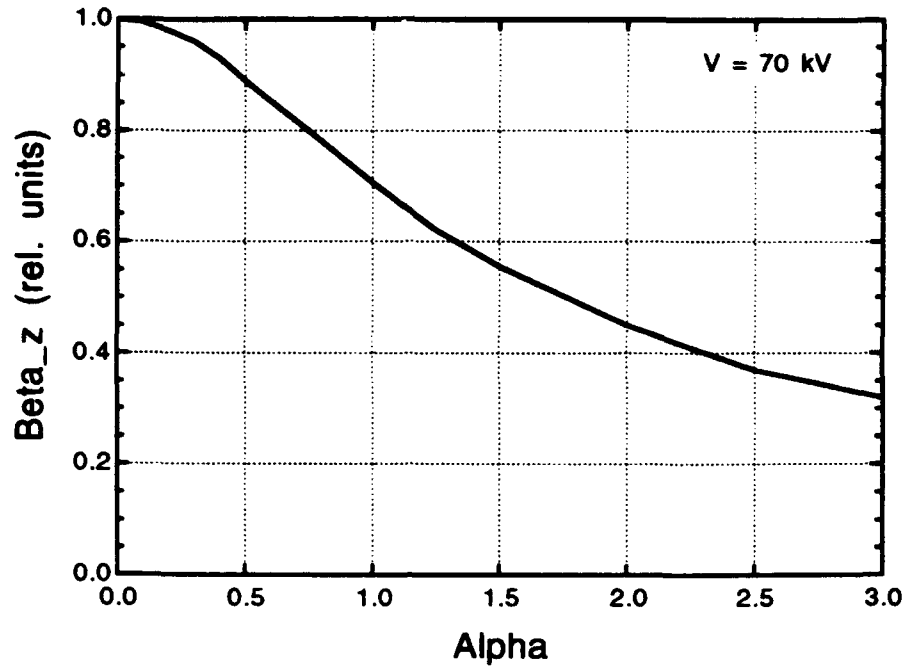


Figure 31: Normalized $\beta_{||}$ versus pitch angle α .

is increased to a large value, electrons are reflected from the collector and follow the magnetic field lines back through the main resonator. The probes can be used to indicate the onset of these reflections via a large increase in the probe signal. Lastly, the probes can be used to detect oscillations in the drift tube or the prebunching resonator. Gyrotron oscillations induce high frequency noise on the beam which is readily observed on a downstream probe. This measurement is quite valuable when drift tube oscillations are a candidate for poor tube performance. Note that since the output radiation is perpendicular to the direction of beam propagation in the quasioptical gyrotron, drift tube oscillations may not be detected in the output of the tube.

There is a gap between the end of the drift tube and the beginning of the uptaper to allow the beam to interact with the fields in the main resonator. This open resonator is formed by a pair of spherical mirrors separated by many radiation wavelengths. The characteristics of the output resonator used in the gyrokystron experiment are summarized in Table 3, where the resonant frequency is on the order of 85 GHz. Radiation is coupled out of the resonator via diffraction of the TEM_{00q} mode(s) around the mir-

Mirror Separation	21 cm
Radius of Curvature	38.7 cm
Mirror Diameter	5.5 cm
Mode Density	0.84%
Mode Separation	714 MHz
Tilt Angle	2°
Radiation Waist	1.39 cm
Ohmic Q	408 000
Diffraction Q	41 000
Total Q	37 300
Output Coupling	2%
Interacting Modes	~4
Interaction Length μ	14.8

Table 3: Summary of typical output resonator parameters

ror edges, where q is approximately 120 in the present configuration. This output is collected by the mirror holders and transported outside the magnet dewar to the rf diagnostics. The mirror holders are mounted using three precision micrometers so that the mirror separation and alignment can be adjusted with high precision. The mirror separation can be varied between 20–28 cm in the experiment, although most of the data is collected at a separation of 21 cm. The output coupling varies from 1.5 to 4.3% over this range of mirror separations, and allows for a technique to optimize the strength of the rf fields in the resonator.

The number of interacting modes in the gyrotron is estimated using the expression

$$N_m = \frac{\beta_{||0} d}{r_0}, \quad (56)$$

where d is the mirror separation and r_0 is the radiation waist. This expression is derived by dividing the longitudinal mode spacing ($\Delta f = c/2d$) into the interaction bandwidth. The resonator parameters for the gyrokystron experiment are very similar to previous resonators used in 120 GHz gyrotron experiments, which facilitates a direct

comparison of the results. The separation between the uptaper and drift tube must be large enough so that the surrounding structure does not interfere with the mode in the open resonator. Cold tests indicate that 1.7 radiation waists are required between a nearby obstruction and the center of the resonator so that there is no degradation in Q . The gap in the present experiment is 5.08 cm, resulting in a ratio of 1.8. The length of this region should be minimized to reduce the effect of space charge depression as the electrons traverse the open resonator. It should be noted that a small interaction between the resonant mode and the surrounding structure has little effect on Q initially. The quality factor will be reduced by a factor of 2 when the distance to the obstruction is approximately 1.3 radiation waists.

In the gyrokystron experiment, the axis of the output resonator is tilted by 2° relative to the plane perpendicular to the direction of beam propagation. It has been shown theoretically that the region of stable, single-mode operation of the QOG is dramatically reduced when an annular electron beam is used, as opposed to a pencil beam[16]. Tilting the resonator axis by a few degrees allows all electrons to interact with both even and odd longitudinal modes, which increases the ability of the working mode to suppress competing modes. The region of single-mode operation is essentially increased to that of the pencil beam, although higher electric fields are required in the resonator for optimum efficiency. Nonlinear mode suppression is particularly important in the present experiment to demonstrate techniques such as mode priming, where the beam is bunched by the EIO only during the rise of the voltage pulse.

The operating parameter space of the gyrotron can be characterized in terms of three normalized variables. The slow time scale equations of motion for a single mode are characterized by the normalized wave amplitude F_s , interaction length μ , and detuning Δ . The benefit of this approach is that the transverse efficiency of the gyrotron can be plotted as a function of F - μ for optimized detuning. The normalized variables for a quasioptical gyrotron operating at the fundamental cyclotron frequency are[15]

$$F_s = \frac{E_c \beta_{\perp 0}^{-3}}{B_0 c} \quad (57)$$

$$\mu = 2\pi \frac{\beta_{\perp 0}^2 r_0}{\beta_{\parallel 0} \lambda} \quad (58)$$

$$\Delta = \frac{2}{\beta_{10}^2} \left(1 - \frac{\Omega/\gamma}{\omega} \right) \quad (59)$$

In the above equations, E_c is the electric field in the resonator, B_0 is the axial magnetic field, and Ω is the nonrelativistic cyclotron frequency. A pencil electron beam is assumed where the beam is placed on the peak of the standing wave. An annular beam is used in the experiment, so a better description requires averaging the efficiency for each electron according to its position with respect to the standing electric field. For a beam voltage of 70 kV and a pitch angle of 1.5, the normalized interaction length is 14.8, which is typical of recent QOG experiments. One drawback to the above formulation is the sensitivity of the interaction length on α . Reducing the pitch angle to 1 for the above conditions results in $\mu = 8.4$, which is a rather large variation.

Accurate alignment of the mirrors is important in a high- Q Fabry-Perot-type resonator. In the present experiment, the mirrors are initially aligned in the crossbore while the magnet is warm using a pair of HeNe lasers. Due to the small clearance between the mirror holder and crossbore, these two pieces come into contact when the magnet is cooled to cryogenic temperatures. However, the degradation in alignment is on the order of 0.2° . From the cold test results in Figure 32, a 3° misalignment is required to reduce the quality factor by 30%. This data is obtained for a frequency of 94 GHz, mirror diameters of 5.0 and 5.5 cm, 38.7 cm radii of curvature, and a mirror separation of 23.8 cm. Thus, this data should be a good indication of the sensitivity of the experimental resonator to misalignment. In general, poor mirror alignment can have a dramatic effect on the interaction efficiency, so care must be taken when translating the mirrors over large distances (several cm).

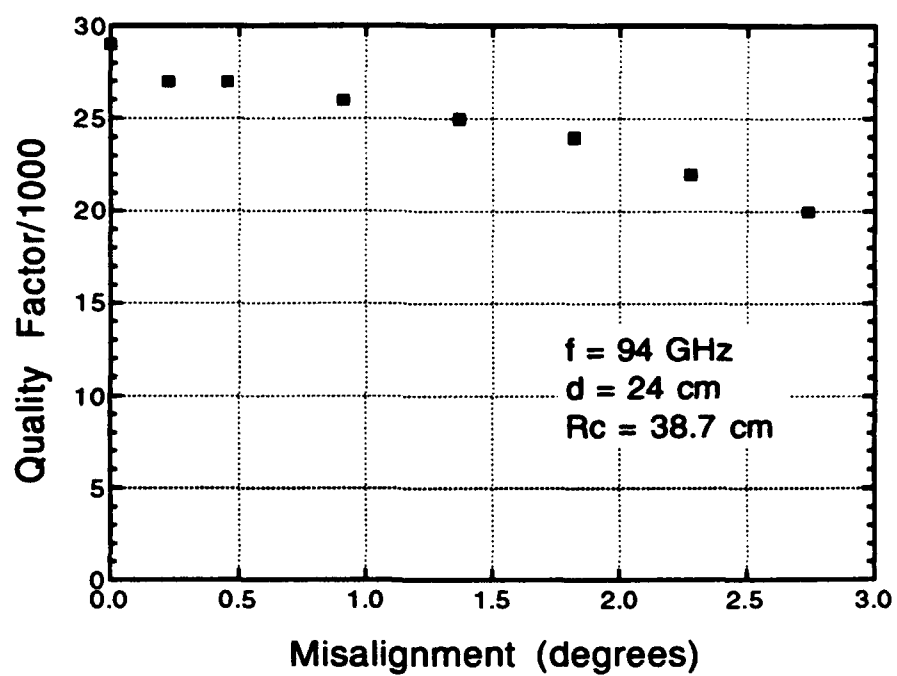


Figure 32: Resonator Q versus mirror misalignment.

B. Millimeter-Wave Diagnostics

A simplified schematic diagram of the millimeter-wave diagnostics used in the quasi-optical gyrokystron experiment is shown in Figure 33. A modified laser calorimeter which preferentially absorbs radiation at 85 GHz is used to measure the average power from one side of the experiment. Standard W-band waveguide and detectors are used to monitor the output pulse from the gyrotron and the input/output signals from the prebunching resonator. A unique heterodyne system is used to measure the frequency of the gyrotron and EIO, and also functions as a spectrum analyzer. Each of these components will be described in detail in this section, as well as a balanced mixer/phase detector which is used in the amplifier and phase-locking studies.

The average power from the experiment is monitored using a commercially available laser calorimeter from Scientech which is coated with additional absorbing paint. The incident wave is absorbed in the layer of lossy paint on an aluminum surface, where the temperature rise of the surface is measured by thermopiles. Several lossy coatings were tested during fabrication of the calorimeter to maximize absorption at 85 GHz, including Aerodag (graphite suspended in alcohol), solar absorbing paint, and Scientech Black paint. Scientech Black proved to have the highest absorption at approximately 90%, where the absorption of the paint is measured as a function of coating thickness.

The absorption of the calorimeter is measured using the cold test apparatus depicted in Figure 34. The BWO source between 75-110 GHz is used to radiate the calorimeter using standard WR-10 waveguide components and standard gain horns, where the components F and A refer to a frequency meter and variable attenuator, respectfully. The calorimeter is placed in the far field of the horns, and the incident and reflected signals are measured as the angle of incidence between the wave and the calorimeter is optimized. The maximum reflection from the calorimeter is then compared with a reference reflection from a circular metal plate which is identical in shape to the calorimeter. Absorbing material is placed around the calorimeter surface and the reflecting plate to minimize spurious reflections due to edge effects. In general, though, the spot size of the radiation pattern is confined to the center of the plate so that the fields at the edge are small. The calorimeter and reference plate are mounted

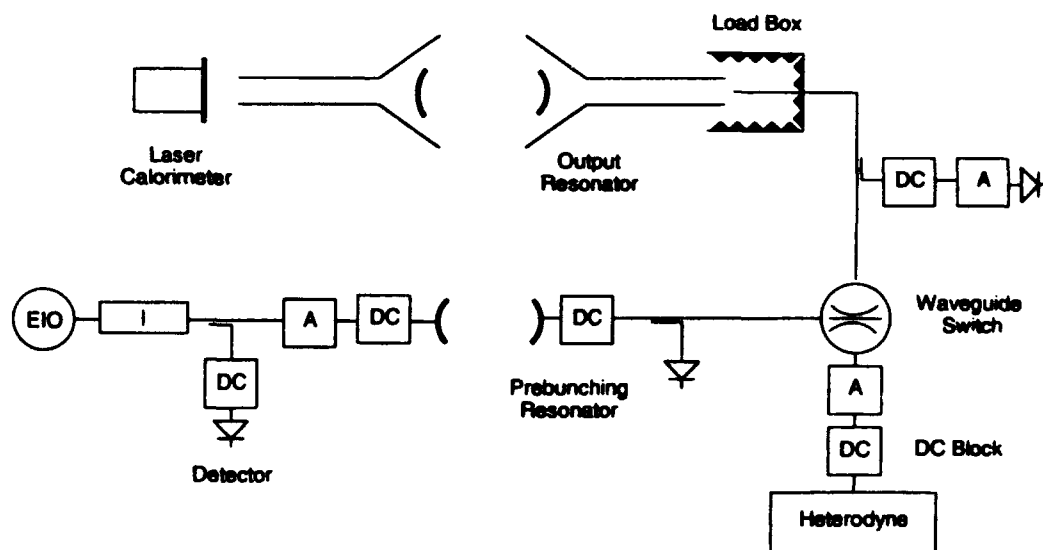


Figure 33: Simplified schematic of the millimeter-wave diagnostics.

using a 3-D translational stage and another pair of mounts to rotate and adjust the tilt of the surface. An accurate measurement of the reflection requires that the reference and calorimeter surfaces have the same position with respect to the incident electric field, which is accomplished by varying the tilt so that the reflection is maximized.

The absorptivity of the calorimeter is measured to be 85% at frequencies within ± 1 GHz of 85 GHz. The response of the calorimeter is flat as a function of frequency, with the absorption remaining near 90% from 80-115 GHz, which is quite unexpected. The calorimeter coating can be modelled as a layer lossy material on a metal plate with dielectric constant $\epsilon = \epsilon_r - j\epsilon_i$. Such a structure shows characteristic resonant behavior where the reflection from the surface is minimized at thicknesses of $d = \frac{\lambda_c}{2}(n + \frac{1}{2})$, where λ_c is the wavelength in the dielectric. A number of trial calorimeter coatings using other materials did exhibit the resonant behavior predicted by the model. Possible explanations for the flat absorption response of the Scientech Black paint include dielectric properties which vary with frequency or the coating cannot be described as a homogeneous thin film.

Another test of the calorimeter is performed using the EIO operating at 1.5 kW and

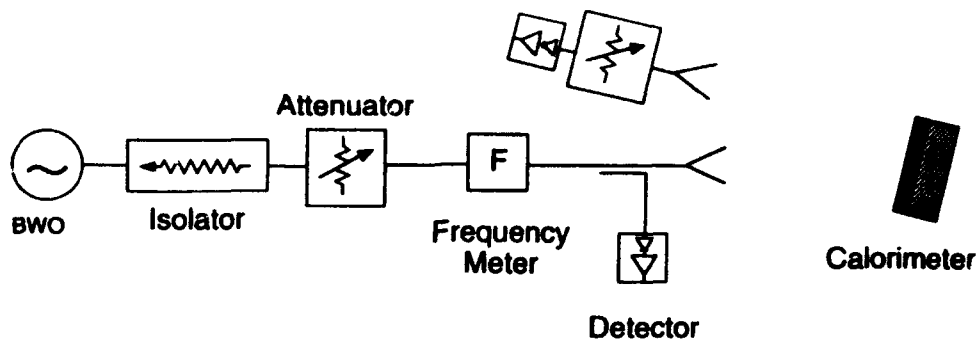


Figure 34: Cold test set-up used to measure calorimeter absorption.

a 0.5% duty factor. The absorbtivity value of 85% is confirmed when the calorimeter is radiated using the EIO. Varying the angle of incidence of the radiation with respect to the calorimeter surface has no effect on the measured power for angles up to 45°. It is important that the thickness of the absorbing paint is uniform across the surface of the calorimeter, or else the absorption will vary as a function of angle.

The output frequencies of the gyrotron and the EIO are measured using the heterodyne system shown in Figure 35. The input rf signal is beat against the output from a frequency-locked, YIG-tuned local oscillator (LO) in a W-band harmonic mixer. The intermediate frequency (IF) is directed through one of several bandpass filters centered at 160 MHz. The resulting signal is amplified and observed on an oscilloscope using a standard video detector. Thus, different longitudinal modes are resolved on the oscilloscope as a function of time during the duration of the voltage pulse. The intermediate frequency is related to the input frequency via

$$f_{IF} = \pm(f_{RF} - n f_{LO}). \quad (60)$$

For example, an input signal at 85.0 GHz and a harmonic number $n = 6$ results in the two frequencies 14.140 and 14.193 GHz observed on the oscilloscope. The separation between these beat frequencies is $\delta f = 320 \text{ MHz}/n$. Any second harmonic radiation present in the output will be characterized with a different harmonic number and a smaller δf . An input rf signal at 170 GHz with $n = 12$ results in local oscillator fre-

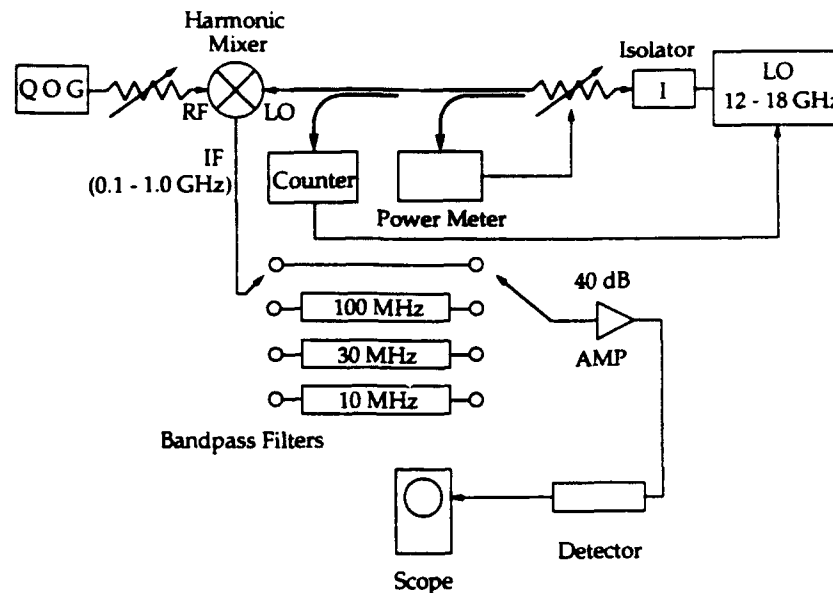


Figure 35: Schematic diagram of the heterodyne system.

quencies of 14.153 and 14.180 GHz. Another technique which is used to differentiate fundamental from second harmonic radiation involves using a section of cut-off waveguide. A short section of WR-03 (170-260 GHz) heavily attenuates the fundamental but passes the 170 GHz signal with little loss.

Frequency measurements are made on all of the data presented in this work on the gyrokystron. Subtle changes in the electron beam parameters result in the excitation of different longitudinal modes with different detuning values. Thus, simply monitoring the calorimeter is not sufficient to fully understand the operation of the tube or optimize performance. Previous experiments on the QOG were often forced to operate without frequency measurements because of noise generated by both the modulator and the electron beam that coupled into the heterodyne circuit. In this work, the noise has largely been removed through modification of some circuits and careful isolation of all heterodyne components. Thus, heterodyne measurements are possible even during high noise conditions such as depressed collector and reflexing electron operation.

The heterodyne is also used to measure the frequency spectrum of the gyrokystron and the EIO as a function of time. The video detector immediately before the oscil-

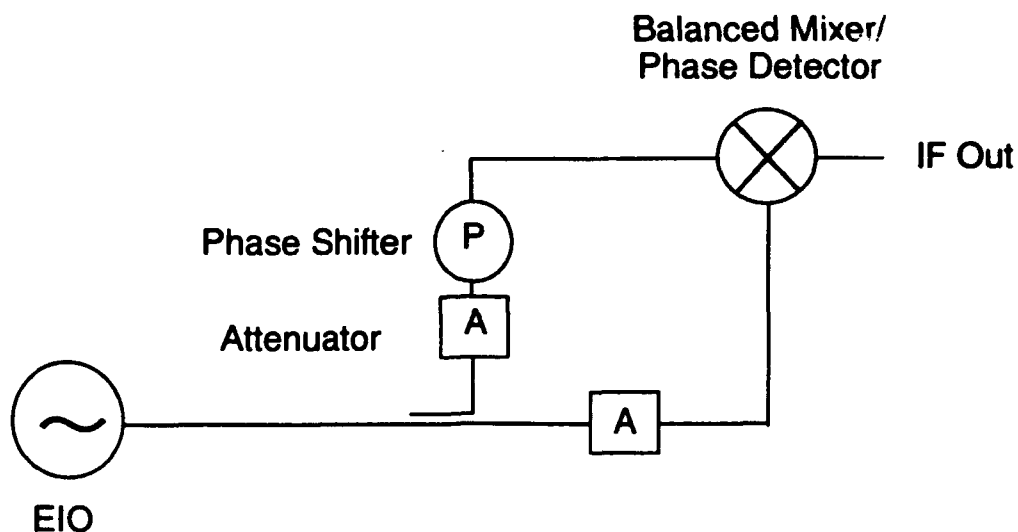


Figure 36: Cold test apparatus for the phase detector.

loscope in Figure 35 is removed so that a signal near 160 MHz is displayed on a fast oscilloscope (400 MHz). The frequency is measured by counting rf cycles during a small portion (200 nsec) of the total pulse. This is a powerful technique which allows 85 GHz signals to be measured with 1 MHz precision.

An 85 GHz balanced mixer/phase detector is used to measure the beat frequency or the relative phase difference between the input/output signals. Consider first the case of the phase detector, where the cold test set-up is illustrated in Figure 36. The EIO signal is split into two arms using a directional coupler, then recombined on the phase detector. As the phase shifter in one arm is varied, the output of the phase detector changes according to $V_{\phi} = \sin \Delta\phi$, where $\Delta\phi$ is the phase difference between the two signals. The input signal levels into the mixer ports should be approximately equal to obtain 100% variation of the output signal as the phase shifter is varied.

Operation in the balanced mixer mode is illustrated in Figure 37. If two free-running oscillator frequencies are combined on the mixer, the difference frequency is observed on the output. During phase-locked operation, the beat frequency is zero and the output of the mixer is related to the relative phase difference through the above

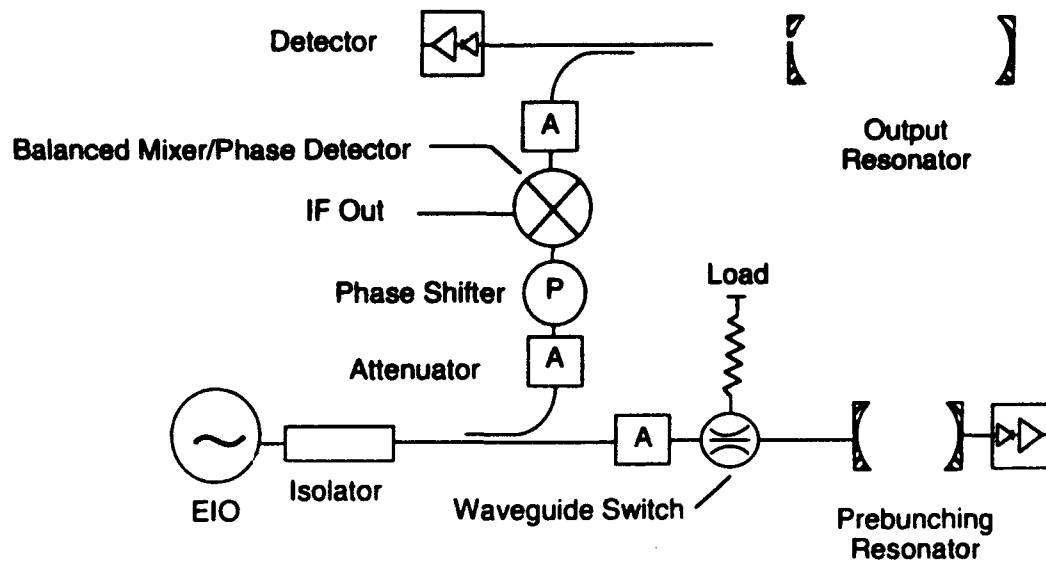


Figure 37: Diagnostic set-up for phase-locked operation.

relation. In the experiment, the phase shifter is remote controlled so that the mixer output is observed in the control room without turning off the gyroklystron. A 25 dB isolator is placed after the EIO to prevent the drive source from being locked by the gyrotron. The EIO signal can be switched into the load so that the beat frequency is observed between the drive source and the gyrotron in the absence of prebunching.

Chapter V

Experimental Results

A. Beam Alpha Measurements

The pitch ratio of the beam electrons $\alpha = v_{\perp}/v_{\parallel}$ is a critical parameter in gyro devices, where a large value of α is required for high interaction efficiency. In the present experiment, measured values of α using the capacitive probes are compared to electron trajectory simulations[51]. The electron gun parameters used in the simulations are summarized in Table 4, where the beam voltage is 65.8 kV and the current is 6 A. The positions and currents of the magnetic field coils are supplied to the code, which accounts for space charge and relativistic effects, as well as the self magnetic field of the electron beam in the azimuthal direction. The geometry of the simulations is given in Figure 38 with the calculated magnetic field in the gun region, where the mesh size is fixed at 0.254 mm in the code. The values for the guiding center radius and the Larmor radius are averaged over 9 rays and are provided by the code. The magnetic field has no taper across the output resonator and is obtained for currents of 49.6 and 49.3 A in the upper and lower coils of the superconducting magnet. The magnetic compression ratio, B_{cav}/B_{gun} , is somewhat lower in the present experiment than in the original design of the gun. There is no gun trim coil in this experiment, so the compression ratio is essentially fixed and the beam α is varied by adjusting the mod anode voltage via the resistive divider. The mod anode voltage can be written $V_{mod} = V_{cath}(VD)$, where VD is the voltage divider setting. Thus, low ratios of the voltage divider correspond to high electric fields at the cathode and generally larger values of pitch angle. Adiabatic scaling theory can be used to write[53]

$$\beta_{\perp} = \frac{E_{\perp gun}}{cB_{gun}} \sqrt{B/B_{gun}}, \quad (61)$$

where the general electric field dependence is clearly seen.

Figure 39 gives a comparison between the measured data using the capacitive probes and values calculated from electron trajectory simulations. The qualitative agreement between the measured and calculated values for α is quite good. Pitch ratios greater

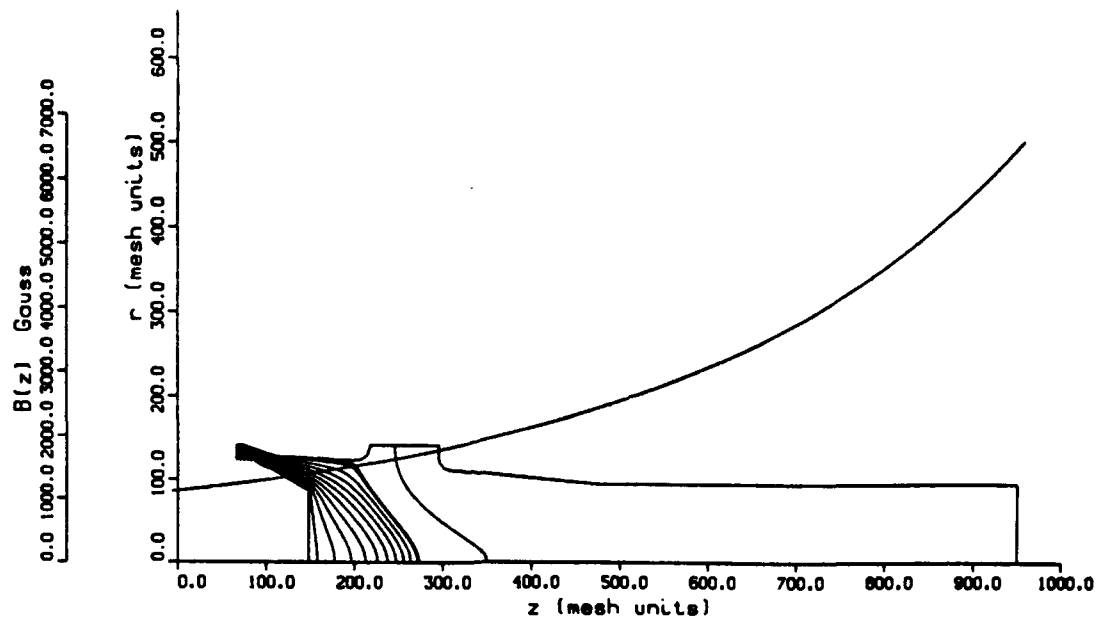


Figure 38: Geometry for the electron trajectory simulations.

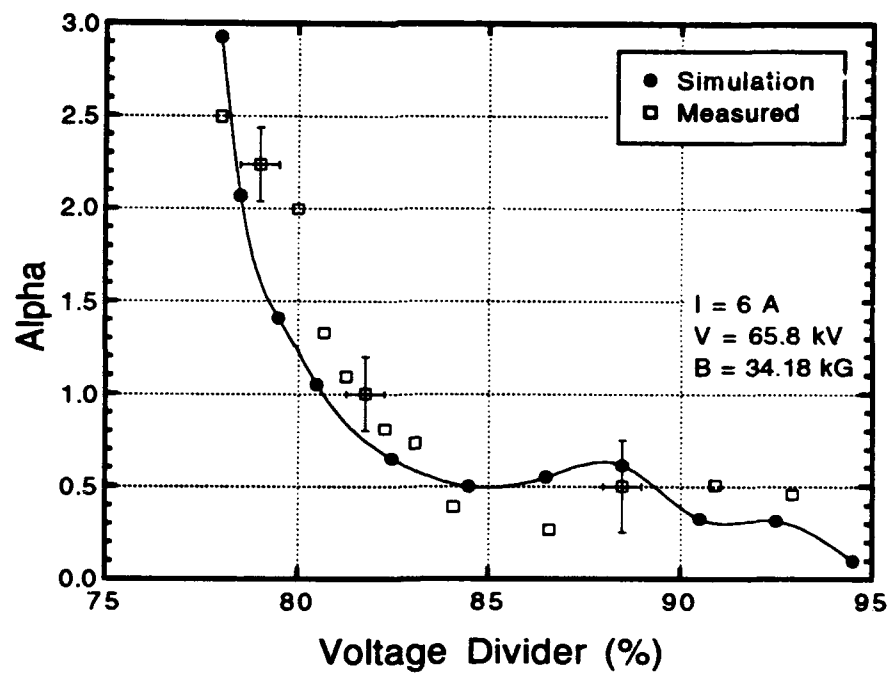


Figure 39: Beam alpha as a function of mod anode voltage divider.

Cathode Voltage	65.8 kV
Cathode Current	6 A
Resonator Magnetic Field	34.18 kG
Cathode Magnetic Field	1.28 kG
Magnetic Compression	26.8
Magnetic Field Taper	0%
Gun Position	-51.5 cm
Guiding Center Radius	5.39 mm
Larmor Radius	0.23 mm

Table 4: Electron gun parameters for simulations

than two are achievable for voltage divider settings somewhat less than 80%. The probe capacitance is calculated to be 5.9 nF, where the minimum α of 0.3 is assumed in the calibration. The measured data are somewhat greater than the simulations in the range 79-84%, where the measured data tend to rise nearly linearly with mod anode voltage. The capacitive probes indicate no reflecting electrons for all of the voltage divider settings in this data. Reflexing electrons appear as an increase in the probe signal accompanied by large noise fluctuations during the flat-top of the voltage pulse. In this regime, large noise signals are observed on all of the scope traces. For voltage divider settings below 77%, the operation of the gun becomes unstable and arcing will soon occur. The discrepancy between the two sets of data is meaningless for $\alpha \leq 0.5$ because of the error in the measurement due to the small change in longitudinal velocity in this region. The error in the measurement amounts to $\pm 10\%$ for $\alpha \sim 2$ and $\pm 20\%$ for $\alpha \sim 1$. The general conclusion from these measurements is that the electron beam is more than sufficient for generating millimeter waves in the gyrokystron experiment. Also, the pitch angle of the beam is probably not responsible for the low efficiencies observed in previous QOG experiments using this electron gun for low currents.

The velocity spread of the beam can be important in both gyrotrons and gyrokystrons. In gyrokystrons, velocity spread manifests itself by reducing the phase

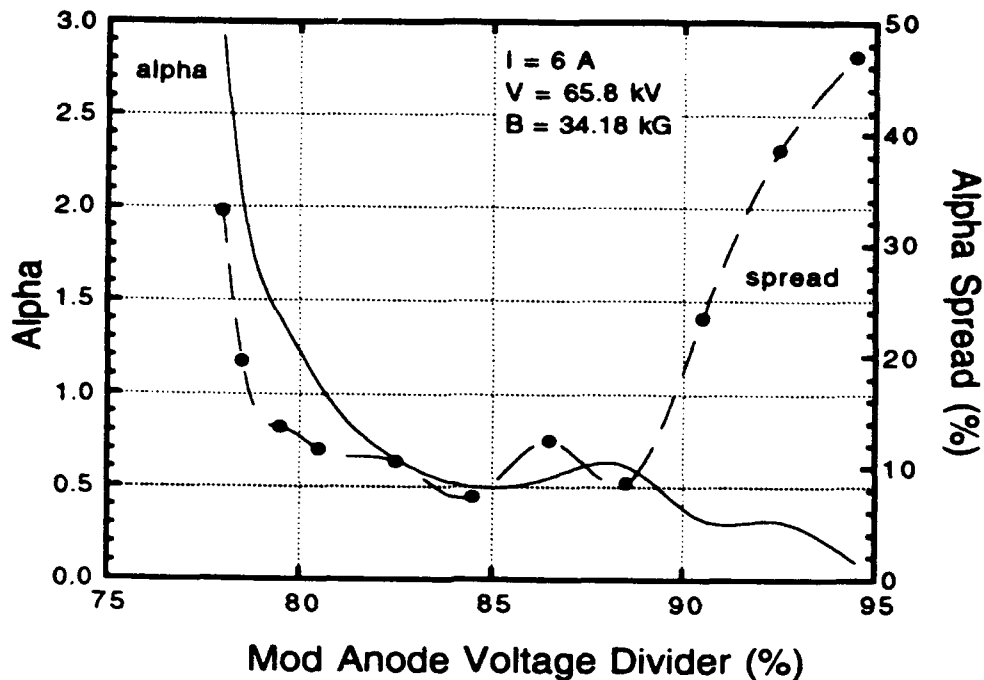


Figure 40: Calculated beam quality as a function of mod anode voltage divider.

bunching of the electrons in the drift region, causing the device to operate with a smaller bunching parameter. In the quasioptical gyrokystron, very large velocity spreads will cause the device to operate as a single-resonator gyrotron, where the prebunching is completely washed-out in the drift region. A small velocity spread of several percent is not harmful in a gyrotron because the tube operates close to cut-off so that $k_z \cong 0$ and the $k_z v_z$ term in the resonance condition is relatively small. However, it has been shown theoretically that large velocity spreads will degrade the efficiency of the gyrotron even though the interaction length is relatively short.

Figure 40 plots the simulation results for the average α and the spread in α as a function of mod anode voltage divider for the parameters listed above. For large electric fields at the cathode, the spread in pitch angle is quite large. Thus, it may be desirable to operate at slightly lower α to minimize the effects of velocity spread. The beam optics/space charge are also poor at large values of voltage divider settings, even though the average α is small. Operation at higher voltage tends to produce a beam with lower velocity spread, since the gun was originally designed for 80 kV, 35 A, and a magnetic compression of 30.

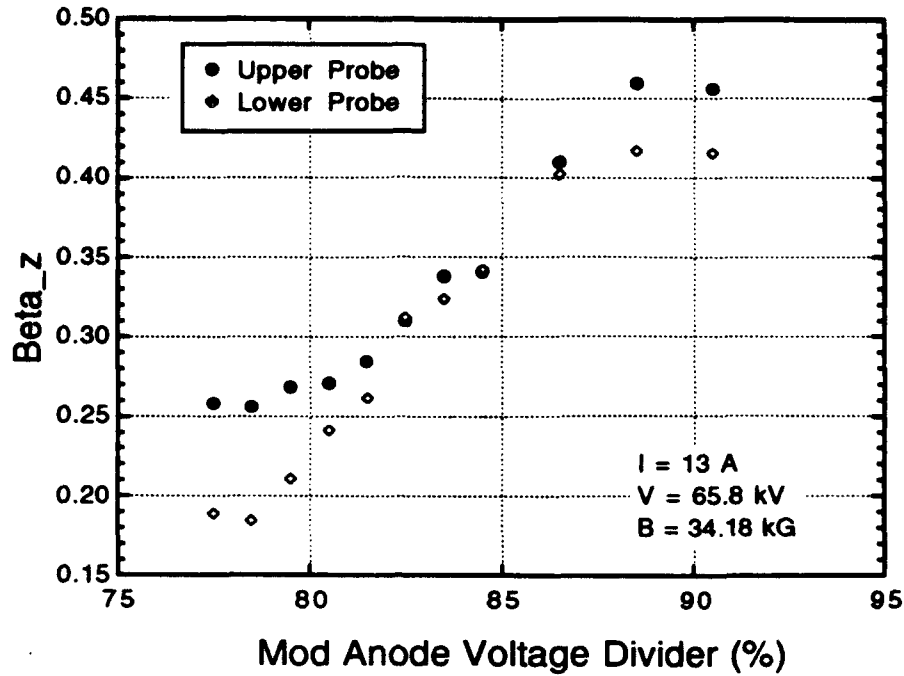


Figure 41: $\beta_{||}$ as a function of mod anode voltage at 13 A.

Measuring the beam α at higher current provides some interesting information on the prebunching resonator. Figure 41 shows the measured longitudinal velocity ratios for the lower and upper capacitive probes, where the lower (upper) probe is placed immediately before (after) the input resonator. The two measurements agree for mod anode settings between 82–86%, where variations above 88% are due to the accuracy of the measurement. However, there is a large disagreement for voltage divider settings less than 81.5%, where the lower probe consistently gives a smaller velocity ratio. The accuracy of the measurement is within $\pm 10\%$ in this region, so the difference between the probes is genuine.

The different measured values of $\beta_{||}$ before and after the input resonator are explained by considering oscillations in the prebuncher. At a voltage divider setting of 81.5%, the beam α is large enough to start oscillations at a current of 13 A. The fundamental TEM_{00} mode at 85.55 GHz is observed in the input resonator using a detector and the heterodyne to monitor the signal from the prebuncher. As the voltage divider is lowered, the average α of the beam increases as does the amplitude of the prebuncher oscillations. The kinetic energy of the particles is $(\gamma - 1)mc^2$, so that the interaction

efficiency in the input resonator can be written

$$\eta = \frac{\gamma_i - \overline{\gamma_f}}{(\gamma_i - 1)}. \quad (62)$$

In this equation, $\overline{\gamma}$ denotes the average over all electrons and the subscripts refer to the initial and final relativistic mass factors. The electron beam is assumed to be monoenergetic when it enters the prebunching resonator, which should be a valid assumption in the present discussion. For mildly relativistic beams, $\gamma - 1 \ll 1$ and the change in the mass factor is small for reasonable values of interaction efficiency. For example, a 10% efficiency in the prebunching resonator results in only a 2% change in γ for a 70 kV electron beam. The longitudinal velocity ratio is expressed

$$\beta_{||} = \frac{\sqrt{1 - \gamma^{-2}}}{\sqrt{1 - \alpha^2}}, \quad (63)$$

where the mass factor can be approximated as a constant before and after the prebunching resonator. The difference between the upper and lower longitudinal velocity ratios is now

$$\beta_{||u} = \beta_{||l} \sqrt{\frac{1 - \alpha_u^2}{1 - \alpha_l^2}}, \quad (64)$$

where the subscripts refer to the lower and upper capacitive probes.

A plot of the measured α versus mod anode voltage divider is given in Figure 42 for a beam current of 13 A. Also shown are the results of the electron trajectory simulations assuming a beam voltage of 65.8 kV and a magnetic field of 34.18 kG at the center of the output resonator. As predicted, the measured values for α from the upper probe are considerably lower than the values immediately preceding the prebuncher after the onset of oscillations. The lower values for α are attributed to oscillations in the prebunching resonator, which lowers the average perpendicular energy of the beam. The measured pitch ratios are somewhat greater than the calculated values in the range of voltage divider settings between 79-86%, which is consistent with the previous results at 6 A.

Qualitatively, the data from Figure 42 appears correct: the average α of the beam decreases due to the oscillations in the prebunching resonator. However, the measured decrease in average pitch angle is too large for the relatively low (5%) efficiencies

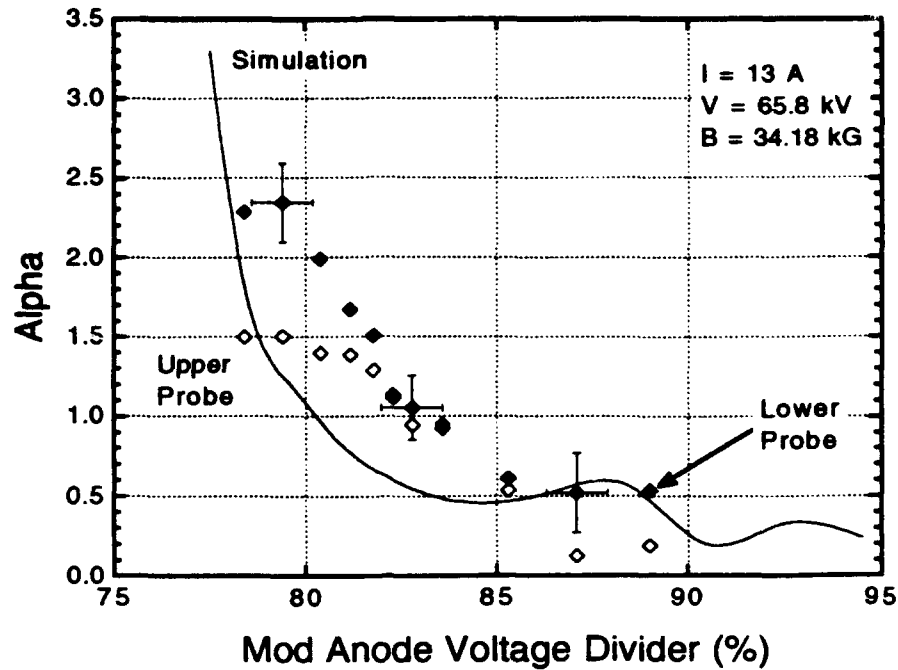


Figure 42: Measured and calculated α as a function of mod anode voltage at 13 A.

measured in the experiment in the input resonator. Consider the case where a monoenergetic electron beam passes through a resonator and loses energy according to Eq. (62). The longitudinal momentum of the electrons is conserved during the gyrotron interaction so that $p_z = m\gamma\beta_z c = \text{constant}$. The resulting α at the exit of the resonator is calculated using the new values for γ and p_z . Figure 43 shows the initial and final values for α as a function of interaction efficiency for a 70 kV beam. For an initial pitch angle of 2, a 40% interaction efficiency is required to reduce the average α to 1.4. This is the reduction in α observed in the experiment using the capacitive probes after the input resonator begins oscillating.

A possible explanation for the large measured variation in pitch angle is energy spread of the beam due to oscillations in the prebunching resonator. Although the average γ of the beam is reduced, there is a relatively large energy spread of several percent since some electrons lose energy and some gain energy. The orbits of the electrons also change according to their larmor radii. It is likely that a spread in γ and α can cause variations in the upper capacitive probe signal after the onset of oscillations.

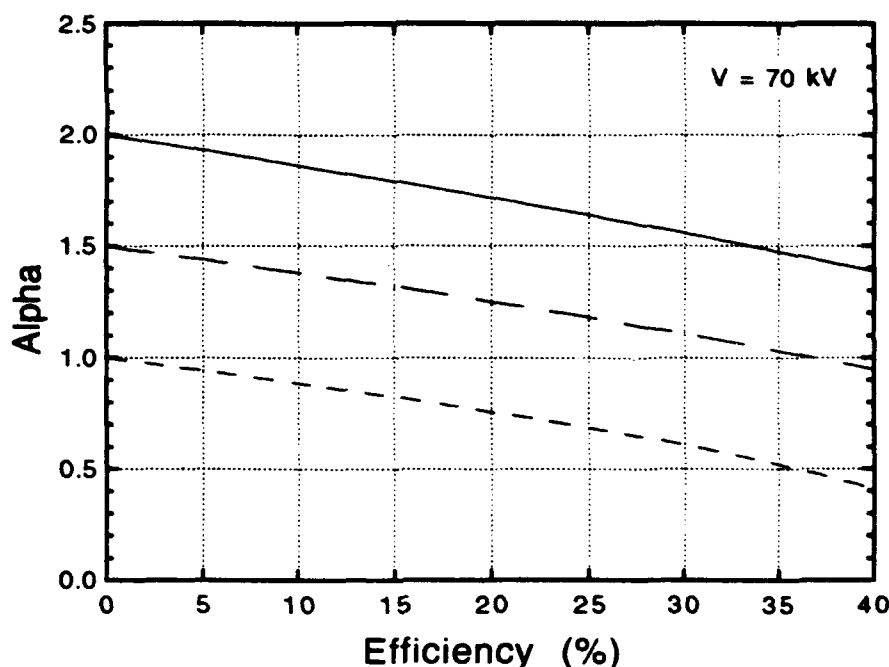


Figure 43: Calculated α as a function of interaction efficiency.

Figure 44 shows measured and calculated values of pitch angle as the cathode voltage is varied between 20–80 kV. The mod anode voltage divider is fixed at 82.5% for all of the data, the magnetic field is 33.42 kG at the output resonator, and the beam current is approximately constant at 4 A. The measured voltage divider setting is 82.44% under these conditions, so that there is little uncertainty in the cathode and mod anode voltages. For low voltages near 20–30 kV, the measured data agree with the electron trajectory simulations. However, cathode voltages of 55–75 kV consistently produce pitch angles greater than the calculated values. This behavior is consistent with the earlier measurements where the cathode voltage was fixed and the mod anode voltage varied. In all cases there is a greater sensitivity to voltage than the simulation predicts. Varying the cathode voltage over this range is an indication of how α varies during the rise of the voltage pulse.

One explanation for the discrepancy between the measured and calculated values of α would be a systematic error in the cathode or mod anode voltage measurement. The voltage monitors were independently calibrated several times over a period of six months and the measured variation was less than 0.5%. The accuracy of the measure-

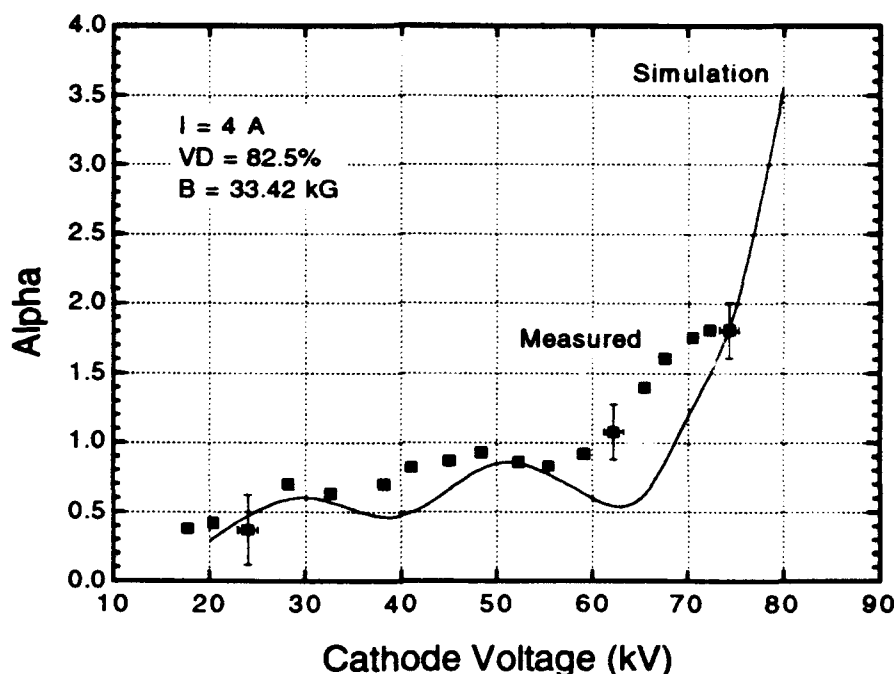


Figure 44: Measured and calculated α as a function of cathode voltage.

ment is approximately 0.2%, which is much less than the difference suggested in the α measurements. A more likely explanation for the discrepancy is that there are some differences between the model and the experiment that are not presently included in the simulations. Note that the same type of behavior is observed when comparing the measured and simulation values for α in the MIT 140 GHz gyrotron tube[53]. For example, pitch angles of $\alpha = 2.1$ are measured prior to saturation, whereas the simulation gives $\alpha = 1.5$. Possible improvements to the code include modelling the self magnetic field of the beam in the longitudinal direction and a denser mesh near the electron beam.

As the average pitch angle of the electrons increase, the outer electrons move closer to the wall of the uptaper due to their larger Larmor radii. Figure 45 plots intercepted current as a function of cathode voltage for the conditions described in the previous figure. The trim coil current is 190 A, which results in 98% of the beam collected in the collector for low cathode voltages. The 2% difference between the cathode and collector current monitors is probably due to ground noise in the experiment that shows up on the collector monitor. At a beam voltage of 40 kV, the intercepted current begins to

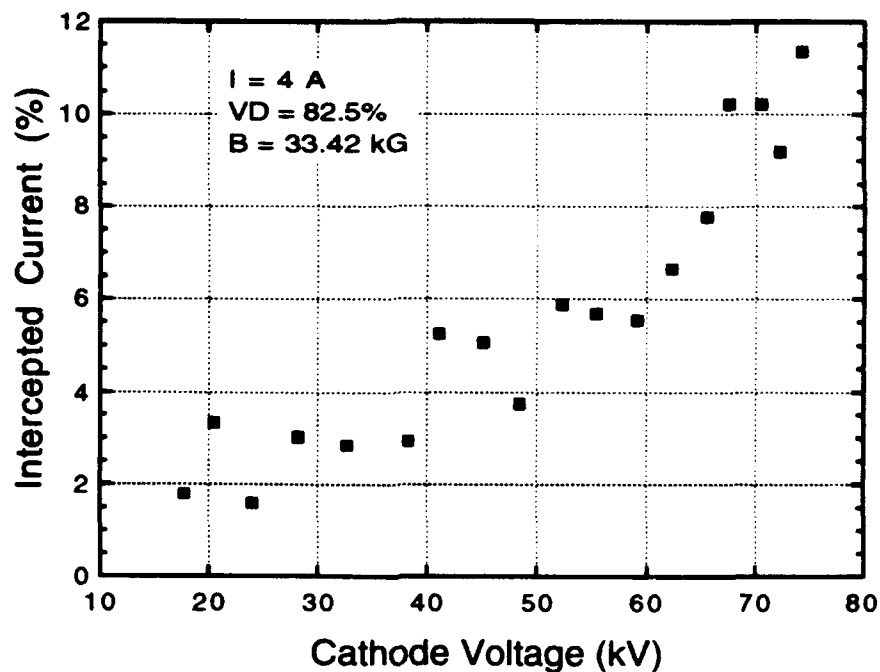


Figure 45: Intercepted current as a function of cathode voltage.

increase, with a corresponding pitch angle of 0.8. By 70 kV, over 10% of the current is collected on the uptaper and fails to reach the collector. Increasing the collector trim coil current allows nearly all of the beam to pass the uptaper and enter the collector. Maximizing the collector current is important in depressed collector studies so that the peak collector efficiency may be achieved.

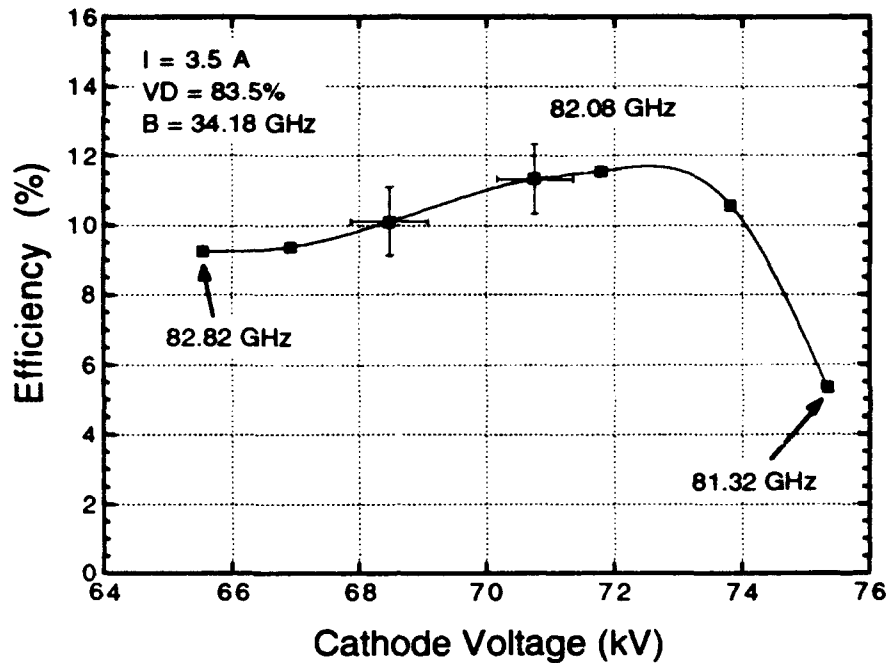


Figure 46: Efficiency of the free-running oscillator versus beam voltage.

B. Mode Priming By Prebunching the Beam

In order to understand mode-primed operation of the gyrokystron using the EIO, first consider the behavior of the free-running oscillator. Figure 46 shows measured values of efficiency and frequency for a current of 3.5 A as the beam voltage is varied. The measured values for α are approximately 1.6 for this data and are obtained for a voltage divider setting of 83.5%. Similar powers and efficiencies are obtained for lower mod anode settings and higher pitch angles. The capacitance between the cathode and mod anode is 1.25 nF, which results in the mod anode voltage closely following the cathode. Under these conditions, α reaches its peak at the leading edge of the voltage flat-top and is constant during the duration of the 13 μ sec pulse. This behavior is verified by observing the output radiation pulse shape, where a flat detector signal indicates that α is constant during the pulse. The capacitive probes in the drift tube give similar results.

For a voltage of 65.5 kV, mode skipping is observed between the 82.82 GHz and 82.08 GHz modes. The term **mode skipping** refers to the case where the output

frequency varies on a pulse-to-pulse basis but is single-moded during any one pulse. The frequency separation between these neighboring longitudinal modes is 740 MHz, which is consistent with a mirror separation of approximately 20.5 cm. For higher voltages, the lower frequency mode is present for 100% of the pulses and the efficiency increases monotonically with voltage. This is due to the increased frequency detuning between the rf field and the electrons, which can be written $\frac{\Delta\omega}{\omega} = 1 - \frac{\Omega}{\gamma\omega}$ where Ω is the nonrelativistic cyclotron frequency. A peak efficiency of 11.5% is obtained for this mode at a voltage of 72 kV. As the voltage is further increased, mode skipping begins between the desired mode and another lower frequency longitudinal mode at 81.32 GHz. At a voltage of 75 kV, 100% of the pulses are in the low frequency, low efficiency mode. Further increases in voltage cause the process to repeat, where the 81.32 GHz mode peaks in efficiency and is then overtaken by a low frequency mode.

One of the most remarkable aspects of the operation of the gyrokystron is that the output is single-moded even though the longitudinal mode density is high. Analysis of the output radiation using the heterodyne diagnostic reveals that only a single longitudinal mode is present even at the highest powers. This is in contrast to all other QOG experiments with large mirror separation [17,13,55], where the output was always multimoded at high power. Data obtained in this experiment consistently and reproducibly yields single-mode output at the highest powers and efficiencies over a wide range of parameters. Several explanations for this behavior, which is highly desirable for nearly all applications, will be discussed in the next chapter.

A typical millimeter-wave pulse from the detector is shown in Figure 47 with the voltage waveform for reference. The duration of the free-running oscillator pulse is essentially that of the voltage flat-top. As the cathode voltage is raised to where an efficiency maximum occurs, the ripples on the radiation pulse saturate so that a very flat pulse is obtained. The rise time of the 85 GHz signals is $\sim 0.2 \mu\text{sec}$, as opposed to the $4 \mu\text{sec}$ rise of the voltage pulses. The efficiency is calculated by measuring the average power and dividing by the pulse repetition rate and the measured FWHM of the detector trace.

The calculated longitudinal mode density of the output resonator is shown in Figure

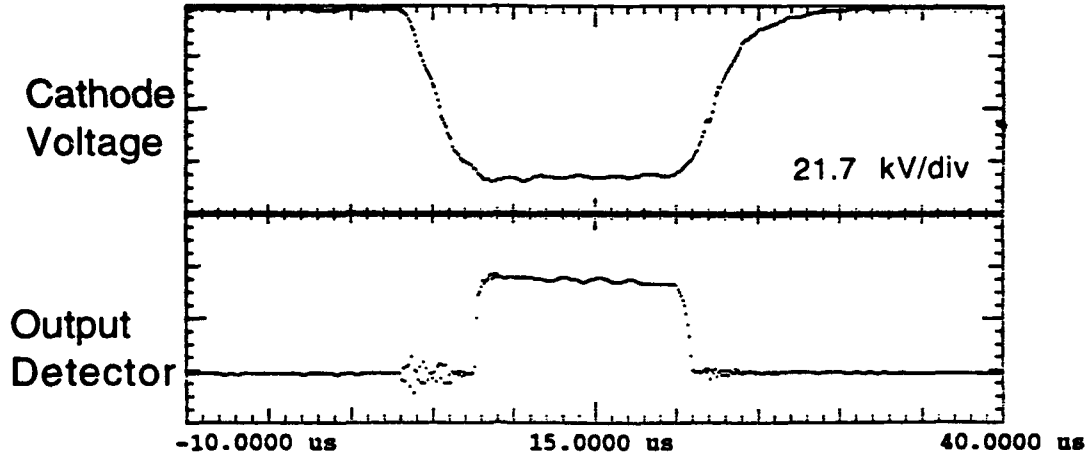


Figure 47: Output pulse shape of the free-running oscillator.

48 in terms of the starting currents. The magnetic field is 34.18 kG, the beam α is 1.5, and the resonator parameters are those listed in Table 3. The TEM_{00q} modes are identified by the longitudinal mode index q , where the mirror separation is $d = 20.7$ cm and q satisfies $q\lambda/2 \cong d$. The theory predicts minimum starting currents for all modes of approximately 0.5 A, where[4]

$$I_{st} = \frac{2.79 \times 10^9}{V_b Q} \left(\frac{d}{w_{02}} \right) \gamma_0 (\gamma_0 - 1) \frac{\beta_{||}}{\alpha^2} \exp \left[\frac{1}{2} \left(\frac{\Delta\omega}{\omega} \xi_0 \right)^2 \right] / \left(\frac{\Delta\omega}{\omega} \xi_0 \right). \quad (65)$$

Here, V_b is the beam voltage in volts and $\xi_0 = 2\pi w_{02}/\lambda\beta_z$ is the normalized interaction length for an annular beam in an untilted resonator. Tilting the resonator changes the starting current in two ways. First, the electron beam exchanges energy with only one component of the travelling wave in the resonator, which reduces the electric field and tends to increase the starting current. Second, all of the electrons in the annular beam now interact with the wave fields, which decreases the starting current. For a rough estimate, simply consider the expression for the starting current with no tilt. The minimum starting current is obtained for a detuning $\frac{\Delta\omega}{\omega} = \frac{1}{\xi_0}$, where $\xi_0 \gg 1$ in most instances. Even for beam currents of only 3.5 A, there are 3-4 modes which are above

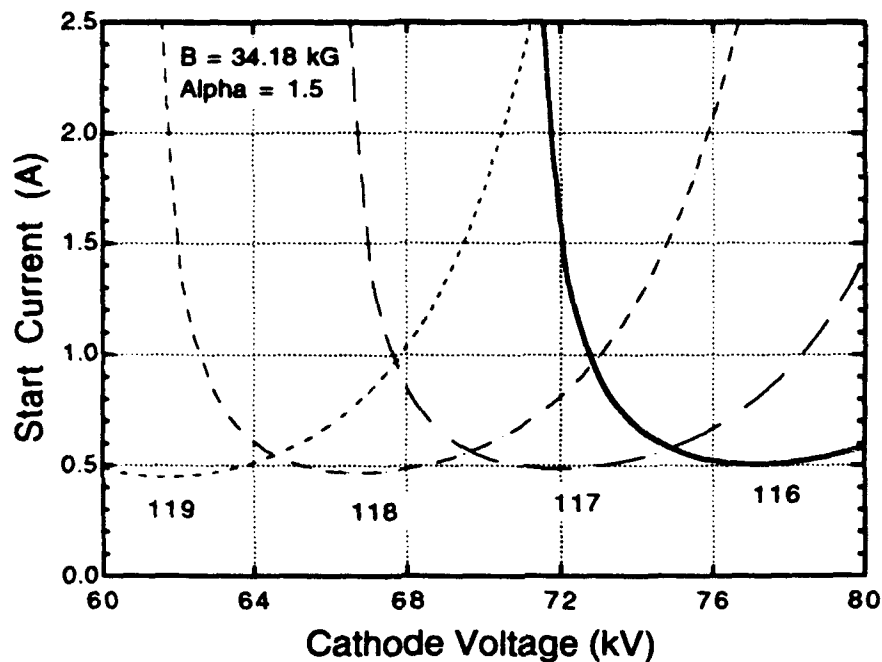


Figure 48: Calculated starting currents of several longitudinal modes.

the starting current in the output resonator. Thus, mode competition is an important issue and multimode operation may occur. However, Figure 48 yields no information on the nonlinear behavior of the gyrotron, where it is possible for the working mode to nonlinearly suppress competing modes.

Free-running oscillator operation has been characterized over a wide range of experimental parameters in the present work, including currents up to 15 A, voltages of 60–80 kV, pitch angles from 0.5–2.0, various magnetic fields, and different mirror separations. A general result is that the output is single moded and the maximum efficiency is $\sim 13\%$ and is obtained at the maximum frequency detuning for a particular longitudinal mode. As the voltage is increased further, mode skipping occurs between the desired mode and a low frequency mode oscillating at low efficiency. The output of the gyroklystron is single-moded, and this fact does not depend upon above-mentioned parameters. It is interesting to note that the maximum efficiency observed in this free-running oscillator work similar to previous data obtained on a high power QOG operating at 120 GHz. Thus, the general operation of the gyroklystron is consistent with results from past single-resonator experiments. However, past results were for

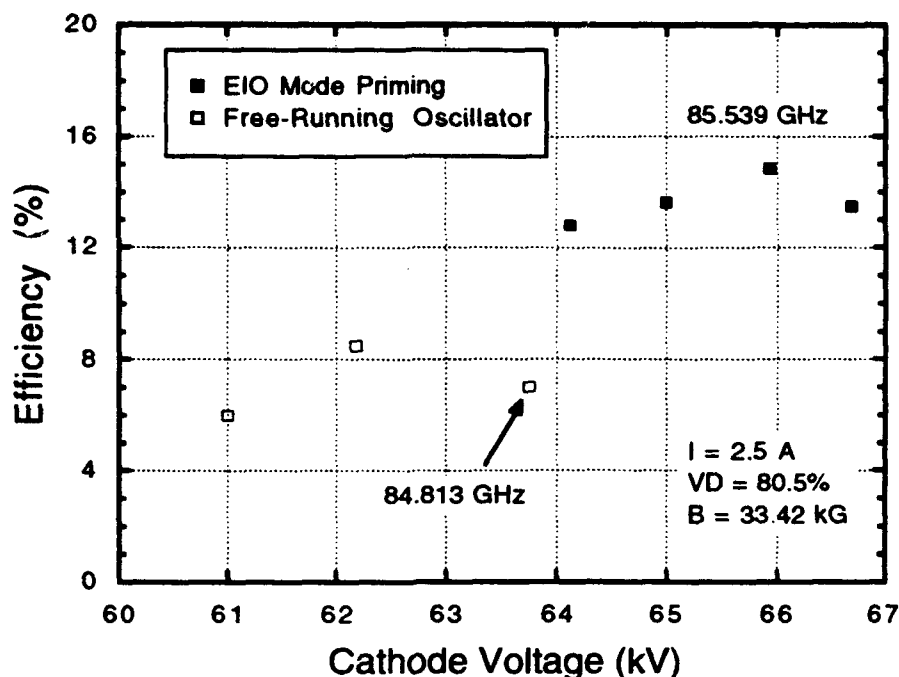


Figure 49: Efficiency versus voltage for EIO mode priming operation.

multimode efficiencies, whereas this experiment is single-moded.

An example of the benefit of EIO mode priming is shown in Figure 49, where efficiency is plotted as a function of beam voltage. The open points are free-running oscillator data and the closed squares correspond to EIO mode-primed results. The beam current is 2.5 A and the mirrors are adjusted so that the output frequency is close to the prebuncher frequency. For the free-running oscillator case, the maximum efficiency of 8.5% is achieved at voltage of 62.2 kV. Further increases in cathode voltage cause mode skipping between the working mode and a low efficiency mode oscillating at 84.813 GHz. At a cathode voltage of 64 kV, mode priming is initiated by injecting the 2 μ sec EIO pulse at 85.55 GHz during the 4 μ sec rise of the voltage pulse. Now the desired mode is excited for 100% of the pulses and the efficiency increases. A maximum efficiency of 14.9% is measured for a cathode voltage of 66 kV, which is well above the maximum voltage for this mode during free-running oscillator operation. Thus, EIO mode priming allows operation at higher detuning and higher efficiency than obtained in the free-running oscillator regime.

At a beam voltage of 66.5 kV, the efficiency of the high frequency mode begins to

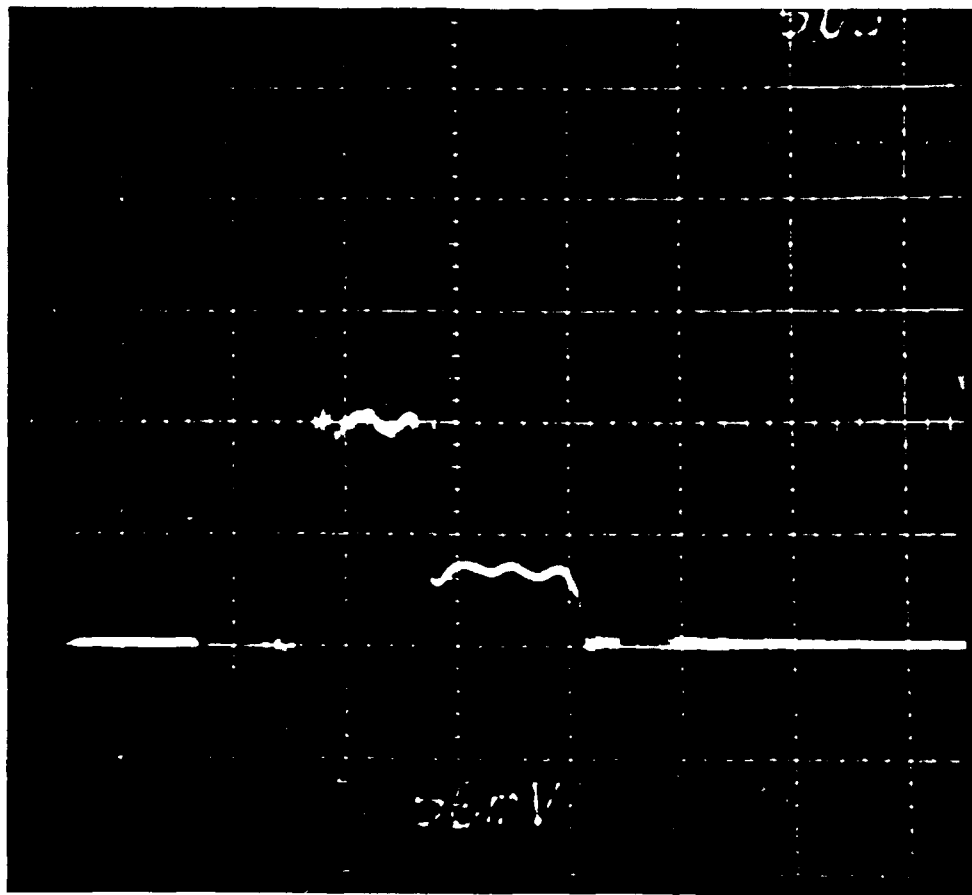


Figure 50: Detector pulse showing mode competition between two modes. The high frequency mode turns on first but is overtaken by the low-frequency mode ($5 \mu\text{sec}/\text{div}$).

fall due to mode competition. Approximately half-way through the pulse, the 84.81 GHz mode overtakes the desired mode and suppresses it. This is an interesting feature of mode primed operation that is qualitatively different from free-running oscillator results. Previously, mode skipping occurred when the voltage was raised too high for a particular mode. In mode priming, though, the desired mode turns on at the leading edge of the voltage pulse, but is eventually suppressed by the low frequency competing mode. An oscilloscope trace of this behavior is shown in Figure 50, where the 85.54 GHz mode is present for the first half of the pulse and the 84.81 GHz mode overtakes it. Notice that the transition from one mode to the next occurs on a relatively short time scale ($\sim 0.5 \mu\text{sec}$).

The general behavior of the mode-primed oscillator is understood as follows. During free-running operation, the rf fields in the output resonator evolve from noise generated by the beam. The noise bandwidth is on the order of the gyrotron interaction bandwidth of several percent, and is filtered into narrow resonances by the high- Q output resonator. If the frequency detuning becomes too large for a particular mode, a low frequency, less detuned mode can have a higher linear growth rate. This mode can then grow to saturation and nonlinearly suppress the desired mode. By injecting the EIO signal into the prebuncher, the beam is modulated at 85.55 GHz so that this mode's initial amplitude is much greater than the competing modes. The 85.55 GHz mode now has a head start so that it reaches saturation first and effectively suppresses satellite modes. In the high detuning, mode competition regime, the low frequency mode is destabilized and is able to grow and ultimately suppress the desired mode. Thus, we see that the initial conditions play an important role in determining the steady state of the oscillator.

Using the EIO to mode prime the gyrokystron results in higher efficiencies due to the higher obtainable frequency detuning between the rf fields and the electrons ($\Delta\omega/\omega = 1 - \Omega/\gamma\omega$). Figure 51 plots efficiency as a function of frequency detuning for the data presented in Figure 49. The detuning is calculated using a space charge correction factor for an annular beam traversing on open resonator. The voltage depression can be written

$$\Delta V = \frac{I_b}{2\pi\epsilon_0 c\beta_{||}} \ln(r_{gap}/r_g), \quad (66)$$

where r_{gap} is half the distance between the drift tube and uptaper, r_g is the guiding center radius of the electron beam, and ΔV is in Volts. For example, a 6 A beam at 70 kV and $\alpha = 1.5$ is depressed 2.1 kV as it traverses the open resonator. This equation is an approximation, although there is only a logarithmic dependence of the space charge depression with wall radius. The space charge depression can be viewed as potential energy of the beam which is not available for any type of rf interaction.

The maximum detuning of the free-running oscillator is 3.2%, above which the efficiency drops and mode skipping occurs. EIO mode priming allows for operation

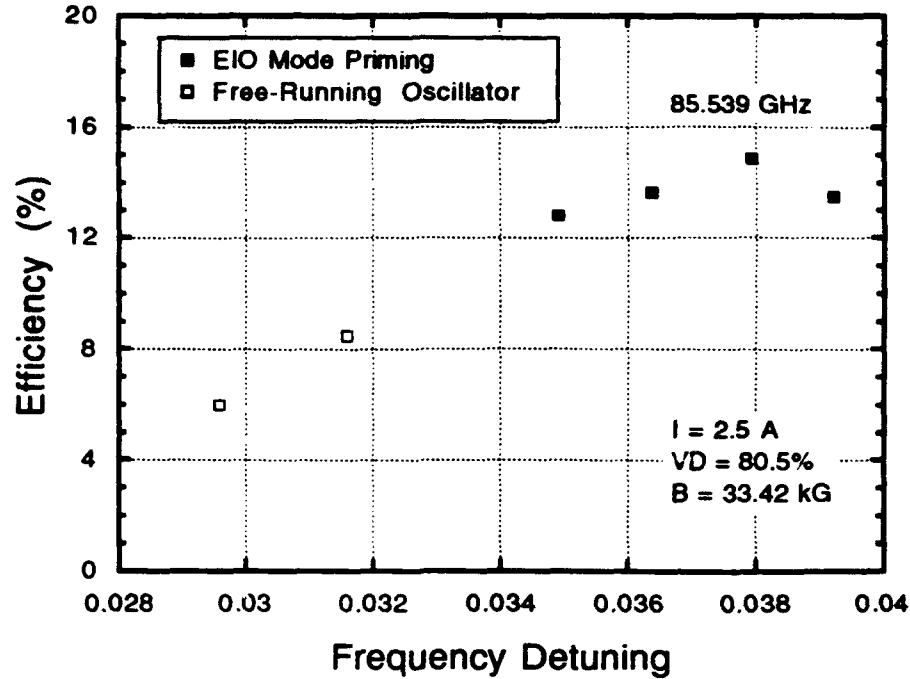


Figure 51: Efficiency versus frequency detuning with EIO mode priming.

at detunings up to 3.8% for this case, where the efficiency is relatively constant near the peak detuning. The longitudinal mode separation is written $\Delta f/f = \lambda/2d$, which results in 0.86% frequency separation for a mirror separation of 20.5 cm. Thus, the benefit of the mode priming under these experimental conditions is on the order of one longitudinal mode in the output resonator.

In most cases, EIO mode priming is used to operate at higher voltage and corresponding higher detuning to increase the interaction efficiency of the gyrokylystron. However, mode priming can also be implemented at low detuning values to select the weaker of two modes. This behavior is seen in Figure 52, where mode-primed and free-running efficiencies are plotted as a function of voltage for a beam current of 4.5 A. The voltage divider is now 82.5%, which is 1% less than the setting in the previous data at 6 A. The two open data points indicate the limit of free-running oscillator operation for the 85.56 GHz mode in the output resonator. Application of the 2 μ sec EIO signal at 85.55 GHz during the rise of the voltage pulse primes the gyrokylystron to run in the desired mode both above and below the free-running oscillator limits. Without priming, the gyrotron operates in the next higher frequency longitudinal mode at low

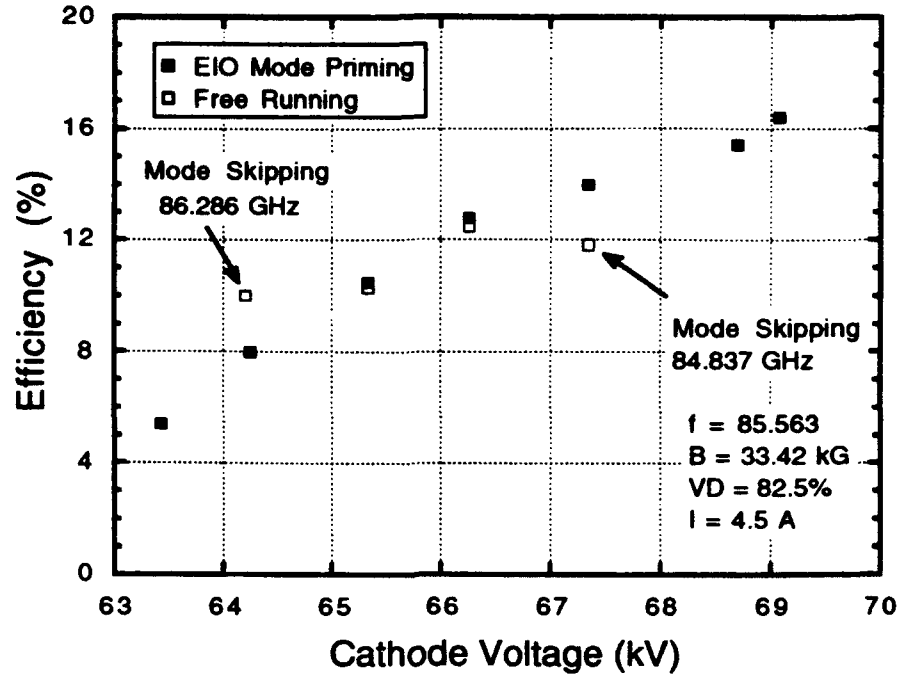


Figure 52: Efficiency versus cathode voltage for EIO mode priming at 4.5 A.

voltage, which is more efficient than the 85.56 GHz mode.

The efficiency is plotted versus frequency detuning in Figure 53 for the experimental conditions described above at a beam current of 4.5 A. A minimum detuning of 2.3% is obtained for the priming case, which is somewhat less than the 2.5% detuning for the free-running oscillator. The efficiency rises monotonically with detuning up to a maximum of $\eta = 16.5\%$ for $\frac{\Delta\omega}{\omega} = 3.3\%$ under mode priming operation. At higher detunings, mode competition commences between the desired mode and the next lower frequency longitudinal mode. Measured values for α are plotted for three voltage divider settings in Figure 54. The measured pitch ratio of the electrons rises nearly linearly with cathode voltage to some peak value and then saturates, which has been observed by other workers[53].

Mode priming the gyrokystron is successful when the prebunching of the electron beam is much larger than the noise present during the start-up of oscillations in the output resonator. Thus, the priming phenomenon does not sensitively depend upon the frequency of the EIO drive signal in the prebunching resonator. Consider a mode priming case where the beam current is 3 A, the magnetic field is 33.42 kG, and the

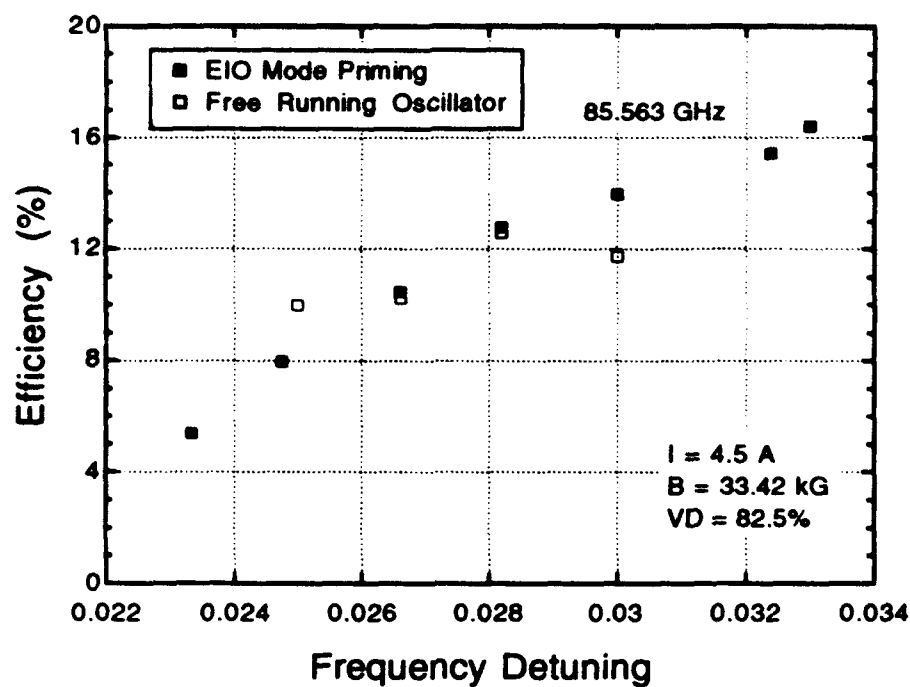


Figure 53: Efficiency versus frequency detuning for EIO mode priming at 4.5 A.

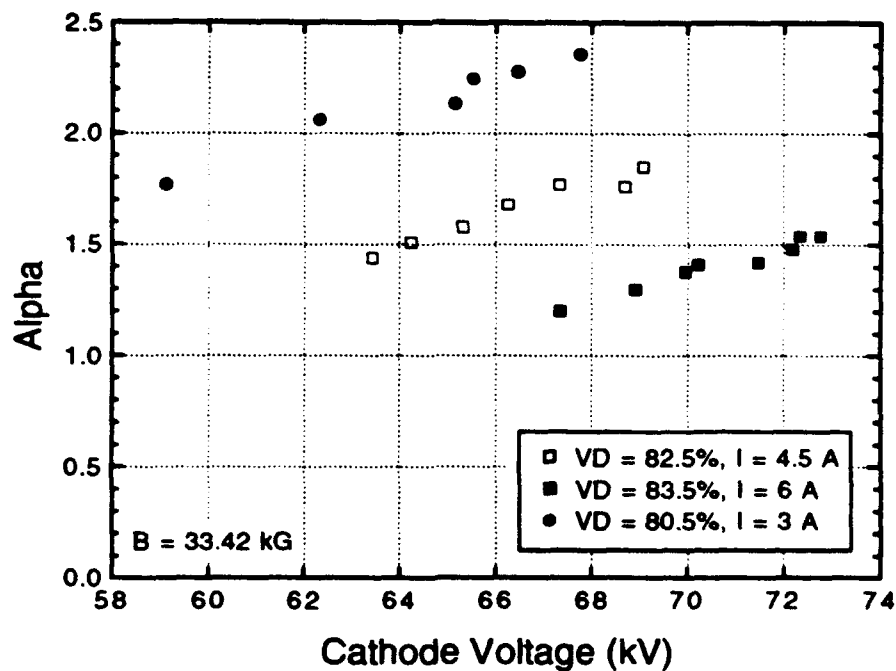


Figure 54: Alpha versus cathode voltage for three voltage divider settings.

mod anode voltage divider setting is 80.5%. The average α of the beam is measured as 1.9, and the mode-primed efficiency is 16.3%. Initially, the gyrokystron is driven near the resonant frequency of 85.55 GHz in the prebunching resonator. The frequency of the EIO is mechanically tuned to higher and lower frequencies to observe when the mode priming fails. The frequency limits are measured as +460 MHz and -330 MHz, where the free-running gyrotron operates in the next lower longitudinal mode in both cases. The quality factor of the input resonator is $Q = 2000$, so that the FWHM of the resonance is approximately 43 MHz and the mode separation in the prebuncher is 2.14 GHz for the mirror separation of 7 cm. Tuning the EIO over such a large frequency range (400 MHz) results in much smaller coupling to the mode in the input resonator, which is measured to be 16 dB down from the coupling value at the resonant frequency.

Consider first the low frequency mode priming limit. The longitudinal mode separation in the output resonator is measured as 750 MHz between the 85.56 and 84.81 GHz modes. When the EIO frequency is 85.56 GHz, the high frequency mode is given an initial advantage in the output resonator due to the prebunched current. When the EIO frequency is lower by approximately 375 MHz, both of the neighboring longitudinal modes are equally excited in the output resonator. However, the 84.81 GHz mode has a lower detuning and a higher linear growth rate, so that it can grow to saturation and suppress the desired mode. This is exactly what is observed in the experiment, where the low-frequency priming limit is measured as 330 MHz.

The high frequency mode priming limit is somewhat more complicated. When the EIO is tuned upwards in frequency by approximately 375 MHz, the 85.56 and 86.29 GHz modes are equally excited in the output resonator. The high frequency longitudinal mode has a large detuning and a smaller linear growth rate, so this mode is unable to suppress the 85.56 GHz mode. The measured priming limit is 460 MHz, which is indeed greater than half the longitudinal mode separation. The upper priming limit may be due to a three-mode interaction, where the 86.29 GHz mode destabilizes the 84.81 GHz mode so that it grows and mode competition occurs. The conclusion from these measurements is that the mode priming limits are approximately one half the longitudinal mode separation in the output resonator and qualitatively agree with the

fundamentals of mode priming.

When the frequency detuning for a particular mode is increased past its maximum during mode priming, mode competition occurs between the desired mode and a low frequency competing mode. However, the leading portion of the output pulse is still primed to run in the desired mode. As an example, consider the case with a beam current of 6 A, a mod anode voltage divider of 82.5%, and a measured pitch ratio of 1.8. The priming limit for the 85.59 GHz mode is 69.5 kV for a magnetic field of 33.42 kG in the output resonator. The frequency detuning is 3.76% without space charge and 3.36% with the space charge correction. Above 69.5 kV, the 84.89 GHz mode overtakes the desired mode 5 μ sec into the 13 μ sec voltage pulse. The cathode voltage can be increased to over 76.5 kV, which results in detunings greater than 4.5% with the space charge correction. The 85.59 GHz mode lasts for approximately 2 μ sec at this voltage, after which the low frequency modes takes over. Thus, the 85.59 GHz mode is supported for detunings more than 1% greater than the mode competition limit.

Mode priming the gyrokystron is only possible while the amplitude of the competing longitudinal modes is small. Once one of the modes has grown in amplitude, mode priming becomes ineffective in determining the final state of the oscillator. As an example, consider the experimental conditions where the beam current is 5 A, the voltage divider is 82.5%, and the average α of the beam is measured to be 1.8. The maximum operating voltage for the 85.44 GHz mode is 71.6 kV, where the magnetic field is 33.42 kG. The detuning at this voltage is 3.63%, where the space charge depression across the output resonator is taken into account. If the EIO pulse is injected into the prebuncher after the voltage flat-top has been reached, no mode priming is observed. Figure 55 shows the earliest the EIO trigger can occur and still prime the 85.44 GHz mode in the output resonator. The EIO pulse is 1.4 μ sec before the leading edge of the 13 μ sec voltage pulse, which corresponds to a cathode voltage of 67 kV. Thus, the cathode voltage is 6% lower than its final value, with a frequency detuning of 2.9% at this point. Moving the EIO earlier in the voltage rise causes the mode priming to fail and the lower frequency mode is excited for 100% of the pulses. The EIO pulselength can be shortened to 100 nsec and the priming is still effective in exciting

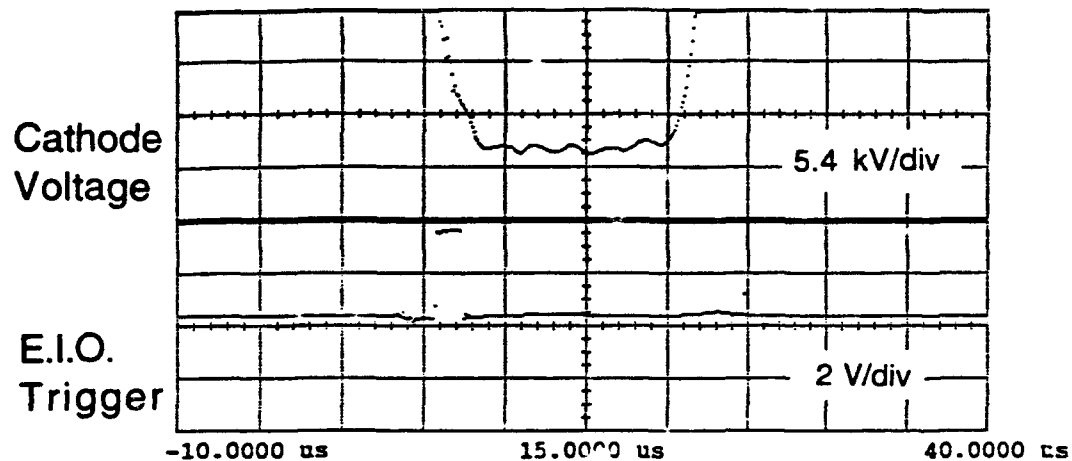


Figure 55: EIO position for mode priming during rise of the voltage pulse.

the desired mode. However, the ability to mode prime at these short drive pulsewidths depends critically on the position of the EIO signal within the rise of the voltage pulse.

C. Alpha Priming

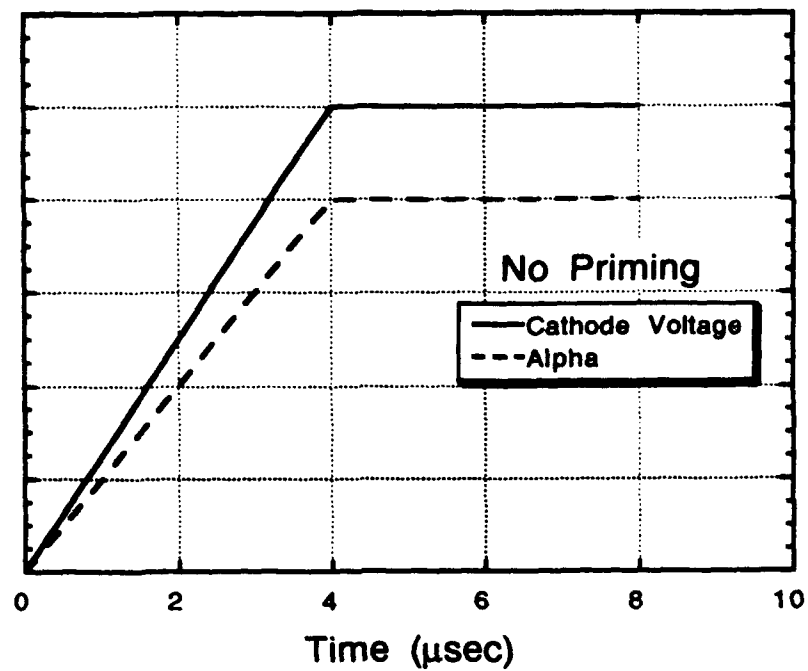
In the previous section, it was demonstrated that the initial amplitudes of the modes in the output resonator play an important role in determining the final state of the oscillator. Thus, mode selection can be accomplished by preferentially exciting one of these modes by prebunching the beam at the desired frequency during the rise of the voltage pulse. In this section, a new technique is described to achieve high detunings and high efficiencies, which is denoted as **alpha priming**. Alpha priming is accomplished by controlling the evolution of α during the rise of the voltage pulse, which has been discussed by a number of authors as a method of exciting the desired mode in a cavity gyrotron[56].

During free-running and EIO mode-primed operation, the mod anode voltage closely follows the cathode voltage. This results in α reaching its maximum on the leading edge of the flat-top of the voltage pulse and remaining constant for the duration of the 13 μsec pulse. This is verified experimentally by observing the radiation pulse shape on the output detector, where a flat pulse is indicative of a constant α . The rf pulse shape is square and begins on the leading edge of the cathode voltage pulse. In the alpha-priming regime, the cathode-mod anode capacitance is lowered so that the mod anode voltage rises more slowly with respect to the cathode, causing α to rise more rapidly. The pitch angle now reaches its maximum during the rise of the voltage pulse, just before the flat-top of the cathode voltage. This rapid rise of α during the evolution of the longitudinal modes has an important consequence. There is now enough perpendicular energy in the beam to excite a mode at slightly lower voltage and lower detuning. By the time the voltage has reached the flat-top, this mode has grown and now is highly detuned. If this mode is stable, it will nonlinearly suppress competing modes and dominate the spectrum. This results in a higher frequency longitudinal mode which operates at high efficiency, which is what is observed in the experiment. It should be stressed that alpha priming does not involve the prebunching resonator, so that this technique should be applicable to single-cavity oscillators. Rather, it relies solely upon varying the rise of α to excite a high frequency mode slightly before the peak of the voltage pulse.

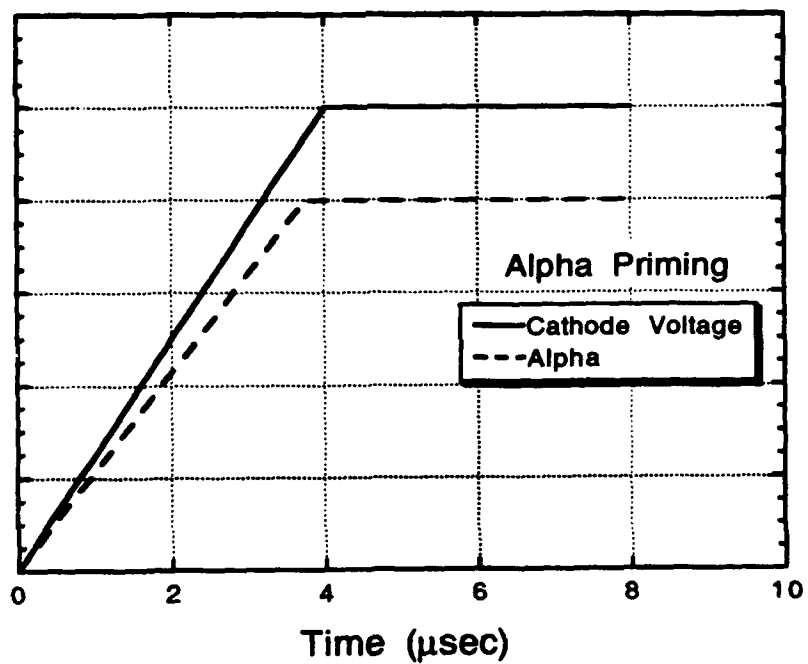
The rise of the cathode voltage and beam α is shown pictorially in Figure 56. In (a), both the pitch angle and beam voltage rise from 0 at time $t = 0$ to their peak values at $t = 4 \mu\text{sec}$. These are the typical conditions for both free-running and mode-primed operation of the gyrokystron, where the rf pulse turns on at $t = 4 \mu\text{sec}$. The situation is somewhat different in (b), where the cathode voltage is unchanged but the beam α peaks $0.25 \mu\text{sec}$ earlier. This tends to excite a mode in the output resonator at an earlier time at slightly lower voltage, which corresponds to higher frequency. In the experiment, the estimated time shift in the peak value of α is approximately 100 nsec.

To demonstrate the benefit of this technique, first compare alpha priming to normal oscillator operation with no priming as a function of cathode voltage. A plot of efficiency versus beam voltage is given in Figure 57 for a beam current of 10 A. The voltage divider setting is 82.5%, which results in an average measured α of 1.6 at lower cathode voltage. If the pitch angle of the electrons is raised higher, strong oscillations begin in the prebunching resonator which rapidly degrade the output pulse shape and the efficiency. The magnetic field is 33.42 kG for this data with no taper across the output resonator. The free-running oscillator efficiency peaks at 12% for a cathode voltage of 67 kV. For higher voltages, the output pulse begins mode skipping between the desired 86.30 GHz mode and the competing 85.58 GHz mode. For a cathode voltage of 68 kV, 100% of the pulses are in the low frequency, low efficiency mode. The cathode-mod anode capacitance is 1.25 nF for this free-running oscillator data with no priming, so that α reaches its maximum on the leading edge of the voltage flat-top. The pulse length of the millimeter-wave signal is limited to $11 \mu\text{sec}$ and turns on just after the beginning of the flat-top.

To initiate alpha priming, the capacitance between the cathode and mod anode is lowered to 1 nF. The beam α now reaches its maximum just prior to the flat-top of the voltage pulse and has a slight droop during the $13 \mu\text{sec}$ pulse, as evidenced by the millimeter-wave pulse shape and the capacitive probe signals. The pulse length of the radiation is now $12.5 \mu\text{sec}$, which is essentially that of the flat-top of the voltage pulse. Under these conditions, the cathode voltage can be increased past the limit for



(a)



(b)

Figure 56: Beam parameters (a) without and (b) with alpha priming.

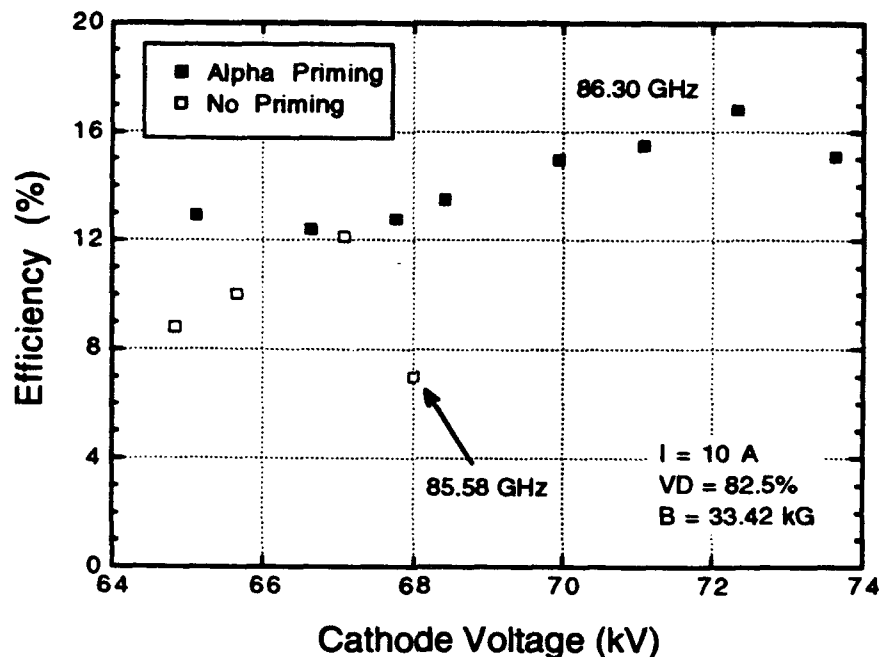


Figure 57: Efficiency versus voltage for alpha priming at 10 A.

the free-running oscillator at 86.30 GHz. This results in higher frequency detunings and higher efficiencies. The maximum efficiency for this data is 17% at a beam voltage of 72.5 kV. Further increases in voltage for these particular conditions cause strong oscillations in the input resonator which degrade the output efficiency.

Alpha priming results in higher efficiencies because it allows for single-mode operation at high detunings. Figure 58 plots the efficiency of the no-priming and alpha-primed data versus frequency detuning for the previous experimental conditions. The frequency detunings are calculated using the space charge correction factor, which results in 0.6% lower values in the output resonator. The maximum detuning for the gyrotron with no priming is 3.5%, while alpha priming allows operation up to 4.6%. This 1.1% detuning benefit amounts to more than 1 longitudinal mode in the output resonator, which is somewhat better than the previous results for EIO mode priming. Note that in this high current, relatively low α operating region, the detunings for maximum efficiency are shifted to larger values, which is consistent with results from the previous section.

Alpha priming is successful in achieving large detunings because the desired mode

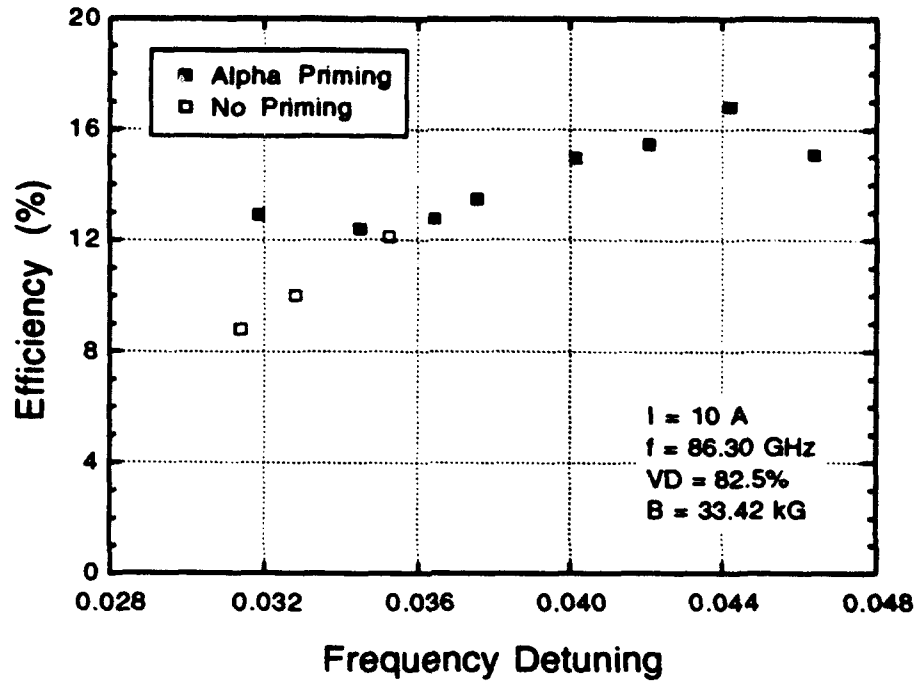


Figure 58: Efficiency versus frequency detuning for alpha priming at 10 A.

begins growing during the rise of the voltage pulse. A comparison of the oscilloscope traces for alpha-priming and free-running operation with no priming is given in Figure 59 with the cathode voltage pulse as a reference. The beam current is 7 A, the beam voltage is 70.4 kV, and the magnetic field is 33.42 kG. The voltage divider is 82.5%, which results in a measured $\alpha = 1.8$. During alpha priming, the gyrotron is running in the 85.41 GHz mode in the output resonator at an efficiency of 17% with a rather flat detector signal. The cathode-mod anode capacitance is 1.25 nF under these conditions. The frequency detuning at this maximum efficiency point is 3.3% with the space charge correction factor. To obtain free-running oscillator operation in the absence of priming, the capacitance is increased to 1.5 nF. The gyrotron now operates in the 83.96 GHz mode with an efficiency of 7.8%. Note that the detector trace now has a relatively large ripple, which is indicative of a mode which is not being driven close to saturation. The cathode voltage can be increased to 74.35 kV for this mode, with a corresponding efficiency of 9.1% and a frequency detuning of 2.3%. Thus, the different capacitance setting results in more than a factor of 2 increase in efficiency and roughly 2 longitudinal modes in detuning between the alpha-priming and no-priming cases.

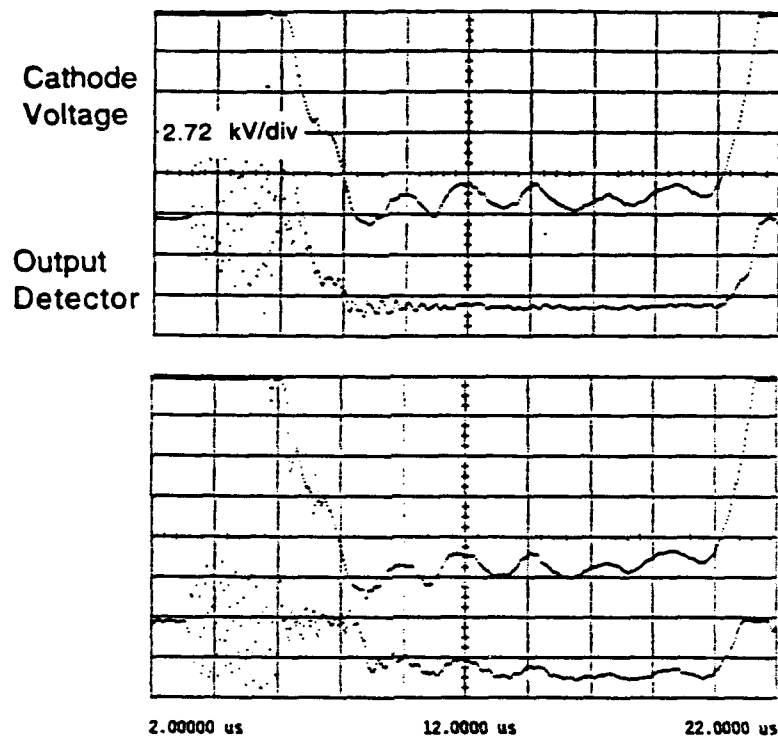


Figure 59: Oscilloscope traces: (a) alpha priming and (b) no priming. Notice that the detector trace for alpha priming turns on before the leading edge of the voltage flat-top and is flat compared to the no-priming trace.

The main difference between the two cases is seen by examining the leading edge of the millimeter-wave pulse. For the alpha-primed case, the mode begins $\sim 0.6 \mu\text{sec}$ before the flat-top of the voltage pulse with a rise time of $0.5 \mu\text{sec}$. The free-running oscillator with no priming begins on the leading edge of the flat-top, with a rise time of approximately $0.2 \mu\text{sec}$. The 85.41 GHz mode starts when the voltage is 3.9% below the final value, which results in a detuning of 2.8% at this instant in time. The pulsewidth of the free-running 83.96 GHz mode is $11.5 \mu\text{sec}$, while the alpha-primed mode is $13 \mu\text{sec}$. This longer pulsewidth is due to the earlier start-up time for the high frequency mode and a slightly longer fall time.

The usual data-taking procedure is to fix the magnetic field and the mod anode voltage divider setting and vary the cathode voltage. The electron beam current is determined largely by the cathode heater setting and is fairly constant as the voltage is increased. For beam voltages such that the output resonator is slightly above threshold, one or two radiation spikes of $\sim 1 \mu\text{sec}$ duration are observed using a millimeter-wave detector. If α is large at the beginning of the modulator pulse, a spike is observed immediately after the flat-top is reached. If the pitch angle of the electrons is constant during the $13 \mu\text{sec}$ pulse, the output spike(s) occurs during the center of the pulse. The position of the spikes correspond to the maxima of the ripples on the high voltage pulse produced by the modulator. As the cathode voltage is increased further, the radiation pulsewidth increases to $\sim 13 \mu\text{sec}$ and the structure caused by the high voltage ripple decreases. When the output resonator is driven close to maximum efficiency for a particular mode, the rf pulse is quite flat with little or no evidence of the modulator ripple. Pushing the oscillator past this point often causes a slight decrease in efficiency and a reappearance of small, irregular ripples on the pulse. The prebunching resonator, when it is oscillating, is always close to the threshold current and behaves in the same manner as the output resonator.

It is interesting to compare the limits of high efficiency performance for the three regimes of operation. For the free-running oscillator with no priming, mode skipping occurs between the desired mode and the next lower longitudinal mode when the maximum detuning for the working mode is exceeded. However, the limits for both alpha

priming and EIO mode priming are due to mode competition during the 13 μ sec pulse with a low frequency mode. If the detuning is large enough at the high efficiency point, the competing mode may be two longitudinal modes down in frequency. The difference between the mode skipping and mode competition phenomena can be understood as follows. In the free-running case, the longitudinal modes begin with the same initial amplitudes and the mode with the highest linear growth rate is dominant. Thus, if the maximum detuning for a particular mode is passed, the next lower mode reaches saturation first and the output is still single-moded. For alpha priming and EIO mode priming, a particular mode is excited during the rise of the voltage pulse and is able to overcome the higher linear growth rates of neighboring modes. The limit in this case is due to the destabilization of a competing mode(s) later in the pulse when the detuning is too large for effective nonlinear suppression of satellite modes. In the next chapter, it will be shown that priming allows access to the hard excitation region of the gyrotron, whereas the free-running oscillator remains in the soft excitation regime.

A large volume of data was collected to compare the performance of alpha priming and EIO mode priming over a wide range of operating parameters. Figure 60 shows the measured values of efficiency versus beam current for the three different operating regions: alpha priming, EIO mode priming, and no priming. The magnetic field is 33.42 kG at the center of the output resonator with no tapering. The beam voltage typically varies from approximately 67 kV at the lower currents to 76 kV at higher currents. Likewise, the mod anode voltage divider is increased from 80.5% to 86.5% as the current is increased to decrease the average α of the beam, which is necessary to keep the prebunching resonator below oscillation threshold as the beam power increases. It is possible to run the gyrotron in both the alpha-priming and mode-primed regimes over a large range of currents and voltages. The data presented here have been optimized with respect to cathode voltage for maximum efficiency for each point. The highest efficiencies are obtained using alpha priming, where a peak efficiency of 19.6% is measured at a beam current of 5 A. By using the EIO to mode prime the gyrotron, 16.5% efficiency is measured at a beam current of 4.5 A. Both of these techniques result in higher detunings and higher efficiencies than the oscillator with no priming for all

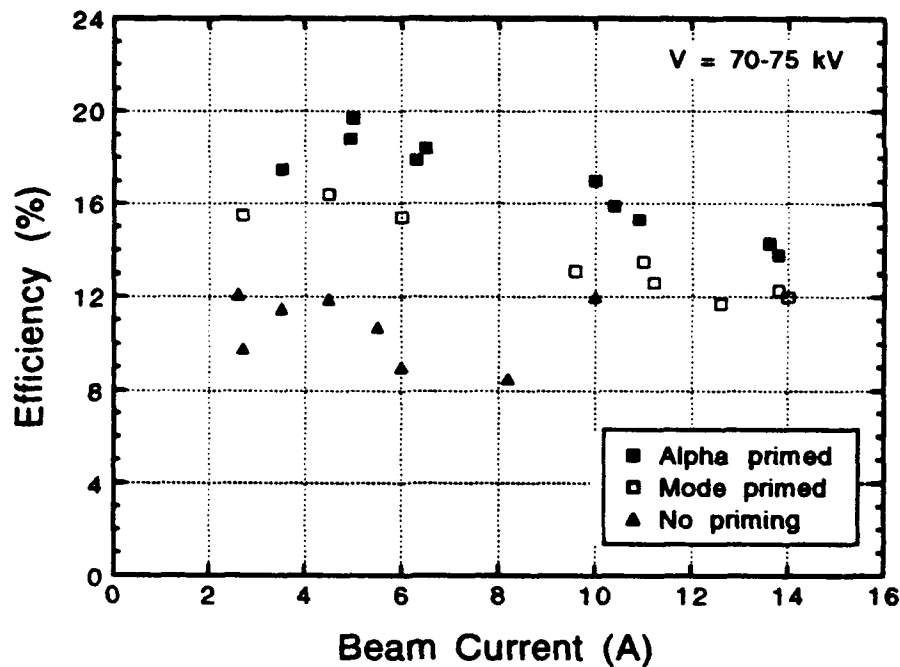


Figure 60: Efficiency versus current for the three operating regimes.

beam currents. The trend for all three operating regimes is towards lower efficiency as the current increases. This decrease in efficiency is due to the decreased α , which lowers the amount of perpendicular energy available to the rf fields. The peak efficiency is measured at the onset of oscillations, so that higher efficiency may be possible at higher current without the prebunching resonator. This interpretation is supported by calculations in the next chapter, where it is shown that the electric field in the output resonator is below the field required for maximum efficiency.

The maximum beam current used in the gyrokystron is limited by the onset of oscillations in the prebunching resonator. Large amplitude oscillations in the input resonator introduce a large energy spread on the beam and rapidly degrade the interaction efficiency in the output resonator. Intentionally driving oscillations in the first resonator allows a technique to measure the gyrotron's sensitivity to energy spread. Consider the experimental parameters where the beam current is 6.8 A, the beam voltage is 71.1 kV, and the output power is 72.6 kW with an efficiency of 15%. The voltage divider setting is 82.5%, resulting in a measured pitch ratio of the electrons of 1.9. The magnetic field is 33.42 kG and has a -1% taper across the output resonator. As the

beam voltage is increased, the frequency detuning in the prebuncher increases, as does the amplitude of oscillations in the prebuncher. At a beam voltage of 71.1 kV, the peak power in the prebuncher is 10 kW, which is approximately 14 dB greater than the power available from the EIO. The pulse shape of the output radiation begins showing structure which is associated with the oscillations in the drive resonator. This structure lowers the output efficiency by several percent, and further increases in voltage serve to rapidly lower the gyrotron efficiency.

Calculations are performed in [57] to study the variation of gyrotron efficiency with energy spread. In this model, a "top-hat" distribution function is used over $\pm\Delta\gamma$ so that the RMS energy spread is $\pm\Delta\gamma/\sqrt{3}$. The normalized gyrotron parameters are interaction length $\mu = 17$, field amplitude $\epsilon_0 = 1.0$, and transit angle $\delta = 2.5$. These values correspond to the maximum operating efficiency for $\mu = 17$ for a quasioptical gyrotron with a pencil electron beam placed on a field maximum in the output resonator. In the calculations, the perpendicular efficiency begins to fall when the energy spread reaches a value of $\sim 2\%$, which is similar to what is observed in the experiment.

One possible mechanism to further increase the efficiency of the gyrokystron is to use alpha priming and EIO mode priming simultaneously. However, it has been demonstrated experimentally that there is no benefit to injecting the EIO signal during the rise of the voltage pulse during alpha priming. This is understood because the limit to alpha priming is not the ability to lock onto the desired mode during the voltage rise, but rather mode competition later in time. Experimental results also show that alpha priming is more powerful than EIO mode priming in determining the mode during the rise of the pulse. A possible explanation is that the limit to mode priming is given by the maximum prebunching power, whereas alpha priming takes advantage of the full power of the electron beam. Consider the case where the gyrokystron is operating the alpha-primed regime in the 86.29 GHz mode at high efficiency. Prebunching the beam at a frequency of 85.55 GHz during the rise of the cathode voltage has no effect on the operation of the output resonator under these conditions. Using the EIO to mode prime the gyrokystron is only effective when the cathode-mod anode capacitance is relatively high and the pitch angle of the electrons reaches its maximum at the leading

edge of the flat-top of the voltage pulse.

Tapering the magnetic field across the output resonator has several possible benefits which have been demonstrated in single-mode and multimode nonlinear calculations. As particles lose energy in the single-mode regime, the relativistic mass factor decreases and the cyclotron frequency increases. Under these conditions, a negative taper on the magnetic field allows the electrons to remain in synchronism with the rf fields ($\frac{\Delta\omega}{\omega} = \text{constant}$) to increase the energy extracted from the beam. In the multimode regime, it may be desirable to increase the magnetic field along the interaction region. Using this technique, a mode is started at a low detuning and moves to the highly-detuned, high-efficiency region of parameter space by the end of the interaction, which helps the working mode suppress other longitudinal modes.

In the superconducting magnet used in the present experiment, the field is tapered by adjusting the currents in the two coils. The coils are separated by a distance greater than a Helmholtz pair, so that there is a field minima at the center of the output resonator. Thus, varying the currents causes a magnetic field variation that is not linear across the interaction region. This can be seen in Figure 61 for several moderate tapers which are used in the experiment. The magnetic field taper is calculated according to

$$\frac{\Delta B}{B} = \frac{B(z_2) - B(z_1)}{B(0)}, \quad (67)$$

where $z_2 = 1.7w_{02}$, $z_1 = -1.7w_{02}$, and w_{02} is the radiation waist in the output resonator. The limits of $z = \pm 1.7w_{02}$ are chosen because this is the separation between the drift tube and the uptaper. As the field is tapered, the magnetic field at the cathode changes. For example, a +2% taper across the output resonator results in a -2% change in the magnetic field at the gun. This tends to raise the average pitch angle of the beam according to Eq. (61). However, this change in the magnetic compression is much smaller than a 1% change in the voltage divider, which results in a 5% change in mod anode voltage.

Figure 62 plots the measured efficiency as a function of the magnetic field taper across the output resonator, where the field at the center of the output resonator is fixed at 33.43 kG. This is accomplished by raising the current in one coil while lowering

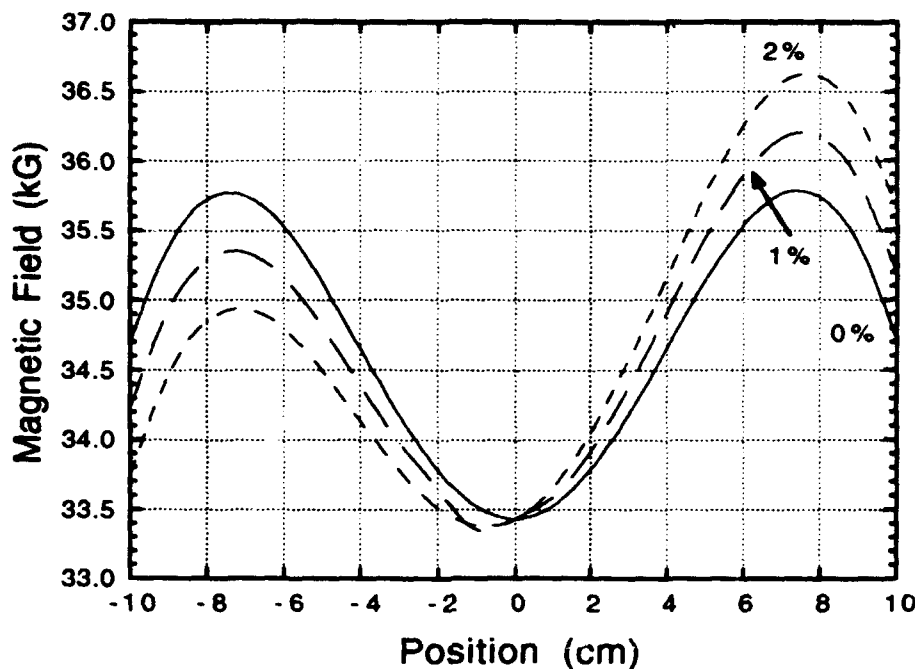


Figure 61: Several calculated magnetic field tapers used in the experiment.

the current in the other coil by an equal amount. The beam current is approximately 8 A for this data, and the voltage divider is adjusted so that the prebunching resonator is just below the threshold for oscillations. The cathode-mod anode capacitance is lowered from 1.25 nF to 1 nF to access the alpha-priming operating regime. The data are optimized by raising the cathode voltage to a maximum efficiency point, where the maximum voltage for this data is 77 kV.

Both alpha priming and EIO mode priming are successful over all of the tapers used in the experiment. Alpha priming is typically the more powerful of the two, resulting in higher detunings and higher efficiencies. In general, a 0% taper provides the highest power and efficiency for both alpha priming and EIO mode priming, although for this particular data set the +3% data point is just as good. The limit to both alpha priming and EIO mode priming is still mode competition later in the pulse, and the detuning for which the efficiency is maximum doesn't change as a function of the magnetic tapering. The basic conclusion from this work is that there doesn't appear to be any benefit to magnetic field tapering in the present experiment, where the device operates in a single mode. In a previous experiment, there was a small improvement in efficiency in the

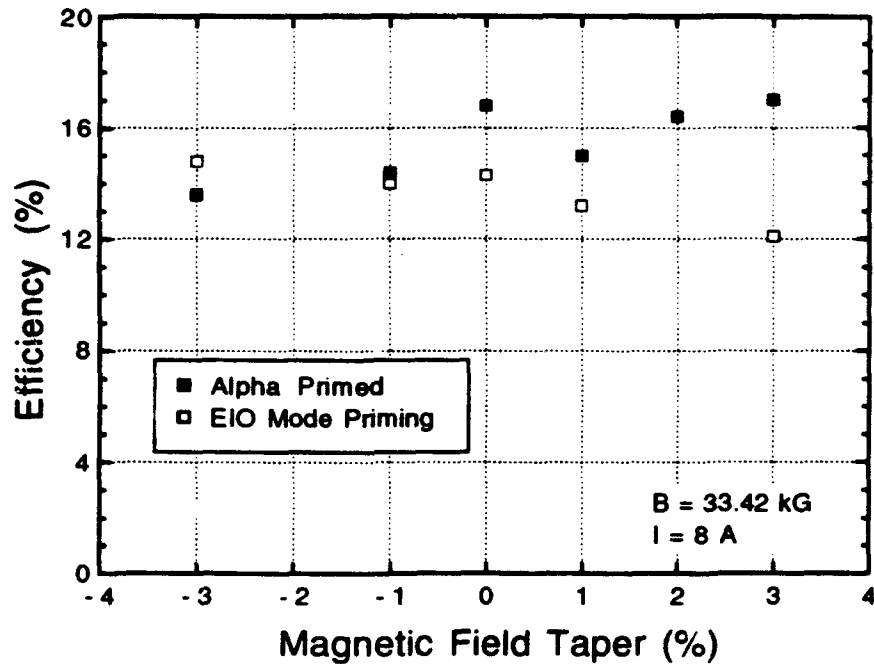


Figure 62: Measured efficiency versus magnetic field taper in the output resonator.

multimode regime for a 2% negative taper across the output resonator[17].

More data is obtained using magnetic field tapers for a beam current of 6 A, where there is no possibility of driving oscillations in the input resonator. Thus, the beam α can be raised to a larger value and the resulting efficiency is higher than the 8 A data. For alpha priming, efficiencies of 19.4, 19.1, and 17.5% were obtained for magnetic field tapers of 0, +2, and -2%, respectively. These results are quite similar to the observed performance at a beam current of 8 A, where the magnetic field taper provides no improvement in efficiency or maximum frequency detuning.

High efficiencies are obtained using the technique of alpha priming because the operating mode is excited at large detuning. Figure 63 plots the maximum cathode voltage for a particular longitudinal mode as a function of beam current for both alpha priming and mode priming. The magnetic field is 33.42 kG with no taper and the output frequencies are near 85.5 GHz. The highest beam voltages and detunings are obtained using alpha priming, resulting in values up to 75.5 kV. Peak voltages for mode priming by prebunching the electron beam are typically somewhat lower, resulting in lower power and efficiency. The scatter in the points is representative of the variations in the

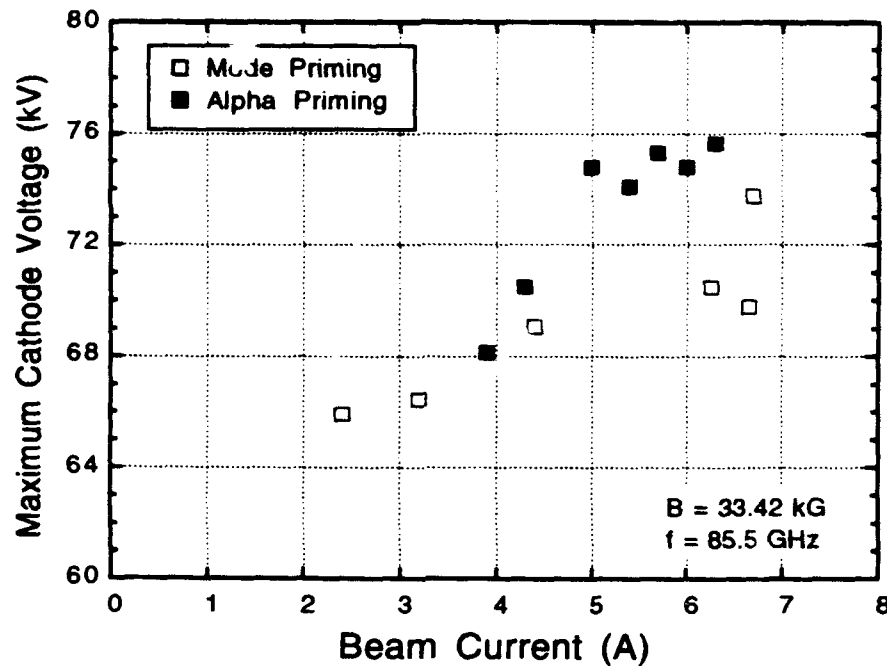


Figure 63: Optimized cathode voltage versus current for mode and alpha priming.

operating conditions of the gyroklystron, such as mirror separation, mirror alignment, and electron beam position in the resonator.

A number of measurements are performed to ensure that the high efficiency data obtained using the alpha-priming technique is independent of the prebunching resonator. When the magnetic field is tapered across the output resonator by +4%, the field in the prebuncher is reduced by 5.6%. The longitudinal mode separation in the prebuncher is only 2.5%, so that any fundamental or second harmonic radiation present in the input resonator will be shifted to a lower frequency. However, no effect on alpha priming is observed for tapered magnetic fields. When the EIO signal is introduced into the prebuncher during alpha priming, no effect is observed. This also confirms that radiation in the input resonator does not effect alpha priming, since the EIO power is much greater than any fundamental or second harmonic radiation present. The beam current can be increased so that oscillations occur in the input resonator, but this also has no effect on the operation of the tube for relatively small oscillations. Varying the magnetic field and the cathode voltage changes the frequency of any radiation present in the prebuncher, again with no effect on alpha priming. Lastly, the mirror separation

is varied to excite different modes in the output resonator. This shifts the frequency difference between the two resonators, but the efficiency and maximum detuning are unchanged. Thus, a variety of measurements have shown that the alpha-priming effect does not depend upon the prebunching resonator.

Another way to explain the phenomenon of alpha priming could be some unique characteristic of the voltage pulse which preferentially excites a high-frequency mode in the output resonator. To test this possibility, the pulse forming network in the modulator is adjusted so that the shoulder on the leading edge of the voltage pulse is moved to earlier and later times. However, this has no effect on the efficiency or the output mode of the gyrokystron. The PFN is also shortened to two stages so that a 2 μ sec voltage pulse is obtained. Again, no change in the output frequency or efficiency is observed. It is concluded that the gyrokystron is not sensitive to changes in the shape of the voltage pulse and that alpha priming is governed by the cathode-mod anode capacitance only.

D. Mirror Alignment and Second Harmonic Radiation

A general observation from the experiment is that misaligning one of the output resonator mirrors by a fraction of 1° can result in a 50% reduction in output efficiency. This effect is quite unexpected from the measurements in Figure 32, where 1° of misalignment only reduces the quality factor by 10%. This section discusses the sensitivity of the gyrotron to mirror alignment, frequency measurements from aligned and misaligned resonators, and second harmonic radiation in the input and output resonators.

The resonance condition for a TEM_{plq} mode in a Fabry-Perot-type resonator with curved mirrors can be written[58]

$$kd - 2(2p + l + 1) \arctan\left(\frac{d}{kw_0^2}\right) = \pi(q + 1). \quad (68)$$

Here, k is the free space wavenumber, w_0 is the radiation waist, d is the mirror separation, and p, l , and q are the radial, angular, and longitudinal mode numbers in cylindrical coordinates. The fundamental transverse mode is denoted the TEM_{00q} mode, and is approximately gaussian in shape with a field maximum at the center of the mirror. The second term on the left-hand side of Eq. (68) is relatively small compared to the other terms, but must be included for comparison with experimental measurements. The finite-sized mirrors cause large diffraction losses for higher-order transverse modes so that they are not usually observed in the experiment.

As the beam voltage is increased in the gyrokystron, a sequence of longitudinal modes is excited in the output resonator with decreasing frequency. The intermode spacing between modes with the same transverse mode numbers is $\Delta f = c/2d$, which allows for a method to verify the transverse mode structure. Such a comparison is presented in Table 5 for calculated and measured frequencies from the output resonator under normal operating conditions. The beam voltage varies from 59.1–65.2 kV, the current is 3 A, the voltage divider is 80.5%, and the magnetic field is 33.42 kG. The measured frequency separation of 729 MHz corresponds to a mirror separation $d = 20.57$ cm. The experimental measurements are accurate to within a few MHz, so that excellent agreement is obtained between the measurements and calculated values.

TEM mode numbers	Calculated Frequency (GHz)	Measured Frequency (GHz)
0,0,117	86.286	86.286
0,0,116	85.557	85.557
0,0,115	84.828	84.828
0,1,115	85.079	
1,0,115	85.331	
1,1,115	85.582	

Table 5: Measured and calculated output frequencies with good alignment.

Several higher-order transverse modes are included in the table to demonstrate that these frequencies should be discernible in the experiment given the accuracy of the measurements. Nearly all of the data collected during this experiment is single-moded where the measured frequencies correspond to different TEM₀₀ modes.

In the experiment, three micrometers are adjusted from outside the magnet dewar to vary the position and alignment of each output resonator mirror. The mirrors are intentionally misaligned by advancing only one of the micrometers on a single mirror. Since the electron beam excites a TEM mode with horizontal polarization, the misalignment of the mirror can be such that the mirror surface is now parallel or tilted with respect to the electric field of the resonator mode. The cold tests described previously were performed for the case where the field is parallel to the misaligned mirror, but there is no preferred polarization in the absence of the beam. We might anticipate that this orientation will be less susceptible to degradation by misalignment under hot-test conditions, which is what is observed in the experiment.

As an example, consider the hot test where one mirror is misaligned such that the surface remains parallel to the electric field of the mode. The beam voltage is 72.5 kV, the beam current is 3.8 A, the magnetic field is 33.42 kG, and the voltage divider is 82.5%. The gyrotron is operated in the alpha-priming regime where the cathode-mod anode capacitance is 1.0 nF. An efficiency of 15.6% is measured with a single

longitudinal mode oscillating at 85.383 GHz with no misalignment. A misalignment of 0.5° results in a measured frequency which is shifted up by 177 MHz, which is consistent with the new position of the center of the resonator mirror. The efficiency is now 13.6%, which is relatively close to the aligned value. Thus, misaligning the mirrors such that the mirror surface remains parallel to the electric field has a relatively small effect on the operation of the gyrotron in the present experiment.

A much different result is obtained when the micrometer is advanced so that the mirror surface is tilted with respect to the electric field of the resonator mode. The beam voltage is initially 72.8 kV, a beam current of 4.55 A, and the capacitance setting is 1.125 nF. The measured frequency is 85.416 GHz, with a corresponding efficiency of 14.5%. The misaligned resonator frequency is upshifted by 153 MHz, with a maximum efficiency of only 7.0% at a beam voltage of 67.9 kV. Increasing the beam voltage results in the 84.534 GHz mode being excited at lower efficiency and power. Thus, a relatively small misalignment of 0.5° results in 50% less efficiency. This is due to both ⁽¹⁾ lower efficiency for a given cathode voltage and ⁽²⁾ the inability to operate at higher voltage (frequency detuning) for a given mode. A large volume of data suggests that mirror misalignments of this type result in a large reduction in power and efficiency over the entire gyrotron parameter space.

An interesting phenomenon is observed when this misaligned resonator is driven at even higher cathode voltages. For a beam voltage of 75 kV and a slightly different mirror separation, the output spectrum becomes multimoded with both the 85.230 and 83.817 GHz frequencies present simultaneously during the 13 μ sec pulse. This multimode behavior is rare and is not observed when good alignment is preserved. The low frequency mode does not correspond to a fundamental transverse mode with a lower longitudinal index. From the calculated frequencies in Table 6, this mode appears to be the $TEM_{1,1,114}$ mode for a mirror separation of 20.83 cm. It follows that the Q of the fundamental transverse mode is spoiled by the mirror misalignment, which allows the TEM_{11} mode to become unstable. The same behavior is observed when the resonator mirrors are translated a short distance with the same misalignment. This represents one of the few instances where a higher-order mode is observed in the experiment,

TEM mode numbers	Calculated Frequency (GHz)	Measured Frequency (GHz)
0,0,117	85.230	85.230
0,0,116	84.510	
0,0,115	83.789	
0,1,114	83.319	
1,0,114	83.569	
1,1,114	83.819	83.817

Table 6: Measured and calculated output frequencies with misalignment.

but serves to demonstrate that good mirror alignment is important in achieving high power, single-mode operation.

In the present experiment, radiation at the second harmonic of the cyclotron frequency is occasionally observed using the heterodyne diagnostic. The power level of the 170 GHz radiation is small compared to the fundamental, although calorimetric measurements have not been performed. Signals from the output detector indicate the presence of the second harmonic via an irregular, spiky signature on the top millimeter-wave pulse. The most striking feature of the second harmonic is that the frequency is almost exactly twice the fundamental frequency. This is unexpected since the calculated frequencies vary significantly due to the transverse mode structure as well as the higher frequency.

As an example, consider the experimental conditions corresponding to the data in Table 6. A small amount of second harmonic radiation is detected at a frequency of 170.460 GHz, which is exactly twice the frequency of the fundamental. Using the same mirror separation $d = 20.83$ cm, a mode chart is formed for the frequencies close to 170 GHz, given in Table 7. The 170.460 GHz mode is most likely the $TEM_{0,1,235}$, which has higher diffraction losses than the fundamental transverse modes at the second harmonic. We expect that second harmonic TEM_{00} modes, if excited, will have very small diffraction losses and will be difficult to observe in the experiment. If the voltage

TEM mode numbers	Calculated Frequency (GHz)	Measured Frequency (GHz)
0,0,236	170.930	
0,0,235	170.209	
0,1,235	170.460	170.460
1,0,235	170.710	
1,1,235	170.960	

Table 7: Measured and calculated second harmonic frequencies with misalignment.

is increased past the maximum operating point for the fundamental mode, the second harmonic signal disappears. Thus, the existence of the fundamental is usually required for the excitation of the second harmonic in the output resonator.

The prebunching resonator oscillates at the fundamental cyclotron frequency for beam currents greater than 6 A and pitch angles of approximately 1.6. The input resonator mirrors are fixed with separation $d = 7.06$ cm and relatively large coupling holes, which allows another opportunity to measure the transverse structure of the excited modes. Measured and calculated frequencies from the prebunching resonator are shown in Table 8. Excellent agreement is obtained between the measured and theoretical resonant frequencies, which are consistent with operation in TEM₀₀ modes. Although the mirrors have centered coupling holes, the fundamental transverse mode remains dominant since the diameter of the mirrors is relatively small.

It is also possible to excite second harmonic radiation in the prebunching resonator at both low and high currents (2-12 A), although the efficiency is low compared to the fundamental. The detector signals from the input resonator show that the oscillation is very spiky as a function of time, which is due to the ripples on the beam voltage pulse. At magnetic field of 34.18 kG, the frequency most often measured is 176.722 GHz. For a prebuncher mirror separation of 7.06 cm, no fundamental transverse modes fall close to this frequency. The closest calculated frequency is the TEM_{2,3,80} mode at a frequency of 176.716 GHz. The transverse mode numbers for this mode are rather

TEM mode numbers	Calculated Frequency (GHz)	Measured Frequency (GHz)
0,0,38	83.427	83.427
0,0,39	85.551	85.554
0,0,40	87.675	87.675
0,1,38	84.008	
1,0,38	84.590	
1,1,38	85.172	

Table 8: Measured and calculated prebuncher frequencies.

high, which makes it difficult to place much confidence in this mode identification. The ceramic rings which surround the input mirrors are designed to absorb radiation near 85.5 GHz, so perhaps their properties near 170 GHz cause large reflections which create a new set of transverse modes. When this mode is downshifted in frequency by lowering the magnetic field, the resulting calculated frequency of 170.343 is fairly close to the second harmonic frequencies measured in the experiment. Hence, it is possible that second harmonic generation in the input resonator excites a nearby frequency in the output resonator. The output mirror separation can be adjusted to match the second harmonic frequency in the prebuncher, but no change in the operation of the gyrotron is observed when this is performed.

E. Depressed Collector Studies

In the quasioptical gyrotron, the electron beam collection and radiation output are separated since the main resonator is transverse to the axis of the beam. This allows for a straightforward implementation of a depressed collector, unlike conventional cavity gyrotrons where the beam must be separated from the output waveguide. A depressed collector is used to increase the overall efficiency of a microwave tube by collecting the spent beam at a negative potential with respect to ground. In the present experiment, this depression is accomplished by inserting different resistances between the collector and ground (see Figure 24). A simple, single-stage collector is used where the electron beam is collected on the inner wall of a stainless steel cylinder. Insulating material is placed between the collector and the rest of the experiment to prevent arcing as the collector is depressed ($V_{coll} \sim 40$ kV).

In the gyrokystron experiment, the current to the collector trim coil is increased to 270 A so that essentially 100% of the beam passes the uptaper and intercepted in the collector. For the case of no beam interception, the overall efficiency of the device is written

$$\eta = P_{out} / [V_b I_{coll} - R_{coll} I_{coll}^2]. \quad (69)$$

In this equation, P_{out} is the output power, V_b is the beam voltage, and R_{coll} is the resistance between the collector and ground. As an example, a 70 kV beam with a current of 6 A is depressed by 36 kV using a 6 k Ω resistance. When a portion of the beam is intercepted by the uptaper, the overall efficiency can be expressed

$$\eta = P_{out} / [V_b (I_{cath} - I_{coll}) + (V_b - R_{coll} I_{coll}) I_{coll}], \quad (70)$$

where I_{cath} is the cathode current. This equation accounts for the fact that a portion of the beam is collected at ground potential.

A plot of the measured overall and output efficiencies is given in Figure 64 as a function of collector voltage depression. The gyrokystron is operating in the alpha-primed regime with a cathode-mod anode capacitance of 1.125 nF and a voltage divider

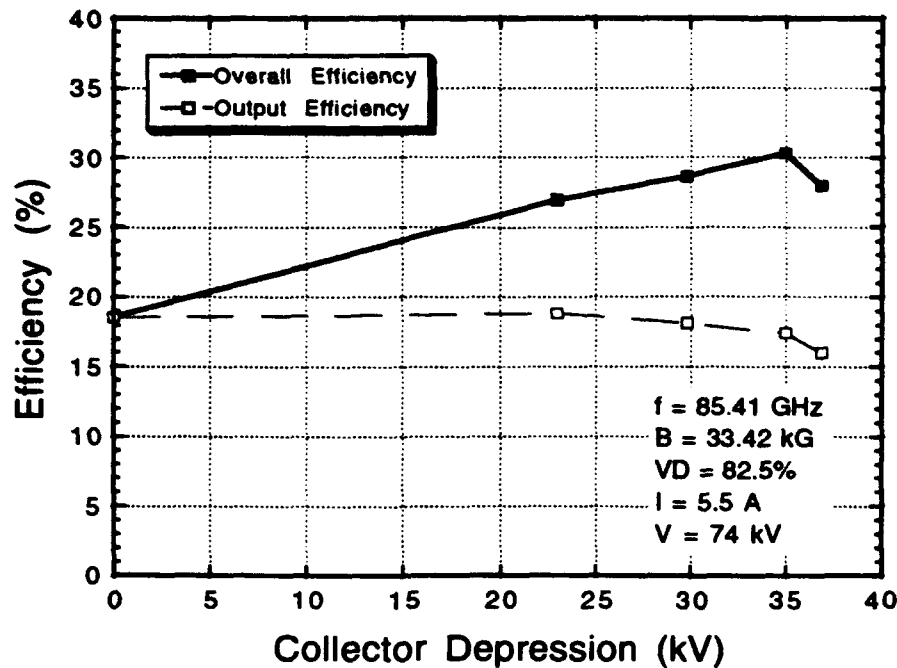


Figure 64: Measured efficiency versus collector voltage depression.

setting of 82.5%. The pitch angle of the electrons is measured as 1.8 using the capacitive probes in the drift tube. The gyrokystron is running in the 85.41 GHz mode with an output efficiency of approximately 18% prior to depressing the collector. As the collector is depressed, the overall efficiency rises to greater than 30% at a collector voltage of -35 kV, with a corresponding output efficiency of 17.5%. As the collector is depressed further, a large portion of the electron beam is reflected from the collector and the operation of the gyrokystron becomes unstable.

As the collector depression is increased, a portion of the beam is reflected from the collector. Define the uncollected current as the difference between the cathode current and the collector current ($I_{uncoll} = I_{cath} - I_{coll}$). This uncollected current is plotted in Figure 65 as a function of collector voltage depression for the data described in the preceding figure. For depression voltages less than 25 kV, essentially 100% of the cathode current is collected by the collector. The initial uncollected current of 3% represents the error in the baseline measurement due to ground loop noise interfering with the collector current monitor. As the collector voltage increases beyond 25 kV, a significant number of electrons fail to be collected on the collector. Simultaneously, the

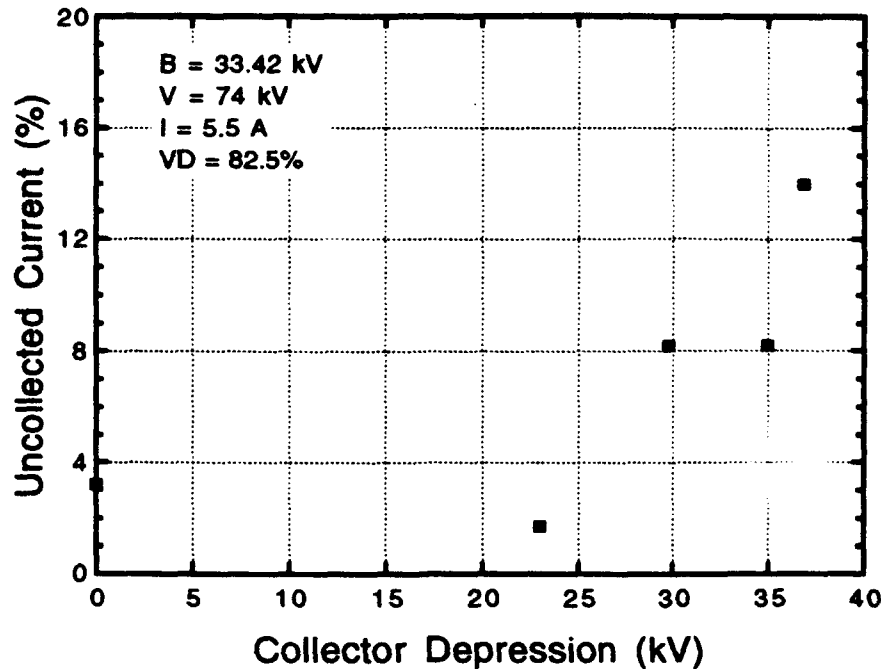


Figure 65: Uncollected current during depressed collector operation.

capacitive probe signals begin to increase, which is indicative of reflecting electrons. The capacitive probe signals are doubled at a depression of 35 kV, although the uncollected current is only 13% of the total. The dewar current monitor also increases over these collector voltages, although this increase accounts for only half of the lost current. This increase in dewar current is possibly due to electrons being collected by the anode of the gun. A likely explanation for this behavior is as follows. At large voltage depressions, electrons are reflected from the collector and follow the magnetic field lines through the output resonator and back towards the gun region. A portion are collected on the anode at ground potential, although no mod anode current is measured. The remaining electrons are either mirrored back towards the collector or contribute to a space charge cloud near the gun. The doubling of the capacitive probe signals tends to indicate that the electrons make many passes through the tube, which supports the reflexing scenario. During these conditions, only a small increase in uptaper current is noticed, which indicates that the electrons are not collected in this region. At no time is current collected on the drift tube.

The electrons which are the first to reflect from the collector have the smallest

amount of parallel energy. Since the beam is essentially monoenergetic at the cathode, electrons which interact most efficiently with the rf fields in the output resonator will have the smallest energy at the cathode. The transverse energy of the beam is converted to parallel energy in the adiabatically decreasing magnetic field at the collector. Thus, the maximum voltage depression of the collector gives an upper bound on the interaction efficiency of the most efficient electrons. For a beam voltage of 75 kV and a collector voltage of 25 kV, the maximum efficiency of these electrons is 67%. This figure should be compared with the output efficiency of 18%, which indicates a large spread in energy due to the interaction in the output resonator.

Up to this point, it has been assumed that electrons which exit the output resonator with low- α are the limiting factor in depressed collector operation since they have the lowest energy and are the first to reflect from the collector. This assumption is tested experimentally by lowering the current to the collector trim coil during depressed collector operation. This causes high- α electrons to be collected on the uptaper. An increase in both the uptaper and dewar current monitors is observed as the trim coil current is decreased. However, there is no change in the capacitive probe signals in the drift tube. The current collected by the uptaper and the dewar is lost directly from the collector current monitor. These observations indicate that the electrons collected on the uptaper do not contribute to the current reflected from the collector. This tends to support the interpretation that electrons which interact efficiently with the rf fields are responsible for reflections from the depressed collector.

The limit to depressed collector operation is due to electrons reflecting from the collector. Consider the experimental case where the beam current is 5.35 A and the collector resistance is 3.9 k Ω , which results in a collector voltage of 20.86 kV. The voltage divider is set to 86.5%, so that the pitch angle is small and there are no oscillations in the output resonator. The cathode voltage is lowered, and the onset of reflections is measured to be 24.62 kV. Since there are no oscillations in the gyrokystron, the electron beam should be monoenergetic. However, this is in contrast to the 15% difference between cathode and collector voltages. There are at least two possible explanations for this behavior. First, secondary electrons from the collector surface may be causing

the unstable operation at the largest collector depressions. Secondly, no effort has been made in the present experiment to design the collector region with the proper equipotential surfaces for beam collection. Space charge depression and the equipotential distribution in the collector may be causing reflecting current.

The collector efficiency is defined

$$\eta_{coll} = \frac{1 - \eta_{out}/\eta}{1 - \eta_{out}} \quad (71)$$

where η_{el} is the output efficiency of the interaction which is uncorrected for the collector depression. The collector efficiency is a measure of how effectively energy is recovered from the electron beam after it emerges from the output resonator. For the data in Figure 64, the maximum collector efficiency is 50% and occurs for a depression of 35 kV. The collector efficiency is 39% at a collector voltage of 23 kV, which is where loss of collector current begins. These values can be compared to an optimized design value of $\eta_{coll} = 76\%$ for a 10 GHz gyrokystron. It may be beneficial to operate the gyrokystron with a somewhat lower α so that the maximum collector depression can be increased. However, this would probably be more than offset by the loss of interaction efficiency in the gyrotron. Reducing the spread in pitch angle should also allow higher collector efficiencies since electrons with very high α values before the output resonator may be the first to reflect from the collector. No attempt has been made to reduce the pitch angle spread of the beam in the present experiment.

There are several important differences between depressed collector operation in the present experiment and previous results on the quasioptical gyrotron at NRL[59]. In the present work, it is possible to operate the gyrokystron at peak efficiency and optimum detuning while depressing the collector. The output is single-moded and quite stable during operation. Previously, the output was always multimoded and the best collector efficiencies occurred for lower interaction efficiencies. Secondly, nearly 100% of the beam current is collected in the collector during this experiment, so that higher overall efficiency is obtained. Approximately 15% of the beam current was collected on the uptaper during earlier depressed collector experiments on the QOG. Lastly, the output efficiency degrades rather slowly as the collector potential is increased in the

present work. This is in contrast to the previous results where the efficiency dropped very quickly when the collector depression became too large.

F. Amplifier Operation

The quasioptical gyrokystron experiment is designed as an oscillator, but amplifier studies may also be performed by lowering the average α of the beam so that the output resonator is below threshold for oscillations. This provides an opportunity to measure the quality of the electron beam prebunching, amplifier gain, bandwidth, and phase and frequency characteristics. Before characterizing the gyrokystron, measurements are performed to study the frequency jitter and chirp of the EIO drive source.

Several techniques are used to observe and measure the frequency chirp of the EIO during the 2 μ sec pulse. First, the EIO signal is passed directly through the heterodyne system and displayed on an oscilloscope (see Figure 35). For the 30 MHz bandpass filter, a 2 μ sec pulse is obtained. However, the 10 MHz bandpass filter gives a considerably shorter pulse, indicating that the chirp is greater than 10 MHz. The video detector on the output of the heterodyne is then removed and the 160 MHz beat frequency between the EIO and the local oscillator is observed directly using a fast oscilloscope. The beat frequency is sampled during the 2 μ sec pulse and a chirp of 15 MHz is measured.

The prebunching resonator may also be used to observe the frequency chirp of the drive source. The input resonator has a quality factor of 2000 and a corresponding FWHM of 43 MHz. The EIO produces a square 2 μ sec pulse whose amplitude is modified upon transmission through the prebunching resonator. The impedance of the resonator may be expressed [60]

$$\frac{Z_{in}}{R} = \frac{1}{1 + j2Q\Delta\omega/\omega} \quad (72)$$

so that the normalized signal transmitted through the prebuncher is

$$T = \frac{1}{1 + 4Q^2(\Delta\omega/\omega)^2} \quad (73)$$

Here, $\Delta\omega$ is the difference between the EIO frequency and the resonant frequency of the input resonator. A frequency chirp of 15 MHz is obtained by measuring the variation in the transmitted signal through the prebunching resonator.

The phase shifter and phase detector are calibrated *in situ* using the set-up in Figure

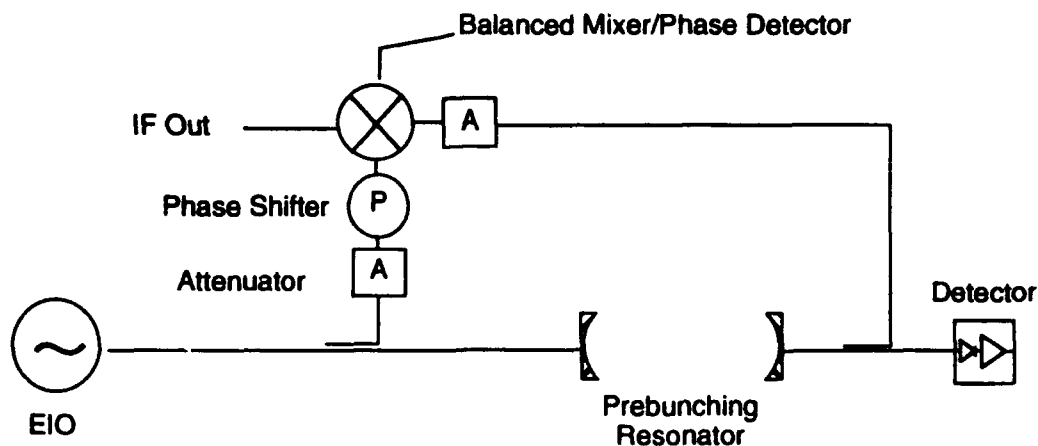


Figure 66: Set-up used to measure the EIO phase chirp through the input resonator.

66. The EIO signal is split so that a portion is transmitted through the prebunching resonator and is combined on the phase detector. The frequency chirp of the EIO causes a phase chirp to appear on the phase detector after it transits the input resonator. The phase shift of the rf signal through the input resonator as a function of frequency is written

$$\phi = \arctan(-2Q\Delta\omega/\omega). \quad (74)$$

Thus, $\phi = 0$ at the resonant frequency and varies from $\frac{\pi}{2}$ to $-\frac{\pi}{2}$ as the frequency moves far from resonance. The FWHM of the resonance is given by the frequency separation between $\phi = \pm\frac{\pi}{4}$. Using this technique, an EIO frequency chirp of 15 MHz is measured. Several representative oscilloscope traces of the phase detector are given in Figure 67 as the phase shifter is varied. The variation in the output of the phase detector during the EIO pulse is due to the frequency chirp of the drive source coupled with the resonance characteristics of the input resonator.

The most accurate measurement of the frequency chirp of the drive source is obtained by observing the beat frequency between the EIO and the gyrotron on the 85

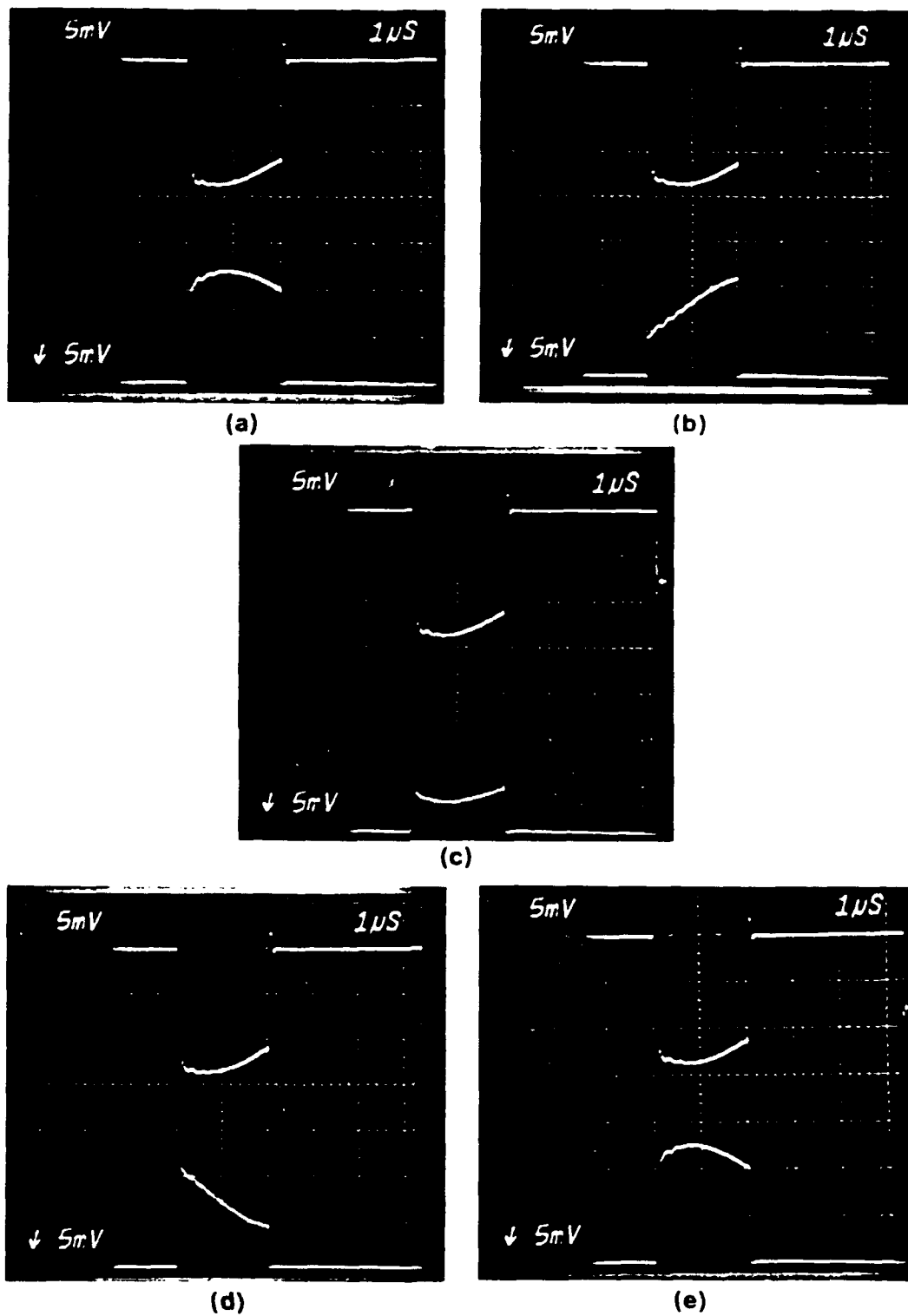


Figure 67: Phase detector signals showing the phase chirp of the EIO. The relative phase shift is 0°, 90°, 180°, 270°, and 360° for (a)-(e), respectfully.

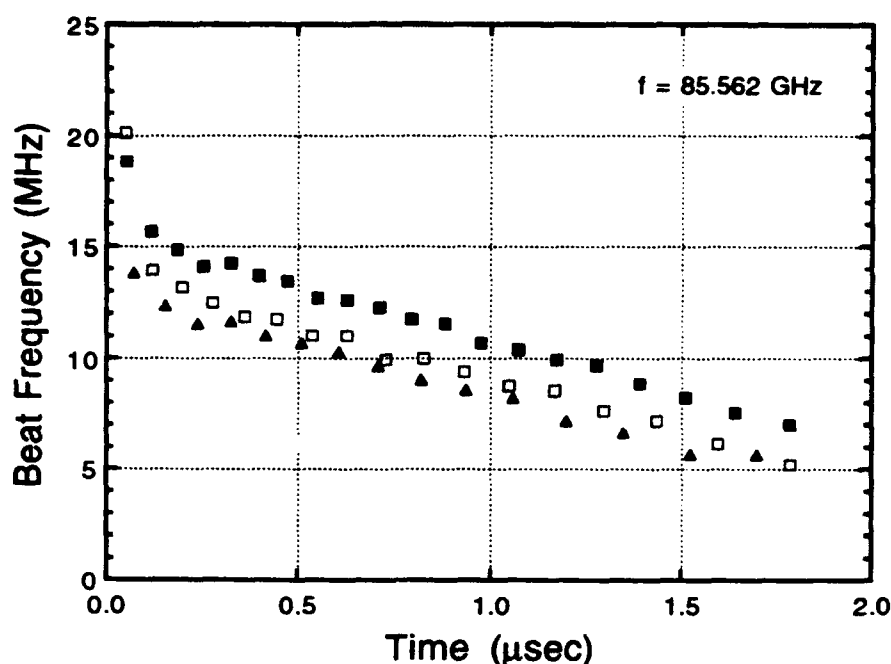


Figure 68: Beat frequency between the EIO and free-running gyrotron.

GHz balanced mixer. The EIO signal is switched into the load in Figure 67 so that the gyrotron and EIO frequencies are unrelated. The EIO frequency is tuned so that the frequency separation is approximately 20 MHz at the beginning of the 2 μ sec pulse. The results of several measurements are shown in Figure 68, where the beat frequency is plotted as a function of time during the 1.8 μ sec pulse. The three sets of data points correspond to different EIO pulses measured within 1 minute, where the EIO is allowed to warm-up for several minutes so that the frequency is fairly stable. However, the EIO frequency continues to drift over a smaller range over long periods of time, which precludes certain measurements of a statistical nature. During the first 0.2 μ sec of the pulse, the measured frequency chirp is approximately 5 MHz. After this time, there is a nearly linear droop in frequency of approximately 4 MHz/ μ sec. The jitter in frequency is given by the vertical separation between the data sets, which is 2 MHz for this data. It should be noted that the chirp is not perfectly linear in time, which becomes more apparent during amplifier and phase-locked oscillator operation.

The gyrokylystron is operated as an amplifier by lowering the mod anode voltage divider so that the output resonator is below threshold for oscillations. The output

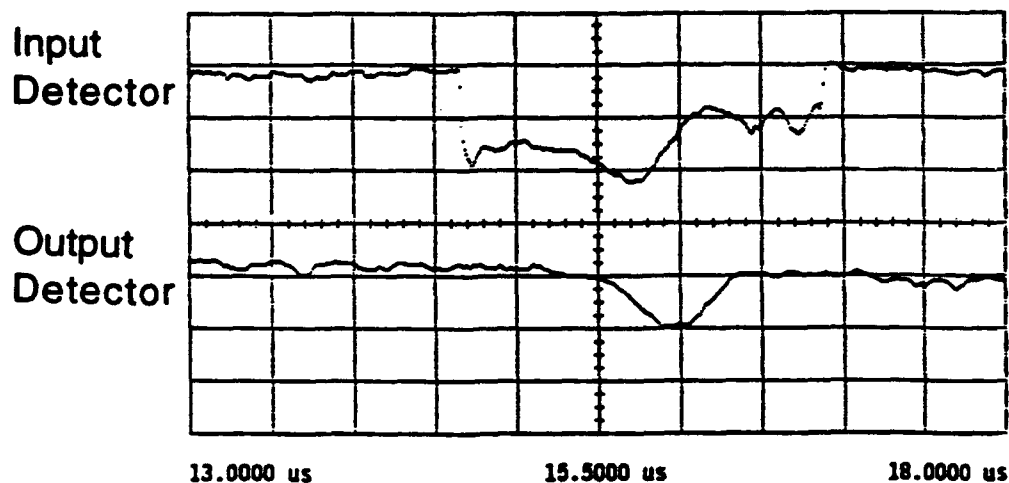


Figure 69: Input and output signals during amplifier operation.

mirror separation is adjusted so that the output frequency matches the input resonator frequency. An oscilloscope trace of the output and input signals during amplifier operation is shown in Figure 69. The cathode voltage is 68.2 kV, the beam current is 6.5 A, and the voltage divider is 84.5%, resulting in a measured pitch angle of the electrons of 1.0. The output frequency is 85.556 GHz and is tuned to the resonance of the input resonator. No amplification is observed when the resonators are not matched in frequency.

The input pulse from the EIO is 2 μsec in duration, but the amplifier FWHM is only 0.6 μsec . This shortened pulse is due to the frequency chirp of the drive source coupled with the narrow resonance of the high- Q output resonator. The measured amplifier bandwidth is 2.4 MHz, which is in excellent agreement with the calculated output resonator bandwidth of 2.3 MHz and corresponding $Q = 37\,000$ (see Table 3). In the past it has been speculated that the presence of the electron beam modifies the fields in the output resonator and causes higher diffraction losses and a lower quality factor. This work shows that the quality factor of the output resonator is not affected by the presence of the electron beam during amplifier operation.

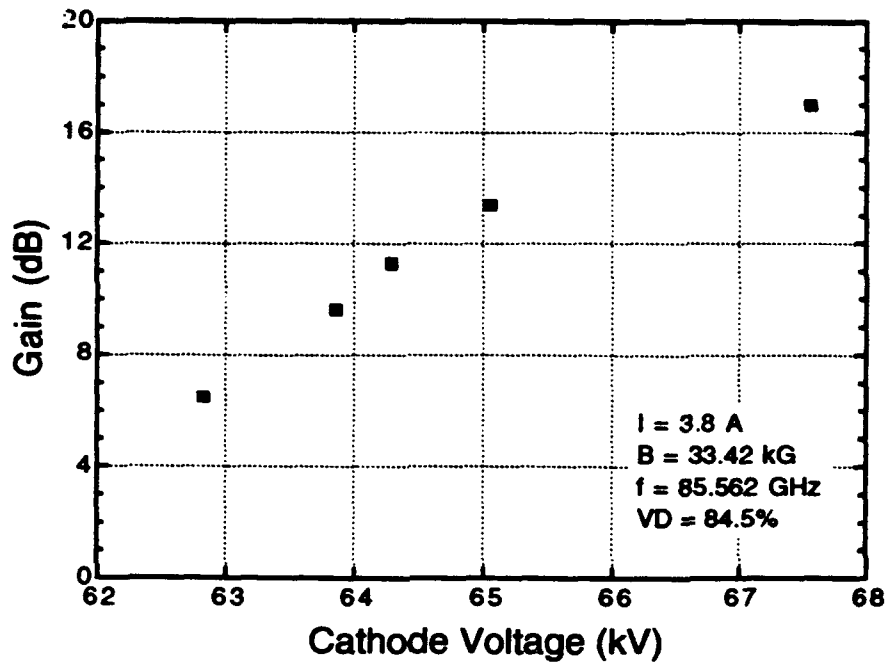


Figure 70: Measured amplifier gain as a function of beam voltage.

Measured amplifier gain as a function of electron beam voltage is shown in Figure 70 for a beam current of 3.8 A. The voltage divider is 84.5% for this data, resulting in measured values of α of approximately 1.0. The gain increases monotonically from 6.5 to 17 dB as the voltage is increased during amplifier operation. The bandwidth of the gain is constant as a function of beam current and voltage, which indicates that the quality factor of the output resonator does not depend upon the beam in this regime. The strong dependence of the gain on the cathode voltage is most likely related to two factors. First, the average α of the beam rises from 1.0 to 1.15 as the voltage is increased. Secondly, increasing the voltage increases the frequency detuning between the rf fields and the relativistic cyclotron frequency ($\Delta\omega = \omega - \Omega/\gamma$). Both of these effects increase the gain of the amplifier as the voltage is raised.

The linear theory of the quasioptical gyrokystron is presented in Chapter II, which can be used to calculate the gain of the device in the linear amplifier regime. Here, the linear efficiency and gain maximize when the detuning between the relativistic cyclotron frequency and the radiation frequency is zero in the output resonator ($\frac{\Delta\omega}{\omega} = 0$). However, the gyrokystron experiment is designed to maximize the prebunching

signal in the nonlinear regime for $\frac{\Delta\omega}{\omega} = 3.7\%$ in the output resonator, where the nonlinear interaction efficiency is large. For a magnetic field of 33.42 kG in the output resonator, the 85.56 GHz mode experiences zero frequency detuning at a beam voltage of 48.3 kV. This voltage is far less than the typical values observed in the experiment for amplifier operation. Thus, we expect that the amplifier is operating in the nonlinear regime so that the previously derived theory is not strictly applicable.

An estimate for the gain of the device may be obtained by evaluating the linear theory expressions when the detuning is zero in the output resonator. With a pitch angle of $\alpha = 1$, a bunching parameter $q = 1$, and an annular electron beam geometry, the electric field in the output resonator is calculated to be $E_{02} = 5.29 \times 10^6$ V/m. The corresponding efficiency of the gyrokystron is calculated as $\eta = 29.6\%$ with a gain of 21 dB for a beam current of 3.5 A and a 48.3 kV beam voltage. The linear efficiency is large, which indicates that the device will saturate at lower efficiency so that it is most likely outside of the linear regime for these parameters. However, the calculated gain of the amplifier is quite similar to the values measured in the experiment for somewhat higher beam voltages.

From the data in Figure 70, the maximum gain in the experiment occurs at a beam voltage of 67.5 kV for the operating conditions in the figure with a tilted output resonator. This beam voltage corresponds to a frequency detuning $\frac{\Delta\omega}{\omega} = 3.2\%$, which includes a small correction for space charge depression as the electrons traverse the output resonator. To compare this value to the linear theory, we must consider the Doppler shift in the resonance condition due to the tilted resonator ($\omega \cong \Omega/\gamma \pm k_z v_z$). Including the $k_z v_z$ term for the forward-travelling wave results in a detuning $\frac{\Delta\omega}{\omega} = 2.1\%$ with respect to an untilted quasioptical resonator. This value is much higher than the detuning for maximum gain for the linear amplifier. However, this is quite close to the detuning for maximum gain of the free-running oscillator, which is calculated as 1.4% for an untilted resonator[4]. Thus, the measured amplifier characteristics place the device outside the linear amplifier regime with a maximum gain which is consistent with theoretical estimates.

An oscilloscope trace of the onset of oscillations is given in Figure 71 when the

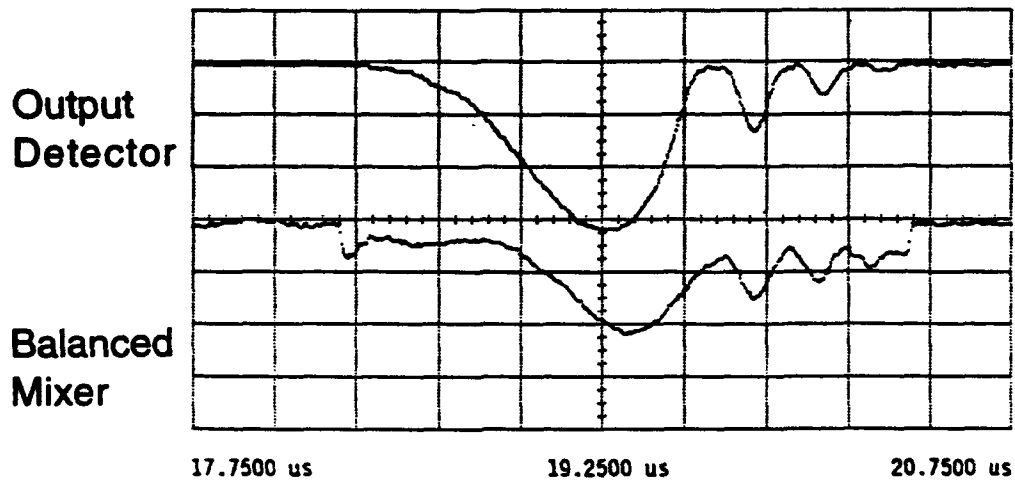
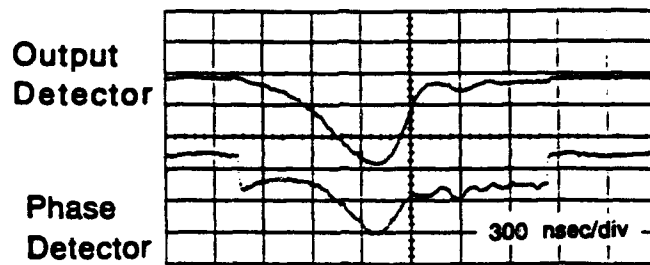


Figure 71: Amplifier operation at the onset of oscillations in the output resonator.

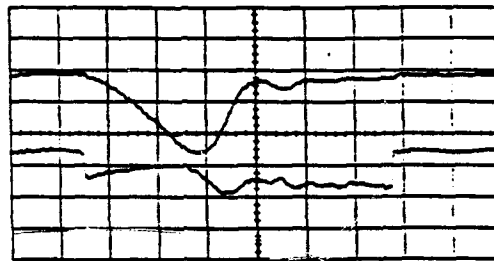
cathode voltage is raised beyond the limit for stable amplifier operation. The top trace is the output detector signal while the bottom trace is the balanced mixer output. This trace is to be compared with Figure 69, where there is only amplification and no free oscillations. There are several oscillations in the output detector trace after the EIO amplification is finished, which indicates that the output resonator is oscillating freely. This effect is similar to EIO mode priming, where the external drive signal initiates the oscillations. Note that there are now oscillations on the balanced mixer signal that occur after the amplifier pulse. This indicates that the output from the gyrotron is no longer phase locked to the EIO input signal. During this portion of the pulse, the EIO frequency is outside of the phase-locking bandwidth so that phase locking is not possible and the beat frequency between the EIO and gyrotron is observed.

One of the most important reasons to perform amplifier studies is to check the operation of the tube using the phase-lock diagnostics. Since an amplifier is phase locked by definition, there should be a zero beat frequency between the EIO and the gyrotron. The phase between the two sources should be fixed, so that varying the phase shifter in Figure 37 results in a variation of the phase detector output. Oscilloscope

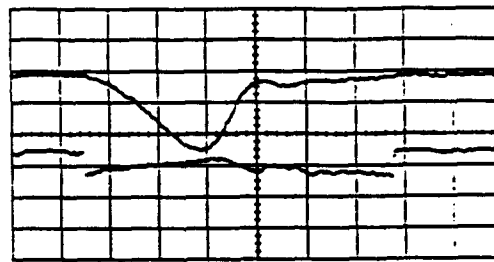
traces of the output detector and balanced mixer pulses are shown in Figure 72 as the phase shifter is varied. The phase shifter is varied by 0° , 90° , 180° , and 270° in (a)-(d) of the figure, respectfully. For a 0° phase shift, the EIO and output signals add constructively so that the balanced mixer output is maximum. For a phase shift of 180° , the signals add destructively so that a minimum is obtained on the mixer. Note that the output from the balanced mixer is asymmetric for phase shifts of 90 and 270° . This effect is due to differences in the relative phase between the EIO and gyrotron inside the frequency bandwidth of the amplifier. This type of behavior is also observed in the next section when phase-locking measurements are performed.



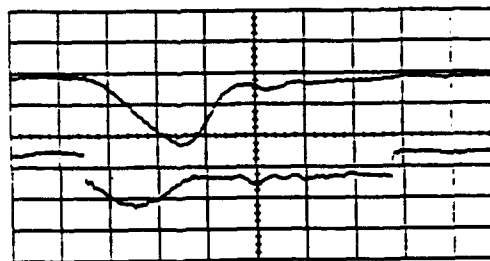
(a)



(b)



(c)



(d)

Figure 72: Balanced mixer signals for the amplifier as the phase shifter is varied. The phase shifter is varied by 0° , 90° , 180° , and 270° in (a)–(d), respectively.

G. Phase Locking

The term **phase locking** refers to the behavior of a nonlinear oscillator subjected to an external drive signal. If the drive source is sufficiently large in amplitude and close to the frequency of the free-running oscillator, the oscillator is pulled to the frequency of the drive. There is now a fixed phase relation between the input and output signals which depends upon the separation between the drive and free-running frequencies. For phase locking via direct injection into the output resonator, the fractional phase-locking bandwidth can be written [61]

$$\frac{|f_d - f_0|}{f_0} = \frac{1}{Q_e} \sqrt{\frac{P_d}{P_0}}, \quad (75)$$

where Q_e is the external Q of the resonator and P_d and P_0 are the drive and output powers, respectively. As the drive frequency is varied across the phase-locking bandwidth, the relative phase varies from $\frac{\pi}{2}$ to $-\frac{\pi}{2}$. These relations have been verified experimentally using direct injection phase locking on conventional cavity gyrotrons [22,23].

In the present experiment, phase locking is accomplished by prebunching the electron beam in an upstream resonator using the EIO. Compared to direct injection, this technique requires less power to phase lock the oscillator due to the gain between resonators. The gyrotron is allowed to reach steady state, then the 2 μ sec EIO pulse is turned on. Ideally, a continuous-wave source is preferred for the drive signal which could be frequency and phase locked using a phase-locked loop. Experimentally, the EIO is free running and has a measured pulse-to-pulse jitter of 3 MHz and a frequency chirp of 10 MHz during the 2 μ sec pulse. This is to be compared to the 3 MHz FWHM of the high- Q output resonator in the gyrokystron. Thus, it is impossible to phase lock over the duration of the entire EIO pulse because of the chirp in the drive source and the narrow spectral width of the output resonator.

An example of phase-locked oscillator operation is given by the oscilloscope traces in Figure 73. The gyrotron is running in the 85.55 GHz mode in the output resonator with a cathode voltage of 67.9 kV, a beam current of 5 A, and a measured pitch angle of 1.8. In trace (a), the EIO signal is diverted into the load so that the electron beam is not

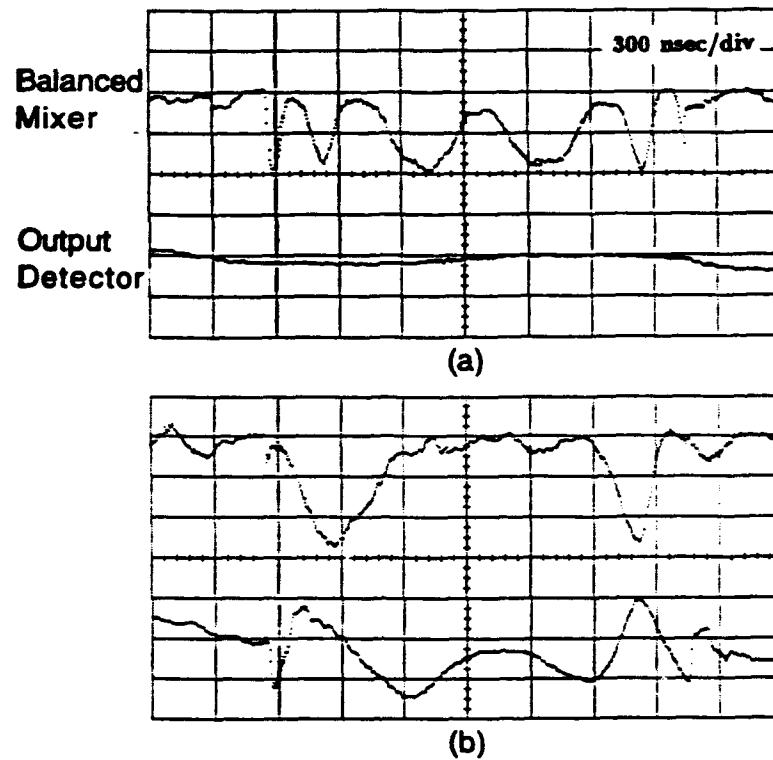


Figure 73: Gyroklystron operation without (a) and with (b) prebunching.

prebunched. The frequency of the drive source is adjusted so that the beat frequency between the two oscillators is minimum. Note that the frequency chirp of the EIO drive source can be seen by comparing the beat frequency at the beginning, middle, and end of the $2 \mu\text{sec}$ pulse. The output detector signal is constant during the duration of the $2 \mu\text{sec}$ EIO pulse. On a shot-to-shot basis, the relative phase between the two free-running oscillators varies randomly, as evidenced by the balanced mixer/phase detector signals. Figure 73 (b) shows the effect of the prebunched beam on the output of the gyroklystron. The beat frequency between the EIO and the gyrotron is driven to zero for approximately $0.9 \mu\text{sec}$, which is indicative of phase locking. A large modulation appears on the output detector due to the prebunched electron beam.

As the frequency of the EIO is electronically tuned away from the gyrotron, the two sources fall out of phase lock and pass into the periodic pulling regime. The EIO frequency is too far away to lock the oscillation in the output resonator, although it is close enough to the free-running frequency to amplitude modulate the output at the

beat frequency. This case is shown in Figure 74, where the gyrokystron is initially phase locked in (a). The drive frequency is tuned so that the beat frequency appears on the balanced mixer and output detector traces. This modulation also appears on both the input detector signal and the collector current monitor, and amounts to $\pm 70\%$ of the output detector signal level in (c). The level of modulation of the output power decreases as the gyrotron operates closer to saturation at higher detuning and higher power. The prebunched electron beam pulls the free-running frequency of the output oscillation so that there is a reproducible beat frequency on the balanced mixer, although the relative phase is random.

The frequency chirp of the EIO during the $2\ \mu\text{sec}$ pulse is much greater than the output resonator bandwidth, so that only a portion of the pulse is phase locked. However, a single shot from the experiment allows for observation of the entire phase-locking bandwidth. Figure 75 shows output detector and balanced mixer signals as the phase shifter in Figure 37 is varied. In case (a), the signals add destructively for a period of approximately $0.9\ \mu\text{sec}$. Immediately before and after the flat portion of the mixer signal are excursions which indicate the edge of the phase-locking band. The phase shifter is advanced by 90° in each of the succeeding traces, which results in a repeatable variation of the phase detector signal. The two signals add constructively in (c) so that a maximum is obtained on the mixer. At the center of the locking band the relative phase between the two sources is 0° . The relative phase varies from -90° to 90° as the EIO frequency chirps through the locking band, which results in the sloping traces observed in (b) and (d).

The present experiment is designed to achieve phase locking by premodulation of the electron beam, so that the EIO is not subjected to the large fields produced by the gyrotron. Nevertheless, it is important to demonstrate that the EIO is locking the gyrotron, as opposed to the gyrotron locking the EIO. This measurement is performed by beating the rf frequency of the gyrotron with the local oscillator of the heterodyne (Figure 35) and displaying the beat frequency ($\sim 160\ \text{MHz}$) directly on a digital oscilloscope. The gyrotron is operating at a cathode voltage of $66.1\ \text{kV}$, a beam current of $5.25\ \text{A}$, and a magnetic field of $33.42\ \text{kG}$. The output frequency is $85.559\ \text{GHz}$ and

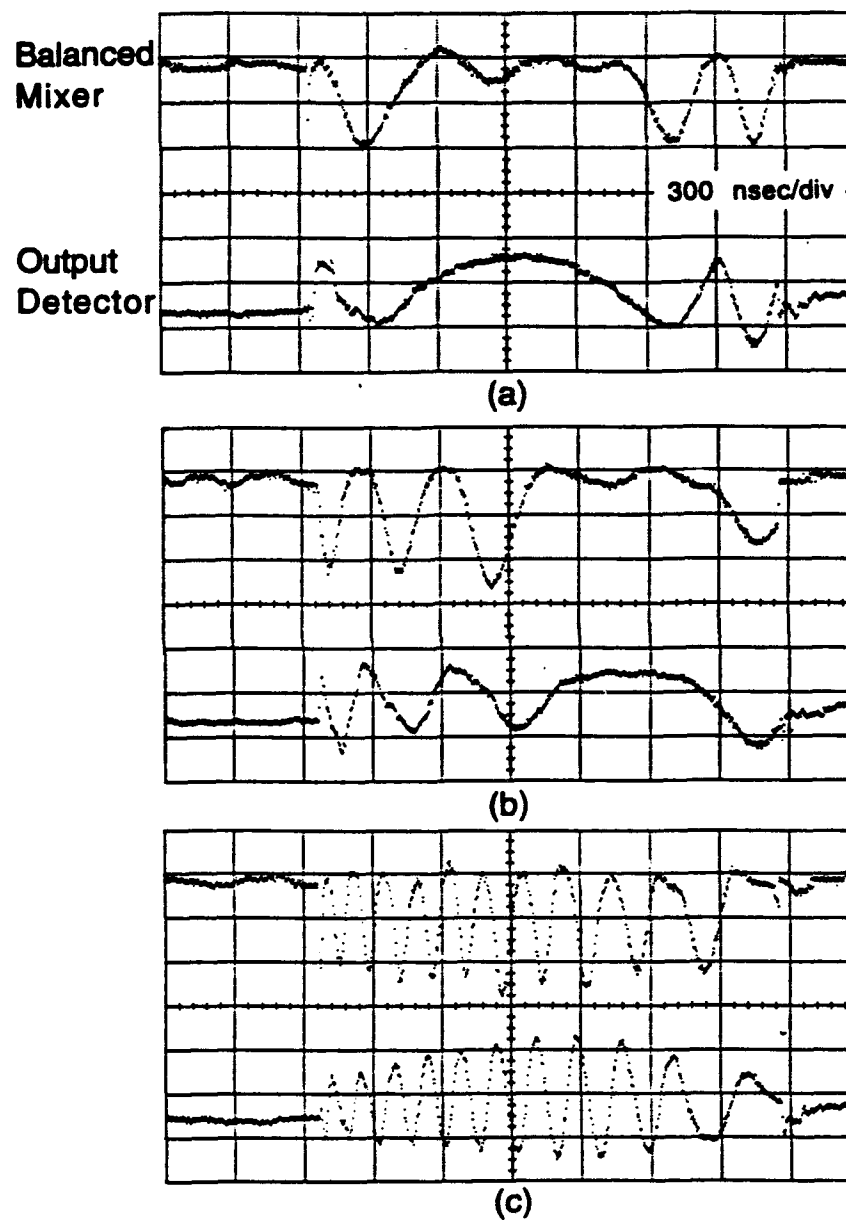


Figure 74: Gyrokystron operation as the EIO is tuned past the locking edge.

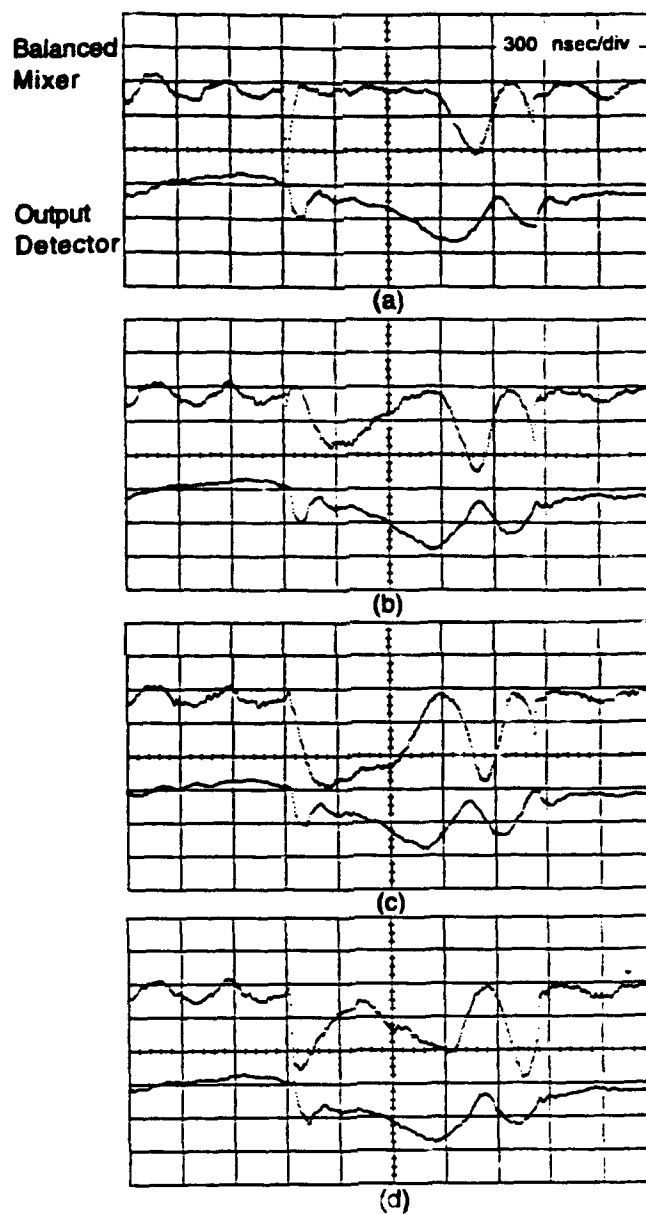


Figure 75: Balanced mixer traces during phase-locked operation. The phase shifter is varied by 0° , 90° , 180° , and 270° in (a)–(d), respectively.

the measured value of α is 1.6. The cathode voltage and frequency detuning are relatively low for this longitudinal mode, resulting in an efficiency of 11%. In the absence of prebunching, the beat frequency is measured as 162.2 MHz. The gyrotron is then phase locked by the EIO, and a 1.9 MHz downward frequency chirp of the gyrotron is measured during the 0.6 μ sec locking band. This chirp is consistent with the frequency droop of the EIO and demonstrates that the EIO is indeed locking the gyrotron.

As the EIO power to the prebunching resonator is decreased, the phase-locking bandwidth decreases. A plot of the measured phase-locking bandwidth versus input power is shown in Figure 76, along with the prediction of Adler's theory (Eq. 75). Although this equation is not applicable in the case of prebunching, Adler's relation is a benchmark for phase locking by direct injection. The experimental parameters are a beam voltage of 71.7 kV, a beam current of 5 A, and a magnetic field of 33.42 kG at the center of the output resonator. The voltage divider is 82.5%, with a measured value of pitch angle of 1.8. The output frequency of the gyrotron is 85.552 GHz and is single moded with a measured efficiency of 16%. With no EIO attenuation, the gyrotron is phase locked over the entire bandwidth of the output resonator at 25 dB below the output power level. The locking bandwidth decreases to ± 0.7 MHz when the drive signal is attenuated by 4 dB. These results are 20 dB below the drive power required for direct injection, and demonstrate the benefit of phase locking by prebunching the electron beam due to intercavity gain.

The experimental results may be compared to the nonlinear phase-locking theory presented in [27], where the slow time scale equations of motion are solved in the output cavity for a beam with predetermined entrance phases. Perturbation theory is used to model the ac current density, so that one can write the maximum phase-locking bandwidth with optimum prebunching as

$$Q \frac{|f_d - f_0|}{f_0} \leq 0.5 \frac{\mu F}{\eta_{\perp}} \exp - \left(\frac{\mu \Delta}{4} \right)^2. \quad (76)$$

Here, μ , F , and Δ are the normalized gyrotron parameters for interaction length, field amplitude, and frequency detuning, respectfully. From the above expression, large values of $\mu \Delta$ result in narrow phase-locking bandwidths due to the exponential term. This equation is the prebunching counterpart to Adler's relation for direct injection

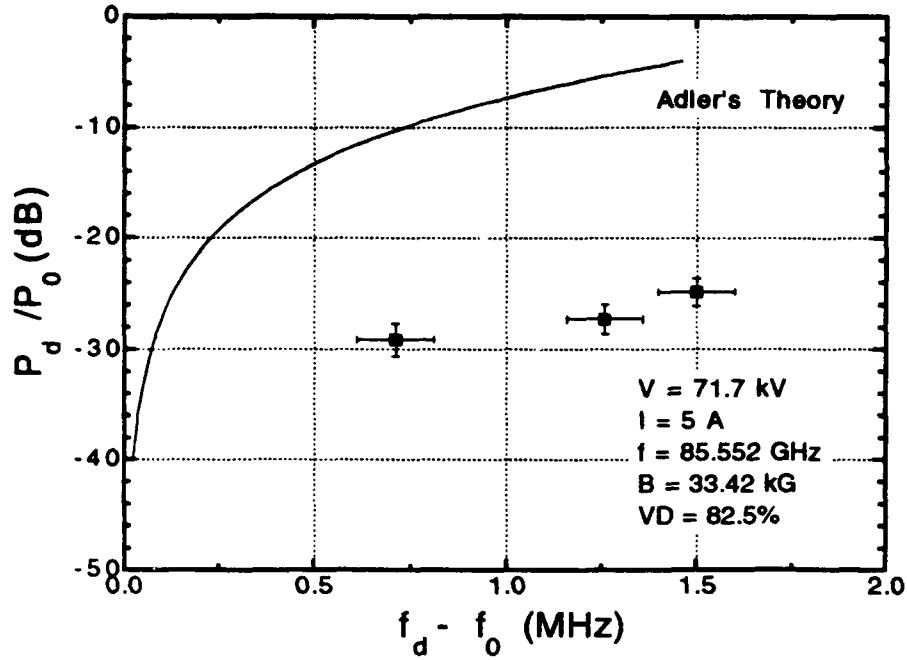


Figure 76: EIO drive power versus phase-locking bandwidth.

phase locking. Typical experimental parameters are $\delta = 0.413$, $F = 0.074$, and $\mu = 20$. To make a comparison with theory, the $k_z v_z$ Doppler term is subtracted from the detuning parameter, resulting in $\delta = 0.327$. The calculated fractional bandwidth from Eq. (76) is 10% of the linewidth of the output resonator, whereas the experimental measurements indicate that the entire linewidth is available for phase locking. In [27], it was shown that the perturbation theory estimate of the phase-locking bandwidth is a factor of 1.8 too low for $q = 0.16$ and large values of detuning. Thus, we expect that the analytical estimate of the locking bandwidth may be much lower than the value calculated using the fully nonlinear klystron approach for bunching parameters $q \sim 2$. A complete simulation is probably required to determine the theoretical phase-locking characteristics for the present parameters. This experiment may represent the first demonstration of phase locking with large values for the bunching parameter and frequency detuning.

It has been shown theoretically and experimentally that increasing the separation between the drive and free-running frequencies increases the time required to achieve phase locking. For short pulses, it is often impossible to obtain phase locking for drive

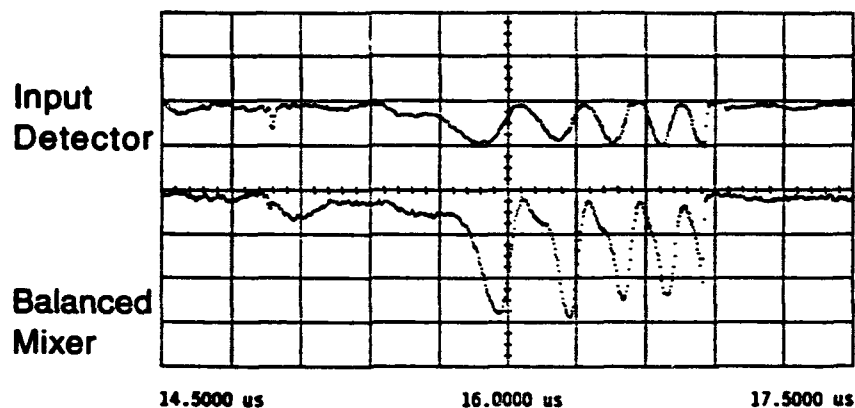


Figure 77: Phase locking at the beginning of the EIO drive pulse.

frequencies near the locking edge. In the quasioptical gyrokystron experiment, it is observed that 100% of the pulses are phase locked when $|f_d - f_0|$ is minimized near the beginning of the EIO pulse. This situation is shown in Figure 77, where the EIO frequency is adjusted so that the gyrotron is locked near the leading edge of the 2 μ sec drive signal. Using this technique, the time required for the EIO to pull the gyrotron into phase lock is minimized. Only a portion of the pulses ($\sim 60\%$) are phase locked when the EIO is allowed to chirp through the entire locking band.

Increasing the pitch angle of the beam electrons increases the bunching parameter q in the input resonator (see Eq. 12). Linear theory is used to show that a larger bunching parameter yields higher inter-resonator gain and increased phase-locking bandwidth, and these trends are also observed in the experiment. Operating the quasioptical gyrokystron at higher α results in higher output power and higher efficiency, but also increases the experimental phase-locking bandwidth and pulse-to-pulse reproducibility. For low values of α , low frequency detuning, and low efficiency, it is observed that the phase-locking behavior is not 100% reproducible. Possible benefits of operating at low detuning include less power to phase lock the output resonator and less time to achieve

locking. However, both of these potential benefits are more than offset by the reduced α and the corresponding reduction in the bunching parameter. The result of these studies, though, is quite desirable in that the operating conditions for optimum power and efficiency coincide with those for optimum phase locking.

One of the keys to designing a highly overmoded amplifier or phase-locked oscillator is providing a high degree of isolation between the input and output cavities. The geometry of the quasioptical gyroklystron is well-suited for gyroklystron operation since it is difficult for radiation to efficiently couple between open resonators which are oriented perpendicular to the drift tube. Measurements performed during the hot test of the gyroklystron demonstrate that the leakage signal is (at most) 35 dB down from the output power. Optimum coupling between the two resonators occurs when the output resonator mirrors are adjusted for precisely the same frequency as the input resonator. When the gyrotron is operated near maximum detuning for the 85.5 GHz mode, it is possible to excite the next lower longitudinal mode at 84.8 GHz during the second half of the pulse. However, only the 85.5 GHz leakage is observed in the input resonator due to the mode selectivity of the prebuncher. The input resonator supports a mode separation for TEM₀₀ modes of 2.1 GHz and a quality factor $Q = 2000$. Adjusting the output frequency outside of the bandwidth of the input resonator results in essentially no leakage power.

Although the leakage power is small compared to the drive signal, tests were performed to verify that the operation of the gyroklystron is unaffected by the undesired feedback. The gyroklystron is operated in the mode priming and alpha priming regimes while the output frequency is varied by ± 100 MHz about the center frequency of the prebunching resonator. As expected, the leakage from the output to the input falls to zero outside the bandwidth of the prebunching resonator. The power, efficiency, and maximum frequency detuning of the output radiation are not affected by the level of leakage in the present experiment.

A phase-locked oscillator can achieve higher interaction efficiencies than a free-running oscillator due to the increased phase bunching of the electrons[25,19]. In the present experiment, measurements are made to compare the two regimes by monitoring

the output pulse using a calibrated detector. When the oscillator is operated in the alpha-primed regime at relatively low detuning and efficiency, the prebunched beam can significantly increase the efficiency of the interaction close to the edges of the locking band. The center of the phase-locking band is usually at the same power as the free-running oscillator. When the frequency detuning of the operating mode is increased so that the efficiency is near optimum for the free oscillations, the prebunched beam has little effect on the efficiency. Thus, it appears that the maximum efficiency for both regimes of operation is $\sim 20\%$ for the parameters typically used in this experiment. As the cathode voltage and frequency detuning are increased past the optimum efficiency point for the 85.5 GHz mode, the prebunched beam drives the output oscillation to zero. Here the beam is overbunched and there is little exchange of energy between the electrons and the rf field in the output resonator. This is similar to increasing the interaction length in a gyrotron so that the bunched electrons gain energy before exiting the cavity.

Chapter VI

Multimode Simulations and Discussion

A. Generalized Gyrotron Theory

In both conventional and quasioptical gyrotron theory, a great deal of research has been performed to study device performance using normalized gyrotron parameters. The normalized variables are used to reduce the number of system parameters, which allows for the study of interaction efficiency and single-mode stability over the entire operating space. In this section there will be a short discussion of single-mode stability of quasioptical gyrotrons and experimental observations in the present experiment.

Figure 78 shows the region of stable, single-mode operation of a quasioptical gyrotron with a pencil electron beam placed at the center of the resonator, plotted in the plane of ϵ - δ [16]. The normalized field amplitude ϵ and normalized detuning δ are related to the more familiar parameters F , Δ , and μ through the relations

$$\epsilon = F\mu \quad (77)$$

$$\delta = \frac{1}{2}\mu\Delta. \quad (78)$$

One of the benefits to using the ϵ - δ notation is that these variables are only weakly dependent on the pitch angle of the electrons. The stable region is labelled S in the Figure (enclosed by the thick solid curve) and is superimposed on contours of constant perpendicular efficiency. The electronic efficiency of the interaction is related to the perpendicular efficiency via

$$\eta = \frac{\eta_{\perp}\beta_{\perp}^2}{2(1 - \gamma^{-1})}. \quad (79)$$

Curves of constant current are also included, where ψ is the ratio of beam current to starting current ($\psi = I/I_{st}$). The parameter T_0 is a measure of the mode density in the output resonator of the quasioptical gyrotron and is defined

$$T_0 = 2dv_z/w_0c, \quad (80)$$

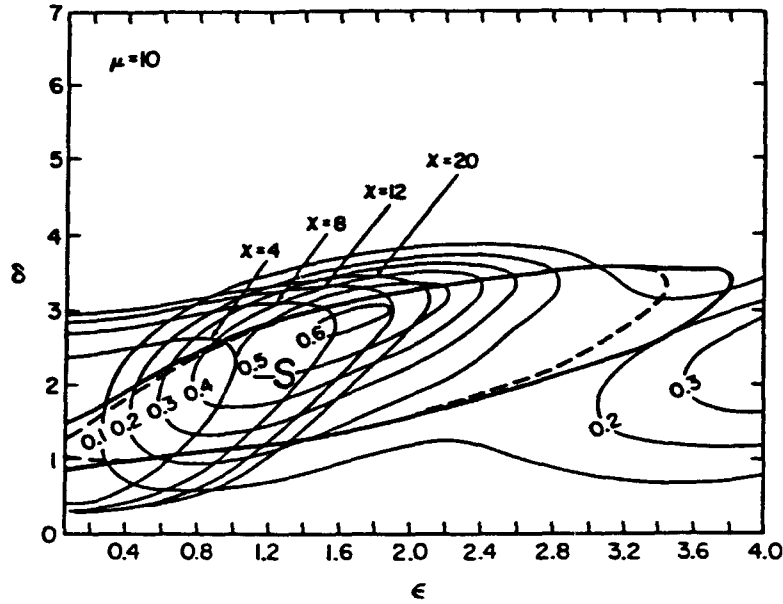


Figure 78: Stability region for a pencil beam with $\mu = 10$.

where d is the mirror separation and w_0 is the radiation waist.

Figure 78 corresponds to a pencil electron beam placed on a field maxima of an even longitudinal mode at the center of the quasioptical resonator with no tilt. The convention is that an *even* mode has a field maximum at the center of the resonator but corresponds to an odd index q for the TEM_{00q} modes. The maximum perpendicular efficiency is 60%, and is obtained for a field amplitude $\epsilon = 1.6$ and a detuning $\delta = 2.8$. The interaction length is rather short for this case, $\mu = 10$, and the current at this point is 9 times the start current. Increasing T_0 from 10 to 50 (dashed region) results in little change to the stable region, which indicates that increased mode density does not necessarily result in increased mode competition effects. For the pencil beam case, the point of maximum efficiency lies inside the region of stable, single-mode operation.

A much different result is obtained for an annular electron beam, as seen in Figure 79. Both the maximum efficiency and single-mode stability region are greatly reduced. The electron beam excites both even and odd longitudinal modes in the output resonator for $kr_b = 4$, where the electron beam radius is denoted as r_b . The maximum

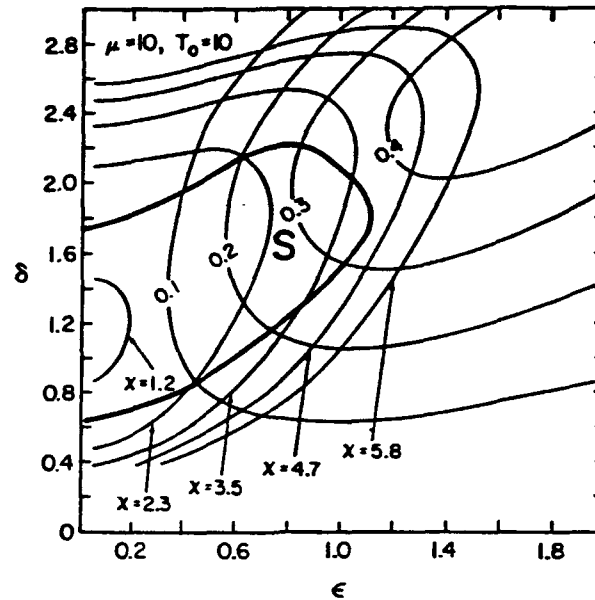


Figure 79: Stability region for an annular beam with $\mu = 10$. Note that the maximum efficiency is greatly reduced from the pencil beam case.

transverse efficiency is now somewhat greater than 30% for a current 3.5 times the starting current. The field amplitude is $\epsilon = 1.0$ at a detuning $\delta = 1.82$, which are both greatly reduced from the pencil beam case. The efficiency of the device is lowered since electrons interact with both peaks and nulls in the standing wave pattern in the output resonator. The stable region is reduced dramatically because some electrons in the annular beam now interact strongly with only the competing odd longitudinal modes.

The stability region for a quasioptical gyrotron with an annular beam is greatly enhanced when the resonator axis is tilted by a small angle θ with respect to the plane perpendicular to the electron beam, as seen in Figure 80. The normalized tilt angle, $\theta' = \theta k w_0 = 1$, is chosen so that all electrons interact reasonably strongly with both even and odd longitudinal modes in the output resonator. The maximum perpendicular efficiency is now greater than 50% and is located inside the stable region with a detuning of $\delta = 3.3$ and a field amplitude of $\epsilon = 2.2$. The detuning for maximum efficiency is larger than the pencil beam case, due in part because the resonance condition $\Delta\omega =$

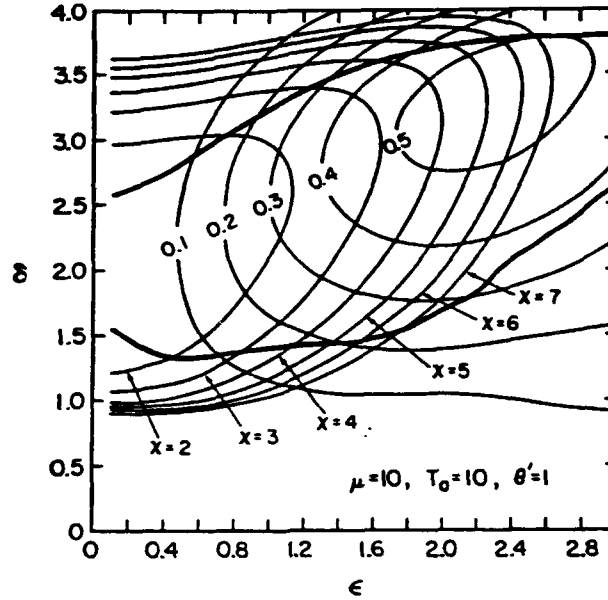


Figure 80: Stability region for an annular beam in a tilted resonator.

$\omega - \Omega/\gamma - k_z v_z$ now contains a finite k_z due to the tilted resonator. Larger electric fields are required for high efficiency since the electron beam is interacting only with one component of the travelling wave in the output resonator. The perpendicular efficiency of a quasioptical gyrotron with an annular beam in a tilted resonator is nearly the same as a pencil beam in an untilted resonator.

Previous work has shown that a shorter interaction length μ results in larger regions of stable, single-mode operation. In the present experiment, the interaction length is relatively long and varies from 14.8 to 20 as the beam α is increased from 1.5 to 1.9. The stability of quasioptical gyrotrons has not been studied computationally for such large values of μ , although insight can be gained from following trends observed in the previous three figures. From the literature[16], consider the case of $\mu = 17$ with a pencil electron beam and an untilted resonator, as shown in Figure 81. The maximum perpendicular efficiency of 60% is obtained for a field amplitude $\epsilon = 2.2$ and a frequency detuning $\delta = 4.1$, which are significantly higher than the $\mu = 10$ results. The beam current for peak efficiency is 21 times the start current. The stable region is limited to $\epsilon = 1.3$ and $\delta = 3.1$, where the best efficiency is now 50%. The stability boundary is

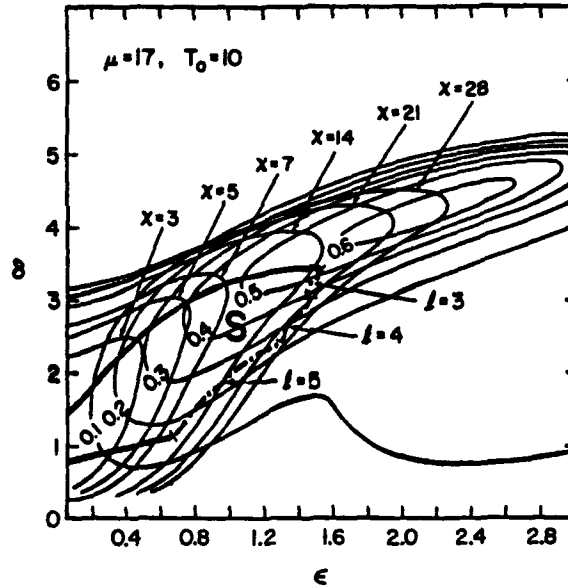


Figure 81: Stability region for a pencil beam with $\mu = 17$.

given by the solid and broken curves in the plot. The solid boundary indicates a phase instability, which manifests itself through mode hopping between the desired mode and a competing mode. The dashed curve denotes the overbunch instability, where multimode behavior is expected beyond the stable region. By using a scaling factor from the $\mu = 10$ plots, the maximum efficiency point for $\mu = 17$ with an annular beam in a tilted resonator will occur for parameters near $\epsilon = 3.0$ and $\delta = 4.8$. However, this maximum efficiency point will not be stable with respect to sideband mode competition. Using a similar scaling factor, we anticipate that the maximum transverse efficiency which lies within the stability boundary will occur for $\epsilon = 2.0$ and $\delta = 4.0$ for a tilted resonator and an annular beam with an interaction length $\mu = 17$.

For the gyrokystron experiment, typical operating parameters are listed in Table 9 for operation near the maximum efficiency point for alpha priming. The peak efficiency is measured as 19.6%, which is revised upwards due to ohmic losses in the resonator mirrors and denoted as the electronic efficiency. A measured pitch angle of the electrons of 1.9 results in a relatively long interaction length, which tends to produce multimode behavior in the calculations. Comparing these experimental parameters to the scaled

Beam Voltage	74.8 kV
Beam Current	5 A
Measured Efficiency	19.6%
Electronic Efficiency	>21.6%
Transverse Efficiency	>29.5%
Magnetic Field	33.42 kG
Frequency	85.43 GHz
Pitch Angle α	1.9
Normalized Interaction Length μ	20.2
Normalized Detuning δ	4.55
Normalized Field ϵ	1.49

Table 9: Experimental parameters for peak efficiency using alpha priming.

results mentioned previously leads to several conclusions. First, the maximum detuning obtained is rather large for single-mode operation. If the transverse efficiency is limited for some reason, it is not likely that the frequency detuning is the cause. Secondly, the normalized field amplitude in the experiment is moderate compared to values needed for maximum efficiency. The field strength can be increased by increasing the beam current or reducing the output coupling of the quasioptical resonator. In the present experiment, the beam current is limited by the start oscillation current of the pre-bunching resonator, so that this parameter is approximately fixed. Lastly, increasing the detuning past the maximum value for a particular mode in the experiment results in mode switching with a lower frequency mode. This behavior is indicative of the phase instability, which is denoted as a solid boundary on the stability plots. Thus, it appears that the operating point in the experiment is located at the top of the stability boundary in the $\epsilon - \delta$ plot, which is to be expected.

B. Alpha Priming Simulations

The stability plots presented in the previous section are derived under the condition that the gyrotron parameters are fixed in time, but say nothing about the accessibility of the states. A time-dependent, multimode simulation code has been developed which is used to model the present experiment[16]. The model includes the tilt of the resonator, the finite rise time of the beam voltage and electron perpendicular velocity, space charge depression of the electrons traversing the open resonator, the realistic magnetic field profile, voltage ripple during the 12 μ sec pulse, the electron beam radius, and displacement of the beam within the resonator. At present, the code does not include the effects of pitch angle spread, guiding center spread, energy spread, or second harmonic radiation in the output resonator. The beam parameters rise linearly in time, which is a good approximation to the measured waveform. The space charge depression of the electrons as they pass through the resonator is given by the prescription in [62]. The space charge depression considers factors such as the gap distance, the electron beam radius, the beam current, the beam voltage, and the pitch angle of the electrons.

Table 10 contains the typical parameters for the multimode simulation runs. The ripple on the flat-top voltage is produced by the pulse forming network in the modulator, which generates 6 periods during the 12 μ sec pulse. Both γ and β_{\perp} are initialized at time $t = 0$ to 25% of their flat-top values. The electron beam radius $r_b = 5.436$ mm is calculated by the electron trajectory code, and will vary somewhat when the magnetic field is tapered.

A typical multimode simulation run is shown in Figure 82 for a beam voltage of 74.8 kV and a current of 4.15 A. The pitch angle is $\alpha = 1.9$, the electron beam radius is 5.0 mm, the beam displacement is 0.0 mm, and the frequency detuning of the $n = 0$ mode is $\delta = 3.3$. This simulation is performed with no alpha priming so that γ and β_{\perp} rise at the same rate and peak at the same point in time. The longitudinal modes in the output resonator are denoted by the relative mode number n , referenced to the $n = 0$ mode at the center of the spectrum, where a larger index corresponds to a higher frequency mode. In the simulation, the $n = -1$ mode rises quickly, but is unable to suppress the

Beam Voltage	60–75 kV
Beam Current	5 A
Magnetic Field	33.42 kG
Voltage Ripple	1.5%
Voltage Ripple Period	2 μ sec
Voltage Rise Time (τ_R , 25–100%)	3.75 μ sec
Rise Time Corner	0.015–0.040
Pitch Angle α	1.3–1.9
Electron Beam Radius	5.0–5.436 mm
Electron Beam Displacement	0.0–0.4 mm
Resonator Drift Gap	5.0 cm
Resonator Tilt Angle	2°
Frequency	85.4–85.6 GHz
Mirror Separation d	21.2 cm
Mirror Radius of Curvature R_c	38.7 cm
Resonator Output Coupling	2.1%

Table 10: Parameters for multimode simulations.

$n = 0$ mode at higher frequency. The state at the end of the simulation appears to be a multimode equilibria where the two modes exist simultaneously. This is in contrast to the experimental observations, where it is nearly impossible to excite two longitudinal modes at the same instant in time. Also note that the simulation predicts that the mode amplitudes vary over a time scale of several microseconds. Mode competition and suppression occur in the experiment on much shorter time scales (typically $< 0.5 \mu\text{sec}$).

A number of simulation runs are performed for the above parameters where only the detuning parameter δ is varied. This is accomplished experimentally by fixing the beam voltage, current, and pitch angle and allowing the magnetic field to vary. Results of the simulations are shown in Figure 83, where transverse efficiency is plotted versus the detuning parameter for the $n = 0$ mode. These code runs are performed for the situation with no priming, so that γ and β_{\perp} rise at the same rate during the rise of the voltage pulse. For $\delta = 2.0$, the $n = 1$ longitudinal mode is excited and the output spectrum is single moded. As the frequency detuning is increased, this mode increases in amplitude up to a maximum transverse efficiency of 37% at a detuning of 2.9. This corresponds to a true detuning $\delta_1 = 3.8$ for the $n = 1$ mode, since it is 1 longitudinal mode above the $n = 0$ reference mode. The longitudinal mode spacing in the output resonator is approximately 0.83% for frequencies near 85 GHz with a mirror separation of 21.2 cm. For detunings above 3.0, the $n = 0, -1$ modes overtake the higher frequency mode and result in a multimode equilibrium.

A trend in the simulations is that multimode states tend to form for values of detuning which are readily obtained in the experiment. One possible explanation for this behavior is that the simulation is not properly averaging over all of the longitudinal modes. The resonator is periodic in the round-trip bounce time $\tau = 2d/c$, where d is the mirror separation and c is the speed of light. Particles are injected during the period $[0, \tau]$ with phases uniformly distributed over $[0, 2\pi]$ and different guiding center positions to model the annular beam. The averaging parameters typically used in the simulations are 15 entrance times, 21 particle phases, and 10 guiding center positions. These values have been increased in the simulations to allow for better averaging, but

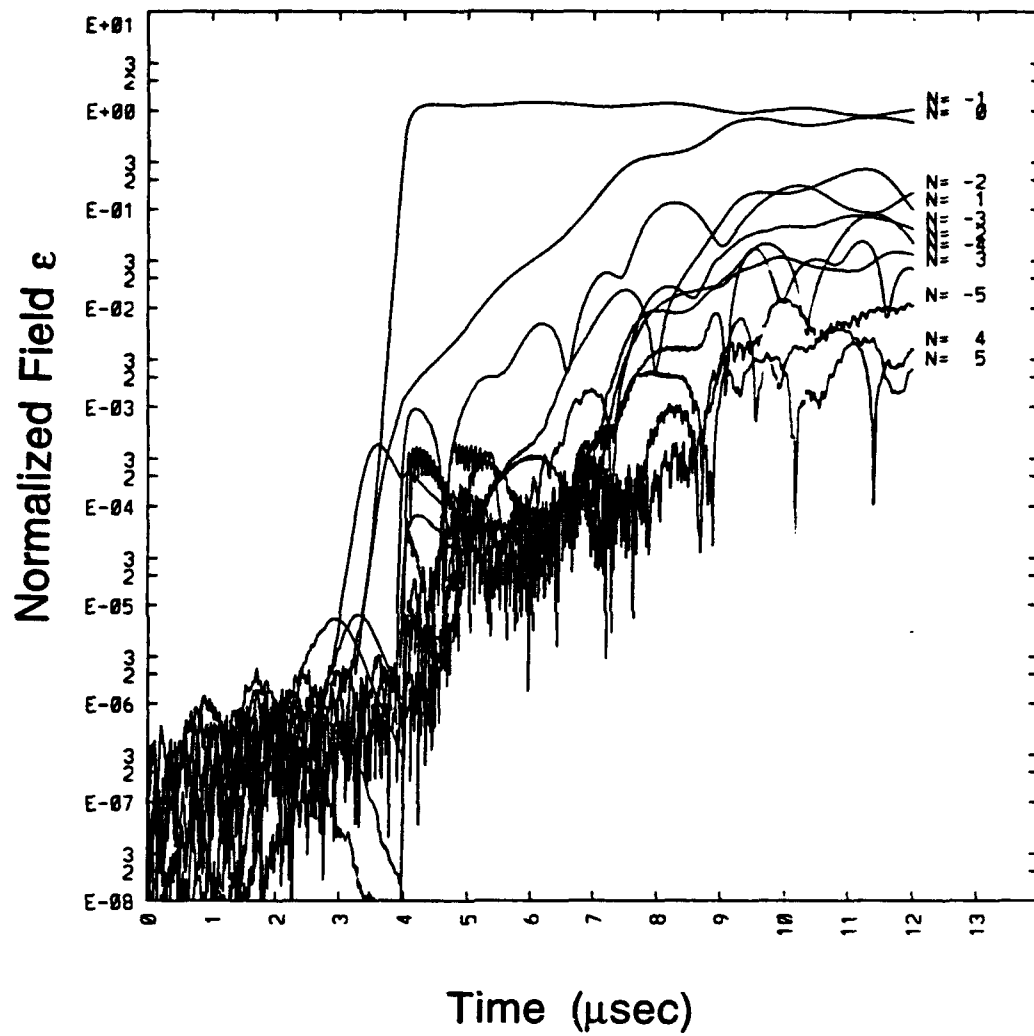


Figure 82: Evolution of modes for $V = 74.8$ kV and $\delta = 3.3$. The current is 4.15 A and the pitch angle is 1.9

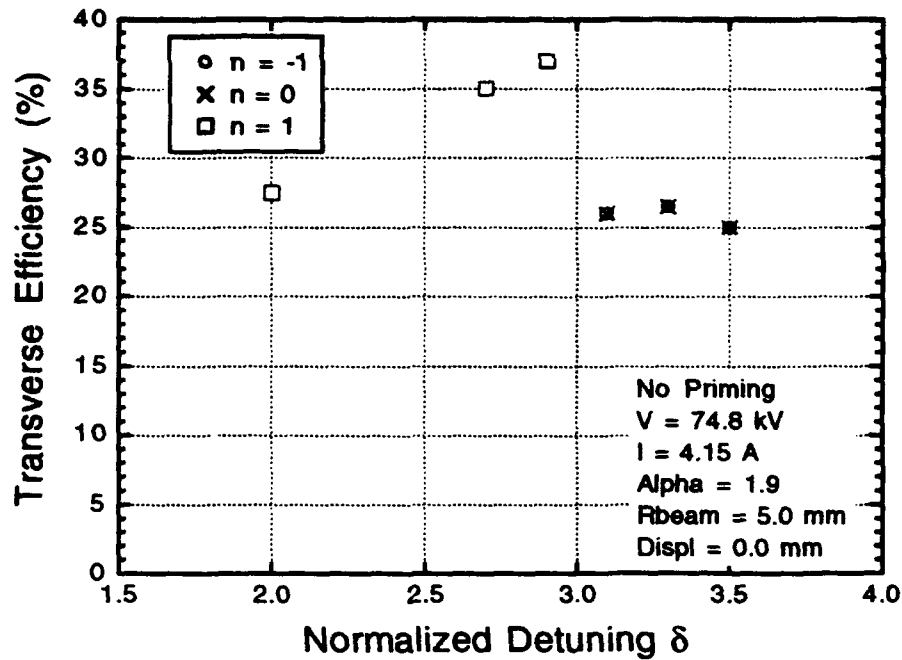


Figure 83: Efficiency versus detuning δ for $V = 74.8$ kV.

no change in the mode spectrum is observed.

Another possible explanation for the multimode nature of the simulations is that a combination of the electron beam radius and the beam displacement results in poor mode suppression of opposite parity modes. If the tilt angle of the resonator is not large enough, the gyrotron will behave as an untilted resonator where the mode suppression is poor and the stability region is quite limited. Moving the beam by $\lambda/2$ should result in no change to the output since this is the spacial periodicity of the resonator. However, beam movement by $\lambda/8$ is sufficient to vary the coupling between the electron beam and the even and odd longitudinal modes. The simulations presented in Figure 83 are repeated for a beam displacement of 0.4 mm and are shown in Figure 84. The $n = 1$ mode is initially excited for $\delta = 2.0$ with transverse efficiency $\eta_{\perp} = 30\%$, which corresponds to a detuning $\delta_1 = 2.9$. Further increases in the detuning parameter cause mode competition to commence with the low-frequency $n = 0$ mode. This mode then dominates the spectrum for higher detunings, which results in single-mode operation up to $\delta = 3.3$ and maximum efficiency $\eta_{\perp} = 32\%$. Beyond this detuning, the $n = 0$ mode encounters competition from the lower-frequency $n = -1$ mode and the efficiency

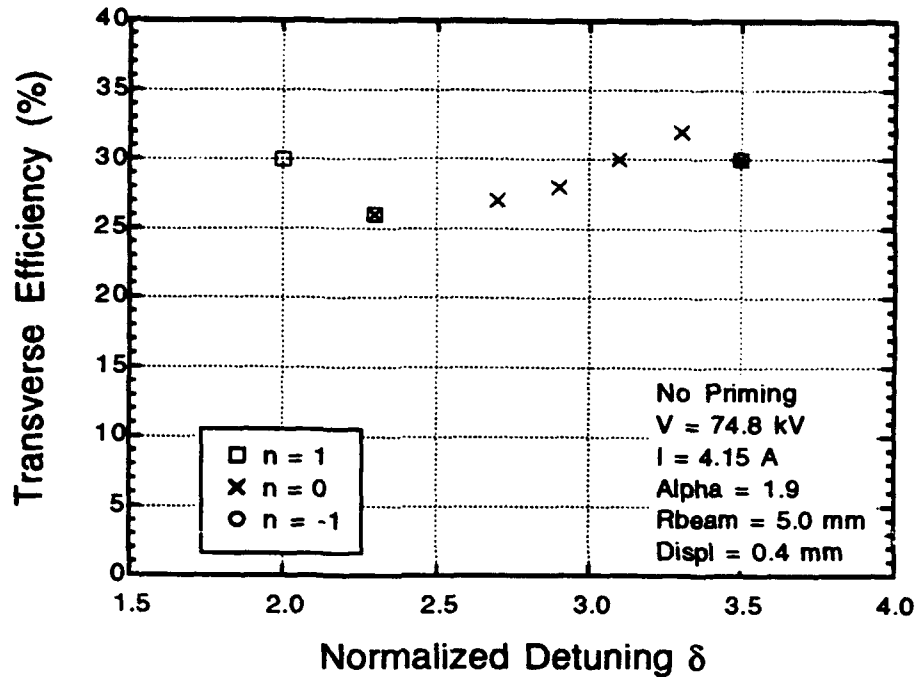


Figure 84: Same as Figure 83 for 0.4 mm beam displacement.

decreases. The 0 mm-displacement simulation results in somewhat higher detuning and efficiency, but the occurrence of multimode states persists for both cases.

Experimental data is typically collected by fixing the magnetic field and varying the cathode voltage to optimize millimeter-wave power and efficiency. This sequence is duplicated in the computational model, with results from measurements and simulations given in Figure 85. The magnetic field is 33.42 kG, the beam current is 5.3 A, the electron beam radius is 5.4 mm, and the beam displacement is 0.4 mm. The values for α are measured in the experiment, and rise linearly from 1.56 at 65 kV beam voltage to 1.9 at 71 kV, with the pitch angle saturating at higher voltages. The experimental efficiencies are corrected for ohmic losses in the output resonator. Alpha priming is simulated by fixing the rise time of β_{\perp} at 3.75 μsec and increasing the voltage rise time to 4.15 μsec , which causes α to rise more quickly than γ .

Experimental efficiencies rise monotonically from 10% to 22% using alpha priming, with the gyrotron operating in a single mode over this entire range of voltages. Typical efficiencies for the gyrotron with no priming are limited to approximately 13% maximum, and mode switching occurs above 67 kV from the 85.5 GHz into a low frequency,

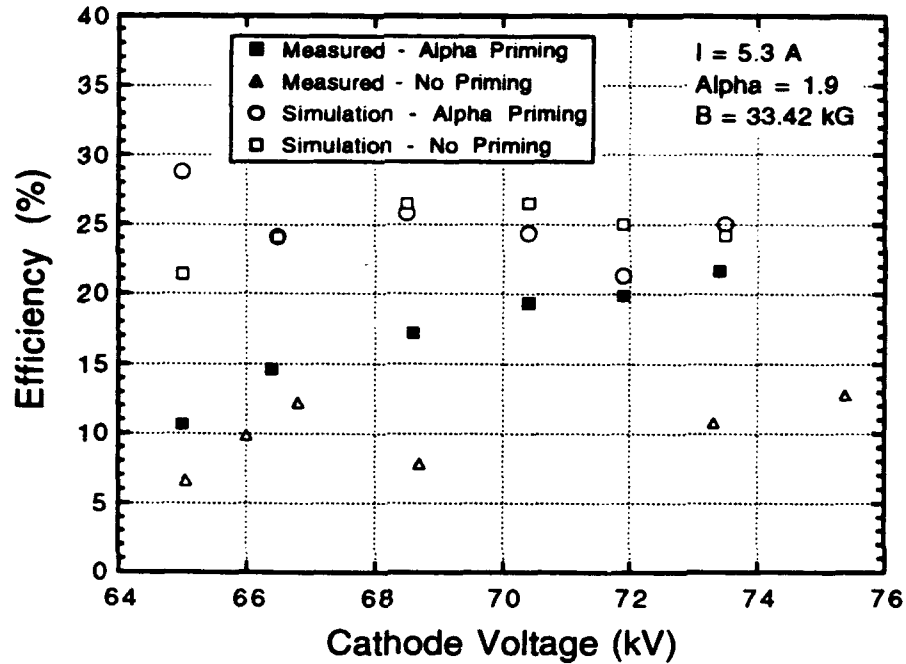


Figure 85: Alpha priming and no priming simulations and measurements. The maximum pitch angle is 1.9 for both sets of data.

low efficiency mode. The simulations predict both single-mode and multimode states as the cathode voltage is increased for these parameters. Most of the simulation runs show no difference between alpha priming and no priming, with the exception being the 65 kV data point. Here the no-priming case yields 21.5% efficiency in the $n = 0$ mode, while alpha priming excites $n = 1$ longitudinal mode with 29% output efficiency. The simulation predicts efficiencies between 20 and 30% for all of the beam voltages considered here, whereas the experiment produces efficiencies as low as 5-10%.

More insight into the gyrotron interaction is gained by considering the interacting modes in the alpha priming simulations and measurements. Efficiency as a function of normalized detuning δ is given in Figure 86 for the data in the previous figure. The measured points correspond to the 85.5 GHz mode operating over the detuning range 2.6-4.45. The output is single-mode, and attempts to further increase the frequency detuning result in mode switching during the second half of the pulse with a low frequency, low efficiency mode. In the simulations, the 65 kV data point translates to a $n = 0$ mode detuning of 2.6, which is a true detuning for this mode of 3.75. If

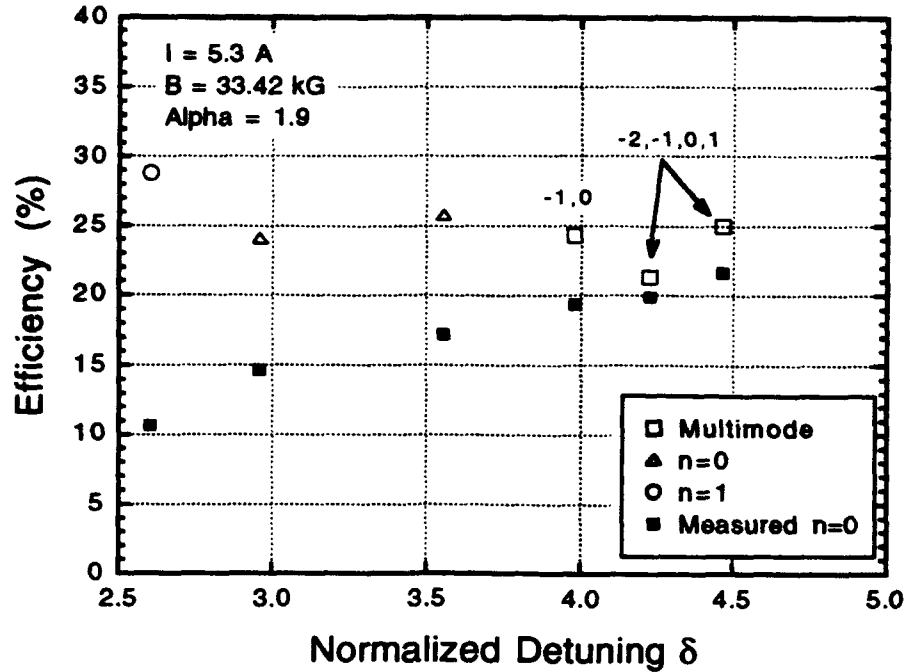


Figure 86: Alpha priming measurements and simulations versus δ .

this mode's detuning is increased past this point, the frequency switches to the next lower longitudinal mode with reduced efficiency. This $n = 0$ mode is supported up to detunings of 3.6, after which the simulations are multimoded with the $n = -2, -1, 0$, and 1 modes oscillating simultaneously. The experiment operates in a single mode over a wide range of detunings, which are typically much larger than the best detunings in the simulations (4.45 versus 3.8).

The normalized interaction length μ varies from 15 to 20 as the cathode voltage is increased from 65 to 73 kV, due mostly to the increase in beam α , which tends to inhibit single-mode operation in the simulations. The values for pitch angle in the simulation are obtained through experimental measurements, so it is unlikely that the interaction length is less than $\mu = 20$ at 73 kV beam voltage. For the purpose of the present discussion, consider reducing the peak α of the simulations from 1.9 to 1.6. The results from these simulations are presented in Figure 87 for the cases of no priming and alpha priming, along with the measured data for alpha priming. The simulation parameters are identical to those in the previous $\alpha = 1.9$ case except for the electron pitch angle.

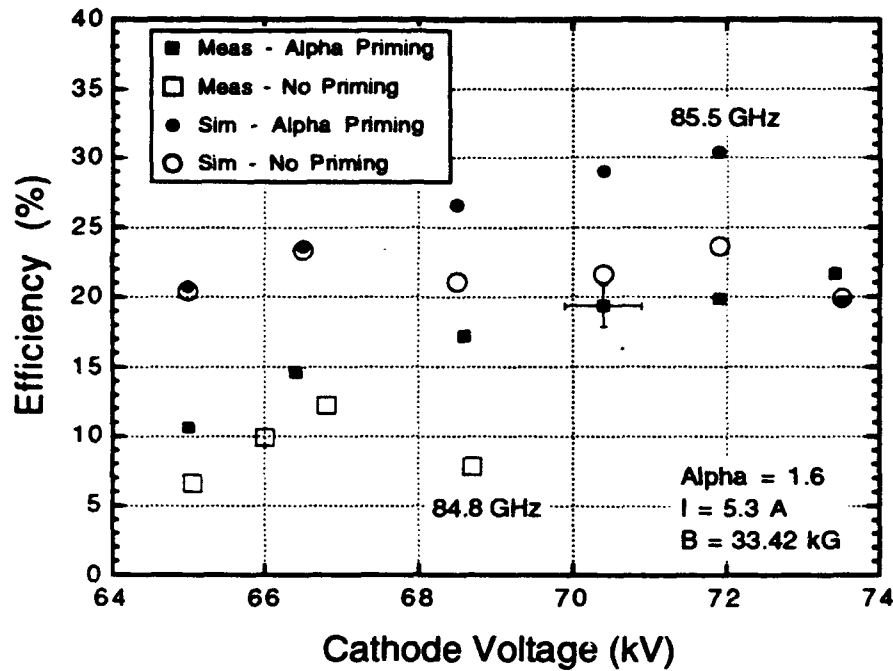


Figure 87: Alpha priming measurements and simulations versus voltage for $\alpha = 1.6$.

Up to a beam voltage of 66.5 kV, the output spectrum of the simulation is now single-moded for both alpha priming and no priming, resulting in 24% efficiency. Further increases in voltage and detuning produce mode switching in the oscillator to the $n = -1$ longitudinal mode for the case with no priming, which reduces the efficiency. The technique of alpha priming causes the $n = 0$ mode to be excited first and suppress the low frequency mode, which is the type of behavior observed in the experiment. This mode is stable up to 71.9 kV beam voltage, which results in 30.5% output efficiency and a corresponding 45% perpendicular efficiency. This efficiency is significantly larger than the maximum efficiency obtained for the free-running oscillator with no priming. Pushing the cathode voltage past 71.9 kV causes a multimode state to form in the simulations, where the $n = -2, -1$ modes oscillate at relatively low efficiency.

The simulations clearly show the benefit of alpha priming: modifying the start-up conditions of the gyrotron so that the desired mode grows to saturation and suppresses competing modes. A plot of efficiency as a function of normalized detuning δ for the $n = 0$ mode is plotted in Figure 88 for the measured efficiencies with $\alpha = 1.9$ and the alpha priming simulations using $\alpha = 1.6$. The simulation shows that the $n = 0$ mode is now

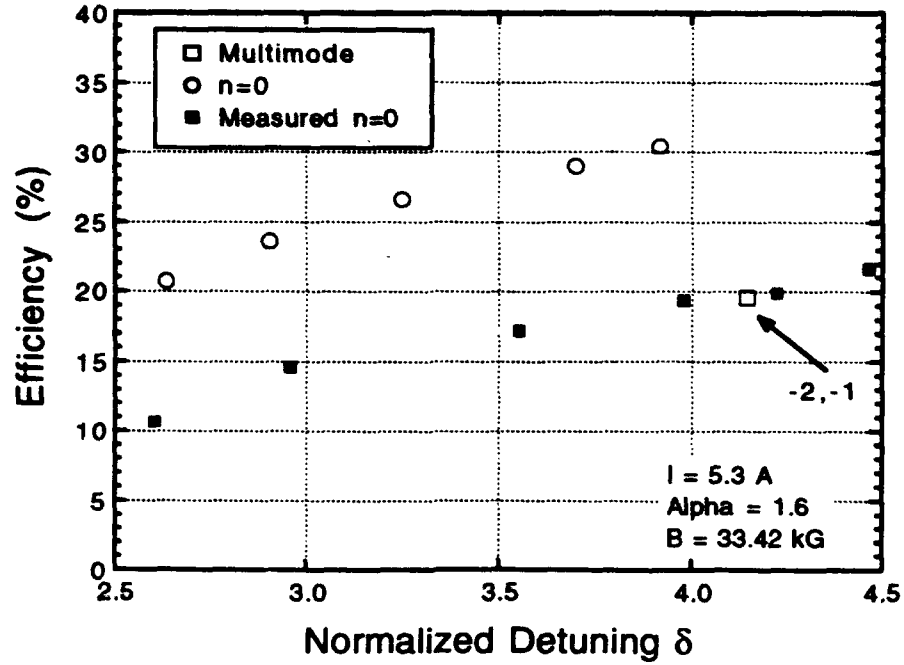


Figure 88: Alpha priming measurements and simulations versus δ for $\alpha = 1.6$.

excited over the detuning range 2.6–3.9, which is a much larger variation than previously obtained. The maximum efficiency of the alpha priming simulation is obtained for a detuning of $\delta = 3.9$, which is still somewhat less than the measured detuning for optimum efficiency. Detunings larger than 3.9 result in multimode behavior in the simulations with the $n = -2, -1$ longitudinal modes overtaking the desired mode.

C. Mode Priming Simulations

In the previous section, simulations and experimental data demonstrated that the technique of alpha priming, where α rises more rapidly than the voltage, allows for gyrotron operation at higher detuning and higher efficiency than operation with no priming. In this section, simulations are performed to model mode priming by pre-bunching the electron beam in an upstream resonator. The slow phase of the particles (θ) at the entrance of the output resonator is no longer uniformly distributed over $[0, 2\pi]$. The slow phase now takes the form

$$\theta = \theta_0 + q \cos \theta_0, \quad (81)$$

where q is the bunching parameter defined in Eq. (12) and θ_0 is evenly distributed over $[0, 2\pi]$. To model prebunching the beam using the EIO in the present experiment, the electron beam is prebunched with a fixed q for a duration of 2 μsec immediately preceding the leading edge of the voltage flat top. Thus, the beam is prebunched during the rise of the pulse so that only the start-up conditions are modified.

The difference between free-running and mode-primed oscillator performance can be seen by comparing the multimode simulations in Figures 89 and 90. The simulation parameters are the same as those given in the preceding section: 70.4 kV beam voltage, 5.3 A beam current, $\alpha = 1.6$, electron beam radius 5.4 mm, and beam displacement 0.4 mm. The gyrotron with no priming is shown in Figure 89, where the $n = -1$ longitudinal mode is excited with 32% transverse efficiency and 21.6% output efficiency. The 2 μsec mode priming simulation is shown in Figure 90 for a prebunching parameter $q = 2$. Now the $n = 0$ mode is excited at time $t = 1.75 \mu\text{sec}$ and then suppresses all competing modes. The transverse and output efficiencies are increased for the mode priming case to 42.5 and 28.7%, respectfully, with a detuning $\delta = 3.77$. Note that the competing mode amplitudes are significantly reduced from the simulation result with no priming. All mode amplitudes are constant with respect to time so that we do not anticipate any mode switching for longer pulse lengths in the simulations.

A series of simulations is performed to study mode priming by beam prebunching for the parameters listed above while the beam voltage is varied, with the results shown

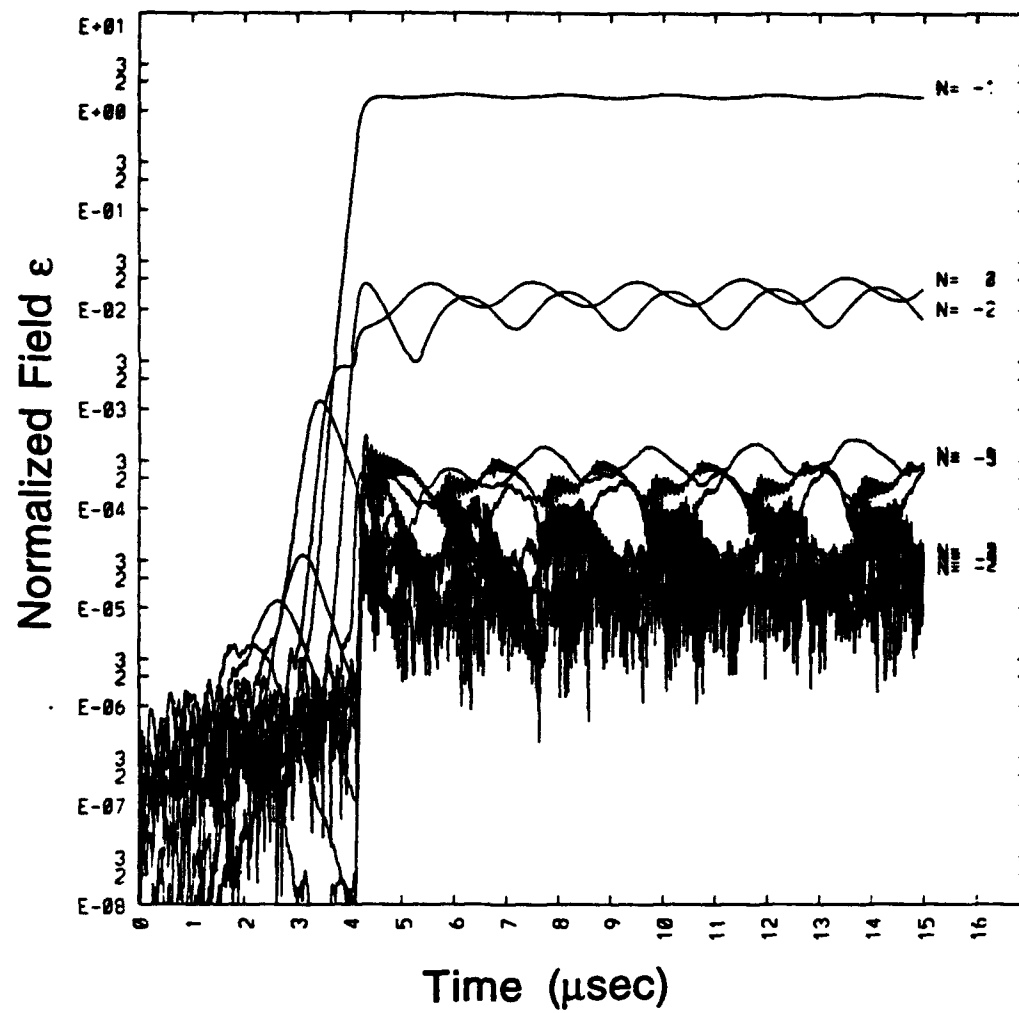


Figure 89: Simulation with no priming for $V = 70.4$ kV and $\alpha = 1.6$.

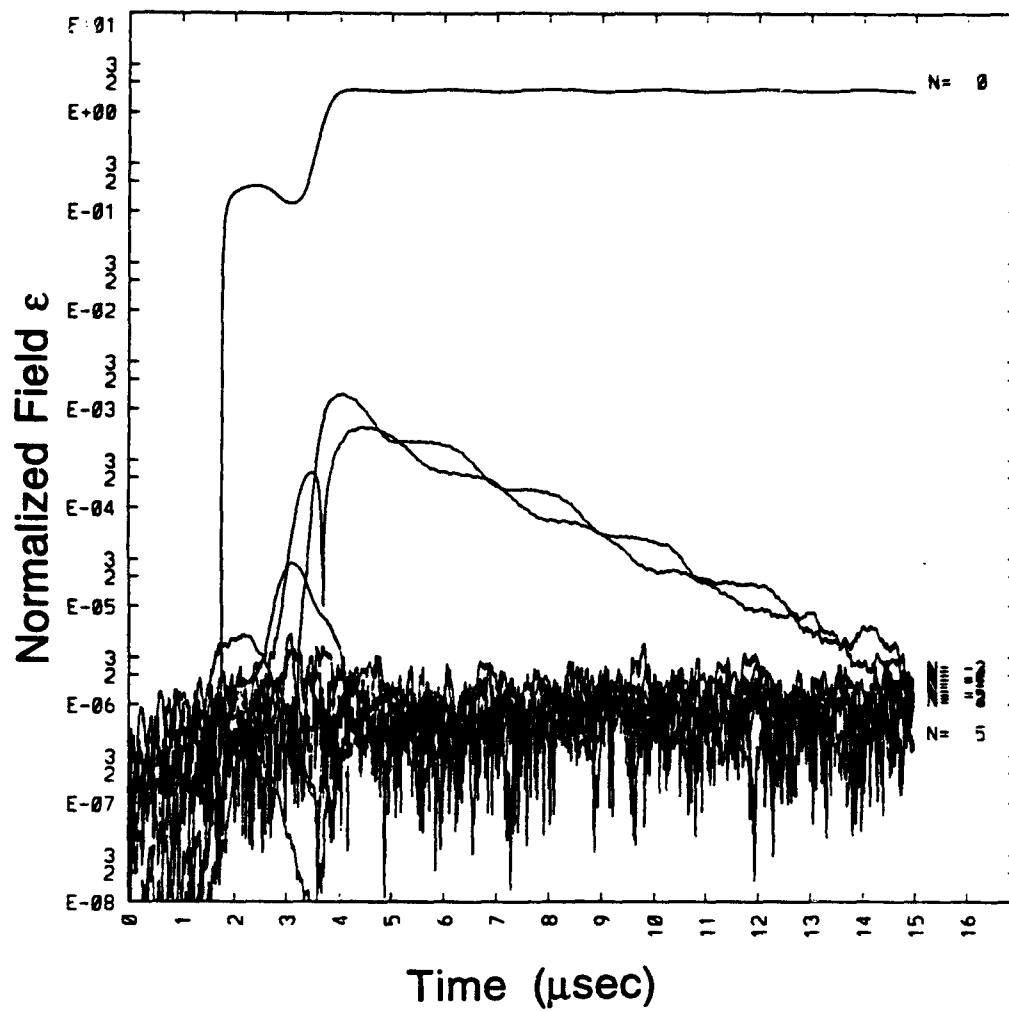


Figure 90: Mode priming simulation for $V = 70.4$ kV and $\alpha = 1.6$.

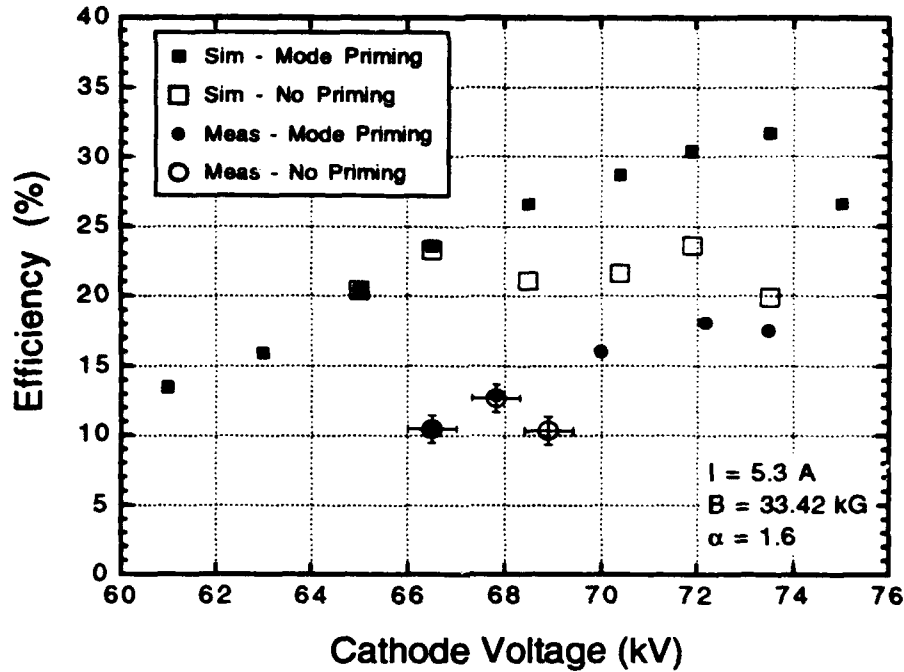


Figure 91: Simulations and measured efficiency versus voltage for mode priming. The simulations use a reduced pitch angle compared to the measurements.

in Figure 91 with some measured data. Applying electron beam prebunching of $q = 2$ for $2 \mu\text{sec}$ starting at time $t = 1.75 \mu\text{sec}$ in the mode priming simulations excites the $n = 0$ mode up to 73.5 kV and 31.7% efficiency. This efficiency is significantly higher than the best efficiency without priming. Also plotted in the figure are measured results for a beam current of 6.5 A , a voltage divider setting of 82.5% , measured $\alpha = 1.9$ at the higher voltages, and a frequency of 85.539 GHz . At a beam voltage of 69 kV , the free-running oscillator switches to the 84.810 GHz mode at low efficiency. Application of the EIO signal in the prebunching resonator allows for operation up to 18% efficiency for this case. The experimental efficiencies in this plot have been increased to account for ohmic losses in the output resonator. For cathode voltages above 73 kV , the efficiency begins to drop due to mode competition during the pulse from low-frequency modes. Here we observe good qualitative and quantitative agreement between theory and experiment for both the mode switching points and the maximum detuning. However, the simulations are using the reduced value of pitch angle $\alpha = 1.6$ while the measured pitch ratio is 1.9 .

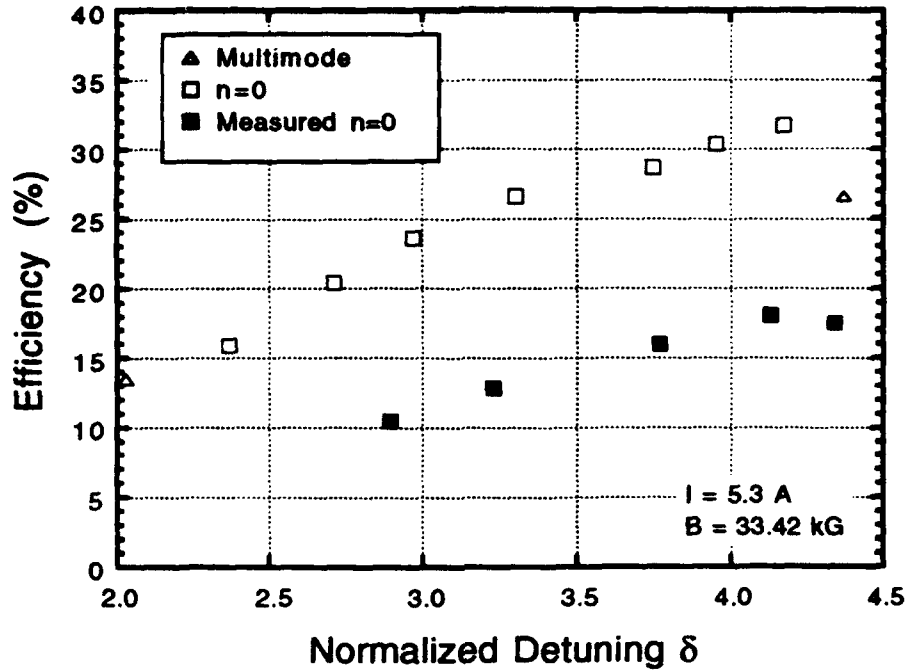


Figure 92: Efficiency versus δ for gyrokystron mode priming.

Efficiency versus normalized detuning is plotted in Figure 92 for mode-primed operation of the gyrokystron using the data from the previous figure. The open points are simulation results with a maximum pitch angle of 1.6, while the solid points are measured data for $\alpha = 1.9$. The $n = 0$ mode is primed in the simulation over a range of detuning from $\delta = 2.4$ to 4.2. The efficiency of this mode rises from 16% to 32% with the gyrokystron operating in a single mode. For detunings below $\delta = 2.4$, the simulation predicts mode competition from a high frequency mode, and low frequency modes limit the maximum detuning to 4.2. The maximum efficiency observed in the experiment for this 6.5 A data is 18%, which is considerably lower than the simulations.

In the simulations, the bunching parameter q is modelled as a constant in time for the 2 μ sec electron beam prebunching. However, the bunching parameter in the experiment is a function of time since both the beam α and the voltage are rising during this period for mode priming. A bunching parameter of $q = 2$ is rather large for gyrokystrons, so a set of simulations are performed for decreased prebunching. The results are shown in Figure 93, which plots the theoretical output efficiency as a function

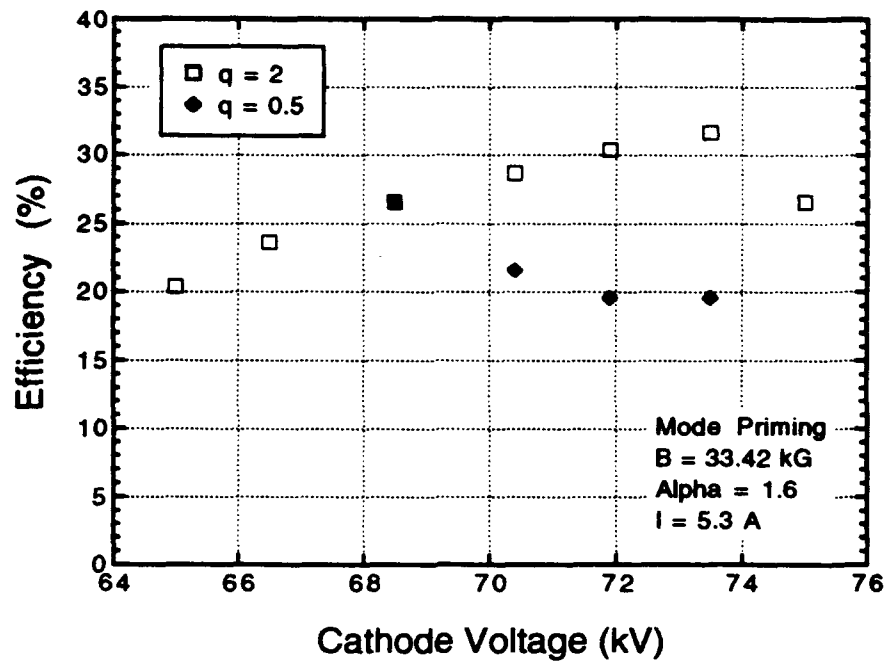


Figure 93: Efficiency versus cathode voltage for different bunching parameters.

of cathode voltage for two values of q . The beam current is 5.3 A, the maximum pitch angle is 1.6, the electron beam radius is 5.4 mm, and the beam displacement in the resonator is 0.4 mm. The larger bunching parameter results in a peak efficiency of 32% at a beam voltage of 73.5 kV. For $q = 0.5$, the $n = 0$ mode is only supported up to 68.5 kV beam voltage with a peak efficiency of 27% and a frequency detuning $\delta = 3.3$. The decreased bunching parameter is not able to prime the desired mode strongly enough to suppress the competing longitudinal modes at higher detunings. However, the bunching is strong enough to change the nonlinear mode competition during the rise of the voltage so that a different multimode equilibrium is obtained in the simulations. These results demonstrate that the maximum efficiency and detuning obtained using mode priming may be limited by the strength of the bunching parameter.

The simulation data point at a beam voltage of 75 kV in Figure 91 is an interesting example of the limit to mode priming by prebunching the electron beam. The 2 μsec prebunching signal excites the $n = 0$ longitudinal mode initially. After approximately 11 μsec , the $n = -2$ mode overtakes the desired mode and suppresses it. A plot of perpendicular efficiency as a function of time is given in Figure 94, which shows the

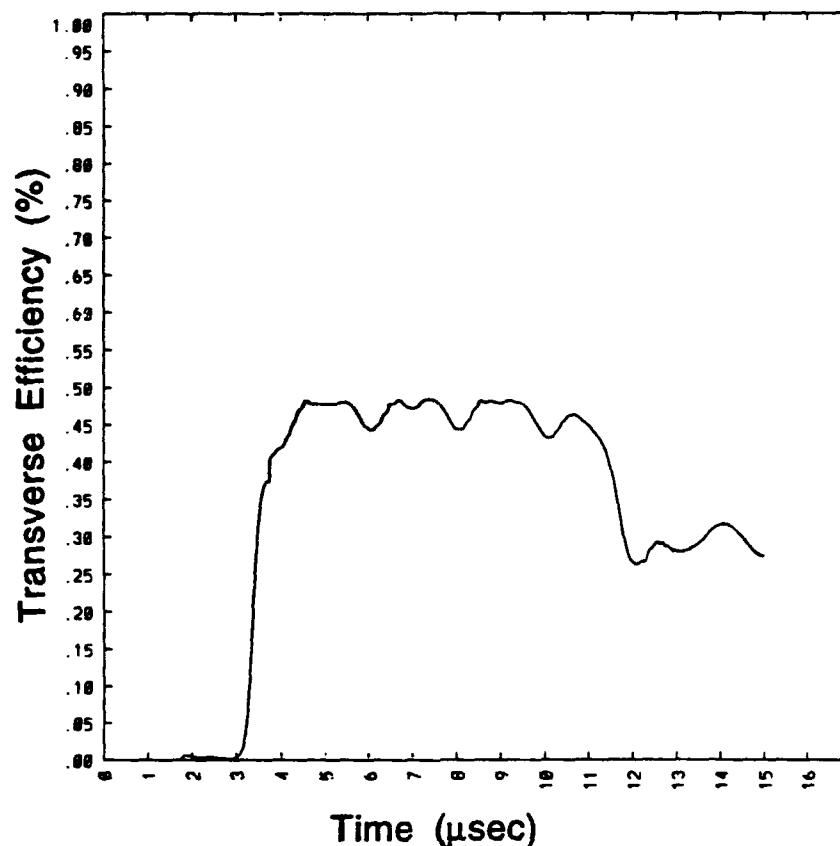


Figure 94: Efficiency versus time for gyrokystron mode priming at 75 kV.

efficiency dropping from 47% to 30% due to mode switching. This type of behavior is exactly what is observed in the experiment: mode competition from a low frequency mode during the second half of the pulse. It is also interesting to note the irregular signature on the flat top of the efficiency plot for the high frequency mode. The irregular ripples begin at a beam voltage of 68.5 kV, and correspond to operation in the hard excitation regime of the gyrokystron. Here, the current of the device is less than the starting current for the $n = 0$ mode and mode priming is required to allow access into this region of parameter space. The signature on the efficiency plot is often observed in measured data on oscilloscope traces at large voltages and high detuning values.

The simulation results presented up to this point are for currents on the order of 5 A. It is instructive to examine the behavior of the gyrokystron at currents closer to the threshold for oscillation. Figure 95 plots measured and simulation efficiencies as a function of cathode voltage for a beam current of 2.5 A. Measured data is taken from

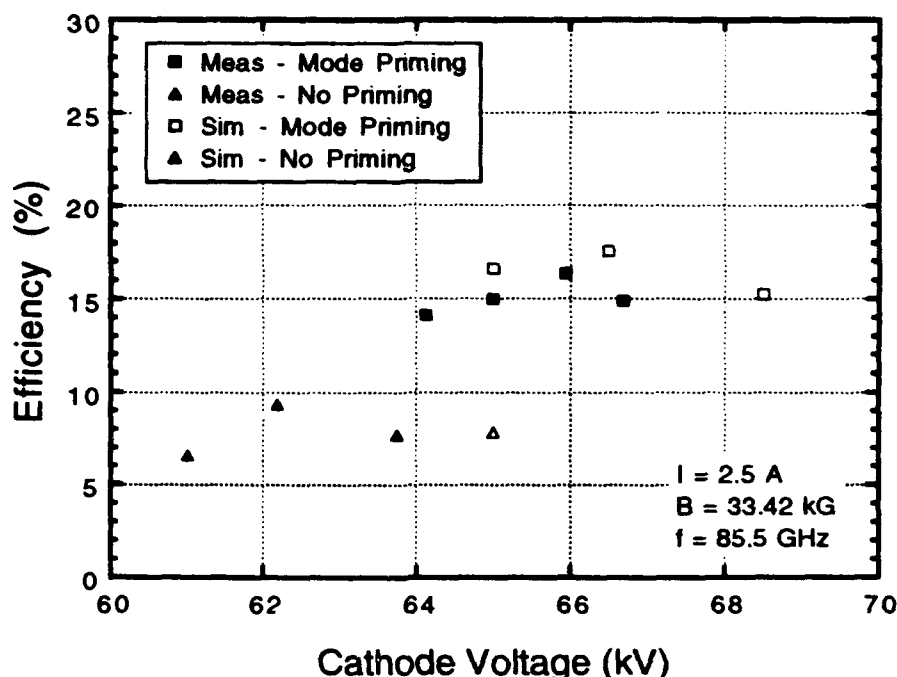


Figure 95: Efficiency versus beam voltage for gyrokystron mode priming at 2.5 A.

Figure 49 and scaled by $\times 1.102$ to account for ohmic losses in the resonator mirrors. The experimental value of the magnetic field is 33.42 kG with no taper, the voltage divider setting is 80.5%, the measured frequency is 85.55 GHz, and the measured α increases linearly with cathode voltage to 1.9 at 69 kV. The simulations are performed for the same parameters as the preceding cases, where the pitch angle rises linearly to 1.6 at 70.4 kV. Good agreement between the simulation and experiment is obtained for both the output efficiency and the maximum voltage for the $n = 0$ mode. Beam voltages greater than 66.5 kV result in mode switching to the low frequency $n = -1$ mode in the simulation. The simulation data point with no priming at a cathode voltage of 65 kV is of interest due to the low efficiency of 7%. Here the output resonator is operating at a beam current of only twice the starting current ($\psi = 2$). For a beam voltage of 66.5 kV and 2.5 A beam current, the $n = 0$ longitudinal mode is just entering the hard excitation regime. The peaks of the voltage ripples result in $\psi < 1$, although the gyrokystron is not able to go to higher voltages due to the low current.

In the output resonator of the gyrokystron, the absence of conducting boundaries causes space charge depression of the electron beam. The detuning between the gy-

rotron frequency and the relativistic cyclotron frequency decreases with space charge depression, which is due to the reduced γ . We can remove the space charge depression factor from the simulation and determine if this limits the maximum detuning for stable, single mode operation. A good point for comparison is the mode priming simulation for a cathode voltage of 73.5 kV, 5.3 A beam current, $\alpha = 1.6$, and a pre-bunched beam with $q = 2$ for 2 μsec . This point represents the largest cathode voltage (detuning) for stable operation in the desired $n = 0$ mode. With the space charge factor, the $n = 0$ mode is excited with a perpendicular efficiency of 47%. Removing the space charge factor increases the detuning for this mode, so that it is no longer able to suppress the $n = -2$ mode at lower efficiency. Thus, space charge depression of the beam as it traverses the open resonator is an important factor in determining the maximum detuning and operating mode of the gyrokystron in the simulations.

A number of simulation runs are performed to test the sensitivity of mode selection with the exact time the beam is prebunched during the rise of the voltage pulse. Up to this point, all of the simulations have used a 2 μsec prebunching duration located immediately before the flat-top of the pulse. The experimental conditions are listed on page 99: 69.5 kV cathode voltage, 5.15 A current, 33.42 kG magnetic field, and a measured pitch angle of 1.8. The simulation parameters are the nearly the same with $\alpha = 1.6$, a beam displacement of 0.4 mm, and a bunching parameter of 1.5. The general mode priming trends observed in the experiment are also seen in the simulations. If the prebunching occurs too early ($t = 1 \mu\text{sec}$) or too late ($t = 3.75 \mu\text{sec}$), the priming fails and the $n = -1$ mode is preferentially excited. When the duration of the prebunching is shortened in the simulation, the desired mode is still excited, which agrees with the experimental observations. Bunching durations of 20 nsec continue to provide mode selection in the simulations. A difference between the experiment and simulations is that mode priming only works over a narrow range of times when the duration of the EIO is ~ 100 nsec in the experiment. Mode priming the gyrokystron to run in the $n = 0$ mode in the simulation continues to work for 100 nsec bunching times even when the pulse is translated in time by $\pm 0.5 \mu\text{sec}$.

A better understanding of the time dependence of mode priming is obtained by

considering the variation of $\psi = I/I_{st}$ during the voltage pulse, as seen in Figure 96. During the flat-top of the pulse, the $n = -2$ mode has the lowest starting current and the highest value of ψ . However, this mode is undesirable because it has a relatively low efficiency. A sequence of 8 different longitudinal modes is excited during the rise of the voltage pulse. However, the voltage is changing so rapidly that only the $n = -1$ mode can grow to saturation in the absence of priming. The $n = 0$ mode, which peaks 2 modes before the flat top, can be primed by placing a short-duration prebunching pulse near the time $t = 3.25 \mu\text{sec}$. The $n = 0$ mode is in the hard excitation regime where $\psi < 1$, so that this mode would not be excited under normal operating conditions. In the present set of simulations, the bunching parameter $q = 1.5$, which is a fairly large value during the rise of the voltage. This large bunching parameter may explain why the simulation is not very sensitive to the exact position of the prebunching. In the experiment, the voltage and pitch angle are changing, which cause q vary in time. A third possibility for the difference is that the exact rise of the beam parameters may be somewhat different from the simulations, which would change the window of opportunity for mode priming.

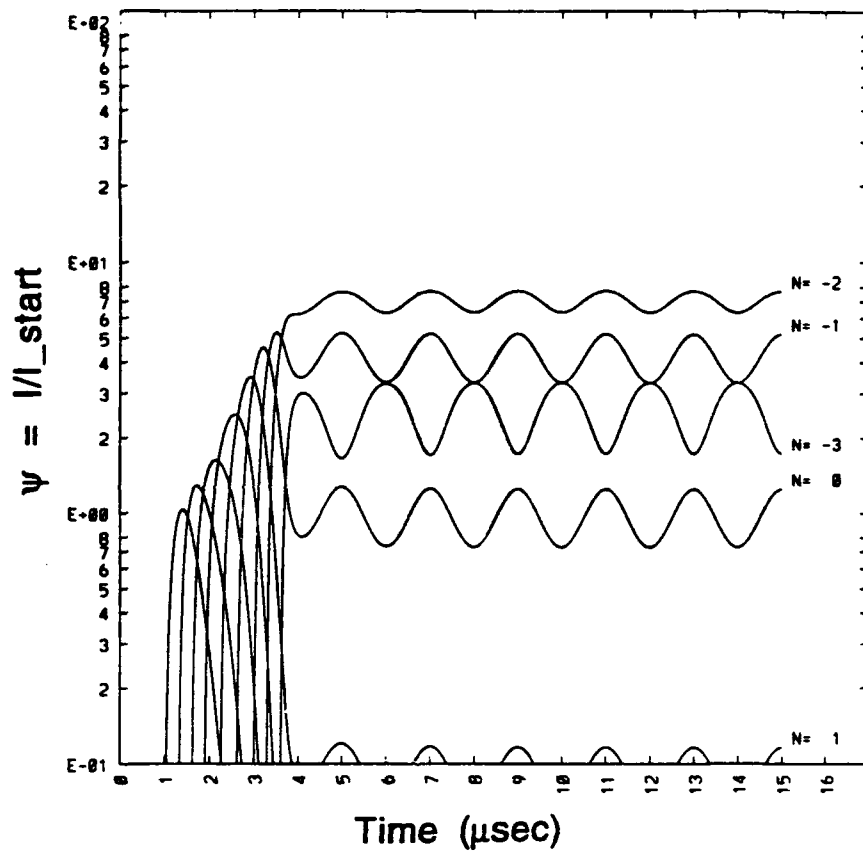


Figure 96: ψ as a function of time for $V = 69.5$ kV.

D. Discussion

A number of general similarities are observed between the time-dependent simulations and the experimental measurements. For a pitch angle of $\alpha = 1.6$, the simulation is usually single-moded with a corresponding $\mu = 15.5$. The operating mode in the gyrotron increases in amplitude with increasing frequency detuning δ up to some maximum value. Higher detunings and efficiencies are obtained by using the techniques of mode priming and alpha priming. Modifying the start-up conditions allows access to the hard excitation region of the gyrokystron parameter space, which tends to be inaccessible during normal operation with no priming. Both the simulations and measurements show an irregular ripple signature on the output power traces in this regime.

There are also several important differences between the theoretical model and the experiment. Peak theoretical efficiencies of 31.7% are obtained, whereas the maximum measured electronic efficiency is 22%. In the experiment, the measured pitch angle of 1.9 results in single-mode operation over a wide range of detunings. However, the simulation is usually multimoded for such large values of α and corresponding interaction length μ . For the free-running oscillator with no priming, mode hopping occurs when the detuning is too large for a particular mode in the experiment. Mode competition is still observed at this point in the simulations for relatively low values of α . Lastly, mode suppression in the experiment occurs on a relatively short time scale of $< 0.5 \mu\text{sec}$, whereas the simulation can vary over several microseconds. The cavity decay time of the quasioptical resonator is

$$\tau_d = \frac{2Q}{\omega}, \quad (82)$$

which results in $\tau_d = 135 \text{ nsec}$ in the present experiment for the fundamental cyclotron frequency. Second harmonic radiation will be characterized by a somewhat faster time constant due to the increased frequency. Presence of the second harmonic may contribute to the mode stability and fast mode suppression observed in this work.

Perhaps the most striking feature of the present experiment is that the output is single moded even though the interaction length is relatively long. This is in contrast to all other QOG experiments with large mirror separation, which were multimoded

at the highest power and efficiency. The main reason would appear to be the use of the tilted resonator, which increases the region of single-mode operation as well as the efficiency for an annular electron beam. This fact is supported by the large frequency detunings obtained in the present work, which are significantly higher than previous experiments. However, there was another experiment at NRL which used a tilted resonator where the parameter space for single-mode operation was nearly unchanged compared to that for an untilted resonator[17]. There are several differences between the two experiments which may explain this discrepancy. First, the mirrors in the original experiment may have been misaligned due to the contact between the mirror holders and the crossbore of the magnet. Some multimode behavior is observed in the present experiment when the output resonator mirrors are misaligned by as little as a fraction of 1° . Secondly, frequency diagnostics were unavailable for much of the initial experiment. Rather subtle variations in the operating parameters of the gyrotron can cause relatively large changes in the output, and the frequency diagnostic is perhaps the most sensitive indication of these changes. A much lower voltage divider setting was typically used in the previous experiment. This can result in somewhat higher α , but also increases velocity spread of the beam and the incidence of reflecting electrons. The noise associated with this reflexing disrupts the operation of the tube, and has been shown to increase the likelihood of multimode states in the current work. The present experiment is operated at more moderate voltage divider settings, which results in very stable operation.

A fourth difference between the two experiments is the operating frequency: 110 versus 85 GHz. One may argue that the higher frequency in the first experiment could result in multimode operation due to the increased mode density for a given mirror separation. This hypothesis is tested in the present experiment by increasing the magnetic field to 43 kG with no prebunching of the electron beam. Output frequencies of 111 GHz are measured, which are equally spaced with $\Delta f = c/2d$. However, the general behavior of the gyrotron is unchanged from the characteristic operation at 85 GHz. A single longitudinal mode is excited and increases in amplitude and efficiency as the cathode voltage is increased. When this mode is pushed past its maximum

detuning, the gyrotron switches to a low frequency mode at lower efficiency. Thus, it is unlikely that the higher frequency of the previous experiment increases the probability of multimode operation.

Another point of discussion is the comparison between measured efficiencies and those calculated by the time-dependent simulations. For a current of 2.5 A, which is relatively close to the threshold current of the output resonator, both efficiencies are on the order of 16%. Increasing the beam current to 5 A results in peak measured electronic efficiencies of 22%, which are approximately $\frac{1}{3}$ lower than the theoretical predictions using a slightly reduced pitch angle. The peak electric field in the output resonator is somewhat less than optimum in this experiment, so that higher efficiencies should be possible with higher currents in the absence of the prebunching resonator. However, it is unknown whether this will decrease the difference between theory and experimental efficiencies.

One possible explanation for reduced experimental efficiency is the presence of second harmonic radiation in the output resonator, which falls into the general category of energy spread on the electron beam. In the present experiment, output radiation at a frequency of approximately 170 GHz is occasionally observed using the heterodyne frequency diagnostic. Previous quasioptical gyrotron studies at Lausanne have shown that 20% of the output power is emitted at the second harmonic for their configuration, although the levels of second harmonic observed in the gyrokystron experiment are always relatively small. However, the quality factor Q for the second harmonic can be much higher than the fundamental, since the radiation spot size at the mirror decreases with frequency. For example, the TEM_{00} mode at 170 GHz experiences round-trip diffraction losses which are much less than 1%, so that this mode would be difficult to observe in the experiment. This introduces the possibility that higher-order transverse modes can oscillate at the second harmonic. These modes have relatively long interaction lengths and round-trip losses on the order of 1%. Such modes can have nulls in their field patterns at the center of the resonator, with stronger fields near the edge of the mirrors. This type of spacial competition would be similar to sideband mode competition recently observed in cavity gyrotrons[8]. When different

cavity modes satisfy the resonance condition $\omega \pm k_z v_z - \Omega_e/\gamma = 0$, mode competition may occur. In particular, mode competition can be severe if the electric field maxima for the two modes occur at different axial positions. Most research on this subject has concluded that the fundamental is dominant and suppresses the second harmonic so that it has little effect on the operation of the gyrotron.

Another possibility is that the small mirror misalignment (0.2°) of the output resonator mirrors in the present experiment contributes to the reduced efficiency. One of the mirror holders is tilted, but the electric field of the resonant mode remains parallel to the mirror surface. Measurements indicate that this type of misalignment has relatively little effect on the gyrotron efficiency and the stability of single-mode operation. However, it is straightforward to test this experimentally by reducing the diameter of the mirror holders so they no longer contact the crossbore when the magnet is cooled. Lastly, the simulation code does not account for velocity spread of the electrons, energy spread, or second harmonic radiation in the output resonator. Inclusion of these effects, although costly in terms of CPU time, may provide additional insight to nonideal features encountered in the experiment.

Chapter VII

Conclusion

A new type of millimeter-wave tube, a quasioptical gyroklystron, has been designed and tested over a wide range of operating parameters. The device is unique in that the drift region between the input and output resonators is long ($L = 30\lambda$) compared to conventional tubes. This long drift region is made possible by a judicious choice of magnetic fields in the two resonators, which minimizes the effect of velocity spread of the beam. The benefit of this approach is that the bunching parameter can be quite large ($q \geq 2$), which is attractive for mode priming, phase locking, and amplifier operation.

The experiment has examined a number of new operating regimes for high power, high frequency oscillators. Mode priming by prebunching the electron beam has been demonstrated, resulting in measured efficiencies of 17%. Here the gyroklystron operates in a more highly detuned longitudinal mode due to the prebunched current at 85.55 GHz, which allows for higher efficiencies than the free-running oscillator. A new technique has been reported, alpha priming, where the pitch angle α peaks just before the flat-top of the voltage pulse. This excites a mode which is highly detuned by the time the voltage flat-top is reached, which results in even higher efficiencies. A peak measured efficiency of 19.6% is obtained for 5 A current and 74.8 kV beam voltage, which corresponds to 73 kW output power. The maximum power measured from the gyroklystron is 150 kW, where both the peak efficiency and power are limited in the present experiment due to oscillations in the prebunching resonator.

The gyroklystron has been phase locked to the EIO drive source over the entire linewidth of the output resonator by prebunching the beam. Typical operating parameters are 60 kW output power, 16% measured efficiency, and a normalized frequency detuning $\delta = 0.41$. The input power required to lock the gyroklystron is approximately 22 dB below that required for direct injection, which demonstrates the benefit of phase locking by prebunching the beam. The best phase locking is obtained for large pitch angles, which is also where the efficiency of the gyrotron is optimized. The gyroklystron has also been operated as an amplifier by lowering the average pitch angle of the elec-

trons so that the output resonator is below threshold for oscillations. Typical operating characteristics of the amplifier are 18 dB gain, 10% efficiency, 30 kW output power, and a bandwidth equal to the linewidth of the output resonator. These results are particularly impressive since no attempt was made to reduce velocity spread in the present experiment, which is estimated as $\pm 10\text{--}20\%$ from electron trajectory simulations.

Measurements indicate that the output of the gyrokystron is single-moded even though the longitudinal mode density is high ($\Delta f/f = 0.8\%$). Tilting the output resonator by 2° relative to the plane perpendicular to the direction of electron beam propagation is shown to increase both the efficiency and region of stable, single mode operation in the experiment. This is the first QOG experiment with large mirror separation which has operated in a single mode at high power and high efficiency. Longitudinal mode selection is accomplished by prebunching the electron beam and by varying the electron beam parameters during the rise of the voltage pulse.

Depressed collector studies have been performed, which increase the overall efficiency of the gyrokystron to greater than 30% with measured collector efficiencies of 50%. This is easily accomplished in the present experiment due to the natural separation of the output radiation and the electron beam in the QOG geometry. No attempt was made to optimize the design of the collector in this work, so that higher collector and overall efficiencies should be possible with little difficulty.

A pair of capacitive probes in the drift tube were used to measure the average pitch angle of the beam electrons. The measured values are in relatively good qualitative and quantitative agreement with electron trajectory simulations, although the experimental pitch angles are somewhat greater than the simulations. The measured values for α saturate at large values of electric field at the cathode, which is in agreement with the fact that the millimeter-wave power saturates over these settings of mod anode voltage. The probes are quite valuable for other general purposes, such as detecting oscillations in the prebuncher and observing the onset of reflecting electrons. Improvements to the simulation code, such as a finer mesh and the axial self-magnetic fields of the beam, may have an effect on the computational values of α .

A number of simulations have been performed to model the experiment using a

multimode, time dependent computer code. The effects of alpha priming and mode priming by prebunching the electron beam are clearly seen in the simulations. These techniques are shown to allow access to the hard excitation regime of the gyrokystron, where higher detunings and higher interaction efficiencies are obtained. Nearly all of the qualitative features of the experiment are observed in the simulations, as well as good agreement for the maximum detuning and mode switching points for a particular mode. For a pitch angle $\alpha = 1.9$ and interaction length $\mu = 20$, multimode states tend to form in the simulations, whereas the experiment is nearly always single-moded. The peak measured efficiencies are approximately $\frac{1}{3}$ lower than the best theoretical predictions. Comparisons with theory are rather easily accomplished in the present experiment due to the single-mode output, beam α measurements, and frequency measurements over the entire operating parameter space of the gyrokystron.

An interesting follow-on experiment would be to simply reconfigure the gyrokystron as an oscillator at 85 GHz. By removing the prebunching resonator, higher currents and efficiencies could be obtained to determine the peak experimental values and optimize the electric field in the output resonator using the technique of alpha priming. A study to determine whether the gyrotron continues to operate in a single mode at the 1 MW power level could be performed, since the electron gun is capable of 50 A at a voltage of 90 kV. Reducing the diameter of the mirror holders would allow for radiation measurements with optimized mirror alignment, which may increase the interaction efficiency of the gyrotron.

Replacing one of the output mirrors with a Littrow-mount diffraction grating would also provide insight into the physics of the gyrotron interaction. A grating can be designed to maximize the Q of the fundamental cyclotron harmonic while attempting to spoil the interaction for the second harmonic. This method of output coupling would provide an opportunity to directly examine the transverse mode structure of all frequencies in the output resonator, so that second harmonic modes are no longer trapped. This may increase the output efficiency of the gyrotron if second harmonic radiation is lowering the interaction efficiency of the fundamental.

Present experiments on gyrotrons have concentrated at frequencies near 100 GHz

for the heating of fusion plasmas. If high power millimeter-wave sources with frequencies of 200–600 GHz are required, gyrotrons operating with higher magnetic fields and harmonics of the cyclotron frequency will be needed. One such application is an electromagnetic wiggler for a free electron laser, where the reduced wiggler period greatly reduces the required accelerating voltage for a given output wavelength. For example, a 3 MeV electron beam could generate 6 μm radiation with a QOG wiggler operating at the second harmonic at 240 GHz[63]. Here, the Littrow-mount grating would preferentially reflect the second harmonic so that the resonator round-trip losses are kept to a reasonable level. The QOG is well-suited to the wiggler application since the figure-of-merit is not the output power but the circulating power, which can be quite high in a quasioptical resonator. A phase locked quasioptical gyrokystron at high frequency could also prove valuable in high resolution radar and atmospheric sensing applications[64].

Acknowledgements

This work served as the Ph.D. dissertation of Richard P. Fischer at the University of Maryland. Dr. Victor Granatstein's contributions as advisor at the University of Maryland are gratefully appreciated. Drs. Baruch Levush and Tom Antonsen, Jr. provided the multimode simulation code and their theoretical expertise. The authors acknowledge helpful discussions with Dr. Tom Hargreaves, Marc Barsanti, Dr. Steve Gold, Dr. Tony Ting, Dr. Amnon Fisher, and Carol Sullivan. This work is supported by the Office of Naval Research and the Department of Energy.

References

- [1] J.L. Hirshfield and V.L. Granatstein, "The Electron Cyclotron Maser- An Historical Survey," *IEEE Trans. Microwave Theory Tech.*, vol. MTT -25, no. 6, pp. 522-527, June 1977.
- [2] V.A. Flyagin, A.V. Gaponov, M.I. Petelin, and V.K. Yulpatov, "The Gyrotron," *IEEE Trans. Microwave Theory Tech.*, vol. MTT -25, no. 6, pp. 514-521, June 1977.
- [3] P. Sprangle and W.M. Manheimer, "Coherent nonlinear theory of a cyclotron instability," *Phys. Fluids*, vol. 18, no. 2, p 224, February 1975.
- [4] P. Sprangle and A.T. Drobot, "The Linear and Self-Consistent Nonlinear Theory of the Electron Cyclotron Maser Instability," *IEEE Trans. Microwave Theory Tech.*, vol. MTT -25, no. 6, pp. 528-544, June 1977.
- [5] W.C. Guss, M.A. Basten, K.E. Kreischer, and R.J. Temkin, T.M. Antonsen, Jr., S.Y. Cai, G. Saraph, and B. Levush, "Sideband mode competition in a gyrotron oscillator," Conference Digest of the Seventeenth International Conference on Infrared and Millimeter Waves, pp. 264-265, 14-17 December 1992.
- [6] K. Felch, R. Bier, L.J. Craig, H. Huey, L. Ives, H. Jory, N. Lopez, and S. Spang, "CW Operation of a 140 GHz Gyrotron," *Int. J. Electronics*, vol. 61, no. 6, pp. 701-714, December 1986.
- [7] K.E. Kreischer, T.L. Grimm, W.C. Guss, A.W. Movius, and R.J. Temkin, "Experimental Study of a High-Frequency Megawatt Gyrotron Oscillator," *Phys. Fluids B*, vol. 2, no. 3, pp. 640-646, March 1990.
- [8] W.C. Guss *et al.*, "Sideband mode competition in a gyrotron oscillator," *Phys. Rev. Letters*, vol. 69, no. 26, pp. 3727-3730, 28 December 1992.
- [9] P. Sprangle, J.L. Vomvoridis, and W.M. Manheimer, "Theory of the Quasioptical Electron Cyclotron Maser," *Phys. Rev. A.*, vol. 23, no. 6, pp. 3127-3138, June 1981.

- [10] T.A. Hargreaves, K.J. Kim, J.H. McAdoo, S.Y. Park, R.D. Seeley, and M.E. Read, "Experimental Study of a Single-Mode Quasioptical Gyrotron," *Int. J. Electronics*, vol. 57, no. 6, pp. 977-984, December 1984.
- [11] A.W. Fliflet, T.A. Hargreaves, W.M. Manheimer, R.P. Fischer, M.L. Barsanti, B. Levush, and T. Antonsen, Jr., "Operating characteristics of a continuous-wave-relevant quasioptical gyrotron with variable mirror separation," *Phys. Fluids B*, vol. 2, no. 5, pp. 1046-1056, May 1990.
- [12] A.W. Fliflet, T.A. Hargreaves, W.M. Manheimer, R.P. Fischer, and M.L. Barsanti, "Initial Operation of a High-Power Quasioptical Gyrotron," *IEEE Trans. Plasma Sci.*, vol. PS-18, no. 3, pp. 306-312, June 1990.
- [13] S. Alberti, M.Q. Tran, J.P. Hogge, T.M. Tran, A. Bondeson, P. Muggli, A. Perrenoud, B. Jodicke, and H.G. Mathews, "Experimental Measurements on a 100 GHz Frequency Tunable Quasioptical Gyrotron," *Phys. Fluids B*, vol. 2, no. 7, pp. 1654-1661, July 1990.
- [14] A.W. Fliflet, T.A. Hargreaves, R.P. Fischer, W.M. Manheimer, and P. Sprangle, "Review of quasioptical gyrotron development," *Journal of Fusion Energy*, vol. 9, no. 1, pp. 31-58, 1990.
- [15] B.G. Danly and R.J. Temkin, "Generalized Nonlinear Harmonic Gyrotron Theory," *Phys. Fluids*, vol. 29, no. 2, pp. 561-567, February 1986.
- [16] T. Antonsen, B. Levush, and W.M. Manheimer, "Stable Single Mode Operation of a Quasioptical Gyrotron," *Phys. Fluids B*, vol. 2, no. 2, pp. 419-426, 1990.
- [17] T.A. Hargreaves, A.W. Fliflet, R.P. Fischer, M.L. Barsanti, W.M. Manheimer, B. Levush, and T.M. Antonsen, Jr., "Tilted resonator experiments on a quasioptical gyrotron," *Int. J. Electronics*, vol. 72, nos. 5-6, pp. 807-825, 1992.
- [18] B. Levush and T.M. Antonsen, Jr., "Mode Competition and Control in High-Power Gyrotron Oscillators," *IEEE Trans. Plasma Sci.*, vol. PS-18, no. 3, pp. 260-272, June 1990.

- [19] A. Bondeson, W.M. Manheimer, and E. Ott, "Multimode Analysis of Quasiop-
tical Gyrotrons and Gyroklystrons," *Infrared and Millimeter Waves*. New York:
Academic Press, Vol. 9, 1983, pp. 309-340.
- [20] B. Levush, A. Bondeson, W.M. Manheimer, and E. Ott, "Theory of Quasioptical
Gyrotrons and Gyroklystrons Operating at Higher Harmonics of the Cyclotron
Frequency," *Int. J. Electronics*, vol. 54, no. 6, pp. 749-775, 1983.
- [21] M.Q. Tran, A. Bondeson, A. Perenoud, S. Alberti, B. Isaak, and P. Muggli, "Mul-
timode simulation of the frequency spectrum of a quasioptical gyrotron," *Int. J.*
Electronics, vol. 61, no. 6, pp. 1029-1040, 1986.
- [22] M. Read, R. Seeley, and W.M. Manheimer, "Observation of phase locking in a
single cavity gyrotron oscillator," *IEEE Trans. Plasma Sci.*, vol. PS-13, pp. 398-
404, 1985.
- [23] A.H. McCurdy and C.M. Armstrong, "Mode selection by priming in an overmoded
electron cyclotron maser," *Phys. Fluids B*, vol. 3, no. 1, pp. 212-227, 1991.
- [24] A.H. McCurdy, C.M. Armstrong, W.M. Bollen, R.K. Parker, and V.L. Granat-
stein, "Improved Oscillator Phase Locking by Use of a Modulated Electron Beam
in a Gyrotron," *Phys. Rev. Letters*, vol. 57, no. 19, pp. 2379-2382, November 10,
1986.
- [25] T.M. Tran, B.G. Danly, K.E. Kreischer, J.B. Schutkeker, and R.J. Temkin, "Op-
timization of Gyroklystron Efficiency," *Phys. Fluids*, vol. 29, pp. 1274-1282, 1986.
- [26] W.M. Manheimer, "Theory of the multi-cavity phase-locked gyrotron oscillator,"
Int. J. Electronics, vol. 63, no. 1, pp. 29-47, 1987.
- [27] A.W. Fliflet and W.M. Manheimer, "Nonlinear theory of phase-locking gyrotron
oscillators driven by an external signal," *Phys. Rev. A*, vol. 39, no. 7, pp. 3432-
3443, 1989 April 1.
- [28] W.M. Manheimer, B. Levush, and T.M. Antonsen, Jr., "Equilibrium and Stabil-
ity of free-running, phase-locked, and mode-locked quasioptical gyrotrons," *IEEE*

Trans. Plasma Sci., vol. 18, no. 3, pp. 350-368, 1990.

- [29] A.K. Ganguly and K.R. Chu, "Analysis of two-cavity gyrokystron," *Int. J. Electronics*, vol. 51, no. 4, pp. 503-520, 1981.
- [30] H. Jory, F. Friedlander, S.J. Hegji, J.R. Shively, and R.S. Symons, "Gyrotrons for High-Power Millimeter Wave Generation," *IEDM Digest*, p. 234, 1977.
- [31] H.R. Jory, "Millimeter Wave Gyrotron Development Phase I," Rome Air Development Center, Griffiss AFB, Rome, NY, Tech. Rep. RADC-TR-77-210, 1977.
- [32] A.A. Andronov *et al.*, *Infrared Phys.*, vol. 18, p. 385, 1978.
- [33] W.M. Bollen, A.H. McCurdy, B. Arfin, R.K. Parker, and A.K. Ganguly, "Design and Performance of a Three-Cavity Gyrokystron Amplifier," *IEEE Trans. Plasma Sci.*, vol. PS-13, no. 6, pp. 417-423, December 1985.
- [34] K.R. Chu, V.L. Granatstein, P.E. Latham, W. Lawson, and C.D. Striffler, "A 30-MW Gyrokystron -Amplifier Design for High-Energy Linear Accelerators," *IEEE Trans. Plasma Sci.*, vol. PS-13, pp. 424-434, 1985.
- [35] J.P. Calame, W. Lawson, V.L. Granatstein, P.E. Latham, B. Hogan, C.D. Striffler, M.E. Read, M. Reiser, and W. Main, "Experimental Studies of Stability and Amplification in Four Overmoded, Two-Cavity Gyrokystrons Operating at 9.87 GHz," *J. Appl. Phys.*, vol. 70, no. 4, pp. 2423-2434, 15 August 1991.
- [36] W. Lawson, J.P. Calame, B. Hogan, P.E. Latham, M.E. Read, V.L. Granatstein, M. Reiser, and C.D. Striffler, "Efficient operation of a high-power X-band gyrokystron," *Phys. Rev. Letters*, vol. 67, no. 4, pp. 520-523, 1991.
- [37] S.G. Tantawi, W.T. Main, P.E. Latham, G.S. Nusinovich, W.G. Lawson, C.D. Striffler, and V.L. Granatstein, "High-power X-band amplification from an overmoded three-cavity gyrokystron with a tunable penultimate cavity," *IEEE Trans. Plasma Sci.*, vol. 20, no. 3, pp. 205-215, June 1992.

- [38] W. Lawson, J.P. Calame, B. Hogan, M. Skopec, C.D. Striffler, and V.L. Granatstein, "Performance characteristics of a high-power X-band two-cavity gyrokystron," *IEEE Trans. Plasma Sci.*, vol. 20, no. 3, pp. 216-223, June 1992.
- [39] Private communication.
- [40] V.L. Granatstein *et al.*, "Pulsed power research in the former Soviet Union," Foreign Applied Sciences Assessment Center, Science Applications International Corp., McLean, VA, February 1993.
- [41] A. Yariv, *Introduction to optical electronics*. New York: Holt, Rinehart, and Winston, 1976, p. 69.
- [42] R.N. Clarke and C.B. Rosenberg, "Fabry-Perot and open resonators at microwave and millimetre wave frequencies, 2-300 GHz," *J. Phys. E: Sci. Instrum.*, vol. 15, pp. 9-24, 1982.
- [43] T.A. Hargreaves, R.P. Fischer, R.B. McCowan, and A.W. Fliflet, "Ohmic effects in quasioptical resonators," *Int. J. Infrared and Millimeter Waves*, vol. 12, no. 1, pp. 9-22, 1991.
- [44] R.G. Jones, "Precise dielectric measurements at 35 GHz using an open microwave resonator," *Proc. Inst. Elec. Eng.*, vol. 123, pp. 285-290, 1976.
- [45] Computer code written by K. Yoshioka, with a formulation similar to that found in [46].
- [46] A. Perrenoud *et al.*, "Open resonator for quasioptical gyrotrons: Structure of the modes and their influence," *Int. J. Electronics*, vol. 57, pp. 985-1001, 1984.
- [47] R.P. Fischer, T.A. Hargreaves, and A.W. Fliflet, "Cold tests of quasioptical gyrotron resonators," *IEEE Trans. MTT*, vol. 39, no. 6, pp. 1010-1012, 1991.
- [48] E.L. Ginzton, *Microwave Measurements*. New York: McGraw-Hill, 1957, section 9.2.

- [49] H. Derfler, T.J. Grant, and D.S. Stone, "Loaded Q 's and field profiles of tapered axisymmetric gyrotron cavities," *IEEE Trans. Elec. Devices*, vol. ED-29, no. 12, pp. 1917-1929, December 1982.
- [50] M.N. Afsar and K.J. Button, "Digest of millimeter and submillimeter wave materials information and measurements," Millimeter and Submillimeter Wave Materials Information and Measurement Center, Massachusetts Institute of Technology, pp. 55-58, 1983.
- [51] W.B. Herrmannsfeldt, "Electron trajectory program," Stanford Linear Accelerator Center, Stanford Univ., Stanford, CA, pub. SLAC Report-226, 1979.
- [52] D.B. Montgomery, *Solenoid Magnet Design*. New York: R.E. Krieger Publishing Co., 1980. p. 4.
- [53] W.C. Guss, T.L. Grimm, K.E. Kreischer, J.T. Plevoy, and R.J. Temkin, "Velocity ratio measurements of a gyrotron electron beam," *J. Appl. Phys.*, vol. 69, no. 7, pp. 3789-3795, 1 April 1991.
- [54] A.T. Drobot and K. Kim, "Space charge effects on the equilibrium of guided electron flow with gyromotion," *Intl. J. Electronics*, vol. 51, no. 4, pp. 351-368, October 1981.
- [55] M.E. Read, M.Q. Tran, J. McAdoo, and M.L. Barsanti, "Experimental study of a 115 GHz quasioptical gyrotron with a large cavity," *Int. J. Electronics*, vol. 65, no. 3, pp. 309-325, September 1988.
- [56] K.E. Kreischer and R.J. Temkin, "Mode excitation in a gyrotron operating at the fundamental," *Int. J. Infrared and Millimeter Waves*, vol. 2, no. 2, pp. 175-196, 1981.
- [57] G.P. Saraph, T.M. Antonsen, B. Levush, and G.I. Lin, "Regions of stability of high-power gyrotron oscillators," *IEEE Trans. Plasma Science*, vol. 20, no. 3, pp. 115-125, June 1992.

- [58] H. Kogelnik and T. Li, "Laser beams and resonators," *Proc. of the IEEE*, vol. 54, no. 10, pp. 1312-1329, October 1966.
- [59] T.A. Hargreaves, A.W. Fliflet, R.P. Fischer, and M.L. Barsanti, "Depressed collector experiments on a quasioptical gyrotron," *Phys. Fluids B*, vol. 3, no. 11, pp. 3171-3176, November 1991.
- [60] R.E. Collin, *Foundations of microwave engineering*, New York: McGraw-Hill Book Co., 1966, pg 314.
- [61] R. Adler, *Proc. IRE*, vol. 34, pg 351, 1946.
- [62] T. Antonsen, Jr. and B. Levush, "Influence of thermal spread on space-charge limiting current," *Int. J. Electronics*, vol. 61, no. 6, pp. 871-880, December 1986.
- [63] A.W. Fliflet, R.P. Fischer, and W.M. Manheimer, "New results and applications for the quasioptical gyrotron," NRL Memorandum Report 6793-93-7138, February 26, 1993.
- [64] W.M. Manheimer, "On the possibility of high power gyrotrons for super range resolution radar and atmospheric sensing," *Int. J. Electronics*, vol. 72, no. 5-6, pp. 1165-1189, 1992.